
Doctoral Dissertations

Student Theses and Dissertations

Summer 2024

Understanding Catalyst Design Principles in Transition Metal Mixed Anionic Chalcogenides for Electrocatalytic Energy Conversion

Ibrahim Abdullahi
Missouri University of Science and Technology

Follow this and additional works at: https://scholarsmine.mst.edu/doctoral_dissertations

 Part of the [Materials Chemistry Commons](#)

Department: Chemistry

Recommended Citation

Abdullahi, Ibrahim, "Understanding Catalyst Design Principles in Transition Metal Mixed Anionic Chalcogenides for Electrocatalytic Energy Conversion" (2024). *Doctoral Dissertations*. 3315.
https://scholarsmine.mst.edu/doctoral_dissertations/3315

This thesis is brought to you by Scholars' Mine, a service of the Missouri S&T Library and Learning Resources. This work is protected by U. S. Copyright Law. Unauthorized use including reproduction for redistribution requires the permission of the copyright holder. For more information, please contact scholarsmine@mst.edu.

UNDERSTANDING CATALYST DESIGN PRINCIPLES IN TRANSITION METAL
MIXED ANIONIC CHALCOGENIDES FOR ELECTROCATALYTIC ENERGY
CONVERSION

by

IBRAHIM MUNKAILA ABDULLAHI

A DISSERTATION

Presented to the Graduate Faculty of the
MISSOURI UNIVERSITY OF SCIENCE AND TECHNOLOGY

In Partial Fulfillment of the Requirements for the Degree

DOCTOR OF PHILOSOPHY

in

CHEMISTRY

2023

Approved by:

Dr. Manashi Nath, Advisor
Dr. Lia Sotiriou-Leventis
Dr. Pericles Stavropoulos
Dr. Amitava Choudhury
Dr. Xinhua Liang

© 2023

Ibrahim Munkaila Abdullahi

All Rights Reserved

PUBLICATION DISSERTATION OPTION

This dissertation consists of the following four articles, formatted in the style used by the Missouri University of Science and Technology:

Paper I, found on pages 48–71, has been published in *Molecules*.

Paper II, found on pages 72–102, has been published in *Catalysts*.

Paper III, found on pages 103–166, has been published in *Energy Technology*.

Paper IV, found on pages 167–190, *in preparation*.

ABSTRACT

This research focused on the synthetic design of transition metal mixed anionic chalcogenide catalysts containing various ligand types around the central metal atom (chalcogen anion and chalcogen-based organic ligand) generating diverse crystal structure types applied for water splitting and carbon dioxide reduction reactions (CO₂RR).

A series of catalysts were synthesized starting with isolated metal complexes (ME_n) with a central metal core ($M = \text{Co, Ni, Cu, and Cr}$) through molecular clusters, to bulk nanostructured solids of similar $M-E$ coordination. Bis(dichalcogenoimidodiphosphinato) were employed as ligands in the metal complexes, and anionic chalcogen ($E = \text{S, Se, and Te}$) in bulk solids and metal clusters. This modulates the electron distribution and energy band structure of the catalyst to optimize their performances in electrocatalytic reactions.

The electrochemical oxygen evolution reaction (OER) and hydrogen evolution reaction (HER) performances of cobalt bis(dichalcogenoimidodiphosphinato) complex, chromium molecular cluster, and nickel (telluro) selenide series were studied. Density functional theory was employed to corroborate evolutionary activity trends and to predict OER catalytic performance using a constructed volcano plot in metal chalcogenides.

The molecular chromium carbonyl cluster was studied for electrochemical carbon dioxide reduction reactions (CO₂RR). The catalyst is based on 3d early transition metal that was stabilized by bridging $\mu\text{-Se}$ and CO π -back bonding, increasing the nucleophilic character of the active center. This was capable of transforming CO₂ into value-added C₂ products and was highly selective with high yield, towards ethanol and acetic acid production at -0.9 and -1.2 V vs RHE potential with high faradaic efficiency.

ACKNOWLEDGMENTS

I want to express my profound gratitude to my academic advisor, Dr. Manashi Nath, for her immense support, encouragement, and guidance throughout my Ph.D. with her expertise. Dr. Nath accepted me, motivated me at my lowest point, and gave me all the necessities to complete my Ph.D. work. I can't appreciate you enough.

I sincerely thank the Department of Chemistry, Missouri S&T, for providing financial assistance and resources during my Ph.D. with an excellent opportunity to serve as a teaching and research assistant. I want to use this opportunity to give my warmest thanks to Dr. Sotirious-Leventis Lia, Dr. Stavropoulos Pericles, Dr. Choudhury Amitava, and Dr. Liang Xinhua (Chemical Engineering department) for serving as members of my Ph.D. advisory committee and providing me with valuable feedback and suggestions throughout my Ph.D., especially during annual committee meetings and my comprehensive exams as well as seminar talks.

My most significant appreciation goes to my parents, Alh. Abdullahi Munkaila and Haj. Maimunah A. Usman, my uncle Barr. Usman A. Usman and brother Engr. Ubaidullahi Abdullahi, and all my family members including Serena Thompson, for their continuous support and prayers from day one, and their support through this incredible journey. And to my wife, Rafiatu Nuhu, and my daughters, Aminah Ibrahim Abdullahi and Maryam Ibrahim Abdullahi, for their unconditional love, motivation, encouragement, and for always being there.

TABLE OF CONTENTS

	Page
PUBLICATION DISSERTATION OPTION	iii
ABSTRACT	iv
ACKNOWLEDGMENTS	v
LIST OF ILLUSTRATIONS	xi
LIST OF TABLES	xv
 SECTION	
1. INTRODUCTION	1
2. LITERATURE REVIEW	3
2.1. TRANSITION METAL CHALCOGEN-BASED COMPLEXES	3
2.2. MOLECULAR METAL-CHALCOGENIDE CLUSTER COMPLEXES	6
2.3. TRANSITION METAL CHALCOGENIDES.....	11
2.3.1. Synthesis of Transition Metal Chalcogenides.....	16
2.3.1.1. Hydrothermal/solvothermal.....	16
2.3.1.2. Electrodeposition synthesis.	20
2.3.1.3. Microwave synthesis	22
2.3.1.4. Nanocrystals self-assembly synthesis.	24
2.3.1.5. Hot injection synthesis	25
2.3.1.6. Chemical vapor deposition (CVD) synthesis.	26
2.4. ELECTROCHEMICAL CARBON DIOXIDE (CO ₂) REDUCTION	27
2.5. ELECTROCHEMICAL WATER SPLITTING.....	37

PAPER

I. A MOLECULAR TETRAHEDRAL COBALT-SELENO-BASED COMPLEX AS AN EFFICIENT ELECTROCATALYST FOR WATER SPLITTING	48
ABSTRACT.....	48
1. INTRODUCTION	49
2. METHODOLOGY	53
2.1. MATERIALS	53
2.1.1. Synthesis of Bis(diselenoimidodiphosphinato) Cobalt(II) Complex $[\text{Co}\{(\text{SePiPr}_2)_2\text{N}\}_2]$	53
2.1.2. Electrochemical Measurement.....	53
2.1.3. Tafel Plot.....	54
2.1.4. Turnover Frequency (TOF).....	54
2.1.5. Electrode Preparation.....	55
2.1.6. Electrodeposition of RuO_2	55
3. RESULTS	55
4. CONCLUSIONS.....	65
REFERENCES	66
II. MOLECULAR CLUSTER COMPLEX OF HIGH VALENCE CHROMIUM SELENIDE CARBONYL AS EFFECTIVE ELECTROCATALYST FOR WATER OXIDATION	72
ABSTRACT.....	72
1. INTRODUCTION	73
2. METHODOLOGY	75
2.1. MATERIALS	75

2.1.1. Preparation of Cr-Se Red (decacarbonyltrichromium diselenide ditetraethylamine).	76
2.1.2. Preparation of Cr-Se Green (decahydrated trichromium diselenide ditetraethylamine).	76
2.1.3. Electrode Preparation.	77
2.1.4. Characterization Methods	77
2.1.5. Chronoamperometry Stability Study.	78
2.1.6. Tafel Slope	78
2.1.7. Electrochemical Impedance Spectroscopy (EIS).....	79
2.1.8. Turnover Frequency (TOF).....	79
2.1.9. Mass Activity.	79
2.1.10. Electrochemically Active Surface Area (ECSA) and Roughness Factor (RF)	79
3. RESULTS	80
4. CONCLUSIONS.....	92
SUPPLEMENTARY INFORMATION	93
REFERENCES	97
III. NANOSTRUCTURED TERNARY NICKEL-BASED MIXED ANIONIC (TELLURO) SELENIDE AS A SUPERIOR CATALYST FOR OXYGEN EVOLUTION REACTION.....	103
ABSTRACT.....	103
1. INTRODUCTION	104
2. EXPERIMENTAL PROCEDURE	108
2.1. MATERIALS	108
2.2. METHODS.....	108
2.2.1. Preparation of NiSeTe.....	109

2.2.2. Preparation of NiTe.....	110
2.2.3. Preparation of NiSe.....	110
2.2.4. Preparation of NiSe@NiTe.....	111
2.2.5. Preparation of NiTe@NiSe.....	111
2.2.6. Electrode Preparation.....	112
2.2.7. Characterization Methods.....	113
2.2.8. Chronoamperometry Stability Study.....	115
2.2.9. Tafel Slope.....	116
2.2.10. Electrochemical Impedance Spectroscopy (EIS).....	116
2.2.11. Turnover Frequency (TOF).....	116
2.2.12. Mass Activity.....	117
2.2.13. Density Functional Theory Calculations.....	117
3. RESULTS.....	119
3.1. DENSITY FUNCTIONAL THEORY (DFT) STUDIES.....	136
4. CONCLUSIONS.....	144
SUPPLEMENTARY INFORMATION.....	145
REFERENCES.....	158
IV. CHROMIUM CARBONYL SELENIDE MOLECULAR CLUSTERS COMPLEX AS EFFICIENT ELECTROCATALYTIC CO ₂ REDUCTION INTO C ₂₊ PRODUCT(S).....	167
ABSTRACT.....	167
1. INTRODUCTION.....	168
2. EXPERIMENTAL PROCEDURE.....	170
2.1. MATERIALS.....	170

2.2. METHODS.....	170
2.2.1. Preparation of Cr-Se Clusters (decacarbonyltrichromium diselenide ditetraethylamine)	170
2.2.2. Characterization Methods	171
2.2.3. Electrocatalytic Studies.....	172
2.2.4. Tafel Plots	172
2.2.5. NMR Analysis	173
3. RESULTS	173
4. CONCLUSIONS.....	186
REFERENCES	187
SECTION	
3. CONCLUSIONS AND RECOMMENDATIONS	191
3.1. CONCLUSIONS	191
3.2. RECOMMENDATIONS	192
BIBLIOGRAPHY	193
VITA.....	217

LIST OF ILLUSTRATIONS

SECTION	Page
Figure 2.1. General synthesis of dichalcogenoimidodiphosphate ligand.....	4
Figure 2.2. Examples of chalcogenoimidodiphosphate complexes.	5
Figure 2.3. Examples of bridging metal-chalcogenide clusters.....	8
Figure 2.4. Synthesis of mixed-metal and metal displacement in metal selenotrichromiumcarbonyl cluster via a metal-metal exchange reaction.....	9
Figure 2.5. Schematic illustration of the exfoliation process of CeSe ₂ to increase the number of active sites (Co _{vac}).	15
Figure 2.6. Schematic diagram for the synthesis of MoS ₂ by hydrothermal method.....	19
Figure 2.7. Schematic illustration of two-step solvothermal synthesis of NiSe-Ni _x S _y compound nanocubes.....	20
Figure 2.8. Schematic of combinatorial electrodeposition.	21
Figure 2.9. Schematic illustration of microwave-initiated MoTe ₂ /graphene nanocomposite synthesis for supercapacitor application.	23
Figure 2.10. Schematic illustration for synthesizing Ni _x Se (0.5 ≤ x ≤ 1) nanocrystals	25
Figure 2.11. Scheme illustrating the experimental setup for grown MoS ₂ layers using the CVD method	27
Figure 2.12. Catalyst design strategies for the heterogeneous CO ₂ RR	30
Figure 2.13. (a) Plausible pathways towards CO ₂ RR; (b) Some <i>in situ</i> characterization.	33
Figure 2.14. Possible intermediates of CO ₂ RR during the first adsorption step	35
Figure 2.15. Some metal chalcogenide catalysts are applied in water splitting	38

Figure 2.16. The OER mechanism for acid (blue) and alkaline (red) conditions.....	40
Figure 2.17. The electrochemical water splitting activity of various bulk metal chalcogenide nanomaterials in N ₂ saturated 1.0 M KOH solution at a scan rate of 10 mV s ⁻¹	42
Figure 2.18. Cyclic voltammetry of molecular complexes	44
Figure 2.19. The electrochemical activity of molecular Ni-selenide complex (Ni ^{II} Se ₄) on different substrates in N ₂ saturated 1.0 M KOH solution at a scan rate of 10 mV s ⁻¹	45

PAPER I

Figure 1. Structure and characterization of the [Co{(SeP ⁱ Pr ₂) ₂ N} ₂] complex (CoSe₄ catalyst).....	56
Figure 2. Scheme for electrode preparation.....	57
Figure 3. Electrochemical OER performance for the CoSe₄ catalyst.....	59
Figure 4. Comparison of achieved overpotentials at 10 mAcm ⁻² for CoSe₄ compared with RuO ₂	61
Figure 5. XPS peaks of Co 2p and Se 3d before and after OER activity confirming the stability of the CoSe₄ catalyst.....	62
Figure 6. Schematic illustration of the proposed OER mechanism on CoSe₄ complex.....	63
Figure 7. Polarization curves for HER with the CoSe₄ catalyst in N ₂ -saturated 1.0 M KOH solution at a scan rate of 10 mV s ⁻¹	64

PAPER II

Figure 1. Synthesis and spectroscopic characterizations of Cr–Se red and CrSe green catalysts.....	82
Figure 2. The high-resolution XPS spectra of Cr-Se red complex showing its elemental states	84
Figure 3. The high-resolution XPS spectra of Cr-Se green complex showing its elemental states	85

Figure 4. Electrocatalytic OER activity of Cr–Se red and Cr–Se green complexes	87
Figure 5. Electrocatalytic performance and stability of Cr–Se red and Cr–Se green complexes.....	89
Figure 6. Raman spectra of Cr-Se and Cr-Se clusters, excited with 632.8 nm HeNe laser radiation	91

PAPER III

Figure 1. Schematics describing the (a) Preparation of nickel mixed anionic chalcogenides; (b) Composition of catalyst deposited on nickel Foam (NF).....	119
Figure 2. SEM images of nickel chalcogenide series and their deposition thickness.....	121
Figure 3. XRD spectra of (a) NiTe@NiSe; (b) NiSe@NiTe; (c) NiSeTe; Raman spectra of (d) NiTe@NiSe; (e) NiSe@NiTe; (f) NiSeTe	122
Figure 4. The high-resolution XPS spectra of NiSeTe.....	125
Figure 5. Electrocatalytic OER activity of nickel chalcogenide series.	129
Figure 6. Electrocatalytic OER performance of NiSe@NiTe(black), NiTe@NiSe(violet), NiSeTe (red), NiSe (blue), and NiTe (green) catalysts.....	132
Figure 7. Chronopotentiometry curve of the NiSeTe recorded at 1.51 V for 12 h.....	133
Figure 8. Slab models of (a) NiSe; (b) NiTe; and (c) NiSeTe supercells.....	136
Figure 9. Crystal structures of $3 \times 3 \times 1$ supercells of bulk (a) hexagonal NiSe; (b) hexagonal NiTe; and (c) trigonal NiSeTe	138
Figure 10. Adsorption energies of $\cdot\text{OH}$ and volcano plot of NiSe, NiTe and NiSeTe	140

PAPER IV

Figure 1. Synthesis and spectroscopic characterizations of Cr-Se electrocatalyst.....	174
Figure 2. Characterizations of Cr-Se electrocatalyst.....	175

Figure 3. The high-resolution XPS spectra of the Cr-Se red complex showing its elemental states	176
Figure 4. Electrocatalytic performance of Cr-Se in the presence and absence of CO ₂	178
Figure 5. CO ₂ Reduction products distribution	180
Figure 6. (a) Current density plot for 12 h of chronoamperometry; (b) EIS of Cr-Se electrocatalyst study at the different applied potentials.....	181
Figure 7. Operando XPS spectra of Cr-Se complex after CO ₂ RR at different potentials from -0.3 to -1.2 V vs. RHE	183
Figure 8. The high-resolution XPS spectra of Cr-Se complex after CO ₂ RR at -0.9 V vs. RHE	184
Figure 9. SEM images of Cr-Se cluster before CO ₂ RR.....	185
Figure 10. SEM-EDS of Cr-Se cluster.	186

LIST OF TABLES

SECTION	Page
Table 2.1. The summary of the advantages and disadvantages of various synthetic methods of metal chalcogenides.....	17
Table 2.2. Electrochemical reactions with equilibrium potentials.	36
 PAPER I	
Table 1. Electrochemical parameters of the catalysts measured in 1 M NaOH.	58
 PAPER II	
Table 1. Electrocatalytic parameters compared in Cr-Se catalytic systems.	90
 PAPER III	
Table 1. Electrocatalytic parameter compared in nickel series catalytic systems	128
Table 2. DFT optimized lattice constant and bond lengths of bulk NiSe, NiTe, and NiSeTe structures.	137
Table 3. The bond length of -OH adsorbed NiSe, NiTe, and NiSeTe configurations as well as the shortest distance between -OH and the Ni-series.	141
 PAPER IV	
Table 1. Liquid and gaseous product ratios in electrocatalytic CO ₂ RR	182

1. INTRODUCTION

Addressing climate change issues is, without question, one of the most critical challenges of the current generation. According to the Intergovernmental Panel on Climate Change (IPCC) reports, humanity has caused a rise in global temperature of about 1°C. And it has been estimated that exceeding a value of 1.5°C based on pre-industrial level could lead to catastrophic consequences, including the melting of ice caps, a further rise of sea levels, and even drastic adverse effects on biodiversity[1]. While the world's fossil fuels are depleting, worldwide CO₂ emissions from fossil fuels are rapidly increasing. Even in 2018, emissions increased by more than 2%[1]. Therefore, strategies are needed to prevent further increases in the CO₂ concentration in our atmosphere and reduce existing levels of CO₂.

Scientists have proposed several ways to address these issues by adopting renewable energy sources; wind, solar, geothermal, hydrothermal, nuclear energy, etc. These require places with abundant sunshine, strong wind, or flowing rivers. While others are costly to start or maintain, and their products are complicated to dispose of. More recently, a few technologies have received considerable attention, including water splitting to generate O₂ and H₂, which is a zero-emission higher energy density source of energy and capturing of carbon dioxide as well as its direct conversion into value-added chemicals for the chemical industry, for energy production or as fuel additives[2], as well as other important feedstock for various products. However, on the one hand, these processes are energy intensive due to the chemical inertness of CO₂ and the electricity consumed for hydrogen production from water, usually more valuable than the hydrogen generated, and

hence, has not widely been employed. Subsequently, there is a need for a catalyst to lower the energy barrier and make these processes viable and scalable.

To address these problems, catalysts must be systematically designed and channeled to be used for a specific process (CO₂RR OER, or HER). However, despite the constantly growing number of studies leading to recent significant progress, existing catalysts for CO₂RR, OER, and HER still operate at high overpotentials to achieve reasonable reaction rates and tend to have poor selectivity toward the desired products. Transition metal chalcogenides have been recognized as one of the most promising compounds that could be used for water splitting and CO₂ reduction to address these issues.

Our work is on catalyst design, aimed towards understanding the inherent property of transition metal mixed anionic chalcogenides. First, going from the core of isolated metal complexes with ME_n central core (M = transition metal; E = S, Se, and Te) formed from chalcogen-based organic ligands. A system based on molecular cluster complexes with a more extended structure as well as extended bulk nanostructured solids with a similar $M-E$ bonding nature was also explored. This systematic study will allow for the prediction of the activity in a general material series toward oxygen evolution reaction (OER) in water splitting and carbon dioxide reduction reactions (CO₂RR) and to understand the active sites in those reactions and their evolutionary and activity trends. We explored how the incorporation of chalcogen atoms in carbonyl clusters' cores impacts the selectivity and activity during electrocatalytic CO₂. This study provides a clear and better understanding of catalyst design principles that can yield novel, highly efficient catalysts, which could serve as a bifunctional catalyst for OER at the anode and CO₂RR at the cathode with high product selectivity.

2. LITERATURE REVIEW

2.1. TRANSITION METAL CHALCOGEN-BASED COMPLEXES

Transition metal complexes have broadly been employed in numerous applications, including catalysis, sensing, and medicine. Till today, intense research aiming towards innovation, advancement in existing processes, and practical applications are being developed. Molecular complexes have been used in electrochemical and other electron transfer processes[4–5], where they allow for an in-depth understanding of the intrinsic properties of the isolated core metal center as its electronic structure is influenced by ligands around it[6]. On the one hand, numerous oxygen and nitrogen donor ligand-based molecular complexes have been employed for homogeneous water oxidation catalysts [7–11], and CO₂RR[12–15]; on the other hand, most of the metal–chalcogen-based electrocatalysts reported are solid nanostructured materials with continuous metal–chalcogen[16–19] bonds throughout their lattice structure, some of which are susceptible to deterioration with prolonged use in an alkaline medium. It is still unclear whether transition metal chalcogenides hydrolyze in alkaline media to form surface oxide layers or partially hydrolyze, resulting in mixed (oxy)anionic surface compositions which act as the actual electrocatalyst.

Cobalt is of particular interest because it has the benefit of being relatively low-cost and abundant, exhibits high catalytic activity and stability, and can be used to synthesize a large variety of structural compositions, giving room for tunable catalytic properties[20]. Cobalt complexes exhibit electrochemical properties relevant to catalysis[4,21], but most have been employed as homogenous catalysts for electrochemical

water reduction in non-aqueous media[21,22]. Several cobalt chalcogenide complexes have been synthesized[23,24]. The ligand type used is essential in these complexes since bulk organic ligands predominantly assist in the packing of molecules. In complexes with bridging chalcogenide ligands, for example, $[(\text{Co}(\text{HC}(\text{C}(\text{Me})\text{NC}_6\text{H}_3\text{-}i\text{Pr}_2)_2)^-)_2(\mu, \eta^2\text{-Se}_2)]$ and $[(\text{Co}(\text{HC}(\text{C}(\text{Me})\text{NC}_6\text{H}_3\text{-}i\text{Pr}_2)_2)^-)_2(\mu, \eta^2\text{-Te}_2)]$, the influence of strong specific interactions is shielded. With asymmetric ligands, the periodic packing of the complex tends to get distorted[23].

Dichalcogenoimidodiphosphinate ligands are an exciting class of bidentate and chelating ligands analogous to β - diketonates. They were first generated in the 1960s by Schmidpeter et al.[25], the selenium analog chemistry of these ligands was established by Woollins and co-workers in 1995 [26]. The ligand is made from the reaction of chlorodiisopropylphosphine with bis(trimethylsilyl)amine under an inert atmosphere. The general schematic describing the synthesis of the ligand is shown in Figure 2.1. below.

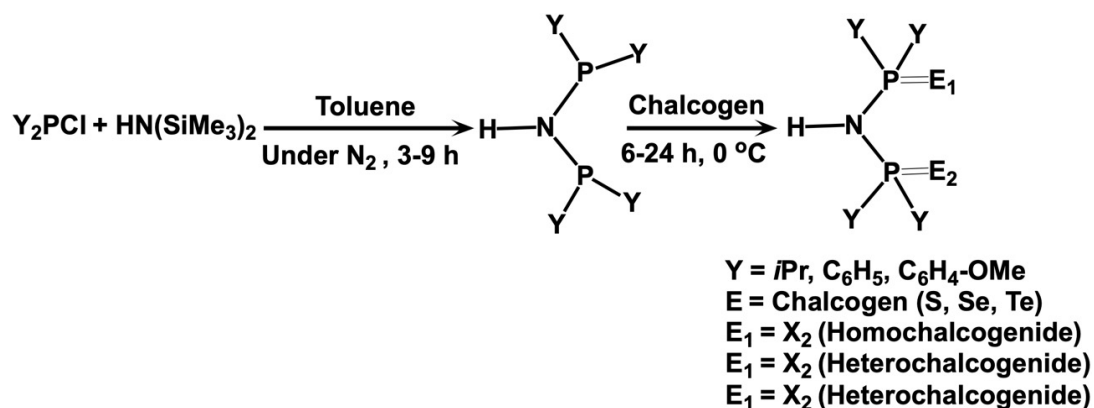


Figure 2.1. General synthesis of dichalcogenoimidodiphosphinate ligand [24,27].

The geometric preferences of the donor chalcogen atoms, combined with the metal ion, have been known to influence the structural features of the resulting complex.

The sodium salt of this ligand reacts in a straightforward metathesis with the metal halide of groups 12 and 15 to yield the corresponding complexes[28]. Actinide–tellurium bonds have also been reported in complexes of La(III) and U(III) compounds[29] as a six-coordinate metal center bonded to three bidentate dichalcogenoimidodiphosphinate ligands through the chalcogen atoms, forming a distorted trigonal-prismatic geometry. The most common chemical structures characterization methods for these molecular complexes include single-crystal x-ray diffraction[24,27], Infrared spectroscopy[24], nuclear magnetic resonance (NMR)[27], and Fast atom bombardment-Mass spectrometry (FAB-MS)[27]. Examples of the synthesis of some of these complexes are shown in Figure 2.2.

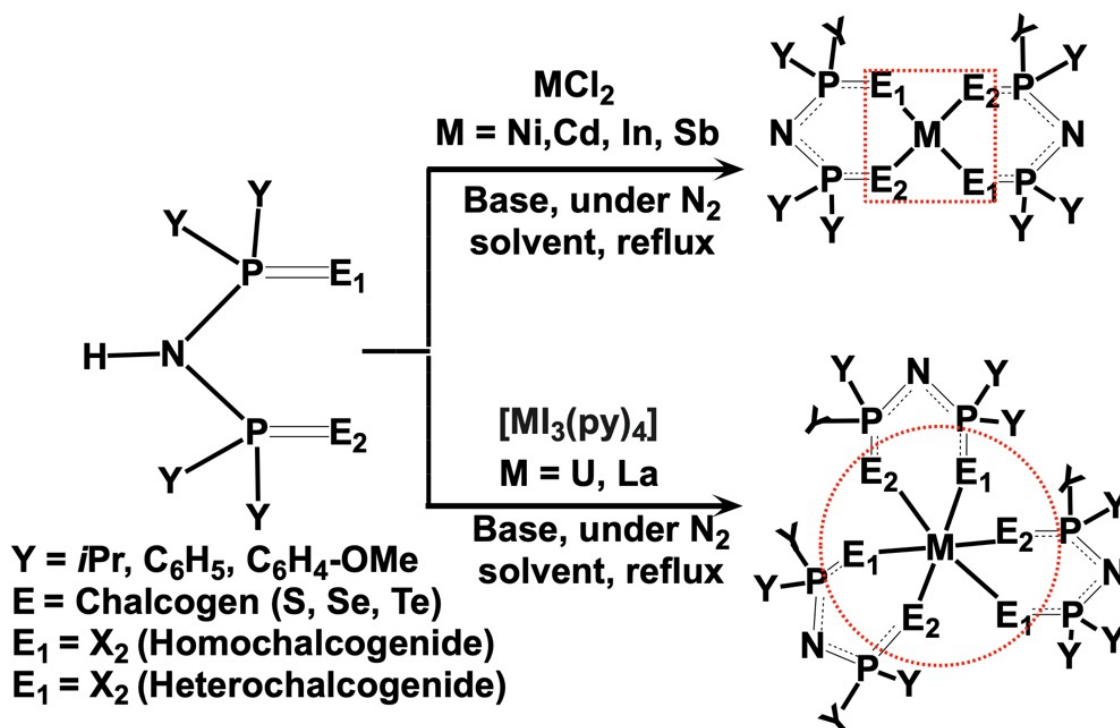


Figure 2.2. Examples of chalcogenoimidodiphosphinate complexes[28,29].

The metal-chalcogen core is highlighted in red; this affects the structural and electron cloud distribution around the metal center, thereby influencing the geometric

structure, and magnetic and electrochemical properties[30–33]. Furthermore, the metal complexes with a more volatile isopropyl-based substituent are specifically captivating because they were found to be excellent chemical vapor deposition (CVD) precursors to produce numerous binary metal selenides. This approach could be used to create thin films of crucial ternary materials such as CuInSe₂ using the thermal decomposition of a simple complex based on copper(I) in the presence of In[N(*i*Pr₂PSe)₂]Cl as an indium precursor[34]. Also, new binary metal chalcogenide thin films have been reported from single-source precursors such as hexagonal Sb₂Te₃ nanoplates[35], In₂Te₃[36], CdTe[37], FeSe and Fe₃Se₄[32].

The investigation of this isolated core of molecular metal complexes with a structural motif obtainable in bulk metal–chalcogenide solids will be an excellent model to understand the effect of anion coordination on the catalytic stability performance and to accurately identify the active surface composition of these transition metal chalcogenide-based electrocatalysts while tuning the electronic structure of these molecular complexes by changing the chalcogenides in the ligand system. This systematic investigation of coordination complexes with changing electronegativity of ligands investigated for OER and CO₂RR catalytic activity has not been studied.

2.2. MOLECULAR METAL-CHALCOGENIDE CLUSTER COMPLEXES

Molecule clusters are compounds consisting of tens of atoms, which are considered a link between molecular and solid-state chemistry[38]. Molecular metal-chalcogenide cluster complexes are a very attractive class of compounds and present complexes with electrochemical, structural, and magnetic properties owing to their high structural symmetry, multinuclear structure type, and chalcogen-bridging, metal-metal

bonds[39–44]. Simple electron-counting rules can predict the oxidation states and structures of molecular clusters and their substituted derivatives [45]. The chemical structures of molecular cluster complexes have been characterized by single-crystal x-ray diffraction[46–49], Infrared spectroscopy[47], NMR[47,50,51], Electron paramagnetic resonance (EPR) spectroscopy[48,52], Electrospray Ionization Time-of-Flight (ESI-TOF) Mass Spectrometry[52], and DFT based on bonding models[48,52–54]. There are two important subclasses of bridging metal-chalcogenide cluster, one in the form of hexanuclear cluster complexes ($M_6E_8L_6$; $M = Cr, Mo, Co, Fe, W, \text{etc.}$; $E = S, Se, Te$; $L = PR_3$) [42,55–57] with cluster cores like those in superconducting metal chalcogenides called Chevrel phases. The M_6E_8 cluster core of group 6, 8, and 9 metal complexes have a valence electron count of $2e^-$ for each μ_3 -E bridge, totally to ($2e^- \times 8 = 32 e^-$) for the eight μ_3 -E bridges, and the remaining electrons are used for the M–M bonding (remaining electrons: 20, 32, or $38e^-$). At the same time, the metal can sometimes have formal mixed valence [52]. They have been made via several approaches depending on the metal employed, some of which include ligand exchange[56] and reductive dimerization[57]. The second class is the $[M_3E_n(CO)_x]^{n-}$, (where $n = 1$ and 2 , $x = 9$ and 10), which has a total of 50 electrons count, typical of the M_3 cluster, which possesses two more electrons than that (48 electrons), hence does not obey Wade's rules.

Most isolated and well-characterized molecular clusters are molecular solid-like compounds, such as polynuclear metal chalcogenide clusters. Therefore, when isolated, it can be acknowledged as distorted fragments of associated solid-state compounds, which makes it fall somewhere between continuous bulk solid and simple molecular complex. Since molecular clusters show remarkable correspondences with their associated extended

solids, some bulk solids have been made from the pyrolysis of their parent molecular clusters; for example, thermolysis of $\text{Cr}_6\text{Te}_8(\text{PEt}_6)$ treated at $315\text{ }^\circ\text{C}$ for $\sim 20\text{ h}$ yields an extended bulk Chevrel phase Cr_3Te_4 solid [43].

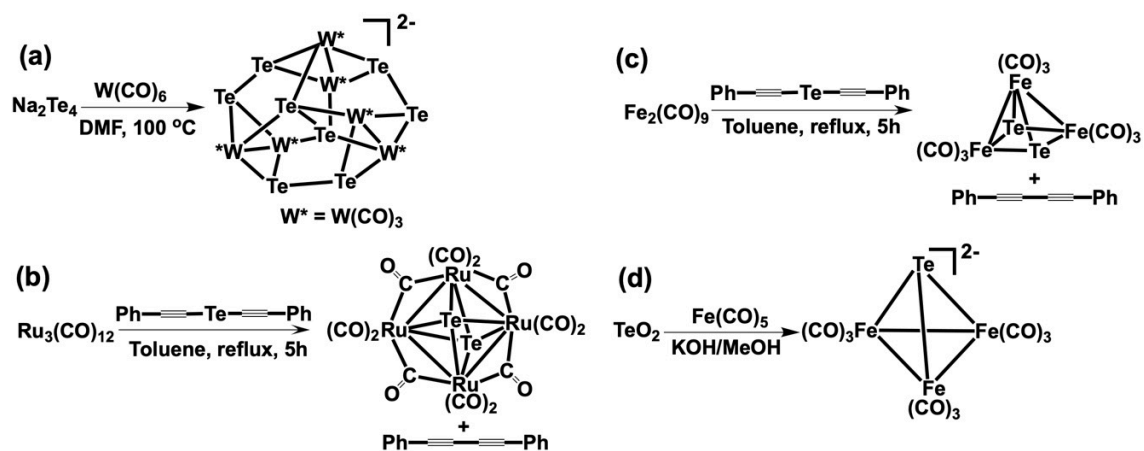


Figure 2.3. Examples of bridging metal-chalcogenide clusters[58,59].

Chromium is an earth-abundant, relatively cheap first-row transition metal that exhibits variable oxidation states (+2, +3, +4, +5, and +6), making it versatile in catalytic reactions. Chromium-based materials have attracted attention in electrocatalysis due to their unique electronic and structural properties[60–62]. Chromium oxide (CrO_x)[63–66] and chromium-based alloys[67,68] have been studied as potential electrocatalysts for various reactions, such as oxygen evolution reaction (OER)[63,69,70] and hydrogen evolution reaction (HER)[71]. The properties of chromium-based electrocatalysts can be tailored by adjusting the material's synthesis method, composition, and morphology. For example, controlling the size and shape of chromium nanoparticles and the surrounding ligands to tune their electronic structure can significantly affect their catalytic activity[72]. Molecular chromium carbonyl clusters are synthesized from a simple chromium carbonyl

precursor[49,59]. The carbonyl precursor has been structurally characterized and assigned an octahedral symmetry of (O_h) as confirmed by IR, proving that all the CO are equivalent.[73] This approach that uses a metal carbonyl precursor and chalcogenide powder precursor in the presence of a concentrated KOH or NaOH is the most practical method for synthesizing molecular clusters[49,50]. During the synthesis, a non-polar solvent (e.g., Toluene, THF, etc.) is used to dissolve the chromium carbonyl; the hydroxide is dissolved in methanol, and a counter-ion source to precipitate the product when the reaction is completed.[74,75]. A synthesis via metal-metal exchange reaction is possible where another metal displaces the metal of a molecular cluster (e.g., see Figure 2.4.)[76].

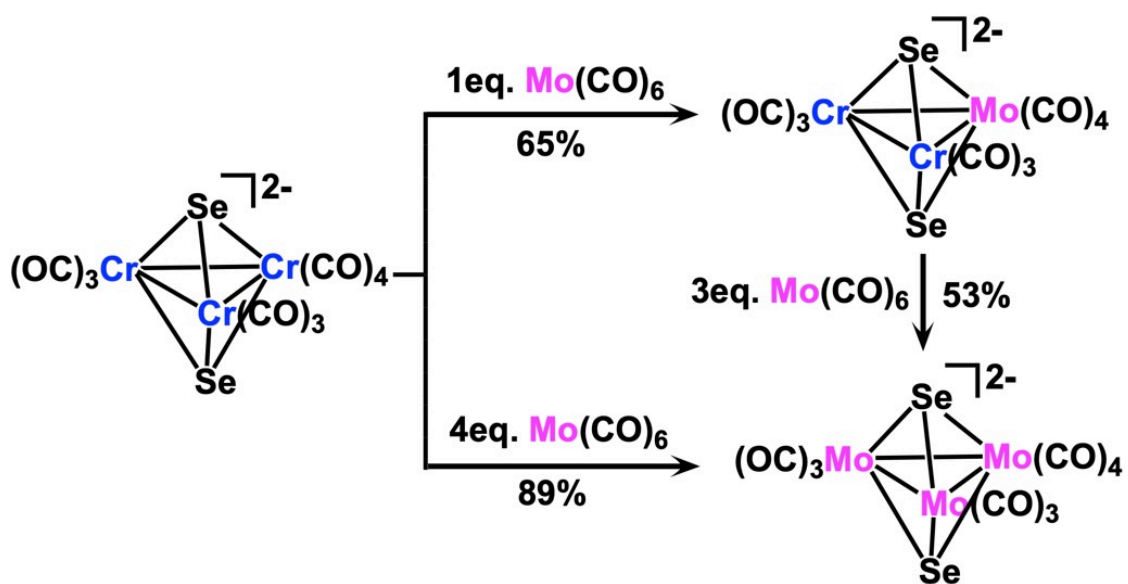


Figure 2.4. Synthesis of mixed-metal and metal displacement in metal selenotrichromiumcarbonyl cluster via a metal-metal exchange reaction.

Although some homometallic chromium carbonyl cluster complexes have been reported[79], many are yet to be tested for applications. This could be because these complex cluster types containing Cr–Cr bonds are uncommon, owing to their relatively

long Cr-Cr bond length, indicating the weakness of the bonds, hence highly unstable. These usually were found in clusters containing stabilizing ligands such as μ_3 -chalcogen and phosphine-based ligands. However, most phosphines are air- and moisture-sensitive, limiting their application. The trichromiumcarbonyl μ_3 -Se stabilized anion complex[51] is potentially interesting for many reasons. First, it contains Cr–Cr bonds stabilized by μ_3 -Se atoms could increase the conductive property of the complex; secondly, it includes a Cr-Se bond with a covalency of interest in electrocatalytic applications. Furthermore, it consists of an early transition metal that can have coordination expansion and could potentially be promising in electrocatalytic applications.

Only minimal reports investigating the intrinsic catalytic activity of complexes based on selenium and late-transition metal have surfaced over the past few years[30]. Chromium is almost between late and early transition metals, so it will exhibit higher reactivity than late transition metals and frequently exhibit different structures and orthogonal reactivity [78]. This can be useful in designing and adopting novel catalysts in water-splitting and CO₂RR. And since Chromium is more oxophilic than late transition metals, it can form hydroxides. Such a phenomenon will be valuable for the catalytic pathway, which is generally initiated by the coordination of hydroxide at the transition metal site. So far, very few early transition-metal complexes have been reported in water-splitting[79,80] and CO₂RR[81,82] applications. Even fewer chromium complexes were documented, especially carbonyl chromium chalcogenide complexes with a tendency to form clusters with Cr–Cr bonds. Here, we studied molecular decacarbonyltrichromium diselenide $[(\text{CO})_{10}\text{Se}_2\text{Cr}_3]^{2-}$ complex as a potential candidate in OER and CO₂RR. Understanding the structural transformations of these clusters and the effect of carbonyl

and changing anion will be relevant in using their complexes in water splitting and CO₂ applications.

2.3. TRANSITION METAL CHALCOGENIDES

Transition metal chalcogenides (TMC) have been known for a very long time; however, only in recent years have these materials been explored for various applications. TMCs are inorganic compounds comprising of ME_x ($E = S, Se, Te$; and $M =$ transition metal) and exhibiting different optical, electronic, magnetic, and catalytic properties[83]. Depending on chalcogen composition and metal type, these materials may have varying structure types and geometry. Furthermore, most TMCs exist as three main polymorphs: trigonal (1T), hexagonal (2H), and rhombohedral (3R) phases. Depending on certain conditions of temperature, solvent, additive addition, synthesis route, or crystallization method, phase transformations can occur in these TMCs. For example, MoS₂ generally crystallizes in the 2H phase consisting of two layers of edge-sharing MoS₆ trigonal prisms per unit cell; however, lithium intercalation led to its transformation into an octahedrally coordinated molybdenum, with one layer per unit cell metastable metallic 1T phase[84]. Due to their unique structural features, the 2H and 1T phases are the most broadly used MoS₂ phases for HER. Moreover, studies have shown that because TMCs have a large surface area, a higher percentage of exposed atoms, and moderate thermo-neutral H-binding energy[85], they exhibit excellent catalytic properties compared to other transition metal catalysts.

Non-precious TMCs with the general formula M_mX_n (M : transition metal; X : chalcogen) include two-dimensional (2D) layered (MX_2) and nonlayered structural materials[86–89]. The 2D layered MX_2 nanosheets generally exhibit unusual physical,

chemical, and electronic properties compared with their bulk counterparts[90–92]. One of the most common structure types is the layered metal dichalcogenides, which is analogous to graphite ME_2 ($E = S, Se, Te$; $M =$ transition metal), where the metal can have varieties of coordination. Examples are MoS_2 , WS_2 , ReS_2 , and NbS_2 [93–96]. Experimental findings have shown that the edges of 2D MX_2 (e.g., MoS_2 and $MoSe_2$) are the electrocatalytic active sites for H_2 production[97]. Moreover, density functional theory (DFT) calculations have shown that the Gibbs free energy for hydrogen adsorption (ΔG_{H^*}) for hydrogen evolution reaction (HER) of MoS_2 is comparable to the state-of-the-art catalyst (Pt), signifying its promising potential toward HER applications[98]. At the same time, the nonlayered TMCs materials have been generally employed as bifunctional electrocatalysts for both OER and HER[99–101]. It has been demonstrated that a partially filled, e.g., band contributes toward the superior OER activity[100]. Even with the incredible progress made in TMC-based electrocatalytic materials, their electrocatalytic activities remain largely limited by their poor electrical conductivity, poor durability over time, serious agglomeration and restacking, inert basal plane, and unfavorable water adsorption and dissociation abilities[102–104]. Over the past few, attempts have been made through some developed strategies to improve the activity of TMC electrocatalysts, which are based on two broad categories as follows:

- (i) Increasing the number of active sites *via* structural engineering:

This could still show limited enhancement in their overall activities because only a tiny fraction of active sites contribute to the electrocatalytic reaction rate[97]. In addition, increasing the catalysts loading onto an electrode has physical limits where further loading would lead to mass/charge transport restriction[105], thereby resulting in a plateau effect,

seen in practice at higher catalyst loadings. Consequently, these shortcomings have triggered the need to develop alternative strategies. This can be done in several ways, including vertical alignment, porous structures, stepped surface structure, nanostructuring, or increasing the loading of catalysts to ensure more active sites.

- (ii) Increasing the intrinsic activity of each active site by controlled tuning of the electronic structure:

This approach revolves around modulating the energy band structure and electron distribution to optimize their performances in electrocatalytic reactions[106]. This is achieved through surface vacancy/defect creation, heteroatom doping, strain regulation, phase transition, and heterostructure engineering. Improving the intrinsic activity results in an appreciable enhancement in the electrode activity while mitigating the mass/charge transport problem from high catalyst loadings. With enhanced inherent activity, the catalyst loadings can be decreased, thereby minimizing the cost of the catalyst. It is important to note that, on the one hand, the intrinsic activity of a suitable catalyst can be more than ten orders of magnitude better than that of a poor one. While on the other hand, a high-loading catalyst is generally only one to three orders of magnitude better than a low-loading[107]. And so, increasing the intrinsic activity through controlled tuning of the electronic structure has a broader spectrum for improving the electrocatalytic activities of TMCs.

The metal oxides (or hydroxides/oxyhydroxides) have shown excellent electrocatalytic abilities for OER and moving the chalcogen series from oxides to other chalcogenides (sulfide, selenides, or telluride) increases the inherent electrical conductivity of the materials. It's been claimed that synthesized metal chalcogenides undergo surface transformation into oxides (or oxyhydroxides) during OER[108,109]. Examples include

sulfides, selenides, and tellurides of first-series transition metals (Mn, Fe, Ni, Co, and Cu)[110–117], the most common of which are the Ni and Co compounds. These materials have been inspected for OER activity to search for potential bifunctionality (HER and OER) to perform the overall water-splitting reaction[19,111,112,118-120]. These chalcogenide compounds were initially applied only in HER due to their excellent fast charge transfer capability as an electronic conductor and their moderate stability in acid/alkaline electrolytes hence less susceptible to corrosion. Furthermore, incorporating foreign metal ions has effectively enhanced the overall OER activity. For example, ternary FeNiS₂ ultrathin nanosheets were investigated to show acceptable performance[108] in which the overpotential was 290 mV at 10 mA cm⁻² with a Tafel slope of 46 mV dec⁻¹. Also, doping of reactive metals, into a metal chalcogenide has getting popular, few studies have shown the that Ni can be been doped in Co_{0.85}Se [121-123]and demonstrated an appreciable enhancement in electroconductivity and improved OER activity with an overpotentials 255 mV and 324 mV at 10 mA cm⁻² for (Ni, Co)_{0.85}Se and Co_{0.85}Se respectively[123]. In addition, it exhibits long-term OER stability, where the overpotential at 10 mA cm⁻² did not change significantly even after 24 hours of operational time. Decorating the surface of (Ni, Co)_{0.85}Se further with LDH by electrodeposition was reported to improve the OER activity of (Ni, Co)_{0.85}Se–NiCo LDH by decreasing the overpotential even lower to about 216 mV[123]. In addition, doping can be done through the nitrogen of carbon material; for example, MnSe@MWCNT catalyst composite and CoSe₂ nanobelts synthesized on nitrogen-doped graphene support were found to exhibit a very low overpotential of 290 mV and 366 mV to achieve 10 mA cm⁻², respectively. Both with OER kinetics evidenced a small Tafel slope of around 54.76 mV dec⁻¹ and 40 mV

dec^{-1} , which outperforms state-of-the-art RuO_2 and other oxide-based electrocatalysts [101,118]. In layered systems like CoSe_2 , where the exfoliation process can further increase the active sites, this was reported to expose the more active site and improve the OER activity[100] (Figure 2.5.).

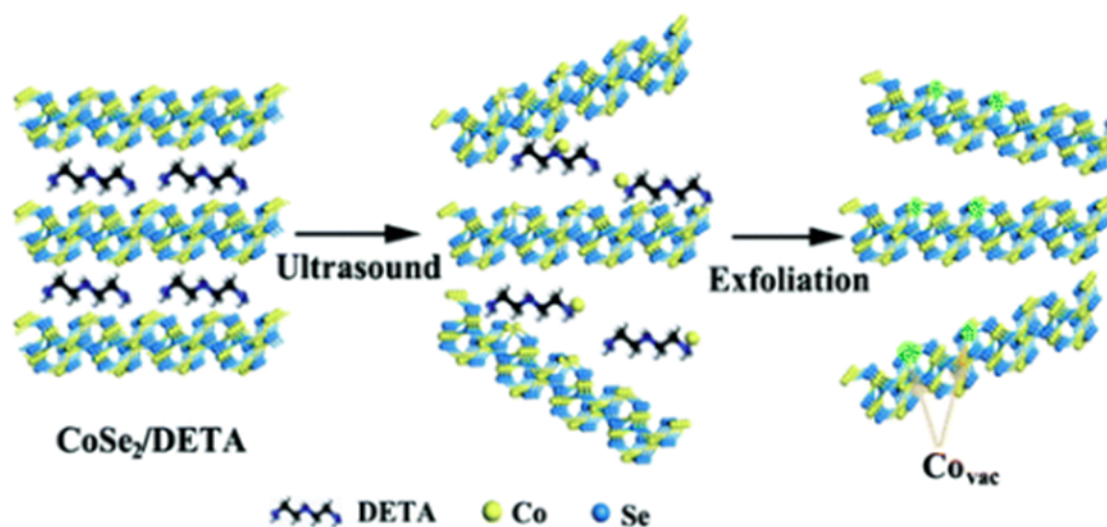


Figure 2.5. Schematic illustration of the exfoliation process of CoSe_2 to increase the number of active sites (Co_{vac})[100].

Not all metal chalcogenides undergo phase transformation during OER. The structural characterization using XRD, Raman spectroscopy, and elemental analysis of Ni_3Se_2 before and after OER activity were similar, indicating that the OER activity of Ni_3Se_2 could be attributed to its intrinsic activity and stability[110]. It is worth mentioning that reports have shown that a high-index facet Ni_3S_2 nanosheet material with a similar crystal structure as Ni_3Se_2 has demonstrated excellent electrocatalytic ability both for HER and OER in 1 M KOH electrolyte with outstanding stability over 150 hours. This high durability of Ni_3S_2 for overall water-splitting could be attributed to the intrinsic stability of this phase[124].

2.3.1. Synthesis of Transition Metal Chalcogenides. The method employed in synthesizing any material greatly influences the structure and properties of the materials, including morphology, particle size, dispersibility, and crystallinity. Even though the composition of the same catalyst prepared using different methods is the same from the same constituents and dosages, the catalytic performance of the prepared catalyst may still vary depending on some of the properties mentioned above differences. Subsequently, considering the advantages and disadvantages of the preparation method is crucial in choosing the most suitable method for synthesizing a catalyst based on the end catalytic application. Transition metal-based chalcogenides electrocatalysts have been prepared using various approaches, including electrodeposition[110,120,125], hydrothermal or solvothermal treatment[103,126–128], Chemical vapor deposition (CVD)[129-132], microwave irradiation[133-135], and hot injection method[136], solid phase chemical synthesis, self-assembly of nanocrystals and ion exchange method have been widely reported[137-141]. Different synthesis methods can be used to obtain specific physical and chemical properties for varieties of applications, as shown in Table 2.1.

2.3.1.1. Hydrothermal/solvothermal. Hydrothermal synthesis is a standard synthesis method in transition metal chalcogenides material synthesis, which is simple, universal, and flexible to control the composition and morphology of the material. Most TMC catalyst materials could be made this way, provided the reaction conditions are well maintained, particularly when selecting an appropriate precursor reagent. Since the method employs moderately high temperature and pressure to drive the reaction, generally, the boiling point of a solvent (water or organic solvent) is always lower than the reaction temperature. And as the temperature increases, a high pressure is established in the closed

system to enhance the reaction and promote the crystallinity. Several catalyst compositions have been synthesized in Dr. Nath's group by a simple and scalable hydrothermal strategy and drop-casted on carbon fiber cloth (CFC), most of which have been tested as stable bifunctional electrocatalysts for overall water splitting[19,112,118]. Other reported were Cu-doped Co_3Se_4 , such as CuCo_2Se_4 synthesized through a one-step hydrothermal method,

Table 2.1. The summary of the advantages and disadvantages of various synthetic methods of metal chalcogenides.

Methods	Advantages	Disadvantages
Solid phase Chemical	<ul style="list-style-type: none"> ● Low cost 	<ul style="list-style-type: none"> ● Low purity
	<ul style="list-style-type: none"> ● Simple equipment and process ● Rapid reaction rate 	<ul style="list-style-type: none"> ● Uneven morphology ● High temperature
Hydro/solvothermal	<ul style="list-style-type: none"> ● High selectivity and efficiency 	<ul style="list-style-type: none"> ● Unclear reaction mechanism
	<ul style="list-style-type: none"> ● Good dispersion ● Controlled morphology 	<ul style="list-style-type: none"> ● Use of surfactants ● Time-consuming
Electrodeposition	<ul style="list-style-type: none"> ● Any conducting substrate 	<ul style="list-style-type: none"> ● Precursor must dissolve in solvent
	<ul style="list-style-type: none"> ● Thin films ● Directly grown on substrates 	<ul style="list-style-type: none"> ● Difficult to control composition ● Non-Uniform growth
Hot-injection	<ul style="list-style-type: none"> ● Uniform size and morphology 	<ul style="list-style-type: none"> ● Small organic molecules residuals removal
	<ul style="list-style-type: none"> ● High crystallinity ● Controlled morphology 	<ul style="list-style-type: none"> ● Low yield ● Difficult to scale up.
Self-assembly of nanocrystals	<ul style="list-style-type: none"> ● Wide application 	<ul style="list-style-type: none"> ● Delicate control of the reaction process
	<ul style="list-style-type: none"> ● Ordered multistage nanostructure ● Rapid reaction rate 	<ul style="list-style-type: none"> ● High-quality nanocrystals required ●

Table 2.1. The summary of the advantages and disadvantages of various synthetic methods of metal chalcogenides (cont.).

Ion exchange	<ul style="list-style-type: none"> ● High selectivity and efficiency 	<ul style="list-style-type: none"> ● Relatively low
Microwave	<ul style="list-style-type: none"> ● Cost effective 	<ul style="list-style-type: none"> ● Difficult to scale-up
	<ul style="list-style-type: none"> ● Shorten crystallization time 	<ul style="list-style-type: none"> ●
	<ul style="list-style-type: none"> ● aggregation of nanostructures 	<ul style="list-style-type: none"> ●
Chemical vapor deposition (CVD)	<ul style="list-style-type: none"> ● High efficiency for 2D nanocrystals 	<ul style="list-style-type: none"> ● Specific equipment required
	<ul style="list-style-type: none"> ● Multi Heterostructure engineering 	<ul style="list-style-type: none"> ● High temperature
		<ul style="list-style-type: none"> ● Limited application

providing a novel composition of excellent bifunctional HER and OER electrocatalysts made from cost-effective and earth-abundant transition metals[126].

A simple two-steps hydrothermal approach has been reported in synthesizing Ti@Ni_{0.85}Se electrodes with a triple hierarchy architecture and employed in water splitting[142]. Similarly, 3D MoSe₂/NiSe₂ were made hydrothermally and drop-casted on carbon fiber paper (CFP) to test in water splitting; it demonstrated an improved electrocatalytic activity for HER[103]. Molybdenum disulfide (MoS₂) with reduced graphene oxide (RGO) nanocomposite was synthesized using hydrothermal methods, and their thermoelectric properties were studied and found to exhibit higher thermoelectric performance[127]. The synthesis schematics are shown in Figure 2.6. Compounds that are moisture/water sensitive (reacted with water, hydrolyzed, decomposed, or unstable) cannot

be made via the hydrothermal method, so a different approach must be adopted; this promotes the generation and development of the solvothermal process.

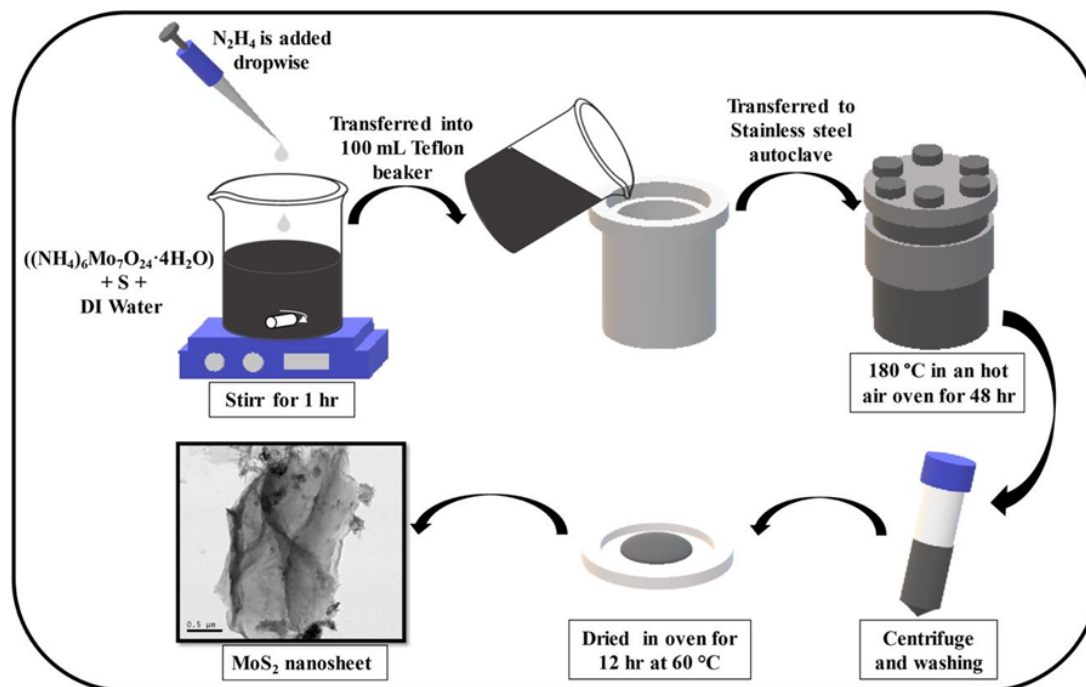


Figure 2.6. Schematic diagram for the synthesis of MoS₂ by hydrothermal method[127].

The solvothermal method was developed on the principles of the hydrothermal process to replace it in the case of the synthesis of water-sensitive compounds. This differs from the hydrothermal reaction by the solvent used, where an organic solvent is employed instead of water. In addition, compared with the hydrothermal method, the solvothermal process can better control phase formation and particle size and has better dispersion[143]. The comparative study of Ni_{0.85}Se nanocrystalline materials synthesized in *N*-dimethylformamide (DMF) solvothermal reaction gave superior electrocatalytic performance compared to the hydrothermally synthesized Ni_{0.85}Se[144]. It can be attributed to the better dispersion of the solvothermal method, making the size distribution

more uniform, in addition to its rough surface morphology and porosity of the catalyst. Furthermore, $\text{NiSe-Ni}_x\text{S}_y$ has been synthesized using a simple two-step solvothermal method[145]. A uniform array of NiSe/NF nanocubes was obtained in DMF, providing a large specific surface area and a uniform conductive substrate. This was followed by an ion exchange reaction that partially replaces Se^{2-} with S^{2-} during solvothermal sulfurization leading to the formation of $\text{NiSe-Ni}_x\text{S}_y/\text{NF}$ [145] (Figure 2.7.).

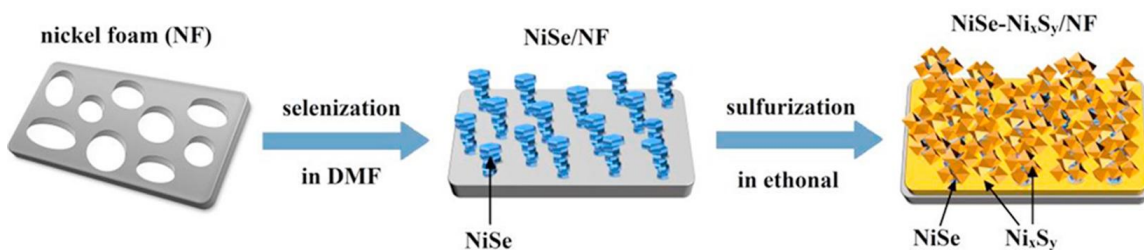


Figure 2.7. Schematic illustration of two-step solvothermal synthesis of $\text{NiSe-Ni}_x\text{S}_y$ compound nanocubes[145].

Another example of a unique hydrothermal synthesis is the transformation of porous $\beta\text{-Ni}(\text{OH})_2$ nanoplates formed by selective etching into mixed porous metal hydroxide and metal sulfide nanoplates by simple hydrothermal method[146]. Some of the major cons of hydrothermal and solvothermal processes are that the reaction mechanism is ambiguous and unclear, and the reaction time is usually long, mainly because the chemical reactions are generally different from the normal state, and a long reaction time is required to obtain a stable and pure catalyst.

2.3.1.2. Electrodeposition synthesis. Electrodeposition is a simple and cost-effective method to directly prepare and grow nanomaterials on current collectors with various morphologies. The nanomaterials were deposited on the surface of substrates by

cathodic reduction reaction in an aqueous or organic solvent, in which the precursors were dissolved. Commercial nickel foam (NF), carbon paper (CC), Cu foam (CF), stainless steel (SS), and carbon fiber cloth (CFC) are generally employed as substrates. Several metal-doped Ni series have been synthesized using electrodeposition methods. A typical experimental setup is shown in Figure 2.8. Simple potential electrodeposition using a nickel salt and selenium oxide precursor to produce a nickel selenide phase at room temperature in the open air was reported to be successfully achieved and exhibited good catalytic performance in HER and OER[147]. A. T. Swesi reported the synthesis of Ni_3Se_2 via electrodeposition on Au-coated glass, Au-coated Si, glassy carbon (GC), ITO-coated glass, and Ni foam, and was found to show high OER activity[110]. It was explained that the electrodeposition parameters, such as deposition time and pH of the electrochemical bath, annealing, and the nature of the substrate, greatly influence the activity. X. Cao reported the quaternary mixed-metal selenide compositions by incorporating Ni-Fe-Co through combinatorial electrodeposition to explore the ternary phase diagram of Ni-Fe-Co systems shown in Figure 2.8.[128].

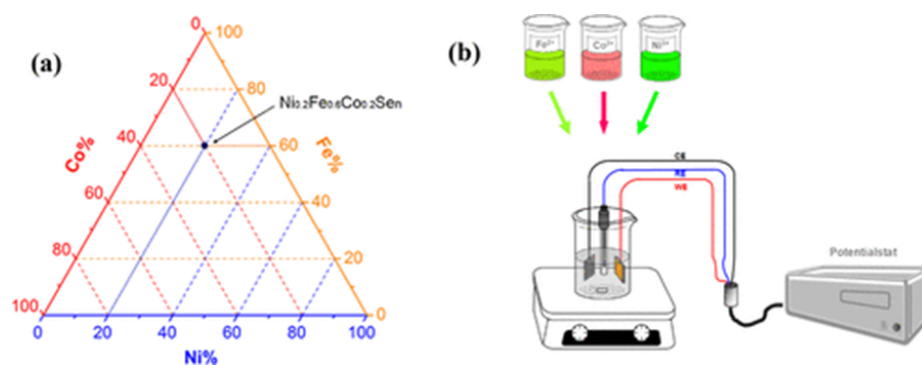


Figure 2.8. Schematic of combinatorial electrodeposition. (a) Ternary phase diagram for exploring compositions of the mixed-metal selenide (b) Typical experimental set-up for electrodeposition[128].

The drawback of electrodeposition is that the voltage and current may be unstable, which leads to the nonuniformity of the prepared nanomaterials and affects the electrocatalytic performance.

2.3.1.3. Microwave synthesis. Microwave irradiation involves electromagnetic waves in the range of 1 mm – 1 m (300 MHz–300 GHz). Generally, microwave ovens or microwave reactors' electric field in the waveguide was defined at a frequency of 2.45 GHz. Microwave irradiation produces effective internal heating by directly coupling microwave energy with the precursor and solvent molecules[133]. The heating in microwave radiation has been associated with two main mechanisms: dipolar polarization and ionic conduction. And it depends on the ability of the heated materials to absorb microwaves and convert them into heat. A microwave-assisted synthesis method is an elegant approach that is easy to operate, efficient, and cost-effective compared to hydrothermal methods. It promotes the reduction of metal precursors and nucleation of metal clusters, thereby reducing the crystallization time and minimizing the aggregation of nanostructures. S. Anantharaj et al. proposed a cheap, faster, and easy method of microwave-assisted synthesis that does not require sophisticated equipment and eliminates high-temperature and-pressure reactions. Here, a hierarchical 3D nano assembly of Ni₃Se₄ was fabricated on Ni foam in a comparatively more straightforward methodology using NaHSe solution as the Se source with the assistance of a simple microwave initiation (300 W) for the first 3 min and 5 h of aging at RT. The fabricated Ni₃Se₄ nano assemblies have demonstrated excellent HER and OER activity with the lower Tafel slopes suggesting its superior electrocatalytic bifunctional water-splitting. This proposed synthesis method can be chosen for the facile formation of other metal chalcogenides on suitable

substrates[133]. Furthermore, Zheng et al. proposed the rapid microwave-assisted synthesis of layered and tubular interwoven carbon nanotube (CNT) coated NiSe₂ nanosheets (NiSe₂@CNT) within 2 min for high-performance supercapacitors. Another excellent green, universal, and scalable approach for synthesizing micro-/nanostructured metal chalcogenides from elemental precursors was reported by K. Ding et al. [134].

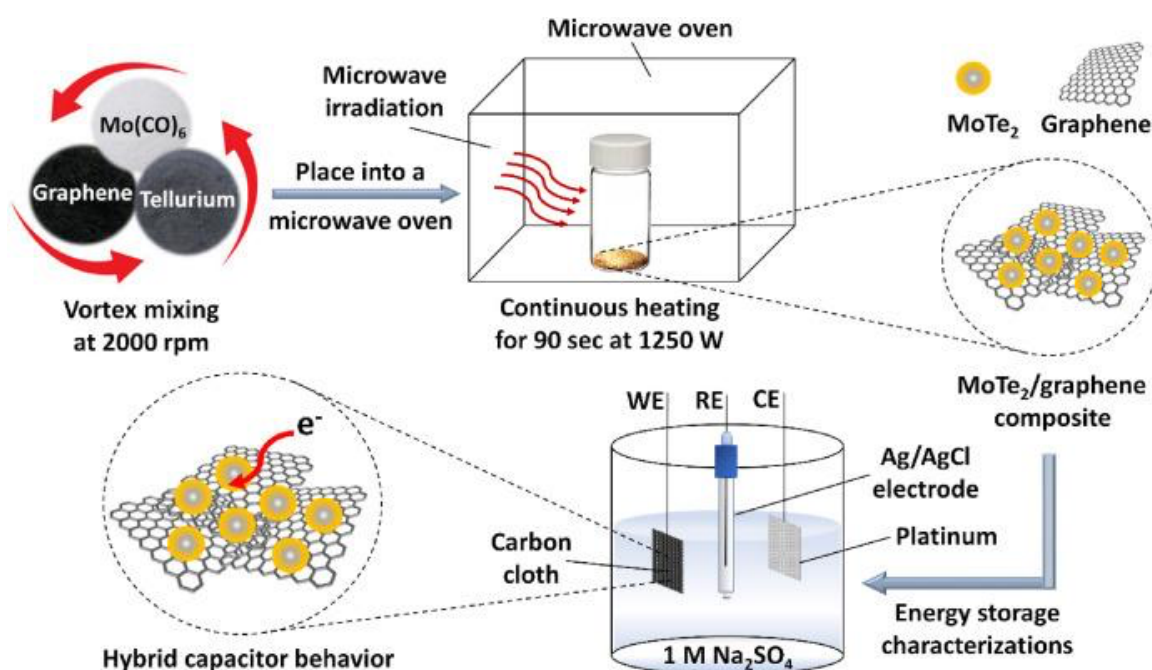


Figure 2.9. Schematic illustration of microwave-initiated MoTe₂/graphene nanocomposite synthesis for supercapacitor application[135].

The method suggests that all chalcogens, sulfur, selenium, and tellurium have excellent solubility in phosphonium ionic liquids. Upon microwave-assisted heating this promotes faster kinetics between the chalcogens and various metal powders, producing nanocrystalline materials[134]. S. Sarwar et al. reported a fast and facile microwave-irradiated synthesis approach to making 2D-molybdenum ditelluride nanosheets deposited

on graphene substrate (MoTe₂/graphene), as shown in Figure 2.9. This method constitutes a clean, ultrafast (90 seconds) synthetic approach employing microwave heating without inert gas protection or intense facilities. To yield a nanostructured hybrid material that could be used as an efficient energy storage material[135].

2.3.1.4. Nanocrystals self-assembly synthesis. Self-assembly of nanocrystals is a synthesis method in which pre-synthesized a spontaneously self-arrange of nanocrystals into an ordered structure, fundamentally due to weak interactions between nanocrystals such as electrostatic, van der Waals, and hydrogen bonding[137, 148–151]. Various nano architectures can be created with integrated or multi-catalytic functionality. Recently, many scientists found interest in developing self-assembly strategies for nanocrystal fabrication and application. This is now an emerging method widely employed in metal chalcogenide synthesis. The synthesis of a highly ordered Cu₂S multilayer superlattice was reported via a self-assembly approach, in which these highly uniform Cu₂S were formed in a confined reaction at water–oil interface[150]. This technique provides a simple bottom-up approach to create numerous self-assembled metal chalcogenide superlattices structures by providing controllable size and shape of the pre-synthesized block nanocrystals for integrating nanocrystals, as well as their properties for the potential applications in catalysis and energy conversion devices.

Similarly, self-assembled ZnS 2D superlattices with two interesting morphologies, hexagonal bipyramid, and hexagonal bipyramid, were reported by Donega et al.,[148]. The self-assembly process was found to be driven by interfacial free-energies minimization and packing density maximization, while assembly structure determines the

morphology structure. This emphasizes the importance of precise morphology control in the self-assembly field.

2.3.1.5. Hot injection synthesis. Hot injection is a standard method for preparing monodisperse colloidal nanocrystals with controllable particle size, shape, morphology, and composition. Typically, this method starts with a fast addition by injecting the reactants into a hot reaction solution containing a critical surfactant. A series of nickel selenide nanocrystals Ni_xSe ($0.5 \leq x \leq 1$) was prepared by Zheng et al. with the following crystal phases; NiSe and $\text{Ni}_{0.85}\text{Se}$ as pure hexagonal), $\text{Ni}_{0.75}\text{Se}$ and Ni_3Se_4 as monoclinic, and $\text{Ni}_{0.5}\text{Se}$ and NiSe_2 as cubic with accurate phase and controlling component by adjusting the addition dosage and raw material ratio using a rapid and ambient pressure thermal injection method (Figure 2.10.)[136].

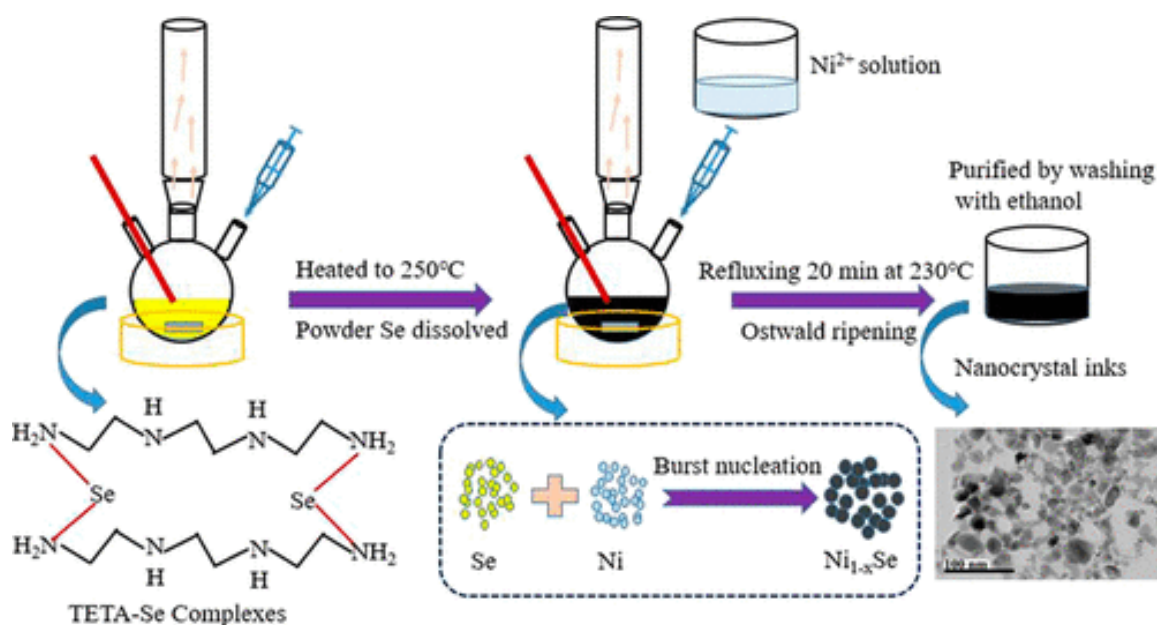


Figure 2.10. Schematic illustration for synthesizing Ni_xSe ($0.5 \leq x \leq 1$) nanocrystals[136].

Furthermore, an even anchor NiSe nanocrystalline on carbon nanofibers (CNFS) was made simply by hot injections to prepare CNFs@NiSe core/shell nanostructures that can be used for selective conversion of methanol and hydrogen production[152]. This method yields high-quality nanomaterials; however, transforming metal precursors to the corresponding metal-chalcogenide generally requires high temperatures, which limits their widespread application outside of lab-scale synthesis. Also, long-chain surfactants are generally employed in the reactions and are difficult to remove after the reaction, which poisons for catalysis, batteries, and other energy storage applications. Furthermore, the solvent choice is limited due to the high boiling point solvent requirement since a high temperature is usually required for the metal precursor to be converted to metal chalcogenide.

2.3.1.6. Chemical vapor deposition (CVD) synthesis. CVD is an exciting synthesis technique with the promising capability to fabricate high-quality TMC layers with controllable size, manipulative thickness, and superior electronic properties. The generated TMC films can be used as the active components for nanoelectronics and as the building blocks for layered heterostructures. Currently, the CVD or CVD-like methods are the only techniques available that can be used to achieve wafer-scale TMCs[129, 130]. The conventional CVD setup used to grow 2D TMCs such as MoS₂ is illustrated in Figure 2.11. In the process, a crucible containing a chalcogen powder (precursor 1) is loaded upstream in the low-temperature region of the furnace. Large MoS₂ monolayers with excellent optical and electrical properties have been CVD-grown by sulfurization of a Mo film and MoO₃[153]. The growth of MoS₂ monolayers follows the typical vapor–solid–solid (VSS) mode, where sulfur and MoO₃ powders are heated to vaporize. In contrast, transition metal oxide powder (precursor 2) and growth substrates are loaded in the high-temperature center

of the furnace at some intervals, as shown in Figure 2.11. An inert carrier gas transports these vapors onto the growth substrates to initiate the chemical reaction. This leads to the nucleation and growth of solid MoS₂ monolayers. The CVD growth technique has become the universal method for fabricating various 2D TMDC monolayers[130]. However, CVD is not without challenges. One is that more critical growth conditions are required to grow some compositions, e.g., WSe₂ monolayers[92].

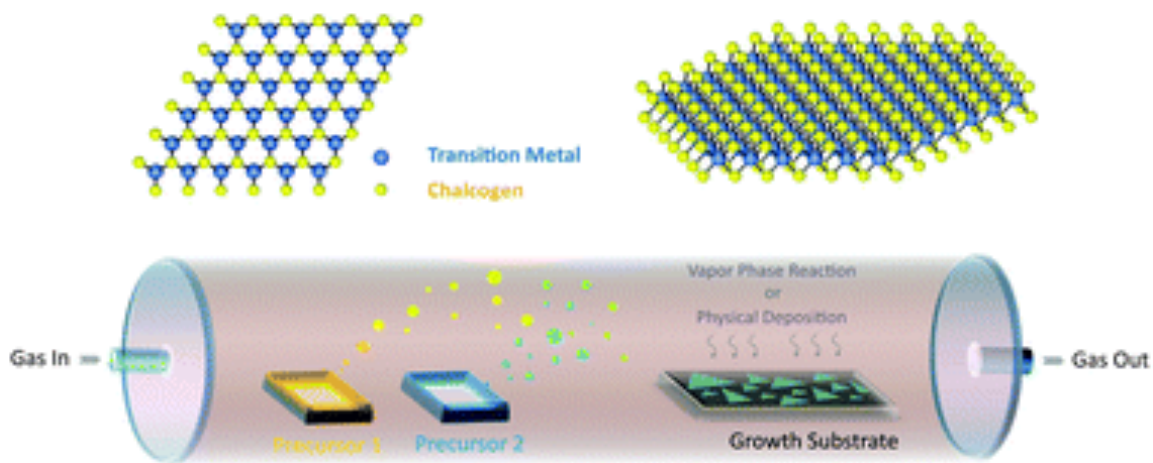


Figure 2.11. Scheme illustrating the experimental setup for grown MoS₂ layers using the CVD method.

Understanding these synthesis methods, their advantages and disadvantages, and the properties of the obtained transition metal chalcogenide product(s) are crucial in determining the best way to fabricate electrodes for a specific application(s).

2.4. ELECTROCHEMICAL CARBON DIOXIDE (CO₂) REDUCTION

The natural escape route for atmospheric CO₂ is jgenerally allowed through sequestration by forest cover on the Earth's surface, which over the past several decades has been depleted significantly due to deforestation and industrialization, paving the way

for the industrial landscape. The current CO₂ level has exceeded 400 ppm in the atmosphere, so CO₂ sequestration and storage alone will not be sufficient to combat this issue[154]. Subsequently, a practical solution is urgently needed that will allow for the transformation of this vast amount of atmospheric CO₂ into valuable chemical products, as a result, closing the loop. The conversion of CO₂ gas through electrochemical CO₂ reduction reaction (CO₂RR) into various value-added products is an important step towards addressing the problem of global warming. However, the chemical inertness of CO₂ makes its reduction an extremely challenging task, which requires an energy source and a catalyst to accelerate the reaction rate and improve the selectivity of products in the reaction[155]. Over the past few decades, colossal research has been conducted to transform CO₂ using Pt, Pd, Ru, Au, Ag, and their alloys[156-161] both in heterogeneous[156,158] and homogeneous[157,159] catalysis. These catalysts are costly and hence scalability is limited.

More recently, several non-precious transition metal-based catalysts have been identified for CO₂RR. However, these catalysts are limited in the product type and selectivity of products obtained. Generally, CO₂RR product(s) is represented by (C_{≥x}, where x=1,2,3 or 4) depending on the mechanism of formation and extent of C–C linkage. Commonly, Cu and Ni-based catalysts have been observed to produce a mixture of predominantly C₁ products, consisting primarily of carbon monoxide (CO), formate ion, and a small relative quantity of methanol and formaldehyde[162-164]. This poses two main concerns: selectivity towards desirable products is horrendous, and CO being very toxic, is highly undesirable and must be transformed into something useful, e.g., syngas, thereby reducing the efficiency and increasing the overall cost of the process. Despite the

constantly growing number of studies leading to recent significant progress, existing catalysts still operate at large overpotentials to achieve reasonable reaction rates. The selectivity toward the desired products is often low. A highly selective direct electrochemical reduction of CO₂ to alcohols or other value-added hydrocarbons with a higher carbon content (C₂ or higher) is more desirable.

Copper-based catalysts have drawn much attention due to the range of reduction products they can generate at standard conditions and the considerably low electrochemical applied potential for CO₂ reduction[165,166]. Both bulk and nanoparticles of Cu were observed to produce CO and CH₄[165,166] primarily. Cu was also reported to have produced C₁–C₃ CO₂RR products[165-168]. The nanoparticles size, morphology, and surface roughness of Cu catalyst in CO₂RR have been reported to influence the faradaic efficiency, product(s) type, and product selectivity[168-170]. For example, C₂ products are generated with surface oxidized Cu films[167], while Cu nanocrystals produce formic acid (HCO₂H) at low potential V (vs. RHE)[165]. Cu₂O has also been reported as an electrocatalyst towards CO₂RR[163].

In general, even though Cu electrocatalyst has proven to be cost and energy efficient for CO₂RR, there is a limitation in the selectivity of product at room temperature under ambient conditions[174-178]. Furthermore, they suffer from numerous drawbacks, including the poisoning of the catalyst surface by CO and other reaction intermediates and the subsequent deactivation of the catalysts shortly after[170,177]. Modifying the metal surface with oxide layers could minimize catalyst poisoning and prevent deactivation. However, studies have shown that although using ZnO support with Cu₂O electrode

demonstrates sustained catalytic activity towards CO₂RR, decreases the faradaic efficiency of the hydrocarbon products, leading to less product selectivity[178].

Aside from Cu-based catalysts (Cu₂O)[163,174,178], other transition metal chalcogenides have demonstrated good activity for the CO₂RR, such as WSe₂ and MoSe₂[179-181]. Copper sulfide has been tested theoretically and experimentally for CO₂RR, and formate was selectively produced in an aqueous electrolyte, while CO was produced only in trace amounts.[182] Several molecular-based complexes in the literature are reported for CO₂RR, most of these complexes are porphyrin-based complexes[12-15].

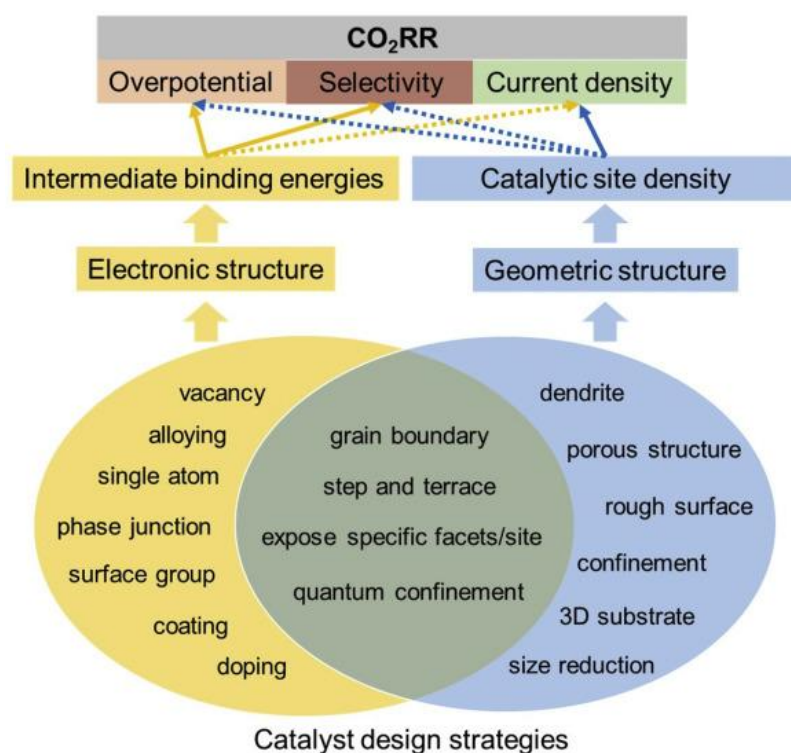


Figure 2.11. Catalyst design strategies for the heterogeneous CO₂RR[183].

In designing a catalyst, surface electronic structure is critical in determining its potential and selectivity for CO₂RR as it influences the binding energies of reaction

intermediates. The geometric structure relates to an atomic arrangement and catalytic site density, which could impact the product selectivity and current density (Figure 2.12.)[183]. In general, nanomaterials are generally composed of grain boundary defects that have specific electronic and geometric properties. Doping or alloying one metal or transition metal chalcogenide with a second metal or additional anion will inevitably affect both the electronic and local geometric properties. In this way, many new catalysts can be designed. It was reported that altering the anion electronegativity around a catalytically active transition metal site leads to better modulation of the electrochemical redox of the catalytic site and, subsequently, lowers the activation energy of the electrocatalytic reaction[169,182]. On that note, for our catalyst design approach, we propose the use of transition metal-based chalcogenides in two ways:

- (i) Mixed anionic chalcogenides by alternating the anion electronegativity using multiple anions, e.g., $M_xE_yE_z$ (M = metal, E = S, Se, or Te) and x , y , and z could be any positive real numbers. This is proposed to change the electron density around the transition metal center, which will subsequently affect the binding energy of the CO intermediate on the surface. This is important for the preferential selectivity of C_1 and C_2 products. It is understood that the most suitable CO adsorption for C_2 products is one whose energy allows for enough dwell time for further reduction of carbon-rich products. Weak CO adsorption energy leads to the desorption of C_1 products.
- (ii) The use of transition metal complexes that are based on chalcogen ligands, where the core of metal bonded chalcogens through the ligands will be isolated as either metal chalcogen complexes ME_4 (M = metal, E = S, Se, or Te) or

metal mixed chalcogen complexes ME_2E_2 ($M = \text{metal}$, $E = \text{S, Se, or Te}$). This will include an understanding of the intrinsic properties of the core catalyst and its role in the CO_2RR process.

To indicate the selectivity of a catalyst (electrode), the so-called Faraday efficiency (FE) Equation (1) is given by

$$FE = \frac{z.n.F}{I.t} 100 \quad (1)$$

where: $z =$ the number of electrons transferred; $n =$ amount of substance of product; $F =$ Faraday constant, $I =$ current applied; $t =$ reaction time.

Studies focusing on catalyst design and synthesis use H-type cells, with cathode and anode compartments filled with liquid electrolytes, separated via an ion exchange membrane. The catalyst is usually deposited on glassy carbon or carbon paper and the CO_2 is dissolved in the bicarbonate electrolyte to improve CO_2 solubility thereby enhancing its mass transport.

- **Mechanistic Principles and Catalyst Design for CO_2 Reduction Reaction**

The electrochemical CO_2 reduction process starts with an electrochemical transfer of H^+/e^- to CO_2 , forming an intermediate that binds to the catalyst surface through either oxygen or carbon. The product depends on the nature of the binding and the element through which the binding occurs. When the binding is via oxygen, HCOOH can be expected, whereas CO is formed when the binding is through carbon (Figure 2.13.). This makes this step a crucial product formation in CO_2RR [183–186]. Also, this implies that CO is generally regarded as an essential intermediate for the further reduction of C_1 and C_2 products. This has been carefully and systematically studied by investigating CO by *in situ* measurements [187–192]. The C-C bond formation is the crucial reaction step that

separates the pathways for single and multi-carbon products. The dimerization of two *CO species is an important step in forming the C-C bond, resulting in bidentate *CO*CO as intermediate species. Figure 2.13. shows the proposed mechanistic pathway for forming ethanol and n-propanol[192]. The subsequent reduction steps to *CO*CHOH or *CO*COH species have been proposed as plausible intermediates steps[190–192].

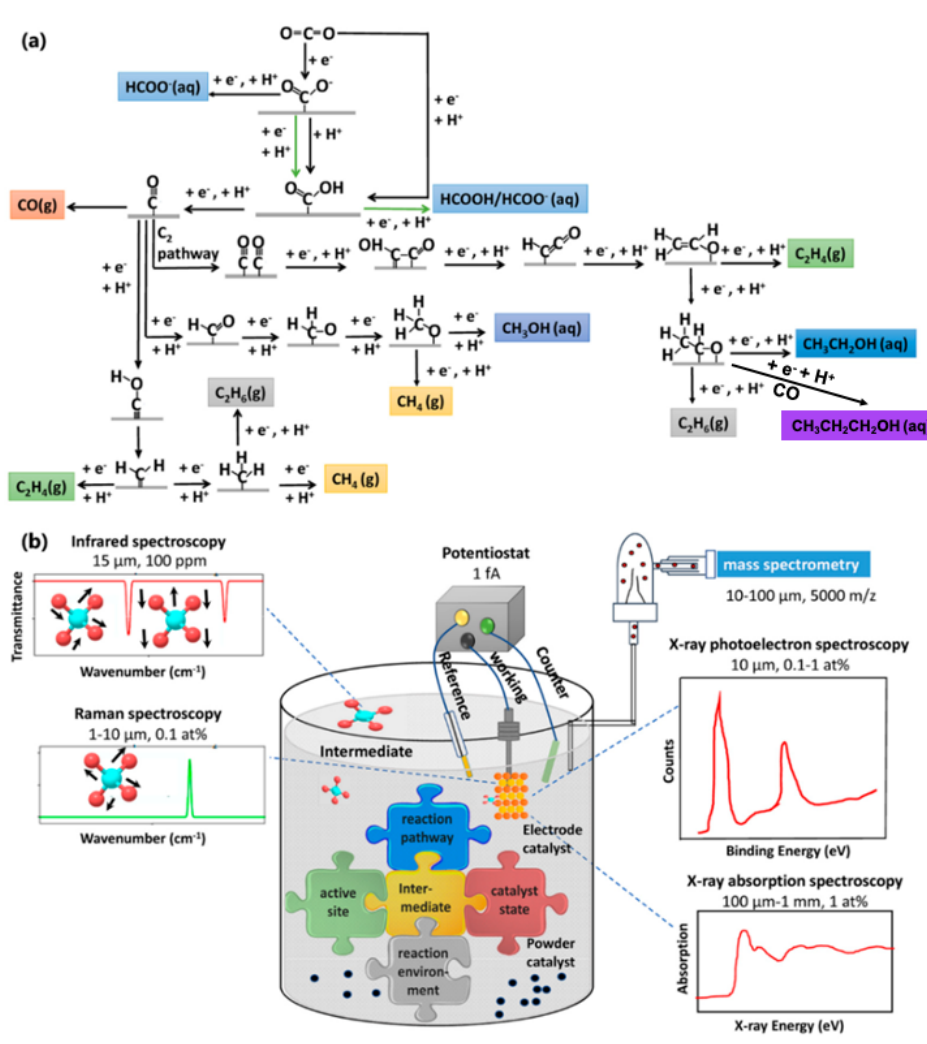


Figure 2.13. (a) Plausible pathways towards CO₂RR. (b) Some *in situ* characterization. (Presents insight into reaction intermediates, active sites, reaction pathways, the effect of the reaction environment, and catalyst transformation after reaction)[192].

These intermediate species could be observed by characterization using *in situ* IR spectroscopy[189]. In addition, operando Raman spectroscopy results revealed that *CO dimerization reaction competes with hydrogenation *COH or *CHO, which are further reduced to C₁ products.[193,194] Along this line, C-C coupling steps via the reaction of *CHO or *COH with CO to *COCHO or *COCO₂H also have been postulated[191–193]. Methyl Carbonyl represents the most likely intermediate where a distinction occurs as to whether hydrogenation to ethanol or acetaldehyde occurs or whether further coupling with *CO and thus, the formation of propanol occurs. In this case, the *CO attacks the carbonyl carbon of acetaldehyde[195]. *In situ* spectroscopic systems generally characterize catalytic systems under reaction conditions and assist in comprehensively understanding the nature of active sites and reaction mechanisms[192,194]. These techniques have been employed in CO₂RR systems to provide the following:

- (i) Identification and capture of reaction intermediates
- (ii) Identification of active sites
- (iii) Determination of preferred reaction pathways
- (iv) Understanding the role of the reaction environment
- (v) Investigating the state changes of catalysts under reaction conditions.

Multi-analysis using operando X-ray absorption spectroscopy (XAS) and quasi-in-situ X-ray photoelectron spectroscopy (XPS) provides a correlation between catalytic structure and product formation multi-carbon (C₂₊)[167,169,172]. This would help in catalyst design to improve C₂₊ or any desired product selectivity and yield maximization[162,163]. This broadens our perspective on electrocatalytic CO₂RR systems

and enables the rational design of efficient electrocatalysts and electrolytes for this reaction. Also, it is worth mentioning that the first adsorption intermediate determines the mechanistic pathway and subsequently the possible product(s) in the reaction, this could be from CO_2 or the electrolyte. For example, using bicarbonate in the aqueous medium, a two-electron reduction of the adsorbed carbonate is possible[175], as schematically described in Figure 2.14. shown below.

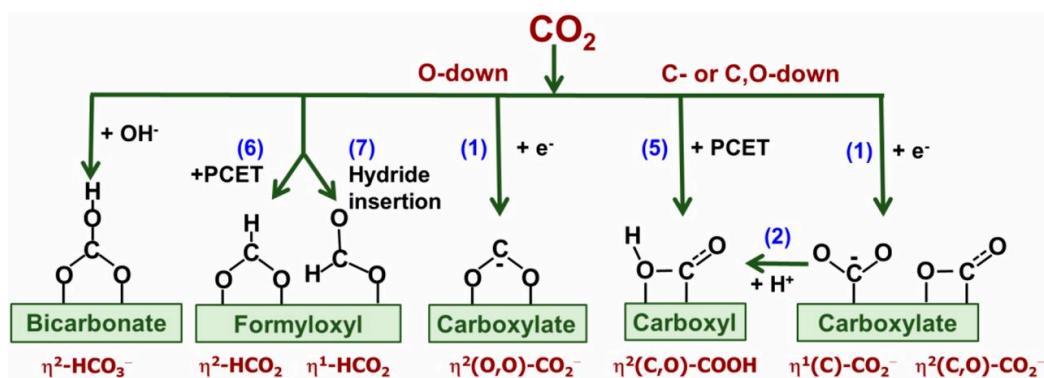


Figure 2.14. Possible intermediates of CO_2RR during the first adsorption step[175].

The products formed during CO_2RR have both economic and thermodynamic requirements. Ideally, the most desirable products should have high economic value and should require less energy to produce. The equilibrium potentials of popularly documented electrochemical CO_2R products are summarized in Table 2.2. below [196]. The Gibbs free energy of reaction employing gas-phase thermochemistry data and Henry's Law data for aqueous products[197] was used to calculate the CO_2R standard potentials. The state of the products is aqueous or gaseous, while CO_2 and water are considered as gas and liquid respectively. For any CO_2R process, all the CO_2 products are formed at the cathode, while an oxidation reaction mostly OER will necessarily take place at the anode to complete the

Table 2.2. Electrochemical reactions with equilibrium potentials.

Reaction	E^0 / [V vs RHE]	Reaction, Product
$2\text{H}_2\text{O} \rightarrow \text{O}_2 + 4\text{H}^+ + 4\text{e}^-$	1.23	OER
$2\text{H}^+ + 2\text{e}^- \rightarrow \text{H}_2$	0	HER
$x\text{CO}_2 + n\text{H}^+ + n\text{e}^- \rightarrow \text{product} + y\text{H}_2\text{O}$		CO ₂ RR
$\text{CO}_2 + 2\text{H}^+ + 2\text{e}^- \rightarrow \text{HCOOH}_{(\text{aq})}$	-0.12	Formic acid
$\text{CO}_2 + 2\text{H}^+ + 2\text{e}^- \rightarrow \text{CO}_{(\text{g})} + \text{H}_2\text{O}$	-0.10	Carbon monoxide
$\text{CO}_2 + 6\text{H}^+ + 6\text{e}^- \rightarrow \text{CH}_3\text{OH}_{(\text{aq})} + \text{H}_2\text{O}$	0.03	Methanol, MeOH
$\text{CO}_2 + 4\text{H}^+ + 4\text{e}^- \rightarrow \text{C}_{(\text{s})} + 2\text{H}_2\text{O}$	0.21	Graphite
$\text{CO}_2 + 8\text{H}^+ + 8\text{e}^- \rightarrow \text{CH}_4_{(\text{g})} + 2\text{H}_2\text{O}$	0.17	Methane
$2\text{CO}_2 + 2\text{H}^+ + 2\text{e}^- \rightarrow (\text{COOH})_2_{(\text{s})}$	-0.47	Oxalic acid
$2\text{CO}_2 + 8\text{H}^+ + 8\text{e}^- \rightarrow \text{CH}_3\text{COOH}_{(\text{aq})} + 2\text{H}_2\text{O}$	0.11	Acetic acid
$2\text{CO}_2 + 10\text{H}^+ + 10\text{e}^- \rightarrow \text{CH}_3\text{CHO}_{(\text{aq})} + 3\text{H}_2\text{O}$	0.06	Acetaldehyde
$2\text{CO}_2 + 12\text{H}^+ + 12\text{e}^- \rightarrow \text{C}_2\text{H}_5\text{OH}_{(\text{aq})} + 3\text{H}_2\text{O}$	0.09	Ethanol, EtOH
$2\text{CO}_2 + 12\text{H}^+ + 12\text{e}^- \rightarrow \text{C}_2\text{H}_4_{(\text{g})} + 4\text{H}_2\text{O}$	0.08	Ethylene
$2\text{CO}_2 + 14\text{H}^+ + 14\text{e}^- \rightarrow \text{C}_2\text{H}_6_{(\text{g})} + 4\text{H}_2\text{O}$	0.14	Ethane
$3\text{CO}_2 + 16\text{H}^+ + 16\text{e}^- \rightarrow \text{C}_2\text{H}_5\text{CHO}_{(\text{aq})} + 5\text{H}_2\text{O}$	0.09	Propionaldehyde
$3\text{CO}_2 + 18\text{H}^+ + 18\text{e}^- \rightarrow \text{C}_3\text{H}_7\text{OH}_{(\text{aq})} + 5\text{H}_2\text{O}$	0.10	Propanol, PrOH
$x\text{CO}_2 + n\text{H}^+ + n\text{e}^- \rightarrow \text{product} + y\text{H}_2\text{O}$		COR
$\text{CO} + 6\text{H}^+ + 6\text{e}^- \rightarrow \text{CH}_4_{(\text{g})} + \text{H}_2\text{O}$	0.26	Methane
$2\text{CO} + 8\text{H}^+ + 8\text{e}^- \rightarrow \text{CH}_3\text{CH}_2\text{OH}_{(\text{aq})} + \text{H}_2\text{O}$	0.19	Ethanol, EtOH
$2\text{CO} + 8\text{H}^+ + 8\text{e}^- \rightarrow \text{C}_2\text{H}_4_{(\text{g})} + 2\text{H}_2\text{O}$	0.17	Ethylene

overall reaction, balancing the stoichiometric coefficients for electrons and protons in a sustained CO₂RR. To date, there are limited reports on transition-metal-chalcogenide-based molecular complexes towards CO₂RR to understand the role of the core metal center in the chalcogen environment. Therefore, a more systematic approach to studying these complexes is by designing a unique class of ligands that will give varying chalcogenide that can change the electronic structure around the metal center to understand catalyst structure-product selectivity-yield relationship is desirable. This still needs to be explored or investigated for catalytic CO₂ conversion to improve product selectivity and yield. We conducted a systematic study of the chemistry of molecular selenide carbonyl cluster materials, their detailed characterization FTIR, scanning electron microscopy (SEM), Energy-dispersive X-ray spectroscopy (EDX) Raman spectroscopy, and X-ray photoelectron spectroscopy (XPS), and CO₂ catalytic efficiency and selectivity is reported.

2.5. ELECTROCHEMICAL WATER SPLITTING

Water splitting is a form of energy conversion and storage approach based on water electrolysis, in which H₂ and O₂ gasses are produced at the cathode and anode[198]. In this reaction, the water oxidation step is a complex four-electron transfer process and remains the most significant obstacle owing to its sluggish kinetics and high oxidation potential[199]. Platinum, RuO₂, and IrO₂ are the state of art water oxidation catalysts considered the most efficient. However, their industrial-scale application is challenging due to their low abundance (precious metal oxides), high cost, and alkaline conditions[200-202]. Catalysts, therefore, to be scalable, must be cost-efficient, made of readily available earth-abundant elements, have high catalytic activity under mild conditions at low overpotentials, and are stable for long periods or many cycles[203–205].

The varying activity of these transition metal chalcogenides in OER and HER is due to their different compositions, variety of lattice structures, and unique electronic structures. And based on these properties, the transition metal chalcogenides are promising in various energy applications, including photocatalysis[206], electrochemical catalysis, and other energy conversion reactions[83, 86, 204, 205, 207-210],. Mainly for their rich defects sites[89,211], tunable electronic band structure[212–216], and various shapes, sizes, and morphologies[215-217], the transition metal chalcogenides exhibit boosting performance for water splitting. Despite their conductivity and activity, there is limited in their industrial-scale application; this is due to the susceptibility to corrosion that they suffer [19,217], and therefore systematic understanding of this class of material is necessary. Since the systematic synthesis of active and stable transition metal chalcogenide catalysts for wide electrochemical applications is uncommon. These are some strategies aimed towards providing better routes to developing and designing active and stable transition metal chalcogenide catalysts, summarized in Figure 2.15. below.

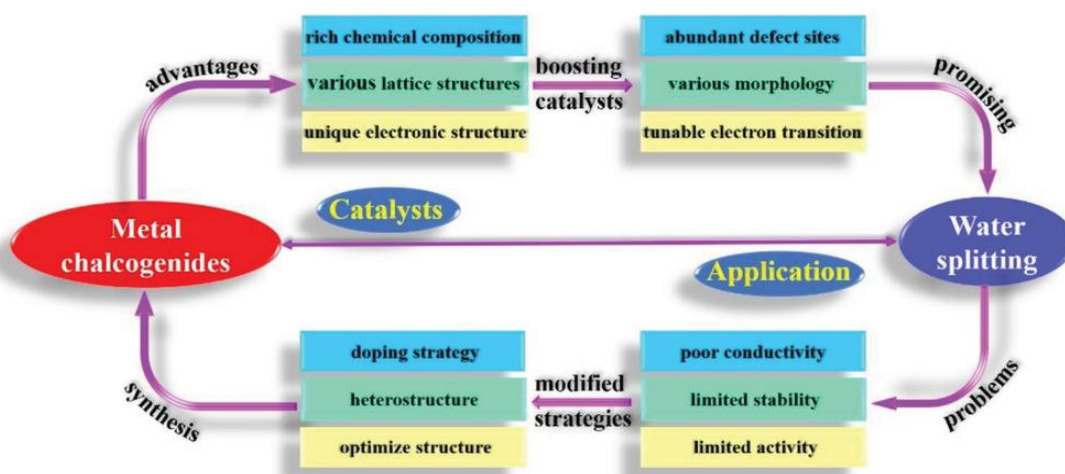


Figure 2.15. Some metal chalcogenide catalysts are applied in water splitting[218].

- **Mechanism of Oxygen Evolution Reaction (OER)**

Oxygen evolution reaction (OER) takes place at the anode, and it's the half-reaction of the water-splitting reaction Equation (2)



Notably, the cathode and anode reactions differ depending on the reaction medium employed for the water-splitting reaction. The sets of Equations (3) and (4), and Equations (5) and (6) below show the reactions under acidic and alkaline conditions, respectively. Many researchers have proposed numerous possible mechanisms for OER at the anode electrode in either acid (Equations (5-9)) or alkaline media (Equations (12-16)). Many of these proposed mechanisms include the same intermediates (MOH and MO), while the significant difference probably centers around the oxygen formation step. Based on these plausible mechanisms, it's understood that there are two different approaches to forming oxygen from a MO intermediate; the first is the green route, as shown in Figure 2.16. via the direct combination of 2MO to produce $\text{O}_{2(\text{g})}$ (Equation (7)); the second one involves the formation of the MOOH intermediate (Equations (8) and (15)), which subsequently decomposes to $\text{O}_{2(\text{g})}$ (Equations (9) and (16)). Despite this difference, it's been shown that the electrocatalysis of OER generally undergoes a heterogeneous reaction that involves the bonding interactions (M–O) within the intermediates (MOH, MO, and MOOH) as crucial steps for the overall electrocatalytic ability.

(i) Acidic conditions

Cathode reaction:



Anode reaction:

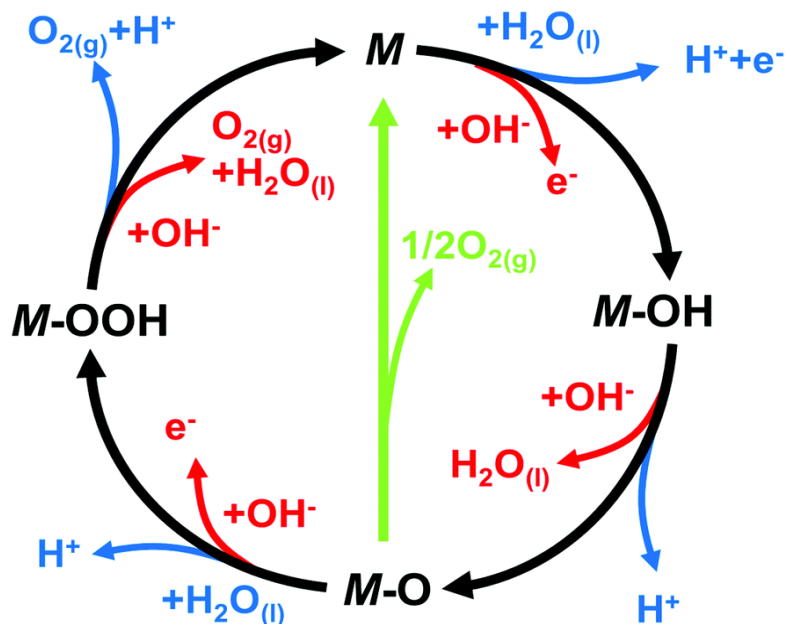
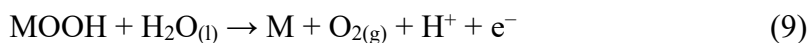
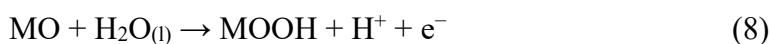
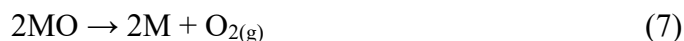
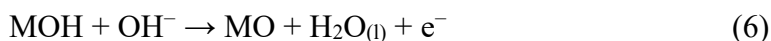
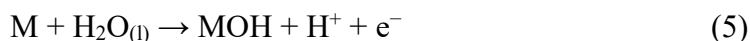


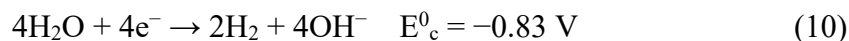
Figure 2.16. The OER mechanism for acid (blue) and alkaline (red) conditions. The black line indicates that the oxygen evolution involves the formation of a peroxide (M–OOH) intermediate (black), while another route for the direct reaction of two adjacent oxos (M–O) intermediates (green) to produce oxygen is possible as well[219].

The proposed mechanism under acidic conditions:



(ii) Alkaline conditions

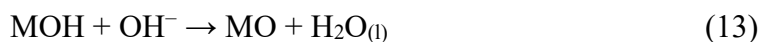
Cathode reaction:



Anode reaction:



The proposed mechanism under alkaline conditions



Several OER catalysts have been reported using various compositions of transition metal chalcogenides (See examples in Figure 2.17.). H. Singh reported a MnSe bifunctional electrocatalyst for OER and ORR activity in 1 M KOH. Its catalytic performance was enhanced by mixing multiwalled carbon nanotubes (MWCNTs) to give MnSe@MWCNT catalyst composite, increasing the catalyst's charge transfer and electronic conductivity. This composite was found to exhibit much higher activity, evidenced by a very low overpotential of 290 mV at 10 mA cm⁻² and a Tafel slope of 54.76 mV dec⁻¹, indicating fast OER kinetics as well as low charge transfer resistance shown by EIS, indicating a rapid movement of the reactant species at the electrode interface[118]. In another report, M. Nath compared hydrothermal and electrodeposited cobalt telluride phases (CoTe and CoTe₂) for OER, HER, and ORR in an alkaline medium[112]. Although both catalysts show efficient electrocatalytic activities. CoTe demonstrated better performance for OER compared to CoTe₂. According to the report, CoTe presented a better performance for OER and HER, with a low Tafel slope (43.8 mV dec⁻¹) and lower overpotential (200 mV) at 10 mA cm⁻², while CoTe₂ shows better efficiency for ORR DFT studies revealed that CoTe showed

higher intermediate $-OH$ adsorption energy on the catalyst surface, which corresponds to the catalyst activation step, and in good agreement with experimentally observed data for its superior performance.

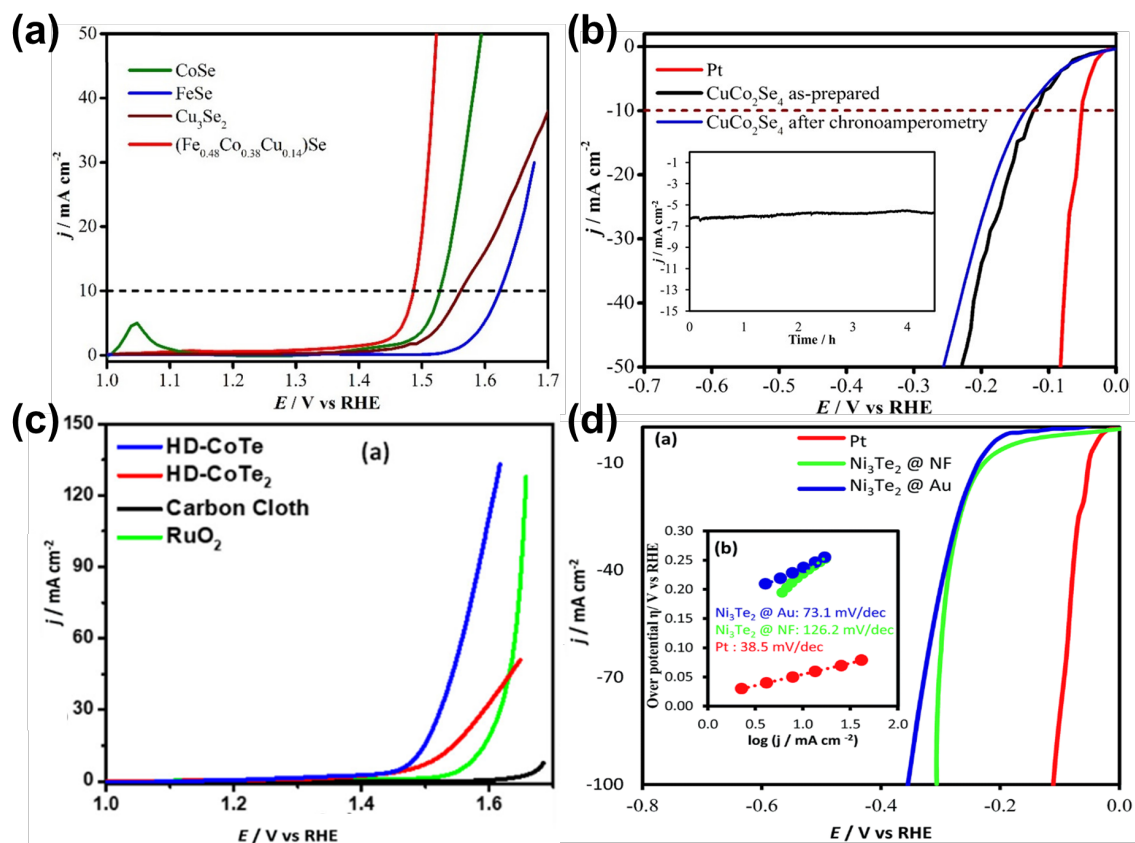


Figure 2.17. The electrochemical water splitting activity of various bulk metal chalcogenide nanomaterials in N_2 saturated 1.0 M KOH solution at a scan rate of 10 mV s^{-1} . (a) OER LSV of iron cobalt copper selenide; (b) HER LSV of copper cobalt selenide (inset is the chronoamperometry); (c) OER LSV of cobalt telluride; (d) HER of nickel telluride (inset is the Tafel plot)[19,112,126,147].

Furthermore, they observed that, although the hydrothermally synthesized catalysts products were of higher quality crystalline nanostructured products with pure phases, the electrodeposited CoTe films showed superior electrocatalyst performance. This

could be due to direct catalyst growth on the electrodes with no binder or additives required[113]. U De Silva et al. tried to understand what happens on chalcogenide-based electrocatalysts surfaces by correctly identifying the catalytically active species on the surface. This was done by studying the evolution of the dynamic surface composition for nickel-selenide and telluride-based electrocatalysts by intentionally creating nickel-oxide-coated Ni_3Se_2 and Ni_3Te_2 surfaces and comparing their electrocatalytic activity before and after extended time activity in KOH electrolyte. They observed that the surfaces remained stable in an alkaline medium, and no nickel oxide coating was detected even after prolonged exposure to KOH under anodic potential. The active surfaces are rather mixed with anionic (hydroxo)chalcogenides[19]. Mixed metal chalcogenides have also been tested for OER to understand the effect of doping metals on the activity and stability of an electrocatalyst. An interesting work on Cu-doped Co_3Se_4 yielded a spinel structure type CuCo_2Se_4 nanostructured phase that exhibits excellent bifunctional electrocatalytic activity OER and HER in alkaline media was reported from our Laboratory. This electrocatalyst required 320 mV and 125 mV overpotential for OER and HER to reach a current density of 50 mA cm^{-2} and 10 mA cm^{-2} , respectively[126]. Furthermore, Fe–Co–Cu quaternary selenides series was studied for OER catalytic activity in N_2 -saturated 1.0 M KOH solution as a function of composition by exploring a trigonal phase diagram. They observed that quaternary Fe–Co–Cu selenides demonstrated more catalytic efficiency with increasing Fe or Cu in the catalysts. Ternary Fe–Cu selenides surprisingly demonstrated a reduced OER activity relative to their parent compounds (FeSe and Cu_3Se_2). $(\text{Fe}_{0.48}\text{Co}_{0.38}\text{Cu}_{0.14})\text{Se}$ showed the best catalytic activity as indicated by a small overpotential and Tafel slope of

256 mV at 10 mA cm^{-2} and 40.8 mV dec^{-1} , respectively[147]. Examples of these complexes and their cyclic voltammetry curves are shown in Figure 2.18. below.

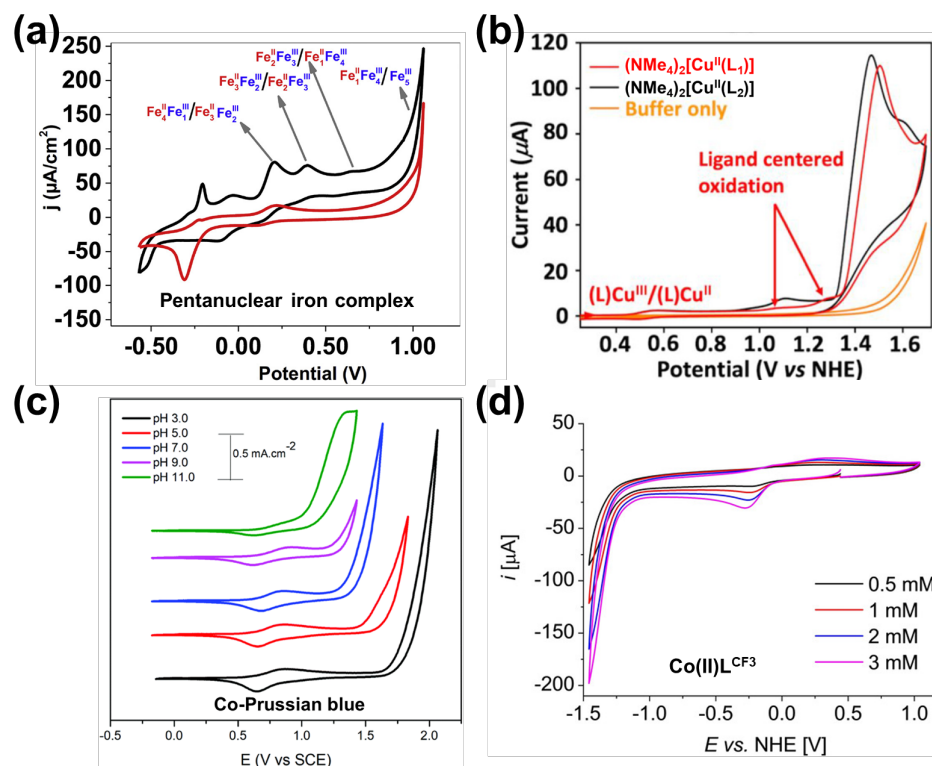


Figure 2.18. Cyclic voltammetry of molecular complexes. (a) 0.20 mM pentanuclear iron complex (black) and $1.0 \text{ mM Fe}(\text{ClO}_4)_3$ (red) homogeneous system in ACN(9): water(1), using a scan rate of 10 mV/s ; (b) CV of $0.5 \text{ mM } (\text{NMe}_4)_2[\text{Cu}^{\text{II}}(\text{L}_1)]$ and $0.5 \text{ mM } (\text{NMe}_4)_2[\text{Cu}^{\text{II}}(\text{L}_2)]$ in pH 9.2 0.1 M carbonate buffer solution. [$\text{L}_1 = N,N'$ -(1,2-phenylene)bis(2-hydroxy-2-methylpropanamide), and $\text{L}_2 = N,N'$ -(4,5-dimethyl-1,2-phenylene)bis(2-hydroxy-2-methylpropanamide)]; (c); of various pH phosphate solutions for on FTO substrate CoHCF at 50 mV s^{-1} scan rate; (d) $\text{Co}(\text{II})\text{L}^{\text{CF}_3}$ at 0.1 V/s in phosphate buffered MeCN/ H_2O (1:1), at various concentrations. pH 7.3–7.5 for HER. (L^{CF_3} =2,6-bis(methoxybis(4-trifluoromethyl-1H-imidazol-2-yl)methyl)pyridine)[7,10,220, 223].

The exceptional catalytic performance of these quaternary selenides could be explained by the possible delocalization of electron cloud among the transition metal sites in the catalytic system through d-bands, resulting in improved film conductivity and lower

charge transport resistance at the catalyst–electrolyte interface. There are only a few reports on molecular-based complexes in the literature for water splitting; most of these reports are non-chalcogen-based complexes and are of homogeneous type system[220–222]. There are very scanty reports on transition-metal-selenide-based molecular complexes towards both OER and HER in alkaline to understand the role of the core metal center in the chalcogen environment[7-8], J. Masud et al. reported $[\text{Ni}\{(\text{SeP}^i\text{Pr}_2)_2\text{N}\}_2]$ that demonstrated excellent performance and efficiency towards water splitting in alkaline solution as evidenced by the low overpotentials, exceptionally high mass activity, and a high TOF value recorded[30]. Their activity for OER was found to be better than the state-of-art- RuO_2 , while their HER was less active as compared with Pt as shown in Figure 2.19. This was the first report to discuss seleno-based coordination complexes in water splitting.

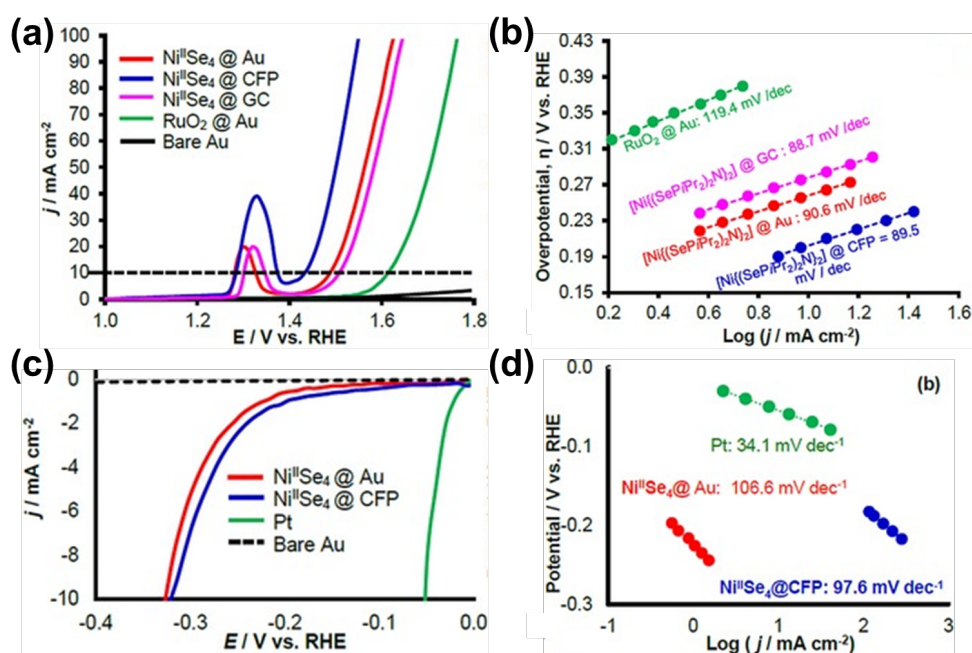


Figure 2.19. The electrochemical activity of molecular Ni-selenide complex ($\text{Ni}^{\text{II}}\text{Se}_4$) on different substrates in N_2 saturated 1.0 M KOH solution at a scan rate of 10 mV s^{-1} . (a) OER;(b) OER Tafel plots; (c) HER; (d) HER Tafel plots[30].

A more systematic approach to studying these complexes is designing a unique class of ligands that will give varying chalcogenides that can change the electronic structure around different metal center types. This has not yet been explored or investigated for OER and HER catalytic activity. This behavior motivated us to investigate the activity of the intrinsic property of catalyst through isolated core metal complex and the effect of mixed anion chalcogenides by gradually replacing some portion of the chalcogen in transition metal chalcogenides with a different chalcogen in a continuous metal chalcogenides solid structure. Understanding the chemistry of these materials, from synthesis to structure-property relationship, could provide a plausible explanation of the interplay of the involving chalcogen anions within the structure and how they affect the charge distribution and electronic band structure, and subsequently tailoring this towards improving the electrochemical properties of transition metal chalcogenides in water splitting applications. This could open doors for many opportunities for the design of different catalytic system types by (i) using molecular complexes to determine the intrinsic properties of the active metal core when perturbed by a surrounding ligand (ii) doping multiple anions in a simple binary metal chalcogenide system and studying their properties evolution and activity in OER and HER in water splitting, with changing catalysts composition as well as tuning their electronic structure. Here we present, for the first time, a systematic study of nickel telluro-selenide and their OER catalytic activity and stability. The electrochemical properties of these materials were investigated and compared with their selenide and telluride pristine binary transition metal chalcogenides. The catalytic activity of the telluro-selenides for OER was observed to be higher than the selenide but lower than the telluride, confirming that increasing anion electronegativity decreased

catalytic activity for OER. A systematic study of the chemistry of these new materials, their detailed characterization with powder X-ray diffraction, scanning, and transmission electron microscopy, Energy-dispersive X-ray spectroscopy (EDX), Raman spectroscopy, and X-ray photoelectron spectroscopy (XPS), and OER catalytic performance is reported.

PAPER**I. A MOLECULAR TETRAHEDRAL COBALT-SELENO-BASED COMPLEX AS AN EFFICIENT ELECTROCATALYST FOR WATER SPLITTING**

Ibrahim Munkaila Abdullahi¹, Siby Thomas², Alessio Gagliardi², Mohsen Asle Zaeem³,
and Manashi Nath¹

¹Department of Chemistry, Missouri University of Science and Technology, Rolla, MO
65409

²School of Computation, Information, and Technology, Technical University of Munich
(TUM) Hans-Piloty-Strasse 1, 85748 Garching, Munich, Germany

³Department of Mechanical Engineering, Colorado School of Mines, Golden, CO 80401

ABSTRACT

The cobalt–seleno-based coordination complex, $[\text{Co}\{(\text{SePiPr}_2)_2\text{N}\}_2]$, is reported with respect to its catalytic activity in oxygen evolution and hydrogen evolution reactions (OER and HER, respectively) in alkaline solutions. An overpotential of 320 and 630 mV was required to achieve 10 mA cm^{-2} for OER and HER, respectively. The overpotential for OER of this CoSe_4 -containing complex is one of the lowest that has been observed until now for molecular cobalt (II) systems, under the reported conditions. In addition, this cobalt–seleno-based complex exhibits a high mass activity (14.15 A g^{-1}) and a much higher turn-over frequency (TOF) value (0.032 s^{-1}) at an overpotential of 300 mV. These observations confirm analogous ones already reported in the literature pertaining to the potential of molecular cobalt–seleno systems as efficient OER electrocatalysts. Keywords: cobalt complex; electrocatalysis; water splitting; hydrogen evolution; oxygen evolution.

1. INTRODUCTION

Over the past few decades, research interest in materials design and synthesis, the applications of which can be channeled towards sustainable energy generation and storage, has increased tremendously, due to the continuing depletion of fossil fuels. Research work on these materials has primarily focused on identifying earth-abundant non-precious metal-based resources affording sustainable energy conversion from renewable sources such as the sun, wind and water. Among these, water splitting capable of generating clean hydrogen fuel on-demand has attracted considerable interest due to its wide range of applicability in various technologies including fuel cells, solar-to-fuel energy conversion, and water electrolyzers.[1,2] Electrocatalytic water splitting comprises two primary reactions occurring simultaneously: a hydrogen evolution reaction (HER) at the cathode, and an oxygen evolution reaction (OER) at the anode. The latter reaction is an energy intensive process involving multi-step proton-coupled electron transfer steps, and is thermodynamically less favorable, making it a major barrier for the advancement of these technologies.[3] Owing to the slow kinetics of oxygen evolution reactions (OER), catalysts are typically used to reduce the activation energy barrier as well as stabilize intermediate adsorption on the catalyst surface. Among these, precious metal-based systems such as iridium and ruthenium oxides are considered as state-of-the-art OER catalysts, while platinum-based materials are best for HER, with only a moderate activity towards OER. The use of precious metal-based oxides, however, is a severely limiting factor for widespread commercial applications due to their high cost and scarcity.[1] Consequently, the search for robust and efficient OER and HER catalysts based on abundant non-precious

transition elements has attracted considerable attention. Numerous types of such catalysts have been investigated with an aim to replace precious metal-based electrocatalysts without compromising either catalytic efficiency or stability. Among the transition metals, cobalt-based electrocatalysts have emerged as an attractive class of non-precious metal-based catalysts for electrochemical water oxidation reactions, due to their abundance, stability, and more importantly superior catalytic performance.[4] Some of the most promising cobalt-based compounds identified as cost-effective and efficient catalysts for OER and HER are oxides [5–7] and chalcogenides (Co_xE_y ; E = S, Se, Te).[8–12] A lot of cobalt selenides of the generic formula Co_xSe_y have been reported to exhibit promising electrocatalytic activity for either HER or OER or both. Huge progress has also been made in efforts to develop bifunctional cobalt selenide catalysts for the overall water-splitting reaction. For instance, Masud et al. reported Co_7Se_8 nanostructured materials as a highly active and stable bifunctional electrocatalyst for both OER and HER in strong alkaline medium.[13] Numerous other cobalt-based electrocatalysts have also been explored; CoSe nanosheets,[14] Co_3Se_4 nanowires on cobalt foam,[15] CoSe_2 nanosheets,[16] and some nonstoichiometric cobalt selenides such as $\text{Co}_{0.85}\text{Se}$ [17] have been reported as overall water-splitting electrocatalysts in alkaline media. Furthermore, the $\text{Co}_{0.85}\text{Se}$ nanosheet network arrayed on a cobalt plate substrate was also reported for HER in both basic and acidic media exhibiting an outstanding catalytic performance, due to its inherent metallic character, giving it abundant surface-active sites as well as higher conductivity.[18,19] In this family of electrocatalysts, it has been observed that the catalytic activity increases with decreasing electronegativity of the lattice anion. This has been confirmed in many transition metal chalcogenides as OER catalysts whereby changing the anion from O down

to Te in the chalcogen group led to significant improvement of the intrinsic catalytic properties in nickel-based chalcogenides.[20,21] Changing the anion leads to decrease in electronegativity in the following order: O (3.44) > S (2.58) > Se (2.55) > Te (2.1), which subsequently leads to increase in the covalency of the metal–chalcogen (M–E) bonds down the chalcogens group, i.e., M–O bonds being less covalent than M–Se or M–Te. This increased covalency assists in local electrochemical oxidation–reduction of the transition metal center by reducing their redox potential as well as by altering the electron density in the catalytically active transition metal site. Increased covalency in the chalcogenides also leads to alteration of the electronic band structure and proper alignment of the valence and conduction band edges with the water oxidation/reduction levels, respectively, leading to more facile charge transfer at the electrocatalyst–electrolyte interface which subsequently reduces the overpotential required for the electrochemical conversion.[22,23] Similar effects have also been observed by doping in transition metal sites which also redistributes electron density around the catalytically active site.[24] Until now, the most common cobalt–seleno-based electrocatalysts reported are from different types of nanostructured materials and solids with infinite Co–Se bonds throughout the lattice. Although some of them have shown both efficient catalytic activity for OER and great stability,[13,15] there are still some concerns about their stability in alkaline media. For instance, it has been suspected that in alkaline medium these transition metal chalcogenides hydrolyze to form surface oxide layers which act as the actual electrocatalyst in such cases. However, another opposing view is that the transition metal chalcogenides are only partially hydrolyzed, resulting in mixed anionic surface compositions. Several research groups are trying to accurately identify the active surface composition of these transition metal chalcogenide-

based electrocatalysts. In that respect, studies of molecular complexes in which the core of the complex represents a structural motif of the metal– chalcogenide solid can shed more light on the effect of anion coordination on the catalytic activity as well as stability of this motif under alkaline conditions. The electronic structure of these molecular complexes can be finely tuned by modifying the electronic and steric properties of the ligands employed in the synthesis. Moreover, the molecular complexes can be very stable, diverse and can exhibit coordination expansion due to ligation of the solvent or other molecules,[25–29] which is very useful for the catalytic pathway typically initiated by hydroxide coordination to the catalytically active transition metal site. These properties are of especially great interest for electrochemical H₂ and O₂ generation. Therefore, investigating the intrinsic catalytic activity of transition metal complexes with limited or no propensity to form surface metal oxides, as well as understanding the inherent activity of the core structural motif is of paramount interest. Numerous molecular cobalt complexes based on different types of ligand designs have been reported as electrocatalysts.[30–39] For instance, pentadentate N-heterocyclic coordinated cobalt complexes exhibit HER activity in water [30]. In addition, a cobalt–polypyridyl complex bearing pendant bases and redox-active ligands, combining stability and appropriate redox potential, has also been reported for good electrocatalytic activity in HERs.[36] Cobalt-based coordination complexes have previously been studied for OER catalytic activity,[37] in instances where the catalysts are immobilized onto the electrode as composite or onto the surface.[38] However, cobalt coordination complexes with seleno-based ligands have not yet been investigated for OER catalytic activity. Such complexes containing the CoSe₄ core that is commonly found in cobalt selenide phases will be very useful in understanding the electrocatalytic activity as

a function of anion coordination (composition and geometry). This will also aid in gaining an insight into the electrocatalysis pathways and the reasons for significantly enhanced activity of the metal chalcogenides for OER and HER. Herein, we report the bifunctional electrocatalytic activity of a seleno-based Co(II) bis(diselenoimidodiphosphinato) complex, $[\text{Co}\{(\text{SePiPr}_2)_2\text{N}\}_2]$, which shows significantly enhanced efficiency for OER and moderate HER, in alkaline medium. A very low onset potential of 1.44 V for O_2 evolution as well as an overpotential of 320 mV at 10 mA cm^{-2} were recorded. The onset potential for H_2 evolution is comparable to that of other non-platinum based HER electrocatalysts.

2. METHODOLOGY

2.1. MATERIALS

Au-coated glass and GC used as substrates were purchased from Deposition Research Lab Incorporated (DRLI), Lebanon, Missouri, and Fuel Cells Etc, Texas, respectively.

2.1.1. Synthesis of Bis(diselenoimidodiphosphinato) Cobalt(II) Complex $[\text{Co}\{(\text{SePiPr}_2)_2\text{N}\}_2]$. The synthesis of the $(\text{SePiPr}_2)_2\text{NH}$ ligand [59] and the $[\text{Co}\{(\text{SePiPr}_2)_2\text{N}\}_2]$ complex [39] was carried out following previously reported procedures.

2.1.2. Electrochemical Measurement. In order to study the OER and HER catalytic activity, the CoSe4 catalyst was mixed with nafion and drop-cast onto different electrodes. All the electrochemical measurements were investigated using an electrochemical workstation (IviumStat potentiostat) in a standard three-electrode cell,

with N₂-saturated 1 M KOH as the electrolyte solution. For all measurements, Ag/AgCl was used as a reference electrode, while GC and Pt mesh served as counter electrodes for HER and OER, respectively. Catalyst loaded on Au or GC served as the working electrode. The LSVs were performed at a scanning rate of 10 mV s⁻¹ while the electrode was rotating at 1000 rpm. To reduce uncompensated solution resistance, all activity data were iR-corrected, which was measured through electrochemical impedance studies. The reference electrode was calibrated by measuring open circuit potential (OCP, -0.199 V) at Pt wire in pure H₂-saturated 1.0 M H₂SO₄ solution. Potentials measured vs. Ag/AgCl electrode were converted to values vs. RHE based on Nernst's equation (Equation (1)):

$$E_{\text{RHE}} = E_{\text{Ag/AgCl}} + 0.059\text{pH} + E^0_{\text{Ag/AgCl}} \quad (1)$$

where E_{RHE} is the converted potential vs. RHE, $E_{\text{Ag/AgCl}}$ is the experimentally measured potential against the Ag/AgCl reference electrode, and $E^0_{\text{Ag/AgCl}}$ is the standard potential of Ag/AgCl at 25 °C (0.199 V).

2.1.3. Tafel Plot. The Tafel slope was calculated by applying Equation (2):

$$\eta = a + (2.3RT/\alpha nF) \log(j) \quad (2)$$

where η is the overpotential, j is the current density, and the other symbols have their usual meanings. The Tafel equation as shown Equation (2) is a fundamental equation which is acquired from the kinetically controlled region of OER/HER and relates the overpotential η with the current density j where the Tafel slope is given by $2.3RT/\alpha nF$.

2.1.4. Turnover Frequency (TOF). The TOF value was calculated by Equation (3):

$$\text{TOF} = I/(4 \times F \times M) \quad (3)$$

where I is current in Ampere, F is the Faraday constant, and M is the number of moles of the active catalyst.

2.1.5. Electrode Preparation. All solutions were prepared using deionized (DI) water. All substrates were cleaned with isopropanol and eventually rinsed with deionized water to ensure a clean surface. Catalyst ink was prepared by dispersing 10.0 mg of the catalyst in 1.0 mL isopropyl alcohol (IPA) and ultrasonicated it for 30 min. Au-coated glass substrates were covered with Teflon tape, leaving an exposed geometric area of 0.283 cm² and GC (geometric area: 0.196 cm²) served as the working electrodes. A quantity of 20 μ L of the ink was pipetted out on the top of the Au or GC substrates. The catalyst layer was dried at room temperature. Then, an aliquot of Nafion solution (10 μ L of 1 mg/mL solution in 50% IPA in water) was applied to the catalyst layer. The Nafion-coated working electrode was dried at room temperature and finally heated at 130 °C in an oven for 30 min in air.

2.1.6. Electrodeposition of RuO₂. Electrodeposition of RuO₂ on Au-coated glass and GC substrate were carried out from a mixture of RuCl₃ (0.452 g) and KCl (2.952 g) in 40 mL of 0.01 M HCl using cyclic voltammetry from 0.015 to 0.915 V (vs. Ag/AgCl) for 100 cycles at a scan rate of 50 mV s⁻¹. This was then heated in ambient air for 3 h at 200 °C.

3. RESULTS

The structural and magnetic properties of [Co{(SePiPr₂)₂N}₂] (referred to as CoSe₄ hereafter) have already been reported. [39,40] The crystal structure of CoSe₄ shows

a first coordination sphere consisting of a Co (II) center tetrahedrally coordinated to four Se atoms stemming from two $[\text{SeP}(\text{Pr}_2)_2\text{N}]$ chelating ligands, as shown in Figure 1a. This complex is structurally similar to the Ni (II) tetrahedral NiSe_4 -containing analogue.[41–44] The complex was further investigated by Raman spectroscopy (Figure 1b) whereby the characteristic peaks observed at 174 and 188 cm^{-1} could be associated to CoSe_2 -like vibrations, while that at 143 and 233 cm^{-1} could be attributed to the trigonal- Se^0 mode; furthermore, the two peaks at around 444 and 468 cm^{-1} could be associated with the cubic CoSe_2 -like phase mode,[45,46] indicating the presence of Co–Se in the CoSe_4 complex.

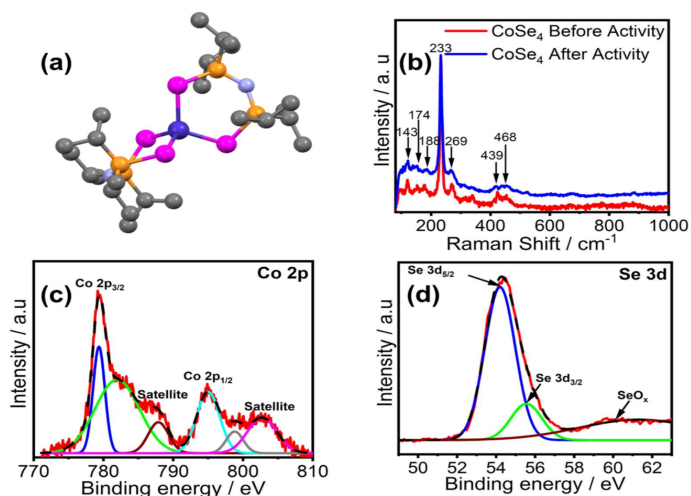


Figure 1. Structure and characterization of the $[\text{Co}\{(\text{SeP}^i\text{Pr}_2)_2\text{N}\}_2]$ complex (CoSe_4 catalyst). (a) The molecular structure showing the tetrahedral cobalt–seleno-coordination. Color coding: Co (dark blue), Se (magenta), P (brown), N (light blue), C (gray). (b) Raman spectra of the complex measured before and after OER catalytic activity. (c) Co 2p XPS peaks. (d) Se 3d XPS peaks.

The CoSe_4 complex was also characterized through X-ray photoelectron spectroscopy (XPS) which showed Co 2p_{3/2} and 2p_{1/2} peaks at 781.2 and 796.3 eV, respectively, characteristic of Co (II), while the Se 3d peaks were observed at 55.1 eV

corresponding to Se^{2-} (Figure 1b,c) [47]. The satellite peaks each found at the higher energy end of the Co 2p signals, are attributed to the contribution from the antibonding orbital [48]. In order to evaluate the electrocatalytic activity of CoSe_4 for water splitting, the drop casting approach was used to prepare the working electrodes. Specifically, the as-prepared CoSe_4 powder was dispersed in isopropyl alcohol (IPA) under ultrasonication without changing its intrinsic properties. The film was fabricated by gradually dropping the catalyst ink (20 μL) onto Au-coated glass as the conductive substrate over a well-defined geometric area. An amount of 0.1% Nafion was dropped on the top of the coating to form a covering layer as illustrated in Figure 2.

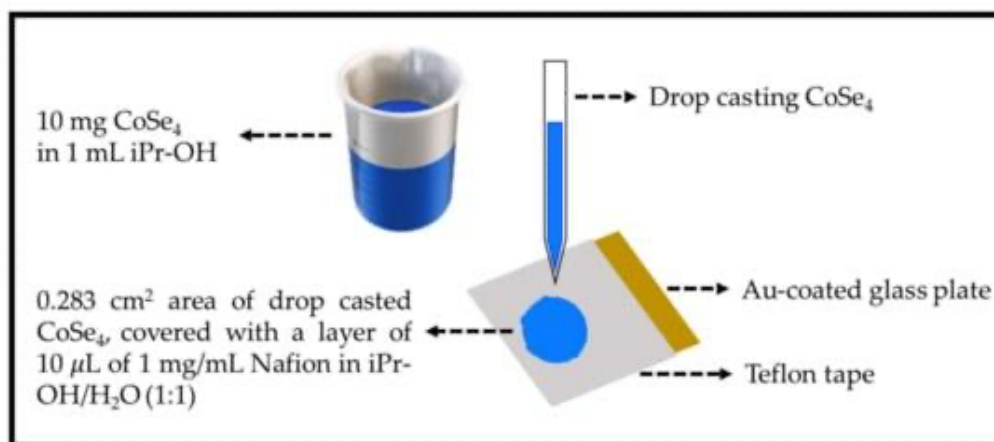


Figure 2. Scheme for electrode preparation.

This method has been widely used in our previous studies for preparing electrode material from powder catalyst samples.[44] Electrodes were also prepared with glassy carbon (GC) substrates. The electrocatalytic activity of CoSe_4 was compared with RuO_2 electrodes prepared on Au-coated glass and GC following the above procedure.

The OER catalytic process was studied by linear sweep voltammetry (LSV) measurements conducted in N₂-saturated 1 M KOH, at a scan rate of 10 mV s⁻¹. Figure 3a shows the LSV plots of electrochemical oxygen evolution at CoSe₄@Au, CoSe₄@GC (GC: glassy carbon), RuO₂@Au and RuO₂@GC electrodes. CoSe₄ loaded on Au-glass and GC electrodes showed high activity for OER with the exchange current density corresponding to O₂ evolution showing a sharp and slow increase for Au and GC, respectively. Among these CoSe₄@Au-glass showed lower onset potential for OER implying that using the Au-coated glass as primary electrode for the CoSe₄ catalyst, the latter showed higher activity toward OER compared to a GC electrode. The typical performance parameters including onset and overpotentials for the CoSe₄@Au-glass catalyst evaluated in this work are listed in Table 1 below.

Table 1. Electrochemical parameters of the catalysts measured in 1 M NaOH.

Catalyst	OER					HER	
	Onset	η	Tafel slope	Mass activity	TOF	Onset	η @10mAcm ⁻²
CoSe ₄ @Au	1.44	0.32	61.6	14.15	0.032	0.52	0.63
RuO ₂ @Au	1.51	0.38	117.2	-	-		
Pt	-	-	-	-	-	0.00	0.05

The onset potentials for CoSe₄@Au-glass and RuO₂@Au-glass were 1.44 and 1.51 vs. reversible hydrogen electrode (RHE), respectively, as shown in Figure 3a. The overpotential required to achieve current density of 10 mA cm⁻² (considering the electrode geometric area) for CoSe₄@Au-glass and RuO₂@Au-glass were 320 and 380 mV, respectively (Figures 3a and 4). Furthermore, Tafel slopes obtained from Tafel plots (η vs. $\log j$) applying Equation (2), were used to investigate OER kinetics of the CoSe₄@Au-glass and RuO₂@Au-glass electrodes, as shown in Figure 3b. Tafel slopes of 61.6 and

117.2 mV dec^{-1} were obtained for $\text{CoSe}_4@Au$ -glass and $\text{RuO}_2@Au$ -glass, respectively. The smaller Tafel slope shown by CoSe_4 -modified electrodes compared to RuO_2 further confirms faster kinetics for OER and consequently better electrocatalytic efficiency of CoSe_4 . The Tafel slope for CoSe_4 is also comparable to reported values for other transition-metal–chalcogenide-based catalysts.[14,24]

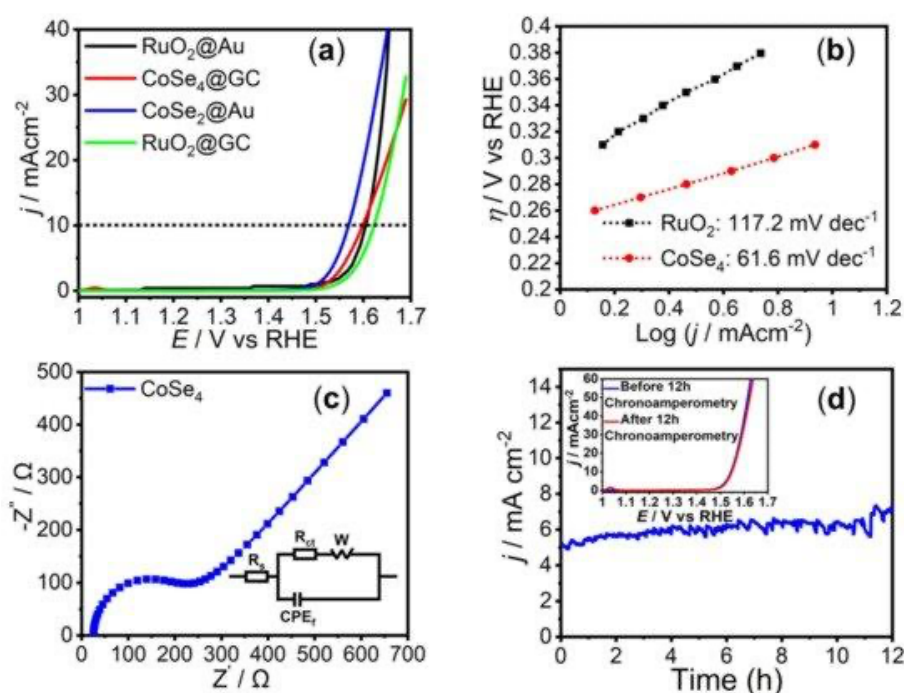


Figure 3. Electrochemical OER performance for the CoSe_4 catalyst. (a) LSV plots of OER for the CoSe_4 catalyst measured in N_2 -saturated 1.0 M KOH solution at a scan rate of 10 mV s^{-1} . Dashed black line shows the current density of 10 mA cm^{-2} . (b) Tafel plots of catalysts. (c) EIS spectra measured at 1.56 V vs. RHE in N_2 -saturated 1.0 M KOH solution over the frequency range of 1 MHz to 1 Hz . Inset shows the equivalent circuit where R_s is the electrolyte resistance and R_{ct} is the charge transfer resistance at the catalyst–electrolyte interface. (d) Stability study of CoSe_4 catalyst under continuous O_2 evolution for 12 h at 1.53 V . Inset shows the LSV plots of the CoSe_4 catalyst in N_2 saturated 1.0 M KOH before (blue) and after (red) chronoamperometry for 12 h .

The $\text{CoSe}_4@Au$ -glass was also analyzed through electro impedance spectroscopy (EIS) to estimate the charge transfer resistance (R_{CT}) at the catalyst–electrolyte interface.

The EIS spectra shown in Figure 3c could be fitted to an equivalent circuit and the R_{CT} was estimated to be approximately 180 ohm. The low value of R_{CT} indicates faster charge-transfer at the catalyst interface. In addition, the mass activity and turn-over frequency (TOF) of the $\text{CoSe}_4@Au$ catalyst was calculated at an η value of 0.320 V (Table 1). The mass activity was estimated to be 14.15 A g^{-1} , indicating better performance than some of the state-of-the-art OER electrocatalysts, such as IrO_x and RuO_x . [49] The OER TOF at an overpotential of 320 mV for the $\text{CoSe}_4@Au$ -glass catalyst was estimated to be 0.032 s^{-1} , under the assumption that all metal ions in the catalysts are catalytically active (Equation (3)). However, since not each and every metal atom is expected to be involved in the reaction, the actual TOF could be evidently underestimated. However, the calculated TOF for $\text{CoSe}_4@Au$ -glass is still important (Table 1), and is comparable or higher than that of other cobalt-based catalysts previously reported under similar conditions. [50,51] The stability of the $\text{CoSe}_4@Au$ -glass electrode under long-term electrolysis in alkaline medium was also investigated using the chronoamperometric technique by which the current density was measured at a constant applied potential of 1.53 V vs. RHE for prolonged period of time, as shown in Figure 3c. The stable current density over 12 h of continuous oxygen evolution indicates high functional durability exhibited by the $\text{CoSe}_4@Au$ -glass catalyst for OER in 1 M KOH. The LSV plots after 12 h of chronoamperometry (inset of Figure 3c) show no noticeable difference with the pristine catalyst, except for the small peak at 1.03 V (RHE) indicating the partial oxidation of Co(II) to Co(III). [52] Interestingly, the LSV plots confirmed that there was no degradation of catalyst performance for OER under conditions of continuous O_2 evolution for an extended period of time. This indicates

the superiority in the catalytic activity of CoSe₄ compared to state-of-the-art (RuO₂) OER electrocatalyst (Figure 4).

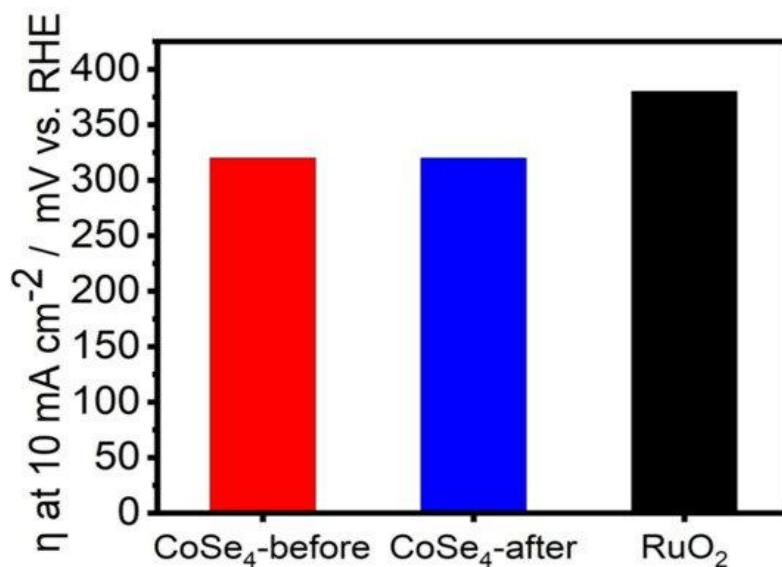


Figure 4. Comparison of achieved overpotentials at 10 mA cm⁻² for CoSe₄ compared with RuO₂.

The stability of the CoSe₄ catalyst was also confirmed with XPS measured after 12 h chronoamperometry measurement as shown in Figure 5. The XPS spectra showed the presence of Co 2p and Se 3d peaks with similar peak positions. The comparison of XPS spectra before and after OER activity showed no noticeable change as shown in Figure 5 confirming that the CoSe₄ complex was indeed stable. This efficient OER electrocatalytic activity observed for the CoSe₄ catalyst is a significant step in an effort to understand the inherent OER catalytic performance of transition metal selenides. It is understood that the stability of the ME₄ center (M = metal, E = chalcogen) increases with decreasing electronegativity of the chalcogen atom, E.[22] The OER catalytic process is expected to be initiated by coordination of the OH⁻ group to the catalytically active Co(II) center.

Tetrahedral Co(II) complexes containing chalcogenated imidodiphosphinato ligands have the tendency to increase their coordination number from four to six in the presence of coordinated solvents such as DMF.[29]

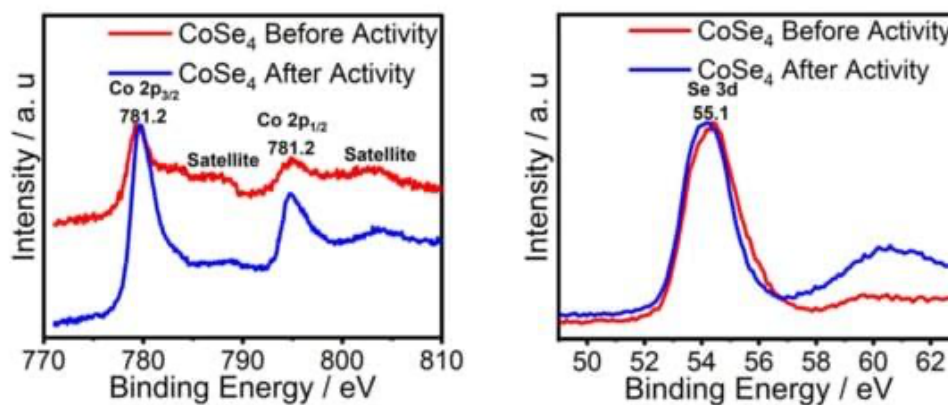


Figure 5. XPS peaks of Co 2p and Se 3d before and after OER activity confirming the stability of the CoSe_4 catalyst.

Consequently, the catalytic process may be initiated by OH^- coordination to the metal center without cleavage of the Co–Se bonds through coordination expansion, where the Co(II) center is concomitantly oxidized to Co(III) in order to accommodate the extra anionic charge. This proposition is also supported by the Tafel slope, which shows a value less than 120 for the CoSe_4 catalyst (Table 1). The lower Tafel slope suggests that the rate-determining step in the catalytic process corresponds to subsequent electron transfer steps from the catalyst's surface to the electrolyte, rather than the initial OH^- coordination to Co(II). Even though there are very scant reports on the proposed mechanisms specific to tetrahedral cobalt-based complexes,[53,54] a mechanism proposed for similar transition metal-based complexes has been reported.[55] Hence, it can be postulated that the tetrahedral CoSe_4 -containing complex is further coordinated to one $\text{OH}^-/\text{H}_2\text{O}$ group

leading to the formation of a square pyramidal transition state, which can then react further to form an O–O linkage, and a subsequent removal of O₂ (Figure 6). The Co site undergoes a reversible change in oxidation states from +2 to +3 and +4 following adsorption of the anionic intermediates and formation of the transition states. The observation of Co oxidation peak in the LSV (Figure 3c inset) supports the formation of higher oxidation states of Co during the catalytic cycles providing some support to this proposed mechanism. However, it must be mentioned here that this proposed mechanism is based on the general scheme of multistep proton coupled electron transfer mechanism for OER that has been observed and reported for other electrocatalytic systems.[53,54]

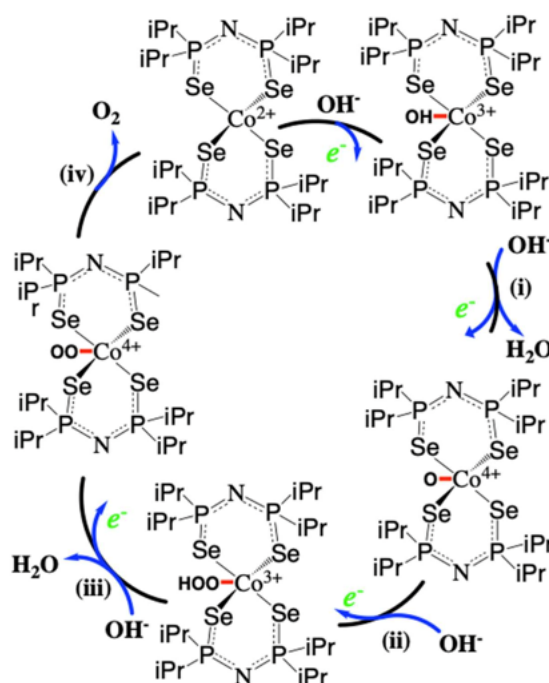


Figure 6. Schematic illustration of the proposed OER mechanism on the CoSe₄ complex. Shown through a vacant metal coordination site for OER showing the formation of a five-coordinated square pyramidal transition state following the catalyst's activation through -OH⁻ coordination to Co (II) and subsequent steps of OER.

To decipher the actual mechanism, one needs to identify the transition states through in situ spectroscopy and other techniques. However, based on characterization of the catalyst after OER activity, it can be clearly seen that the CoSe_4 catalytic core remains intact and maintains its Co-Se bonds and, therefore, even though the catalytic reaction is initiated by coordination of OH^- to the Co(II) center, the complex is not converted into any form of oxide/hydroxide. This confirms that the CoSe_4 core is indeed stable for OER and hence the mechanism proceeds via formation of a mixed anionic (hydroxo)chalcogenide coordination. This mechanistic scheme could be extrapolated to the cobalt–selenide-based extended solids that have been reported as active electrocatalysts for OER.

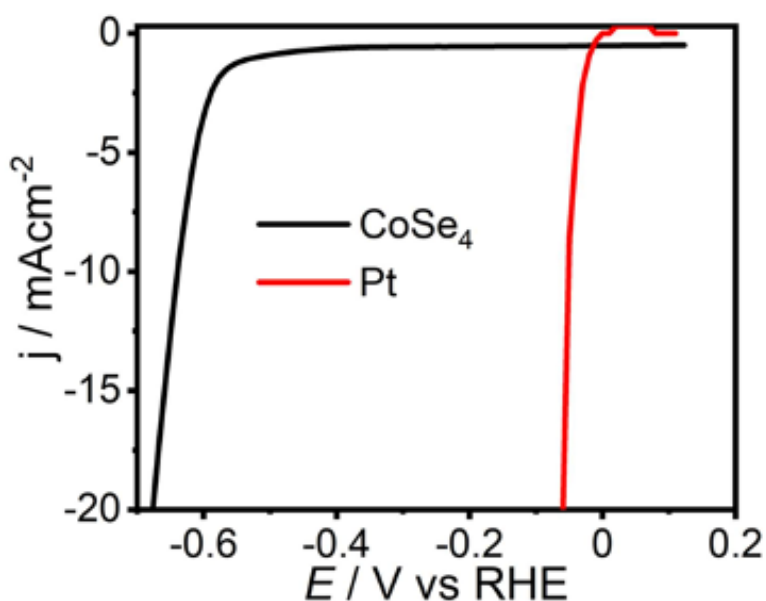


Figure 7. Polarization curves for HER with the CoSe_4 catalyst in N_2 -saturated 1.0 M KOH solution at a scan rate of 10 mV s^{-1} .

The electrocatalytic HER performance of the CoSe_4 catalyst and that of the state-of-the-art Pt catalyst were also studied and compared under similar conditions (in N_2 -saturated 1 M KOH). In order to avoid any form of catalytic activity interference, the HER

activity of CoSe₄ was evaluated using GC as the counter electrode instead of Pt, since Pt could undergo anodic dissolution and redeposit onto the cathode, which would affect the activity. The LSV (Figure 7) obtained with CoSe₄@Au-glass as cathode confirmed that it is active for HER and showed an onset potential of 0.52 V, which was higher than that with a Pt cathode. The cathodic current increased rapidly under more negative potentials. The overpotential for CoSe₄@Au at a current density of 10 mA cm⁻² was 0.63 V, which is also far from that with a Pt cathode. This shows that CoSe₄ is moderately active for HER. The catalytic activity can be possibly improved by intermixing the electrocatalyst with other conducting additives such as activated carbon, graphene or carbon nanotubes as has been reported earlier for other catalysts.[56–58]

4. CONCLUSIONS

A cobalt–seleno-complex, [Co{(SePiPr₂)₂N}₂], was reported as a bifunctional catalyst for OER and HER in alkaline medium. This complex bearing a catalytically active CoSe₄ first coordination sphere shows high inherent catalytic activity for OER as evidenced by the low overpotential and Tafel slope. This observed activity can be attributed to the higher covalency of the metal–chalcogen bond in CoSe₄ relative to cobalt oxides, which explains the observed enhancement in catalytic efficiency. The CoSe₄ complex demonstrated good OER activity in 1.0 M KOH with an overpotential of 320 mV at 10 mA cm⁻². Even though the activity for HER in alkaline medium demonstrated by the complex was low, modifying the ligands with either electron density donating or withdrawing groups[59,60] may improve HER activity. The superior catalytic activity shown by CoSe₄

for OER, as well as its remarkable stability, indicates its promising potential as a noble-metal-free catalyst for OER in water splitting. Further work on the ligand modification and elucidation of the mechanism and kinetics involved, as well as photoelectrocatalytic water splitting using this type of MSe_4 -containing catalysts in the presence of photosensitizers, is under investigation.

REFERENCES

1. Dai, L.; Xue, Y.; Qu, L.; Choi, H.J.; Baek, J.B. Metal-Free Catalysts for Oxygen Reduction Reaction. *Chem. Rev.* **2015**, *115*, 4823–4892.
2. Cook, T.R.; Dogutan, D.K.; Reece, S.Y.; Surendranath, Y.; Teets, T.S.; Nocera, D.G. Solar energy supply and storage for the legacy and nonlegacy worlds. *Chem. Rev.* **2010**, *110*, 6474–6502.
3. Lefrou, C.; Fabry, P.; Poignet, J.-C. *Electrochemistry*; Springer: Berlin/Heidelberg, Germany, 2009; ISBN 9782759804252.
4. Zhong, H.; Campos-Roldán, C.A.; Zhao, Y.; Zhang, S.; Feng, Y.; Alonso-Vante, N. Recent advances of Cobalt-Based electrocatalysts for oxygen electrode reactions and hydrogen evolution reaction. *Catalysts* **2018**, *8*, 559.
5. Deng, X.; Tüysüz, H. Cobalt-Oxide-Based materials as water oxidation catalyst: Recent progress and challenges. *ACS Catal.* **2014**, *4*, 3701–3714.
6. Huang, J.; Chen, J.; Yao, T.; He, J.; Jiang, S.; Sun, Z.; Liu, Q.; Cheng, W.; Hu, F.; Jiang, Y.; et al. CoOOH Nanosheets with High Mass Activity for Water Oxidation. *Angew. Chem.* **2015**, *54*, 8722–8727.
7. Plaisance, C.P.; Van Santen, R.A. Structure Sensitivity of the Oxygen Evolution Reaction Catalyzed by Cobalt(II,III) Oxide. *J. Am. Chem. Soc.* **2015**, *137*, 14660–14672.
8. Zhang, C.; Bhojate, S.; Kahol, P.K.; Siam, K.; Poudel, T.P.; Mishra, S.R.; Perez, F.; Gupta, A.; Gupta, G.; Gupta, R.K. Highly Efficient and Durable Electrocatalyst Based on Nanowires of Cobalt Sulfide for Overall Water Splitting. *ChemNanoMat* **2018**, *4*, 1240–1246.

9. Wang, J.; Zhong, H.X.; Wang, Z.L.; Meng, F.L.; Zhang, X.B. Integrated Three-Dimensional Carbon Paper/Carbon Tubes/Cobalt-Sulfide Sheets as an Efficient Electrode for Overall Water Splitting. *ACS Nano* **2016**, *10*, 2342–2348.
10. Akram, R.; Khan, M.D.; Zequine, C.; Zhao, C.; Gupta, R.K.; Akhtar, M.; Akhtar, J.; Malik, M.A.; Revaprasadu, N.; Bhatti, M.H. Cobalt sulfide nanoparticles: Synthesis, water splitting and supercapacitance studies. *Mater. Sci. Semicond. Process.* **2020**, *109*, 104925.
11. Nisar, L.; Sadaqat, M.; Hassan, A.; Babar, N.U.A.; Shah, A.; Najam-Ul-Haq, M.; Ashiq, M.N.; Ehsan, M.F.; Joya, K.S. Ultrathin CoTe nanoflakes electrode demonstrating low overpotential for overall water splitting. *Fuel* **2020**, *280*, 118666.
12. Gao, Q.; Huang, C.-Q.; Ju, Y.-M.; Gao, M.-R.; Liu, J.-W.; An, D.; Cui, C.-H.; Zheng, Y.-R.; Li, W.-X.; Yu, S.-H. Phase-Selective Syntheses of Cobalt Telluride Nanofleeces for Efficient Oxygen Evolution Catalysts. *Angew. Chem.* **2017**, *129*, 7877–7881.
13. Masud, J.; Swesi, A.T.; Liyanage, W.P.R.; Nath, M. Cobalt Selenide Nanostructures: An Efficient Bifunctional Catalyst with High Current Density at Low Coverage. *ACS Appl. Mater. Interfaces* **2016**, *8*, 17292–17302.
14. Liu, T.; Liu, Q.; Asiri, A.M.; Luo, Y.; Sun, X. An amorphous CoSe film behaves as an active and stable full water-splitting electrocatalyst under strongly alkaline conditions. *Chem. Commun.* **2015**, *51*, 16683–16686.
15. Li, W.; Gao, X.; Xiong, D.; Wei, F.; Song, W.G.; Xu, J.; Liu, L. Hydrothermal Synthesis of Monolithic Co₃Se₄ Nanowire Electrodes for Oxygen Evolution and Overall Water Splitting with High Efficiency and Extraordinary Catalytic Stability. *Adv. Energy Mater.* **2017**, *7*, 1–7.
16. Gao, M.R.; Xu, Y.F.; Jiang, J.; Zheng, Y.R.; Yu, S.H. Water oxidation electrocatalyzed by an efficient Mn₃O₄/CoSe₂ nanocomposite. *J. Am. Chem. Soc.* **2012**, *134*, 2930–2933.
17. Hussain, N.; Wu, F.; Xu, L.; Qian, Y. Co_{0.85}Se hollow spheres constructed of ultrathin 2D mesoporous nanosheets as a novel Bifunctional-Electrode for supercapacitor and water splitting. *Nano Res.* **2019**, *12*, 2941–2946.
18. Qin, R.; Hou, J.; Xu, C.; Yang, H.; Zhou, Q.; Chen, Z.; Liu, H. Self-Supporting Co_{0.85}Se nanosheets anchored on Co plate as highly efficient electrocatalyst for hydrogen evolution reaction in both acidic and alkaline media. *Nano Res.* **2020**, *13*, 2950–2957.

19. Cao, S.; Chen, Y.; Kang, L.; Lin, Z.; Fu, W.F. Enhanced photocatalytic H₂-evolution by immobilizing CdS nanocrystals on ultrathin Co_{0.85}Se/RGO-PEI nanosheets. *J. Mater. Chem. A* **2015**, *3*, 18711–18717.
20. Swesi, A.T.; Masud, J.; Nath, M. Nickel selenide as a High-Efficiency catalyst for oxygen evolution reaction. *Energy Environ. Sci.* **2016**, *9*, 1771–1782.
21. De Silva, U.; Masud, J.; Zhang, N.; Hong, Y.; Liyanage, W.P.R.; Zaeem, M.A.; Nath, M. Nickel telluride as a bifunctional electrocatalyst for efficient water splitting in alkaline medium. *J. Mater. Chem. A* **2018**, *6*, 7608–7622.
22. Zhang, G.; Zang, S.; Lan, Z.A.; Huang, C.; Li, G.; Wang, X. Cobalt selenide: A versatile cocatalyst for photocatalytic water oxidation with visible light. *J. Mater. Chem. A* **2015**, *3*, 17946–17950.
23. Cao, X.; Medvedeva, J.E.; Nath, M. Copper Cobalt Selenide as a High-Efficiency Bifunctional Electrocatalyst for Overall Water Splitting: Combined Experimental and Theoretical Study. *ACS Appl. Energy Mater.* **2020**, *3*, 3092–3103.
24. Cao, X.; Hong, Y.; Zhang, N.; Chen, Q.; Masud, J.; Zaem, M.A.; Nath, M. Phase exploration and identification of multinary Transition-Metal selenides as High-Efficiency oxygen evolution electrocatalysts through combinatorial electrodeposition. *ACS Catal.* **2018**, *8*, 8273–8289.
25. Guionneau, P.; Marchivie, M.; Bravic, G.; Létard, J.F.; Chasseau, D. Co(II) molecular complexes as a reference for the spin crossover in Fe(II) analogues. *J. Mater. Chem.* **2002**, *12*, 2546–2551.
26. Ferentinos, E.; Maganas, D.; Raptopoulou, C.P.; Psycharis, V.; Terzis, A.; Robertson, N.; Kyritsis, P. Conversion of tetrahedral to octahedral structures upon solvent coordination: Studies on the M[(OPPh₂)(SePPh₂)N]₂ (M = Co, Ni) and [Ni{(OPPh₂)(EPPh₂)N}₂(dmf)₂] (E = S, Se) complexes. *Dalton Trans.* **2011**, *40*, 169–180.
27. Maganas, D.; Krzystek, J.; Ferentinos, E.; Whyte, A.M.; Robertson, N.; Psycharis, V.; Terzis, A.; Neese, F.; Kyritsis, P. Investigating magnetostructural correlations in the Pseudo-Octahedral *trans*-[Ni^{II}{(OPPh₂)(EPPh₂)N}₂(sol)₂] complexes, E = S, Se; sol = DMF, THF) by magnetometry, HFEPR and ab initio quantum chemistry. *Inorg. Chem.* **2012**, *51*, 7218–7231.
28. Ferentinos, E.; Raptopoulou, C.P.; Psycharis, V.; Terzis, A.; Krzystek, J.; Kyritsis, P. Magnetostructural correlations in *S* = 1 *trans*-[Ni{(OPPh₂)(EPPh₂)N}₂(dmsO)₂], E = S, Se, and related complexes. *Polyhedron* **2018**, *151*, 177–184.

29. Ferentinos, E.; Xu, M.; Grigoropoulos, A.; Bratsos, I.; Raptopoulou, C.P.; Psycharis, V.; Jiang, S.-D.; Kyritsis, P. Field-induced slow relaxation of magnetization in the $S = 3/2$ octahedral complexes $\text{trans-[Co}\{(\text{OPPh}_2)(\text{EPh}_2)\text{N}\}_2(\text{dmf})_2]$, E = S, Se: Effects of Co–Se vs. Co–S coordination. *Inorg. Chem. Front.* **2019**, *6*, 1405–1414.
30. Sun, Y.; Bigi, J.P.; Piro, N.A.; Tang, M.L.; Long, J.R.; Chang, C.J. Molecular cobalt pentapyridine catalysts for generating hydrogen from water. *J. Am. Chem. Soc.* **2011**, *133*, 9212–9215.
31. Shi, H.T.; Li, X.X.; Wu, F.H.; Yu, W.B. Electrocatalytic oxygen evolution with a cobalt complex. *Dalton Trans.* **2017**, *46*, 16321–16326.
32. Mavros, M.G.; Tsuchimochi, T.; Kowalczyk, T.; McIsaac, A.; Wang, L.P.; Van Voorhis, T. What can density functional theory tell us about artificial catalytic water splitting? *Inorg. Chem.* **2014**, *53*, 6386–6397.
33. Pushkar, Y.; Moonshiram, D.; Purohit, V.; Yan, L.; Alperovich, I. Spectroscopic analysis of catalytic water oxidation by $[\text{Ru}^{\text{II}}(\text{bpy})(\text{tpy})\text{H}_2\text{O}]^{2+}$ suggests that $\text{RuV} = \text{O}$ is not a rate-limiting intermediate. *J. Am. Chem. Soc.* **2014**, *136*, 11938–11945.
34. Ho, X.L.; Das, S.P.; Ng, L.K.S.; Ng, A.Y.R.; Ganguly, R.; Soo, H.S. Cobalt Complex of a Tetraamido Macrocyclic Ligand as a Precursor for Electrocatalytic Hydrogen Evolution. *Organometallics* **2019**, *38*, 1397–1406
35. Wilken, M.; Siewert, I. Electrocatalytic Hydrogen Production with a Molecular Cobalt Complex in Aqueous Solution. *ChemElectroChem* **2020**, *7*, 217–221.
36. Queyriaux, N.; Sun, D.; Fize, J.; Pécaut, J.; Field, M.J.; Chavarot-Kerlidou, M.; Artero, V. Electrocatalytic Hydrogen Evolution with a Cobalt Complex Bearing Pendant Proton Relays: Acid Strength and Applied Potential Govern Mechanism and Stability. *J. Am. Chem. Soc.* **2020**, *142*, 274–282.
37. Jiang, H.; Zhang, H.; Kang, Q.; Ma, H.; Tong, Y.; Gao, F.; Lu, Q. Rapid Solvent-Evaporation strategy for Three-Dimensional Cobalt-Based complex hierarchical architectures as catalysts for water oxidation. *Sci. Rep.* **2019**, *9*, 1–8.
38. Li, G.; Zhang, X.; Zhang, H.; Liao, C.; Jiang, G. Bottom-up MOF-Intermediated synthesis of 3D hierarchical flower-like cobalt-based homobimetallic phosphide composed of ultrathin nanosheets for highly efficient oxygen evolution reaction. *Appl. Catal. B Environ.* **2019**, *249*, 147–154.
39. Gilby, L.M.; Piggott, B. The synthesis and X-ray structure of cobalt(II) complexes of iminobis (phosphinechalcogenides), $[\text{Co}\{\text{N}(\text{XPR}_2)_2\text{-X,X}'\}_2]$ (X = S or Se; R = Ph or Prⁱ). *Polyhedron* **1999**, *18*, 1077.

40. Sottini, S.; Poneti, G.; Ciattini, S.; Levesanos, N.; Ferentinos, E.; Krzystek, J.; Sorace, L.; Kyritsis, P. Magnetic anisotropy of tetrahedral Co^{II} Single Ion Magnets: Solid state effects. *Inorg. Chem.* **2016**, *55*, 9537–9548.
41. Panneerselvam, A.; Nguyen, C.Q.; Waters, J.; Malik, M.A.; O'Brien, P.; Raftery, J.; Helliwell, M. Ligand influence on the formation of P/Se semiconductor materials from Metal-Organic complexes. *Dalton Trans.* **2008**, *33*, 4499–4506.
42. Levesanos, N.; Robertson, S.D.; Maganas, D.; Raptopoulou, C.P.; Terzis, A.; Kyritsis, P.; Chivers, T. Ni[(EPⁱPr₂)₂N]₂ complexes: Stereoisomers (E = Se) and square-planar coordination (E = Te). *Inorg. Chem.* **2008**, *47*, 2949–2951
43. Jiang, S.D.; Maganas, D.; Levesanos, N.; Ferentinos, E.; Haas, S.; Thirunavukkuarasu, K.; Krzystek, J.; Dressel, M.; Bogani, L.; Neese, F.; et al. Direct observation of very large Zero-Field splitting in a tetrahedral Ni^{II}Se₄ coordination complex. *J. Am. Chem. Soc.* **2015**, *137*, 12923–12928.
44. Masud, J.; Ioannou, P.C.; Levesanos, N.; Kyritsis, P.; Nath, M. A Molecular Ni-Complex Containing Tetrahedral Nickel Selenide Core as Highly Efficient Electrocatalyst for Water Oxidation. *ChemSusChem* **2016**, *9*, 3128–3132
45. Li, H.; Qian, X.; Zhu, C.; Jiang, X.; Shao, L.; Hou, L. Template synthesis of CoSe₂/Co₃Se₄ nanotubes: Tuning of their crystal structures for photovoltaics and hydrogen evolution in alkaline medium. *J. Mater. Chem. A* **2017**, *5*, 4513–4526.
46. Campos, C.E.M.; De Lima, J.C.; Grandi, T.A.; Machado, K.D.; Pizani, P.S. Structural studies of cobalt selenides prepared by mechanical alloying. *Phys. B Condens. Matter* **2002**, *324*, 409–418.
47. Kwak, I.H.; Im, H.S.; Jang, D.M.; Kim, Y.W.; Park, K.; Lim, Y.R.; Cha, E.H.; Park, J. CoSe₂ and NiSe₂ Nanocrystals as Superior Bifunctional Catalysts for Electrochemical and Photoelectrochemical Water Splitting. *ACS Appl. Mater. Interfaces* **2016**, *8*, 5327–5334.
48. Yang, J.; Cheng, G.H.; Zeng, J.H.; Yu, S.H.; Liu, X.M.; Qian, Y.T. Shape control and characterization of transition metal diselenides MSe₂ (M = Ni, Co, Fe) prepared by a Solvothermal-Reduction process. *Chem. Mat.* **2001**, *13*, 848–853.
49. Trotochaud, L.; Ranney, J.K.; Williams, K.N.; Boettcher, S.W. Solution-Cast metal oxide thin film electrocatalysts for oxygen evolution. *J. Am. Chem. Soc.* **2012**, *134*, 17253–17261.
50. Bucci, A.; Mondal, S.S.; Martin-Diaconescu, V.; Shafir, A.; Lloret-Fillol, J. Cobalt Amide Imidate Imidazolate Frameworks as Highly Active Oxygen Evolution Model Materials. *ACS Appl. Energy Mater.* **2019**, *2*, 8930–8938.

51. González-Flores, D.; Sánchez, I.; Zaharieva, I.; Klingan, K.; Heidkamp, J.; Chernev, P.; Menezes, P.W.; Driess, M.; Dau, H.; Montero, M.L. Heterogeneous water oxidation: Surface activity versus amorphization activation in cobalt phosphate catalysts. *Angew. Chem.* **2015**, *54*, 2472–2476.
52. Meier, H.G.; Vilche, J.R.; Arvia, A.J. The electrochemical behaviour of cobalt in alkaline solutions Part I. The potentiodynamic response in the potential region of the Co/CoO couple. *J. Electroanal. Chem.* **1982**, *134*, 251–272.
53. Huang, Z.; Song, J.; Du, Y.; Xi, S.; Dou, S.; Nsamzimana, J.M.V.; Wang, C.; Xu, Z.J.; Wang, X. Chemical and structural origin of lattice oxygen oxidation in Co–Zn oxyhydroxide oxygen evolution electrocatalysts. *Nat. Energy* **2019**, *4*, 1–10.
54. Fang, T.; Fu, L.Z.; Zhou, L.L.; Zhan, S.Z.; Chen, S. Electrochemical-driven water reduction catalyzed by a water soluble cobalt(III) complex with Schiff base ligand. *Electrochim. Acta* **2015**, *178*, 368–373.
55. Zhang, M.; Zhang, M.T.; Hou, C.; Ke, Z.F.; Lu, T.B. Homogeneous electrocatalytic water oxidation at neutral pH by a robust macrocyclic nickel(II) complex. *Angew. Chem.* **2014**, *53*, 13042–13048.
56. Xing, Z.; Liu, Q.; Xing, W.; Asiri, A.M.; Sun, X. Interconnected Co-entrapped, N-Doped carbon nanotube film as active hydrogen evolution cathode over the whole PH range. *ChemSusChem* **2015**, *8*, 1850–1855.
57. Zou, X.; Huang, X.; Goswami, A.; Silva, R.; Sathe, B.R.; Mikmeková, E.; Asefa, T. Cobalt-Embedded Nitrogen-Rich Carbon Nanotubes Efficiently Catalyze Hydrogen Evolution Reaction at All pH Values. *Angew. Chem.* **2014**, *126*, 4461–4465.
58. Jin, H.; Wang, J.; Su, D.; Wei, Z.; Pang, Z.; Wang, Y. In situ Cobalt–Cobalt oxide/N-Doped carbon hybrids as superior bifunctional electrocatalysts for hydrogen and oxygen evolution. *J. Am. Chem. Soc.* **2015**, *137*, 2688–2694.
59. Cupertino, D.; Birdsall, D.J.; Slawin, A.M.Z.; Woollins, J.D. The preparation and coordination chemistry of ${}^i\text{Pr}_2\text{P}(\text{E})\text{NHP}(\text{E}')^i\text{Pr}_2$ (E, E' = Se; E = Se, E' = S; E = S, E' = O; E, E' = O). *Inorg. Chim. Acta* **1999**, *290*, 1–7.
60. Haiduc, I. Dichalcogenoimidodiphosphinate Ligands. In *Comprehensive Coordination Chemistry II: From Biology to Nanotechnology*; McCleverty, J.A., Meyer, T.J., Eds.; Fundamentals; Elsevier: Amsterdam, The Netherlands, 2004; Volume 1, pp. 323–347.

II. MOLECULAR CLUSTER COMPLEX OF HIGH VALENCE CHROMIUM SELENIDE CARBONYL AS EFFECTIVE ELECTROCATALYST FOR WATER OXIDATION

Ibrahim Munkaila Abdullahi and Manashi Nath

Department of Chemistry, Missouri University of Science and Technology, Rolla, MO
65409

ABSTRACT

Developing simple, affordable, and environmentally friendly water oxidation electrocatalysts with high intrinsic activity and low overpotential continues to be an area of intense research. In this article, a trichromium diselenide carbonyl cluster complex $(\text{Et}_4\text{N})_2[\text{Se}_2\text{Cr}_3(\text{CO})_{10}]$, with a unique bonding structure comprising bridging Se groups, has been identified as a promising electrocatalyst for oxygen evolution reaction (OER). This carbonyl cluster exhibits a promising overpotential of 310 mV and a low Tafel slope of 82.0 mV dec^{-1} at 10 mAcm^{-2} , with superior durability in an alkaline medium, for a prolonged period of continuous oxygen evolution. The mass activity and turnover frequency of 62.2 Ag^{-1} and 0.0174 s^{-1} was achieved, respectively at 0.390 V vs. RHE. The Cr-complex reported here shows distinctly different catalytic activity based on subtle changes in the ligand chemistry around the catalytically active Cr site. Such dependence further corroborates the critical influence of ligand coordination on the electron density distribution which further affects the electrochemical activation and catalytic efficiency of the active site. Specifically, even partial substitution with more electronegative substituents leads to the weakening of the catalytic efficiency. This report further demonstrates that

metal carbonyl chalcogenides cluster-type materials which exhibit partially occupied sites and high valence in their metal sites can serve as catalytically active centers to catalyze OER exhibiting high intrinsic activity. The insight generated from this report can be directly extrapolated to 3-dimensional solids containing similar structural motifs, thereby aiding in optimal catalyst design.

1. INTRODUCTION

The search for highly active and durable materials for sustainable energy conversion and storage has been attracting significant attention owing to the rapid depletion of fossil fuels amidst the growing concern about global warming. Water oxidation has been identified as an effective approach to generate clean hydrogen, which is one of the most sustainable zero carbon emission energy sources with a high energy density of 142 kJ kg^{-1} [1]. However, because of the sluggish kinetics of oxygen evolution reactions (OER) during water oxidation, electrocatalysts are generally employed to reduce the activation barrier along with stabilizing the OER intermediate adsorption on the catalyst surface [2–4]. Although significant research has led to the identification of precious metal-based oxides as efficient OER electrocatalysts, the high cost and scarcity of precious metals such as Ir, Ru, and Pt, severely limit their widespread practical applications. Over the last several years non-precious transition metal-based compositions have gained attention as OER electrocatalysts owing to their unprecedented high activity, tunable electrochemical property, and amenable band structure [5]. Although recent research has led to the identification of several transition metal-based electrocatalysts, a rational approach is still

missing for optimal catalyst surface design. An interesting approach to achieve this is by targeting transition metal-based coordination complexes (of Ni [6], Co [7], Cu [8], and Mn [9]) where the isolated metal–ligand core can provide significant insight into the intrinsic electrocatalytic activity of the transition metal site in presence of specific ligand environment, that can be then extrapolated into the extended solid.

In this regard, multimetallic molecular clusters can be highly interesting for such catalyst design. These molecular cluster comprising a large number of atoms in the building block serves as the link interconnecting solid state and molecular chemistry [10]. Among these, homometallic metal chalcogenide carbonyls [11,12], clusters containing metal rings and metal–metal bonds stabilized by either phosphines [13,14], or arenes [15], as well as the bridging chalcogenide [16] (μ_3 -S [12,17], μ_3 -Se [18], and μ_3 -Te [13]) ligands are especially attractive due to the packing density and availability of multiple catalytic sites. Of particular interest is the selenium-capped carbonyltrimetallic cluster of which only very few have been reported [18–20]. The first three members of group 6B (Cr, Mo, and W) are known [18,19], and mixed metal [19,20] and Fe-based clusters have been reported [21]. Although some structural, magnetic, and optical studies have been reported [20–22], however, they have not been explored for electrochemical properties.

Despite the unique properties of chromium favoring catalytic properties, very few Cr-based compositions have been studied for electrocatalysis [23–26]. Chromium is a high valance transition-metal and being slightly oxophilic can easily associate with hydroxide ions of the electrolyte. The strength of the Cr-O bond is of significance in catalysis, since higher strength favors chemisorption and O-O bond activation [27]. Recently, a trichromium diselenium carbonyl complex, $[\text{Se}_2\text{Cr}_3(\text{CO})_{10}](\text{Et}_4\text{N})_2$, was reported [19], with

a distinctive triangular metal bonding structure. This complex provides a unique opportunity for understanding the role and effect of the structure and bonding nature of the core Cr-Se bond, and the presence of Cr-Cr bonds on electrocatalytic water oxidation. The activity of the Cr-Se core in the cluster system could demonstrate the intrinsic activity of the Cr-Se linkages and by extension the activity of bulk Cr-based chalcogenides, and other coordination polymers with similar structures.

To date, the electrochemical OER activity of Cr-based molecular clusters has not been studied in any systematic investigations. Herein, we report the use of the Se-capped trichromium carbonyl cluster $[\text{Se}_2\text{Cr}_3(\text{CO})_{10}](\text{Et}_4\text{N})_2$ as a highly efficient electrocatalyst for water oxidation. The OER activity in an alkaline medium revealed a low onset potential of 1.47 V vs. RHE with an overpotential of 310 mV @ 10 mA cm⁻². This enhancement in electrocatalytic activity can be attributed to the optimal binding strength provided by catalytically active Cr sites, which is favorable for the adsorption of oxygen-containing intermediates, assisted by local oxidation of Cr(III) to Cr(VI) during the polarization process.

2. METHODOLOGY

2.1. MATERIALS

Conductive carbon paper (CCP) suitable for battery, fuel cell, and supercapacitor research purchased from MSE supplies, Tucson, AZ 85711 USA. While chromium hexacarbonyl, Nafion (5 wt.%), and selenium (IV) oxide (SeO₂), isopropanol (iPr-OH), cyclohexane (C₆H₁₂) were purchased from Sigma–Aldrich Chemical Reagent Co., Ltd. St.

Louis MO, sodium hydroxide (NaOH), methanol (MeOH), dichloromethane (CH₂Cl₂) and tetraethyl bromide [Et₄N]Br were purchased from Fisher Scientific Pittsburgh, USA. All the reagents were used as received. The deionized (D.I.) water purified through a Millipore system was used in all experiments. The CCP was washed with iPr-OH and D.I water several times to ensure the surface is cleaned before use.

2.1.1. Preparation of Cr-Se Red (deca carbonyltrichromium diselenide ditetraethylamine). The synthesis of this compound has been reported in a previous report.[19] All reactions were carried out under the N₂ atmosphere. A mixed solution of MeOH (30 mL) and cyclohexane (7.5 mL) was added to a mixture containing [Cr(CO)₆] (0.8 g, 3.64 mmol), SeO₂ (0.21 g, 1.89 mmol) and NaOH (3.0 g, 82.5 mmol) taken in 100 mL three neck round flask. This mixture was heated to reflux at 70 °C for 12 h yielding a dark-red solution that was filtered, and the filtrate was concentrated. A MeOH solution of [Et₄N]Br (3.0 g, 14.3 mmol) was added to the concentrated filtrate dropwise, whereby, the red Cr₃Se₂(CO)₁₀[(Et₄N)₂] was precipitated as a solid product in a metathesis reaction. The solid product was washed several times with MeOH and CH₂Cl₂ and dried as Cr-Se red complex. Elemental Analysis found the following composition for Cr-Se red: C, 36.20; H, 5.61; N, 3.28%. Calculated: C, 36.55; H, 4.72; N, 3.28%. Compound Cr-Se red is soluble in MeCN and acetone, but insoluble in other organic solvents.

2.1.2. Preparation of Cr-Se Green (decahydrate trichromium diselenide ditetraethylamine). The Cr-Se green was accidentally formed from Cr-Se red, by leaving the Cr-Se red solid product to remain standing in MeOH and CH₂Cl₂ during washing for 2-3 weeks in the presence of moisture and air and was dried as Cr-Se green complex. Elemental Analysis found for Cr-Se green: C, 28.28; H, 7.91; N, 1.83%. Calculated: C,

25.47; H, 8.01; N, 3.71%. Compound Cr-Se green is soluble in MeCN and acetone, but insoluble in other organic solvents.

2.1.3. Electrode Preparation. All CCP substrates were cleaned with iPr-OH, dried, and covered with Teflon tape, leaving an exposed geometric area of 0.283 cm². Catalyst ink was prepared by dispersing 10.0 mg of the catalyst in 1.0 mL 0.8% Nafion in iPr-OH and ultrasonicated for 30 min. A 20 μ L volume of the ink was pipetted out and drop-casted on the CCP substrate on the exposed geometric area, dried at room temperature, and finally heated at 130 °C in an oven for 30 min in air. This was used as working electrodes.

2.1.4. Characterization Methods. XPS measurements were performed using a KRATOS AXIS 165 X-ray photoelectron spectrometer (Kratos Analytical Limited, Manchester, United Kingdom) using a monochromatic Al X-ray source. The C 1s signal at 284.5 eV was used as a reference to correct all the XPS binding energies.[7] All XPS spectra were collected from the pristine catalyst surface without sputtering. The Raman spectra of the catalyst were recorded with LabRam ARAMIS (HORIBA Jobin-Yvon Raman spectrometer equipped with a CCD detector) in the Raman shift range between 50 cm⁻¹ to 1800 cm⁻¹, 1200 lines mm⁻¹ grating, HeNe laser 632.8 nm excitation with a nominal output power of 100mW, 0.95 cm⁻¹/pixel spectral dispersion, 10% of laser power, 10x objective, 0.25 numerical aperture, 100 μ m slit, 200 μ m hole, 30 seconds exposure time, 10x accumulations for each sample acquisition.[42] Fourier Transform Infrared (FTIR) spectra were recorded using a Thermo Nicolet NEXUS 470 FT -IR Spectrometer, in a range of 400 -4000 cm⁻¹ with 1 cm⁻¹ resolution. Pellets were prepared by pressing a mixture of 2 mg catalyst and 200 mg KBr under a load of 10 -15 tons.[43,44] Thermal

gravimetric analysis (TGA) was performed with a heating rate of $10\text{ }^{\circ}\text{C min}^{-1}$ on a Netzsch STA 449C instrument.[33] Electrochemical measurements were performed using a conventional three-electrode system connected to an IviumStat potentiostat, with catalyst-coated CCP as the working electrode, while graphite rod and Ag/AgCl electrode were used as counter electrode and reference electrodes, respectively, to measure the electrocatalytic performances. Linear sweep voltammetry (LSV), and cyclic voltammetry (CV) were carried out to study the OER catalytic performance and cycling stability. To reduce uncompensated solution resistance, all activity data were iR -corrected, which was measured through electrochemical impedance studies. All potentials measured were calibrated to RHE using the following Equation (1):

$$E_{(\text{RHE})} = E_{(\text{Ag}/\text{AgCl})} + 0.197\text{V} + 0.059 \cdot \text{pH} \quad (1)$$

All electrolytes were saturated by oxygen (for OER) bubbles before and during the experiments.

2.1.5. Chronoamperometry Stability Study. The steady-state performance and durability of Cr-Se red electrocatalysts in OER for long-term chronoamperometric stability in the alkaline electrolyte of 1 M KOH solution were carried out in two forms: (a) At a constant current density of $20\text{ mA}\cdot\text{cm}^{-2}$ for 24 h. (b) At various current densities between $5 - 30\text{ mA}\cdot\text{cm}^{-2}$ as multistep study, both in N_2 -saturated 1.0 M KOH at room temperature.

2.1.6. Tafel Slope. The Tafel slope, an important parameter to explain the electrokinetic activity of these thin film catalysts for OER and HER processes, was estimated from the Tafel plot. The Tafel equation is given as the dependence of overpotential η on the current density j as shown in Equation (2).

$$\eta = \alpha + (2.3RT / \alpha nF) * \log(j) \quad (2)$$

where α is the transfer coefficient, n is the number of electrons involved in the reaction, and F is the Faraday constant. The Tafel slope is given by $\frac{2.3RT}{\alpha nF}$. The Tafel plots in this work were calculated from the reverse scan of CV collected at a scan rate of 2 mV s^{-1} in a non-stirred N_2 -saturated 1.0 M KOH solution.

2.1.7. Electrochemical Impedance Spectroscopy (EIS). The EIS experiments were performed within 10^5 – 10^{-2} Hz frequency range, at an AC signal amplitude of 10 mV , to study the electrode kinetics and estimate the electrolyte resistance (R_1), charge transfer resistance at the electrode (catalyst)-electrolyte interface (R_2), as well as the film resistance (R_3). The Nyquist plots were collected in N_2 -saturated 1.0 M KOH at an applied potential of $0.55 \text{ V vs. Ag|AgCl (KCl saturated)}$.

2.1.8. Turnover Frequency (TOF). Turnover frequency (TOF) for the electrocatalysts was calculated from Equation (3).

$$\text{TOF} = j \cdot A / 4 \cdot m \cdot F \quad (3)$$

where j is the current density in mA cm^{-2} at a given overpotential (e.g., $\eta = 0.39 \text{ V}$), A is the surface area of the electrode (0.283 cm^2), F is the Faraday constant (a value of 96485 C mol^{-1}), and m is moles of catalyst on the electrode.

2.1.9. Mass Activity. Mass activity (A g^{-1}) is the current density per unit mass of the active catalyst at a given overpotential. This is calculated from catalyst loading m and the measured current density j (mA cm^{-2}) of the catalyst, at $\eta = 0.39 \text{ V}$, calculated from Equation (4).

$$\text{Mass activity} = j / m \quad (4)$$

2.1.10. Electrochemically Active Surface Area (ECSA) and Roughness Factor (RF). The electrochemically active surface area (ECSA) of the catalyst was estimated by

measuring the electrochemical double-layer capacitance (C_{DL}) at different scan rates in the non-Faradaic region. It was assumed that the current obtained in the non-Faradaic region is caused by double-layer charging instead of electrochemical reactions or charge transfer. The double-layer current (i_{DL}) was obtained by performing cyclic voltammograms (CVs) with various scan rates in a non-stirred N_2 saturated 1.0 M KOH solution. The ratio of double-layer current (i_{DL}) and the scan rate (v) of CV yielded the specific electrochemical double-layer capacitance (C_{DL}). Averaging of cathodic and anodic slopes gave absolute values obtained from the CV plot in the non-faradaic region as described in Equation (5).

$$i_{DL} = C_{DL} * v \quad (5)$$

The ECSA of the catalyst was calculated using Equation (6) where C_S is the specific capacitance as reported in alkaline solution to be between 0.022 and 0.130 $mF\ cm^{-2}$ in alkaline solution. In this study, we assumed the value of C_S to be = 30 μFcm^{-2} based on previously reported OER catalysts in an alkaline medium.

$$ECSA = C_{DL} / C_S \quad (6)$$

The roughness factor (RF) is another important parameter that defines catalyst surface roughness and can influence observed catalytic properties. It is estimated as the ratio of ECSA and the geometric electrode area (0.283 cm^2) as shown in Equation (7).

$$RF = ECSA / SA \quad (7)$$

3. RESULTS

The Se-capped carbonyltrichromium $[Se_2Cr_3(CO)_{10}](Et_4N)_2$ molecular cluster was synthesized by reaction of $Cr(CO)_6$ with SeO_2 in concentrated methanolic-NaOH

solution using cation metathesis with $[\text{Et}_4\text{N}]\text{Br}$, following reported procedure [19]. This reaction led to the formation of the Cr-Se complex as represented in Figure 1a which had a distinct red coloration and has been referred to as the red Cr-Se complex henceforth. The Cr-Se cluster has an interesting structure exhibiting trigonal bipyramidal coordination with bridging μ_3 -Se atoms capped above and below bonded Cr_3 -ring. In this bonding situation, each Se atom donates $4e^-$ to the Cr_3 triangle forming $48e^-$ species, which supports the Cr_3 having $(3\times)$ Cr-Cr bonds. The washings during the metathesis with $[\text{Et}_4\text{N}]\text{Br}$ were collected, concentrated, washed, and dried, yielding another Cr-Se complex with a distinct green coloration, referred to as a green Cr-Se cluster. The detailed crystal structure analysis of the Cr-Se red cluster from single crystal X-ray diffraction has been reported previously [19]. Raman and FTIR analysis were used to further characterize these Cr-Se complexes, specifically the green cluster. The Raman spectra showed the presence of a Raman peak at 117 cm^{-1} corresponding to the Cr_3 motif, while peaks around 250 and 342 cm^{-1} were attributed to E_{1g} and A_{1g} modes in both clusters. The Raman peak at 847 cm^{-1} corresponds to the vibrational mode of Cr-C in the Cr-Se red cluster while the peak at 850 cm^{-1} indicated the presence of Cr-OH linkage in the Cr-Se green cluster Figure 1b. The FTIR spectra (Figure 1c) also showed broad IR peaks $\sim 3461\text{ cm}^{-1}$ attributed to O-H stretching mode in both Cr-Se red and Cr-Se green clusters, indicating the presence of moisture. However, the peak was much broader and more intense in the Cr-Se green cluster, indicating the higher magnitude of hydrogen bonds, possibly due to the presence of coordinated H_2O molecules, while the IR peak $\sim 1623\text{ cm}^{-1}$ could be assigned to the O-H bending mode of H_2O molecules. The Cr-Se green showed no peak between $1900\text{--}1550\text{ cm}^{-1}$ indicating the

absence of the CO group, while Cr-Se red shows a doublet peak at around 1800 cm^{-1} , indicating the presence of a bound CO group [28].

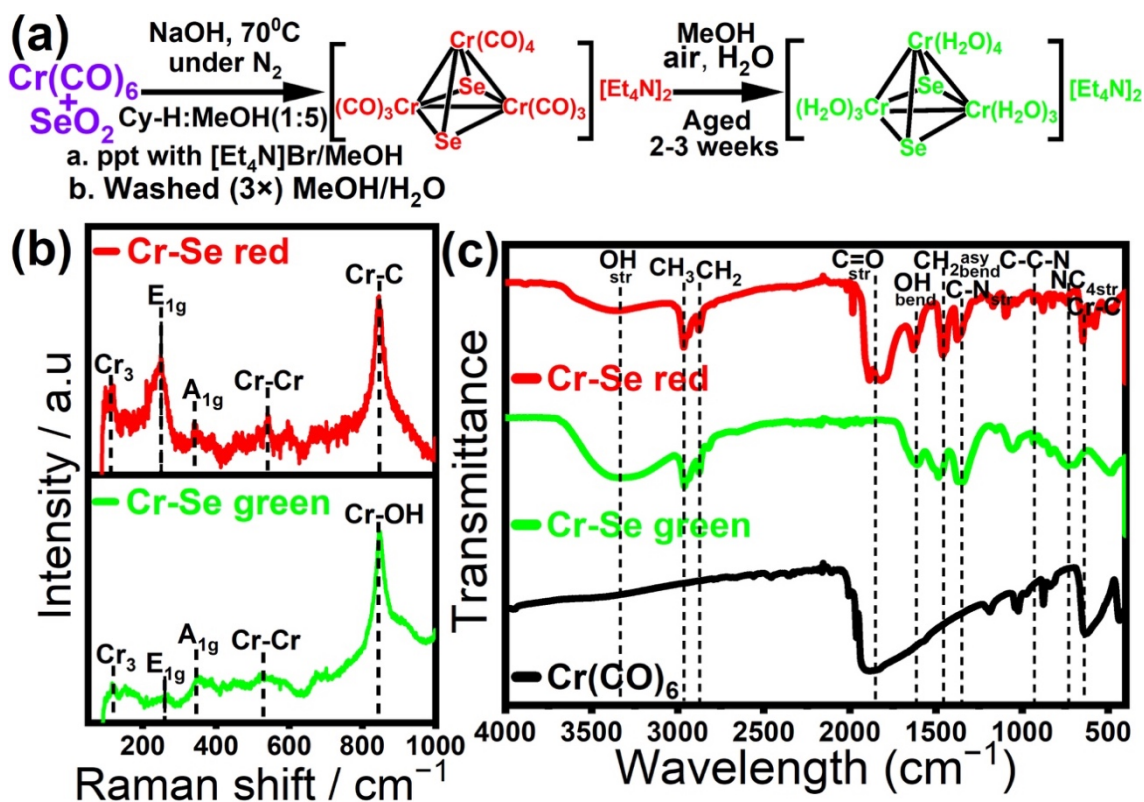


Figure 1. Synthesis and spectroscopic characterizations of Cr–Se red and Cr–Se green catalysts. (a) Reaction scheme describing synthesis method along with compositional details. (b) Raman spectra, excited with 632.8 nm HeNe laser radiation; (c) FTIR spectra.

Furthermore, the IR absorption vibrational peaks that appeared at 1461 cm^{-1} were assigned to CH_3 while 2963 cm^{-1} and 2877 cm^{-1} correlate with CH_3 and CH_2 modes, respectively, confirming the presence of Et_4N counter ions in these clusters [29–31]. The absorption peaks below 800 cm^{-1} , correspond to other bending and stretching vibration modes including Cr-Se at 668 cm^{-1} , while other less obvious peaks are most likely due to O-M-O and M-O-H modes. The CHN elemental analysis of the Cr-Se red and Cr-Se green cluster samples revealed the relative atomic ratio of C, H, and N in the samples. Such

compositional analysis also corroborated the formulation of the green cluster as $\text{Cr}_3\text{Se}_2\text{C}_{40}\text{H}_{117}\text{N}_5\text{O}_{10}$, while the red cluster had a molecular formula of $\text{Cr}_3\text{Se}_2\text{C}_{26}\text{H}_{40}\text{N}_2\text{O}_{10}$ as shown in Figure 1a. Specifically, the CO ligands coordinated to Cr in the red cluster were replaced with water molecules to form the green clusters.

X-ray photoelectron spectroscopy (XPS) was employed to characterize the oxidation states, composition, and local coordination of the cluster surface (Figure 2). Deconvoluted peaks of the Cr $2p$ spectrum (Figure 2a) showed peaks around 576.0 eV and 585.9 eV attributed to Cr(III) of $2p_{3/2}$ and $2p_{1/2}$ states, respectively, while two other peaks around 578.4 eV and 586.7 eV were matched to Cr(VI) of $2p_{3/2}$ and $2p_{1/2}$ states, respectively [1]. This indicates that Cr(III) and Cr(VI) states co-exist in the cluster, with Cr(III) as the main species. The Se 3d spectrum (Figure 2b) shows peaks at 53.3 and 54.6 eV assigned respectively to Se $3d_{5/2}$ and Se $3d_{3/2}$, which corroborates the presence of Se^{2-} , whereas the low-intensity peak around ~ 58.6 eV corresponds to SeO_x species which could be from selenide surface oxidation [6,7,32]. Interestingly, XPS analysis revealed minimal Cr-oxide on the surface. The deconvoluted C $1s$ spectrum (Figure 2c) shows three peaks, corresponding to $\text{sp}^3\text{-C}$ at around 284.8 eV, the C-O of carboxyl, or carbonyl groups at 286.1 eV, and the C=O of carbonyl groups at 288.8 eV. These were corroborated by the O $1s$ spectrum (Figure 2c) showing peaks corresponding to C=O and C-OH, in addition to Cr-C-O and Cr-O peaks. Similar observations were made for the Cr-Se green complex (Figure 3), where the high-resolution XPS spectra for Cr-Se green were measured to determine the valence states of the Cr species by the deconvolution of the Cr $2p$ spectrum. The peaks at 576.2 eV and 586.0 eV were assigned to Cr(III) $2p_{3/2}$ and Cr(VI) $2p_{1/2}$, respectively, while deconvoluted peaks at 574.1 eV and 574.4 eV were attributed to Cr(0)

and Cr(II), respectively. The other two peaks at 576.3 eV and 583.0 eV were due to the presence of Cr(OH) and CrO_x, respectively.

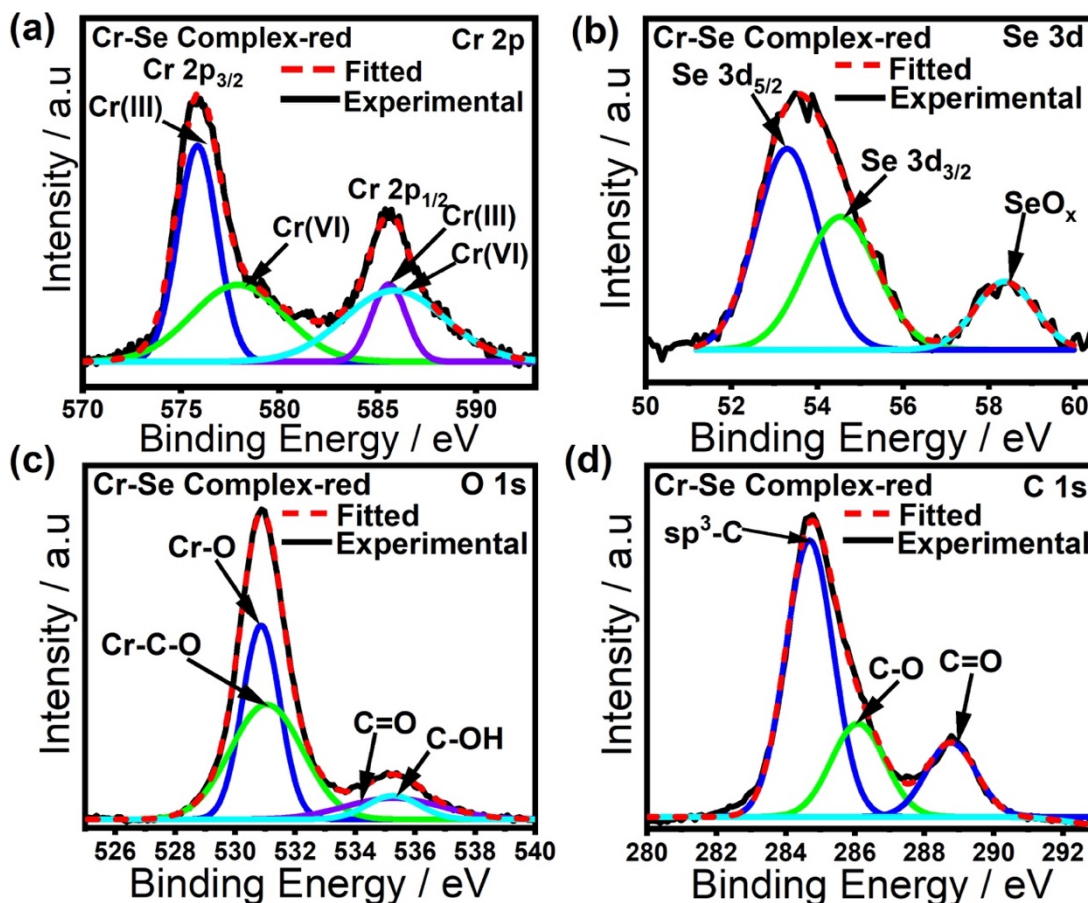


Figure 2. The high-resolution XPS spectra of Cr-Se red complex showing its elemental states. (a) Cr 2p peak; (b) Se 3d peak; (c) C 1s peak; (d) surface O 1s peak.

This is similar to what was observed in the previous report [33], indicating the formation of surface oxides and hydroxyl coordination in the cluster. However, Cr(III) was still observed as the dominant species. The Se 3d spectrum, showed peaks shifted to 57.6 and 58.6 eV corresponding to Se 3d_{5/2} and Se 3d_{3/2}, respectively, which confirmed the presence of Se²⁻. The peak at ~62.0 eV indicates the existence of SeO_x species which could arise from selenide surface oxidation. However, no metal oxides were detected on the

catalyst surface from the XPS analysis. The C 1s spectra were deconvoluted and the peak at 284.9 eV corresponded to the sp^3 -C bond, and the peak at 285.4 eV C-O bond of carboxyl or carbonyl functional groups, and the peak at 288.7 eV was assigned to C=O bond of carbonyl groups [1,23,24]. Furthermore, the thermogravimetric analysis (TGA) described the stepwise decomposition of both of Cr-Se red and Cr-Se green clusters (Figure S1), and the percentage weight loss in both complexes agree with the calculated values estimated from the proposed molecular formulation.

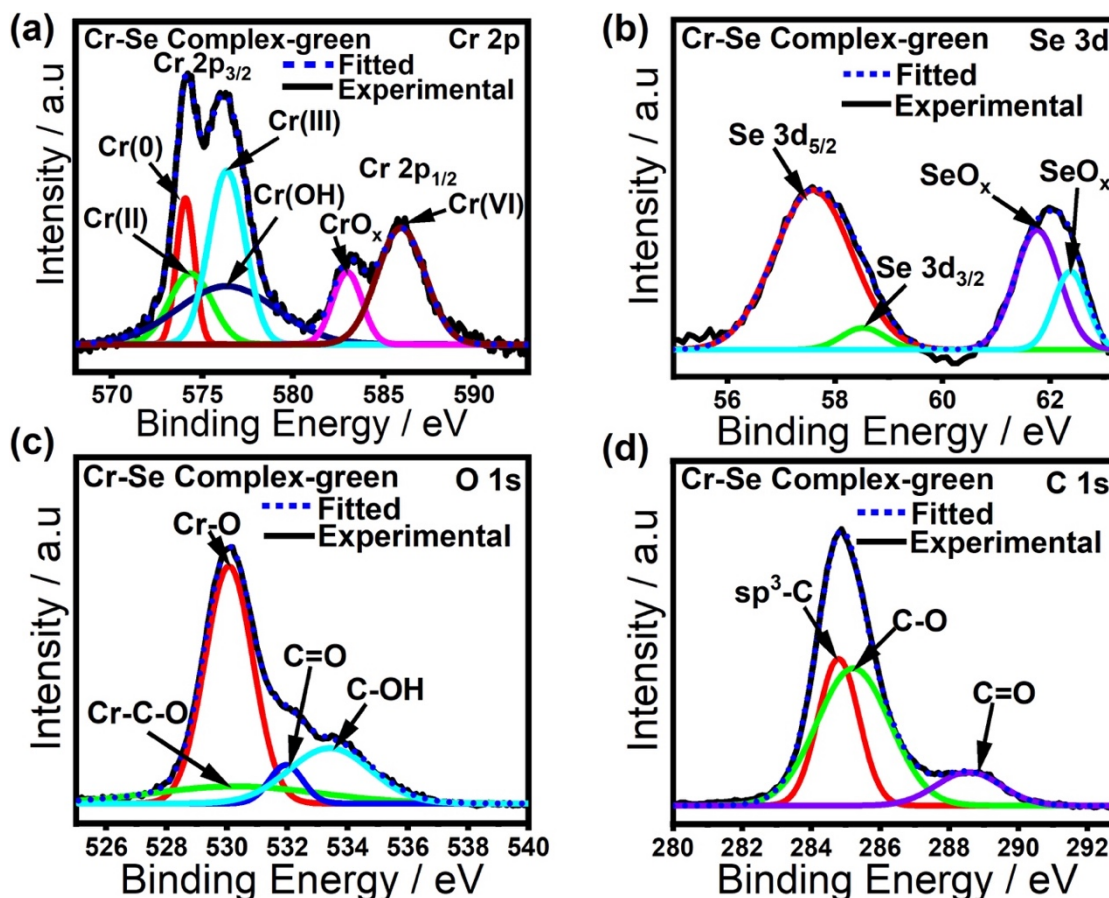


Figure 3. The high-resolution XPS spectra of Cr-Se green complex showing its elemental states. (a) Cr 2p peak; (b) Se 3d peak; (c) C 1s peak; (d) surface O 1s peak.

The electrocatalytic OER performance of Cr-Se red and Cr-Se green clusters was investigated in an alkaline medium of 1 M KOH (pH 13.7) using a three-electrode system, with graphite rod and Ag|AgCl as counter and reference electrodes, respectively, while the catalysts were drop casted on a conductive carbon paper and used as working electrode. The assembly of the catalyst electrode (working electrode preparation) is described in the materials and methods section. The polarization curves obtained using linear scan voltammetry (LSV) (Figure 4a) indicate that Cr-Se red cluster achieved an overpotential of 310 mV at 10 mA cm^{-2} making it a better OER active electrocatalyst in comparison to the Cr-Se green cluster with 350 mV overpotential. It can be observed that the presence of Cr in variable oxidation states in both samples strongly influences the OER performance by improving current density and minimizing overpotential. The presence of Cr in two different oxidation states, not only increases electroactive sites but further enhances the electronic transition, thereby facilitating catalyst activation through hydroxide adsorption on the Cr catalytic sites. Moreover, the higher covalency of the multiple Cr-Se bonds present as well as the enhanced conductivity of Cr-Cr bonds is important factors that could affect the observed catalytic efficiency. Additionally, the lability of the coordinating ligands in the Cr-Se green clusters tends to free up the metal sites for incoming OH^- under applied potential [34]. The activity of Cr-Se green was observed to be moderately good; this can be attributed to the association of Cr sites with water and OH^- which has been demonstrated to show high intermediate adsorption on catalytic sites leading to performance enhancement [24]. The cyclic voltammetry (CV) shown in Figures 4b and 4c illustrates the reduction of the active Cr species during a reverse sweep at potentials of 1.33 and 1.35 vs. RHE for Cr-Se red and Cr-Se green clusters, respectively, which is consistent

with reported literature [35]. The active species is regenerated in the forward oxidation sweep at potentials around 1.46 and 1.48 vs. RHE [36], just before the OER onset, further corroborating with the activity observed by the LSV (Figure 4a). The oxidation and reduction reaction kinetics of the Cr-Se red cluster was measured using variable scan rates between 10 and 100 mV/s in OER (Figure 4d). This shows more obvious reduction peaks shifting slightly more left, while oxidation peaks shifting slightly more right indicate quasi-reversible behavior of Cr species [37].

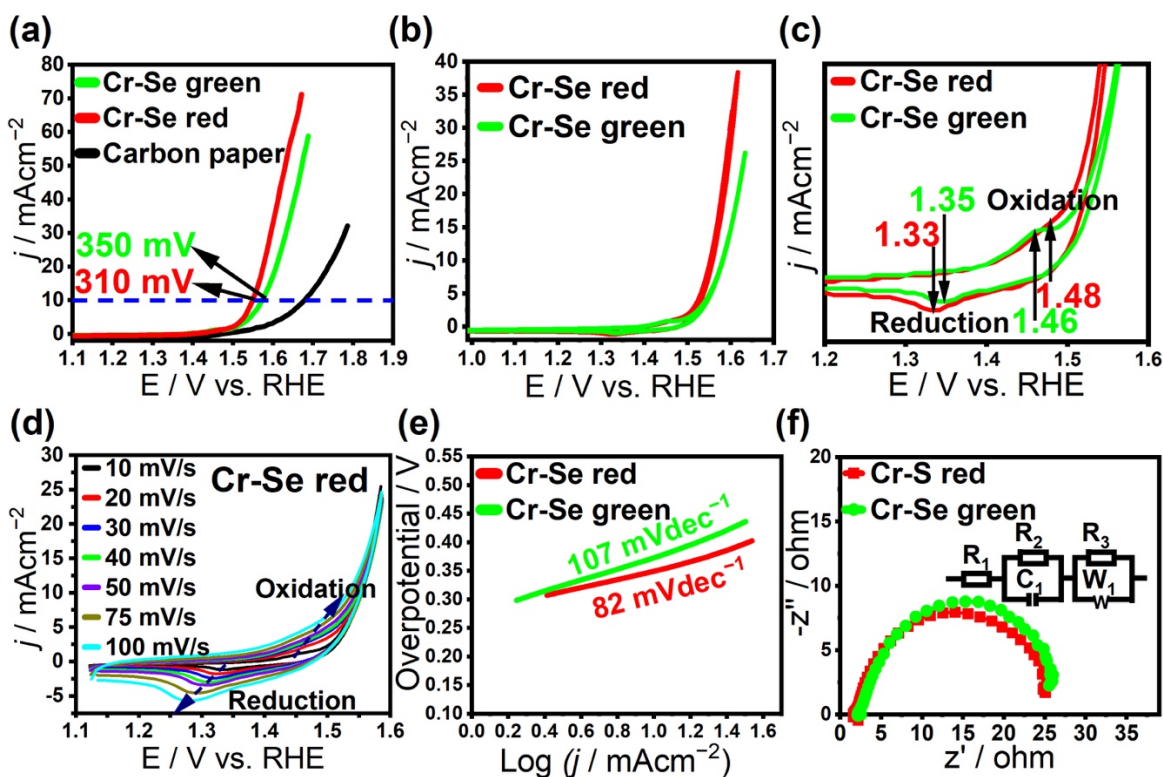


Figure 4. Electrocatalytic OER activity of Cr–Se red and Cr–Se green complexes. (a) Linear scan voltammetry showing overpotential at 10 mA/cm². (b) Cyclic voltammetry. (c) The Cr(III) and Cr(VI) redox potentials for Cr–Se red and green complexes. (d) Cyclic voltammograms of Cr–Se red complex measured at scan rates from 10 to 100 mV/s. (e) Tafel plots. (f) Electrochemical impedance spectroscopy (EIS) showing Nyquist plots in the AC frequency range between 100 kHz and 0.1 Hz, at 1.55 V vs. RHE. Inset shows the fitted equivalent circuit.

The Tafel slope for Cr-Se red was found to be 82 mV dec^{-1} as compared Cr-Se green, which was 107 mV dec^{-1} , which indicates a much faster reaction kinetics and simple electron transfer between the Cr-Se red electrocatalyst and electrolyte (Figure 4e), in agreement with the observation of facile OER. The electrochemical impedance spectroscopy (EIS) plots (Figure 4f) showed semi-circular ellipsoids, which could be fitted to equivalent circuit models depicting the various conducting pathways on the catalyst-electrode composite [38]. Typically, two processes can occur during electrochemical OER: (i) reactive intermediate adsorption through catalyst activation; and (ii) O-O desorption process. An equivalent circuit demonstrating two charge-transfer, a process obtained from EIS plot fitting, is shown in the insert in Figure 4f. The R_1 values are the electrolyte resistance. C_1R_2 represents the transformation of the active intermediate and W_2R_3 for the O-O desorption process. Table S1 shows EIS equivalent circuit parameters. The Cr-Se red revealed a smaller R_1 value indicating a faster charge-transfer process. The OER activity of both Cr-Se red and Cr-Se green molecular complexes were compared with the recently published Cr-based OER electrocatalysts as shown in Table S2 in supporting information. It was found that our catalysts were comparable to or better than the recently published Cr-based electrocatalysts which further confirms the critical influence of ligand coordination on electrocatalytic activity.

To further appreciate the OER activity of the Cr-Se red and Cr-Se green cluster electrocatalysts, the mass activity and turnover frequency (TOF) were obtained as shown in Figure 5. The OER-specific mass activities were measured at 0.39 V overpotential. Cr-Se red and Cr-Se green catalysts exhibit specific mass activities of 62.4 and 37.2 Ag^{-1} , respectively (Figure 5a). Furthermore, the TOF of 0.0174 and 0.0164 s^{-1} was achieved at

0.39 overpotential for Cr-Se red and Cr-Se green catalysts, respectively. The electrochemically active surface area (ECSA) is one of the key descriptors for electrocatalysts which influences the kinetics of electrochemical conversion. The ECSAs of Cr-Se red and Cr-Se green were investigated using cyclic voltammetry (CV) plots collected in the range from 0.05 to 0.25 V vs. Ag|AgCl with scan rates between 20 and 100 mV s^{-1} in N_2 saturated 1 M KOH solution.

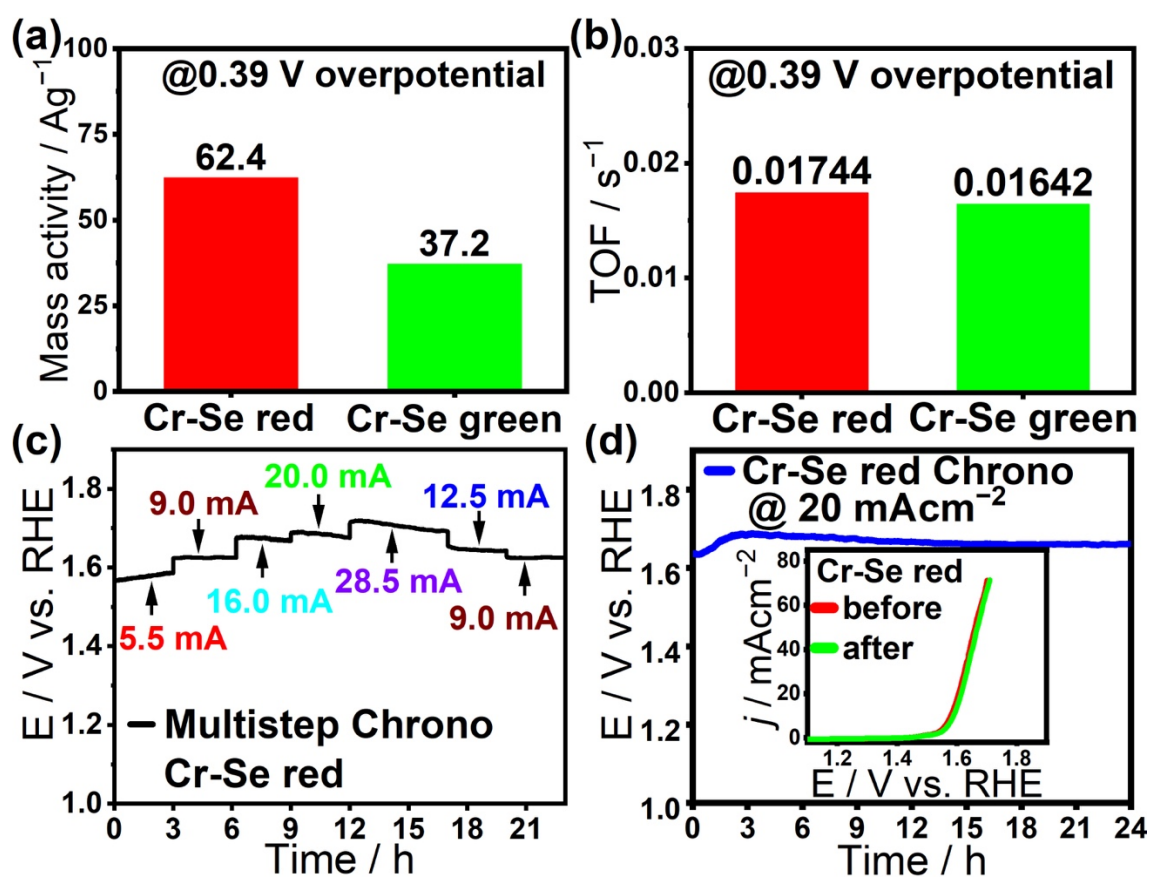


Figure 5. Electrocatalytic performance and stability of Cr-Se red and Cr-Se green complexes. (a) Mass activity; (b) Turnover frequency (TOF); (c) Multistep chronoamperometry study of Cr-Se red at various current densities.; (d) Chronoamperometry at constant current density. Inset shows the comparison of OER activity before and after long-term chronoamperometry.

Figures S2 and S3 show the anodic and cathodic currents plotted as a function of scan rates. ECSA was calculated using the double-layer capacitance of the catalysts and the specific capacitance as described in the Experimental Section. Cr-Se red and Cr-Se green clusters showed ECSA of 91 cm² and 54 cm², respectively, corroborating the accessibility to a larger number of active sites and hence the high activity observed.

The electrochemical OER parameters of Cr-Se red and Cr-Se green are compared in Table 1. The Cr-Se red shows lower overpotential and Tafel slope, indicating better electrocatalytic activity. In addition, its TOF, mass activity, and ECSA were higher for the Cr-Se red, further corroborating its higher performance. A higher ECSA value generally indicates a larger electrochemically active surface area which improves electrolyte/active site interaction, leading to better catalytic performance for OER. A large ECSA value results in high surface roughness (RF), which is another parameter considered that affects catalytic activity.

Table 1. Electrocatalytic parameters compared in Cr-Se catalytic systems.

Material	Cr-Se red	Cr-Se green
Onset potential (V) vs RHE	1.47	1.58
Overpotential @ 10 mA cm ⁻² (mV)	310	350
TOF (s ⁻¹) @ 0.39 V	0.0174	0.0164
Mass activity (A g ⁻¹) @ 0.39 V	62.4	37.2
Tafel slope (mV dec ⁻¹)	82	107
ECSA (cm ⁻²)	289	139
RF	1023	492

The steady-state performance and long-term durability were tested by chronopotentiometry for the most active Cr-Se complex OER electrocatalyst. The multistep chronoamperometry stability test for Cr-Se red cluster at different current densities between 5 mA cm⁻² and 30 mA cm⁻² showed no obvious degradation in potential

under the tested current density (Figure 5c), suggesting that the Cr-Se red cluster is highly stable under a wide range of current densities, exhibiting robustness toward longevity in OER. Furthermore, chronoamperometry sustained at 20 mA cm^{-2} current density for a 24 h period and shows no significant change in the activity as shown in Figure 5d. This confirms that the Cr-Se red cluster material is highly active towards OER as well as durable over a long activity period under an alkaline medium. In the Cr-Se red catalyst, a decrease in the Cr-CO (847 cm^{-1}) peak signal and an increase in the Cr-OH (850 cm^{-1}) peak signal was observed, and a formation of a shoulder at $\sim 900 \text{ cm}^{-1}$ corresponding to O-Cr-O after chronoamperometry (Figure 6).

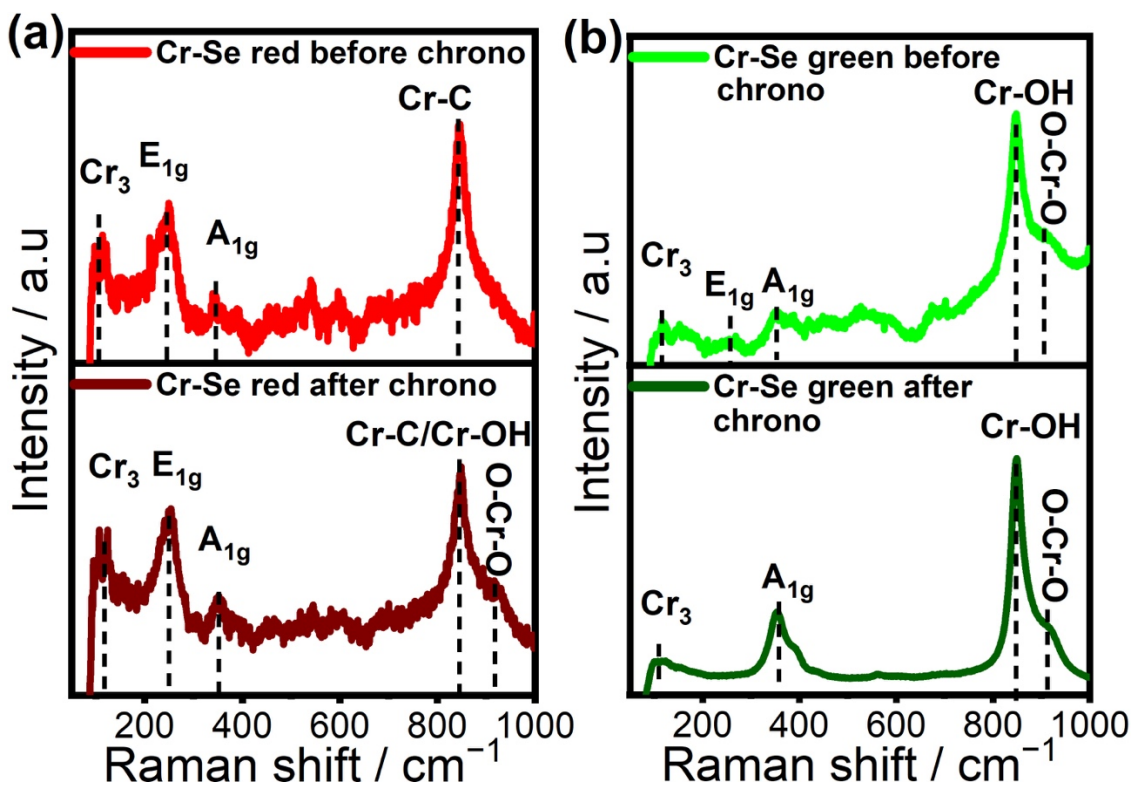


Figure 6. Raman spectra of Cr-Se and Cr-Se clusters, excited with 632.8 nm HeNe laser radiation. (a) Cr-Se red complex before and after chronoamperometry study; (b) Cr-Se green complex before and after chronoamperometry study.

This could be from the adsorption of the OH ion on the surface of the catalyst. The Cr-Se green after chronoamperometry shows a more pronounced A_{1g} (378 cm^{-1}) due to the formation of surface chromium-hydroxide linkage, Cr-OH peak signal (850 cm^{-1}), illustrating more OH adsorption on the catalytic site [39–47]. However, the catalyst characterization after chronoamperometry shows minimal surface oxidation as demonstrated by the XPS in Figures S4 and S5, further corroborating the stability of these complexes while catalytic sites underwent local activation through intermediate adsorption. Moreover, no significant surface-leaching structural changes were observed after the stability study.

4. CONCLUSIONS

In essence, we have successfully demonstrated the use of selenium-capped trichromium carbonyl $[\text{Se}_2\text{Cr}_3(\text{CO})_{10}](\text{Et}_4\text{N})_2$ cluster for the first time as an efficient, high performance, and stable electrocatalyst for OER. This Cr-Se red cluster consists of a catalytically active Se-Cr-Se coordinated sphere which shows high intrinsic catalytic activity supported by its low overpotential and Tafel slope of 310 mV at 10 mA cm^{-2} and 82 mV dec^{-1} , respectively, as well as high TOF (0.0174 s^{-1}) and mass activity (62.4 Ag^{-1}). It also showed excellent stability over 24 h in alkaline (1 M KOH) electrolytes. This indicates the promising potential of high-valence metal complexes and by extension their bulk solids with similar structural composition as highly active electrocatalysts in OER. The covalency of the multiple Cr–Se bonds in the cluster as well as the enhanced conductivity of Cr–Cr bonds are associated with the observed high catalytic efficiency. We

believe that the presence of Cr in two different oxidation states, not only increases electroactive sites but further enhances the electronic transition. This facilitates the intermediate hydroxide adsorption on the Cr atoms, thus improving the electrocatalytic activity. These current findings provide a new avenue to explore the electrocatalytic applications of clustered high-valence metal complexes, as there is no systematic study reported for these cluster types in OER and other electrochemical energy conversions.

SUPPLEMENTARY INFORMATION

The thermogravimetric analysis (TGA) of the Cr-Se red and Cr-Se green clusters describes the stepwise decomposition of each sample (Figure S1). The TGA of Cr-Se red in argon showed a gradual decrease in weight in three steps; at the first step between 0°C and 180 °C, 13.3 % weight loss was observed, due to the loss of lattice water.[16] The second weight loss from 180–240 °C corresponds to 38.7 % (calcd. 30.5%) which can be attributed to the decomposition of tetraethyl amine.[45] Finally, in the range of 240–900 °C a weight loss of 21.52% (calcd. 22.9%) is attributable to the loss of seven coordinated CO molecules. Similarly, Cr-Se green showed three weight loss steps; where 10.7 % weight loss was observed between 0°C and 180 °C at the first step, confined to loss of lattice water. A to 34.4 % (calcd. 30.5%) weight loss from 180–240 °C corresponds to the decomposition of tetraethyl amine. And a weight loss of 16.0% (calcd. 16.7%) in the range of 240–600 °C, attributed to the loss of seven coordinated water molecules. The percentage weight loss in the complexes agrees with the calculated values.

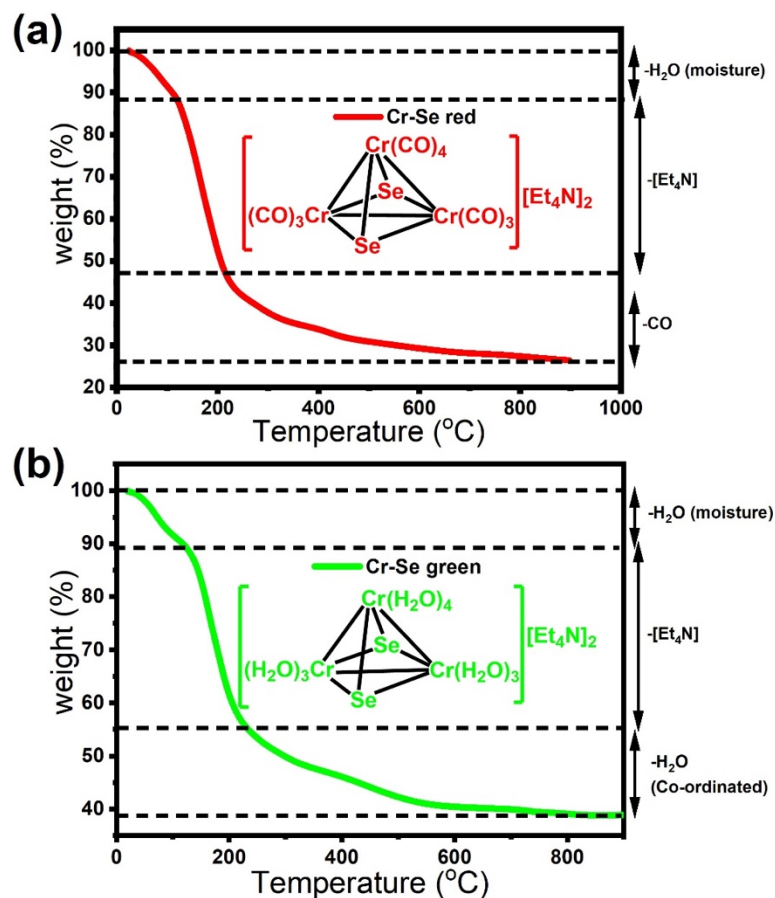


Figure S1. The thermogravimetric (TGA) analysis of (a) Cr-Se red; (b) Cr-Se green.

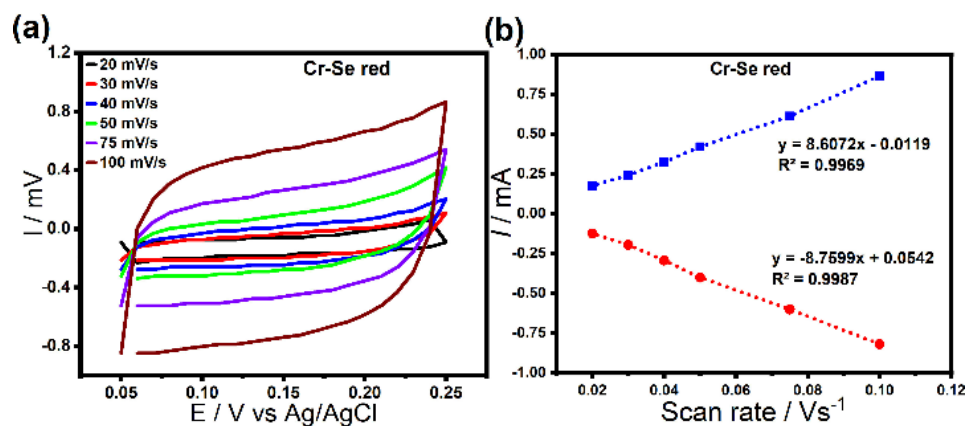


Figure S2. Cr-Se red catalyst (a) Cyclic voltammograms measured at different scan rates; (b) The plots of anodic and cathodic currents measured as a function of scan rate.

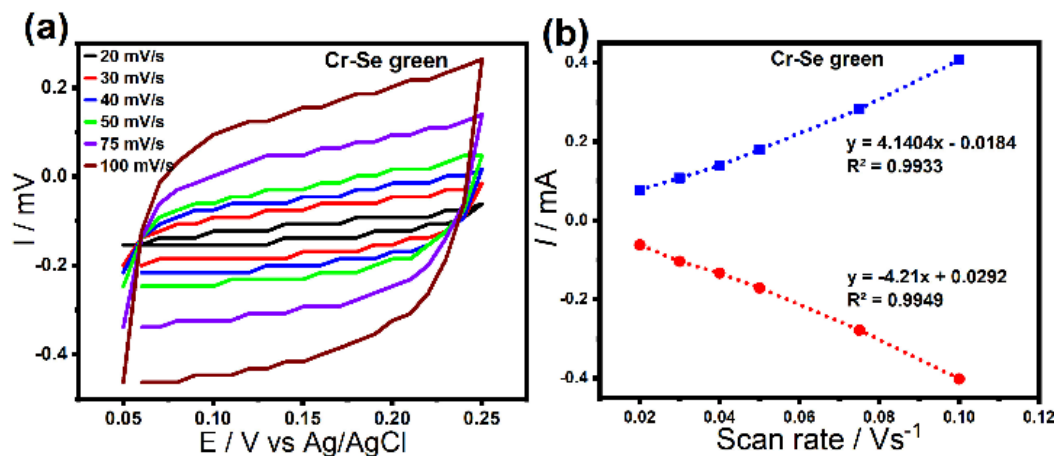


Figure S3. Cr-Se green catalyst (a) Cyclic voltammograms measured at different scan rates; (b) The plots of anodic and cathodic currents measured as a function of scan rate.

Table S1. Parameters of equivalent circuit obtained from fitting of EIS experimental data.

Parameters	Cr-Se red	Cr-Se green
R1 / ohm	1.38	2.0
R2 / ohm	10.10	12.02
R3 / ohm	19.84	16.65
C1 / F	2.24 x10 ⁻²	3.9 x10 ⁻³
W / s ^(1/2) /ohm	6.61 x 10 ⁻²	2.36 x 10 ⁻²

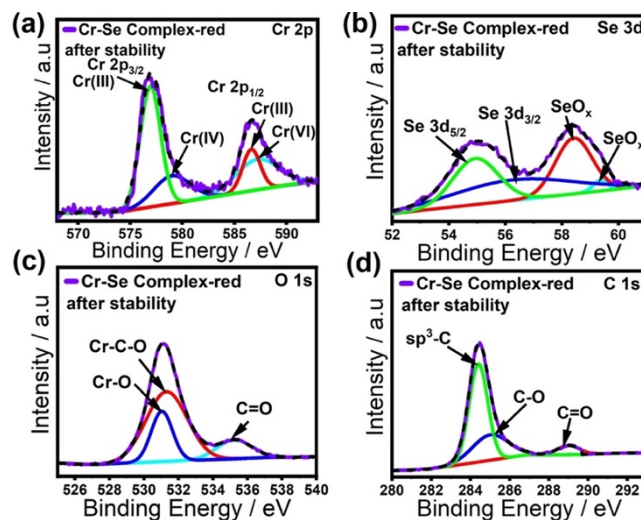


Figure S4. The high-resolution XPS spectra of the Cr-Se red complex after stability showing (a) Cr 2p peak; (b) Se 3d peak; (c) surface O 1s peak; (d) C 1s peak.

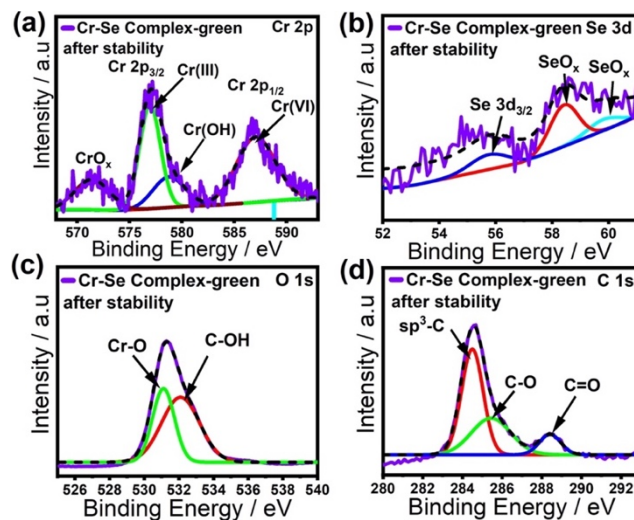


Figure S5. The high-resolution XPS spectra of the Cr-Se green complex after stability showing (a) Cr 2p peak; (b) Se 3d peak; (c) surface O 1s peak; (d) C 1s peak.

Table S2. Comparison of the OER performances in an alkaline electrolyte (overpotential at 10 mA cm⁻² current density, and Tafel slope) of recently published chromium-based catalysts with our work.

Catalysts	Electrolyte	Overpotential (η @ 10 mA.cm ⁻²)	Tafel slope (mV dec ⁻¹)	Substrate	References
*CoCr ₂ O ₄	1.0 M NaOH	400 mV	87 mV dec ⁻¹	Glassy carbon	[25]
*CoFeCr	1.0 M KOH	330 mV	61 mV dec ⁻¹	Ni foam	[46]
*NiCrFeO ₄	1.0 M KOH	298 mV	44.47mV dec ⁻¹	PAN	[47]
*Cr ₂ S ₃	1.0 M KOH	230 mV	162 mV dec ⁻¹	Carbon Fibre	[48]
#Cr(salen)Cl	3.0 M NaOH	426 mV	-	Glassy carbon	[49]
# ^S Cr(H-byp)(bis-bpymd)	OH	390 mV	-	-	[50]
# ^S Cr(tpy)(py)(isoquin)	OH	380 mV	-	-	[51]
# ^S Cr(DPA)(2,2'-bpymd)	OH	320 mV	-	-	[51]

Table S2. Comparison of the OER performances in an alkaline electrolyte (overpotential at 10 mA cm⁻² current density, and Tafel slope) of recently published chromium-based catalysts with our work (cont.).

* γ -CrOOH	1.0 KOH	334 mV	41.4 mV dec ⁻¹	NF	[51]
*CrON	1.0 KOH	409 mV	157 mV dec ⁻¹	Carbon paper	[52]
Cr-Se red	1.0 M KOH	310.0 mV	82 mV dec ⁻¹	Carbon paper	This work
Cr-Se green	1.0 M KOH	350.0 mV	107 mV dec ⁻¹	Carbon paper	This work

* Bulk solid samples

Complexes

\$ Computational study.

REFERENCES

1. Khatun, S.; Roy, P. Cobalt Chromium Vanadium Layered Triple Hydroxides as an Efficient Oxygen Electrocatalyst for Alkaline Seawater Splitting. *Chem. Commun.* **2022**, 58, 1104–1107. <https://doi.org/10.1039/d1cc05745f>.
2. Roy, S.B.; Akbar, K.; Jeon, J.H.; Jerng, S.K.; Truong, L.; Kim, K.; Yi, Y.; Chun, S.H. Iridium on Vertical Graphene as an All-Round Catalyst for Robust Water Splitting Reactions. *J. Mater. Chem. A Mater.* **2019**, 7, 20590–20596. <https://doi.org/10.1039/c9ta07388d>.
3. Lee, Y.; Suntivich, J.; May, K.J.; Perry, E.E.; Shao-Horn, Y. Synthesis and Activities of Rutile IrO₂ and RuO₂ Nanoparticles for Oxygen Evolution in Acid and Alkaline Solutions. *J. Phys. Chem. Lett.* **2012**, 3, 399–404. <https://doi.org/10.1021/jz2016507>.
4. Antolini, E. Iridium as Catalyst and Cocatalyst for Oxygen Evolution/Reduction in Acidic Polymer Electrolyte Membrane Electrolyzers and Fuel Cells. *ACS Catal.* **2014**, 4, 1426–1440. <https://doi.org/10.1021/cs4011875>.

5. Hong, W.T.; Risch, M.; Stoerzinger, K.A.; Grimaud, A.; Suntivich, J.; Shao-Horn, Y. Toward the Rational Design of Non-Precious Transition Metal Oxides for Oxygen Electrocatalysis. *Energy Environ. Sci.* **2015**, *8*, 1404–1427. <https://doi.org/10.1039/c4ee03869j>.
6. Masud, J.; Ioannou, P.C.; Levesanos, N.; Kyritsis, P.; Nath, M. A Molecular Ni-Complex Containing Tetrahedral Nickel Selenide Core as Highly Efficient Electrocatalyst for Water Oxidation. *ChemSusChem* **2016**, *9*, 3128–3132. <https://doi.org/10.1002/cssc.201601054>.
7. Abdullahi, I.M.; Masud, J.; Ioannou Polydoros-Chrisovalantis; Ferentinos, E.; Kyritsis, P.; Nath, M. A Molecular Tetrahedral Cobalt–Seleno-Based Complex as an Efficient Electrocatalyst for Water Splitting. *Molecules* **2021**, *26*, 945. <https://doi.org/10.3390/molecules>.
8. Geer, A.M.; Musgrave, C.; Webber, C.; Nielsen, R.J.; McKeown, B.A.; Liu, C.; Schleker, P.P.M.; Jakes, P.; Jia, X.; Dickie, D.A.; et al. Electrocatalytic Water Oxidation by a Trinuclear Copper(II) Complex. *ACS Catal.* **2021**, *11*, 7223–7240. <https://doi.org/10.1021/acscatal.1c01395>.
9. Najafpour, M.M.; Allakhverdiev, S.I. Manganese Compounds as Water Oxidizing Catalysts for Hydrogen Production via Water Splitting: From Manganese Complexes to Nano-Sized Manganese Oxides. *Int. J. Hydrog. Energy* **2012**, *37*, 8753–8764. <https://doi.org/10.1016/j.ijhydene.2012.02.075>.
10. Schmid, G. *Clusters and Colloids. From Theory to Applications*; VCH Verlagsgesellschaft Weinheim, 1994; ISBN 0195069005.
11. Darensbourg, D.J.; Zalewski, D.J.; Sanchez, K.M.; Delord, T. Cluster Synthesis via Aggregation: Synthesis and Solution and Solid-State Characterization of Sulfur-Capped Group 6 Metal Carbonyl Clusters. *Inorg. Chem.* **1988**, *27*, 821–829. <https://doi.org/10.1021/ic00278a016>.
12. Hoefler, M.; Tebbe, K.-F.; Veit, H.; Weiler, N.E. Synthesis and Structure of [PPN]₂[M₂-CO)₃(CO)₉Cr₃(M₄-S)Cr(CO)₅]: A Chromium Cluster. *J. Am. Chem. Soc.* **1983**, *3*, 6338–6339.
13. Hessen, B.; Siegrist, T.; Palstra, T.; Tanzler, S.M.; Steigerwald, M.L. Cr₆Te₈(PEt₃)₆ and a Molecule-Based Synthesis of Cr₃Te₄. *Inorg. Chem.* **1993**, *32*, 5165.
14. Tsuge, K.; Imoto, H.; Saito, T. Syntheses, Structures, and Molecular-Orbital Calculations of Chromium Chevrel-Type Cluster Complexes [Cr₆E₈(PR₃)₆] (E=S, PR₃=PEt₃, PMe₃; E=Se, PR₃=PEt₃, PMe₃, PMe₂Ph). *Bull Chem. Soc. Jpn* **1996**, *69*, 627–636.

15. Wang, W.; Wang, X.; Zhang, Z.; Yuan, N.; Wang, X. The Long-Sought Seventeen-Electron Radical [(C₆Me₆)Cr(CO)₃]⁺: Isolation, Crystal Structure and Substitution Reaction. *Chem. Commun.* **2015**, *51*, 8410–8413. <https://doi.org/10.1039/c5cc01941a>.
16. Bügel, P.; Krummenacher, I.; Weigend, F.; Eichhöfer, A. Experimental and Theoretical Evidence for Low-Lying Excited States in [Cr₆E₈(PEt₃)₆] (E = S, Se, Te) Cluster Molecules. *Dalton Trans.* **2022**, *51*, 14568–14580. <https://doi.org/10.1039/d2dt01690g>.
17. Darensbourg, D.J.; Zalewski, D.J. Synthesis and Characterization of Sulfur-Capped Trinuclear Group 6B Metal Clusters. *Organometallics* **1984**, *3*, 1598–1600.
18. Hsu, M.H.; Miu, C.Y.; Lin, Y.C.; Shieh, M. Selenium-Capped Trimolybdenum and Tungsten Carbonyl Clusters [Se₂M₃(CO)₁₀]₂⁻ (M = Mo, W). *J. Organomet Chem.* **2006**, *691*, 966–974. <https://doi.org/10.1016/j.jorganchem.2005.10.039>.
19. Shieh, M.; Ho, L.F.; Jang, L.F.; Ueng, C.H.; Peng, S.M.; Liu, Y.H. First Selenium-Capped Carbonyltrichromium Complex [Se₂Cr₃(CO)₁₀]₂⁻: A Novel Cr₃ Ring Cluster. *Chem. Commun.* **2001**, *3*, 1014–1015. <https://doi.org/10.1039/b101283p>.
20. Shieh, M.; Lin, C.N.; Miu, C.Y.; Hsu, M.H.; Pan, Y.W.; Ho, L.F. Chromium-Manganese Selenide Carbonyl Complexes: Paramagnetic Clusters and Relevance to C = O Activation of Acetone. *Inorg. Chem.* **2010**, *49*, 8056–8066. <https://doi.org/10.1021/ic101118y>.
21. Shieh, M.; Chung, R.L.; Yu, C.H.; Hsu, M.H.; Ho, C.H.; Peng, S.M.; Liu, Y.H. The Unusual Paramagnetic Mixed-Metal Carbonyl Chalcogenide Clusters: [E₂Cr₂Fe(CO)₁₀]₂⁻ (E = Te, Se). *Inorg. Chem.* **2003**, *42*, 5477–5479. <https://doi.org/10.1021/ic034081m>.
22. Yeh, H.H.; Hsu, M.C.; Li, Y.H.; Hsu, Y.N.; Shr, F.Y.; Shieh, M. Ternary Antimony–Chalcogen Iron Carbonyl Complexes and Their Derivatives: Syntheses, Structures, Reactivities, and Low-Energy-Gap Characteristics. *J. Organomet Chem.* **2021**, *937*, 121717. <https://doi.org/10.1016/j.jorganchem.2021.121717>.
23. Jin, D.; Kang, J.; Prabhakaran, S.; Lee, Y.; Kim, M.H.; Kim, D.H.; Lee, C. Chromium-Rich Cr_xIr_{1-x}O₂ Wire-in-Tube Alloys for Boosted Water Oxidation with Long Standing Electrocatalytic Activity. *J. Mater. Chem. A Mater.* **2022**, *10*, 13803–13813. <https://doi.org/10.1039/d2ta02984g>.
24. Kong, S.; Lu, M.; Yan, S.; Zou, Z. High-Valence Chromium Accelerated Interface Electron Transfer for Water Oxidation. *Dalton Trans.* **2022**, *51*, 16890–16897. <https://doi.org/10.1039/d2dt02908a>.

25. Lin, C.C.; McCrory, C.C.L. Effect of Chromium Doping on Electrochemical Water Oxidation Activity by Co₃-xCr_xO₄ Spinel Catalysts. *ACS Catal* **2017**, *7*, 443–451. <https://doi.org/10.1021/acscatal.6b02170>.
26. Du, X.; Su, H.; Zhang, X. Cr Doped-Co₉S₈ Nanoarrays as High-Efficiency Electrocatalysts for Water Splitting. *J. Alloy. Compd* **2020**, *824*, 153965. <https://doi.org/10.1016/j.jallcom.2020.153965>.
27. Moltved, K.A.; Kepp, K.P. The Chemical Bond between Transition Metals and Oxygen: Electronegativity, d-Orbital Effects, and Oxophilicity as Descriptors of Metal-Oxygen Interactions. *J. Phys. Chem. C* **2019**, *123*, 18432–18444. <https://doi.org/10.1021/acs.jpcc.9b04317>.
28. Shufler, L.; Sternberg, H.W.; Friedel, R.A. Infrared Spectrum and Structure of Chromium Hexacarbonyl, Cr(CO)₆. *J. Am. Chem. Soc.* **1956**, *78*, 2687–2688.
29. Thalassinos, G.; Stacey, A.; Dontschuk, N.; Murdoch, B.J.; Mayes, E.; Girard, H.A.; Abdullahi, I.M.; Thomsen, L.; Tadich, A.; Arnault, J.-C.; et al. Fluorescence and Physico-Chemical Properties of Hydrogenated Detonation Nanodiamonds. *C J. Carbon Res.* **2020**, *6*, 7. <https://doi.org/10.3390/c6010007>.
30. He, T.; Zhou, T.; Wan, Y.; Tan, T. A Simple Strategy Based on Deep Eutectic Solvent for Determination of Aflatoxins in Rice Samples. *Food Anal Methods* **2020**, *13*, 542–550. <https://doi.org/10.1007/s12161-019-01665-7>.
31. Amirthaganesan, G.; Kandhaswamy, M.A.; Srinivasan, V. Thermal, Phase Transition and FTIR Spectroscopic Studies in Tetraethylammonium Trichlorocadmiate Crystals. *Cryst. Res. Technol.* **2005**, *40*, 680–683. <https://doi.org/10.1002/crat.200410407>.
32. Swesi, A.T.; Masud, J.; Nath, M. Nickel Selenide as a High-Efficiency Catalyst for Oxygen Evolution Reaction. *Energy Environ. Sci.* **2016**, *9*, 1771–1782. <https://doi.org/10.1039/c5ee02463c>.
33. Liu, B.; Han, W.; Li, X.; Li, L.; Tang, H.; Lu, C.; Li, Y.; Li, X. Quasi Metal Organic Framework with Highly Concentrated Cr₂O₃ Molecular Clusters as the Efficient Catalyst for Dehydrofluorination of 1,1,1,3,3-Pentafluoropropane. *Appl. Catal. B* **2019**, *257*, 117939. <https://doi.org/10.1016/j.apcatb.2019.117939>.
34. Ghosh, T.; Maayan, G. Efficient Homogeneous Electrocatalytic Water Oxidation by a Manganese Cluster with an Overpotential of Only 74 MV. *Angew. Chem. Int. Ed.* **2019**, *58*, 2785–2790. <https://doi.org/10.1002/anie.201813895>.

35. Stern, C.M.; Jegede, T.O.; Hulse, V.A.; Elgrishi, N. Electrochemical Reduction of Cr(vi) in Water: Lessons Learned from Fundamental Studies and Applications. *Chem. Soc. Rev.* **2021**, *50*, 1642–1667. <https://doi.org/10.1039/d0cs01165g>.
36. Bose, R.N.; Fonkeng, B.; Barr-David, G.; Farrell, R.P.; Judd, R.J.; Lay, P.A.; Sangster, D.F. Redox Potentials of Chromium(V)/(IV),-(V)/(III), and -(IV)/(III) Complexes with 2-Ethyl-2-Hydroxybutanoato(2-/1-) Ligands. *J. Am. Chem. Soc.* **1996**, *118*, 7139–7144.
37. Guziejewski, D.; Stojanov, L.; Gulaboski, R.; Mirceski, V. Reversible and Quasireversible Electron Transfer under Conditions of Differential Square-Wave Voltammetry. *J. Phys. Chem. C* **2022**, *126*, 5584–5591. <https://doi.org/10.1021/acs.jpcc.2c01188>.
38. Bo, X.; Li, Y.; Chen, X.; Zhao, C. High Valence Chromium Regulated Cobalt-Iron-Hydroxide for Enhanced Water Oxidation. *J. Power Sources* **2018**, *402*, 381–387. <https://doi.org/10.1016/j.jpowsour.2018.09.063>.
39. Zhang, B.; Zhang, B.; Zhao, G.; Wang, J.; Liu, D.; Chen, Y.; Xia, L.; Gao, M.; Liu, Y.; Sun, W.; et al. Atomically Dispersed Chromium Coordinated with Hydroxyl Clusters Enabling Efficient Hydrogen Oxidation on Ruthenium. *Nat. Commun.* **2022**, *13*, 5894. <https://doi.org/10.1038/s41467-022-33625-x>.
40. Gomes, A.S.O.; Yaghini, N.; Martinelli, A.; Ahlberg, E. A Micro-Raman Spectroscopic Study of Cr(OH)₃ and Cr₂O₃ Nanoparticles Obtained by the Hydrothermal Method. *J. Raman Spectrosc.* **2017**, *48*, 1256–1263. <https://doi.org/10.1002/jrs.5198>.
41. Huang, Y.M.; Tsai, H.R.; Lai, S.H.; Lee, S.J.; Chen, I.C.; Huang, C.L.; Peng, S.M.; Wang, W.Z. Bonding between Chromium Atoms in Metal-String Complexes from Raman Spectra and Surface-Enhanced Raman Scattering: Vibrational Frequency of the Chromium Quadruple Bond. *J. Phys. Chem. C* **2011**, *115*, 13919–13926. <https://doi.org/10.1021/jp203065v>.
42. Abdullahi, I.M.; Langenderfer, M.; Shenderova, O.; Nunn, N.; Torelli, M.D.; Johnson, C.E.; Mochalin, V.N. Explosive Fragmentation of Luminescent Diamond Particles. *Carbon N Y* **2020**, *164*, 442–450. <https://doi.org/10.1016/j.carbon.2020.03.057>.
43. Saleh, T.A.; Al-Hammadi, S.A.; Abdullahi, I.M.; Mustaqeem, M. Synthesis of Molybdenum Cobalt Nanocatalysts Supported on Carbon for Hydrodesulfurization of Liquid Fuels. *J. Mol. Liq.* **2018**, *272*, 715–721. <https://doi.org/10.1016/j.molliq.2018.09.118>.

44. Beltz, J.; Pfaff, A.; Abdullahi, I.M.; Cristea, A.; Mochalin, V.N.; Ercal, N. Effect of Nanodiamond Surface Chemistry on Adsorption and Release of Tiopronin. *Diam. Relat. Mater.* **2019**, *100*, 107590. <https://doi.org/10.1016/j.diamond.2019.107590>.
45. Gao, H.; Li, J.; Lian, K. Alkaline Quaternary Ammonium Hydroxides and Their Polymer Electrolytes for Electrochemical Capacitors. *RSC Adv* 2014, *4*, 21332–21339, doi:10.1039/c4ra01014k.
46. Bo, X.; Li, Y.; Chen, X.; Zhao, C. Operando Raman Spectroscopy Reveals Cr-Induced-Phase Reconstruction of NiFe and CoFe Oxyhydroxides for Enhanced Electrocatalytic Water Oxidation. *Chem. Mater.* **2020**, *32*, 4303–4311, doi:10.1021/acs.chemmater.0c01067.
47. Ramakrishnan, P.; Beom Lee, K.; Choi, G.J.; Park, I.K.; Inn Sohn, J. Porous Hollow Nanorod Structured Chromium-Substituted Inverse Spinel Compound: An Efficient Oxygen Evolution Reaction Catalyst. *J. Ind. Eng. Chem.* **2021**, *101*, 178–185, doi:10.1016/j.jiec.2021.06.015.
48. Shifa, T.A.; Mazzaro, R.; Morandi, V.; Vomiero, A. Controllable Synthesis of 2D Nonlayered Cr₂S₃ Nanosheets and Their Electrocatalytic Activity Toward Oxygen Evolution Reaction. *Front. Chem. Eng.* **2021**, *3*, 1–7, doi:10.3389/fceng.2021.703812
49. Shamsipur, M.; Taherpour, A. (Arman); Sharghi, H.; Lippolis, V.; Pashabadi, A. A Low-Overpotential Nature-Inspired Molecular Chromium Water Oxidation Catalyst. *Electrochim. Acta* **2018**, *265*, 316–325, doi:10.1016/j.electacta.2018.01.202.
50. Craig, M.J.; García-Melchor, M. High-Throughput Screening and Rational Design to Drive Discovery in Molecular Water Oxidation Catalysis. *Cell Rep Phys Sci* **2021**, *2*, doi:10.1016/j.xcrp.2021.100492.
51. Sun, Z.; Yuan, M.; Yang, H.; Lin, L.; Jiang, H.; Ge, S.; Li, H.; Sun, G.; Ma, S.; Yang, X. 3D Porous Amorphous γ -CrOOH on Ni Foam as Bifunctional Electrocatalyst for Overall Water Splitting. *Inorg Chem* **2019**, *58*, 4014–4018 doi:10.1021/acs.inorgchem.9b00112.
52. Kumar, U.N.; Malek, A.; Rao, G.R.; Thomas, T. Chromium Oxynitride (CrON) Nanoparticles: An Unexplored Electrocatalyst for Oxygen Evolution Reaction. *Electrocatal.* **2022**, *13*, 62–71, doi:10.1007/s12678-021-00693-4.

III. NANOSTRUCTURED TERNARY NICKEL-BASED MIXED ANIONIC (TELLURO) SELENIDE AS A SUPERIOR CATALYST FOR OXYGEN EVOLUTION REACTION

Ibrahim Munkaila Abdullahi¹, Siby Thomas², Alessio Gagliardi², Mohsen Asle Zaeem³, and Manashi Nath¹

¹Department of Chemistry, Missouri University of Science and Technology, Rolla, MO 65409

²School of Computation, Information, and Technology, Technical University of Munich (TUM) Hans-Piloty-Strasse 1, 85748 Garching, Munich, Germany

³Department of Mechanical Engineering, Colorado School of Mines, Golden, CO 80401

ABSTRACT

Developing protocols for designing high-efficiency, durable, cost-effective electrocatalysts for oxygen evolution reaction (OER) necessitates a proper understanding of the structure-property correlation as a function of composition. In this article, it has been demonstrated that the incorporation tellurium atom into binary nickel chalcogenide (NiSe) and creating a mixed anionic phase perturbs its electronic structure and significantly enhances the OER activity. A series of nanostructured nickel chalcogenides comprising a layer-by-layer morphology along with mixed anionic ternary phase were grown *in-situ* on nickel foam with varying morphological textures using a simple hydrothermal synthesis route. Comprehensive X-ray diffraction, X-ray photoelectron spectroscopy, and *in-situ* Raman spectroscopy analysis confirmed the formation of a trigonal single-phase nanocrystalline nickel (telluro)-selenide (NiSeTe) as a truly mixed anionic composition. The NiSeTe electrocatalyst exhibits excellent OER performance, with a low overpotential

of 300 mV at 50 mAcm⁻², and a small Tafel slope of 98 mV dec⁻¹ in 1 M KOH electrolyte. Its turnover frequency and mass activity were 0.047 s⁻¹ and 90.3 Ag⁻¹, respectively. Detailed electrochemical measurements also revealed enhanced charge transfer properties of the NiSeTe phase compared to the mixture of binaries. Density functional theory calculations revealed favorable OH-adsorption energy in the mixed anionic phase compared to the binary chalcogenides confirming the superior electrocatalytic property.

Keywords: NiSeTe, Oxygen evolution reaction, OH-adsorption, Density functional theory calculations, Water oxidation.

1. INTRODUCTION

Electrochemical water splitting is among the most significant and attractive clean hydrogen generation technology. Hydrogen is considered to be an ideal renewable energy source to substitute conventional fossil fuels owing to its zero-carbon emission, intense energy density, and the ability to utilize periodic renewable energy such as wind and solar energy.^[1] However, due to the high energy requirement for water oxidation reaction, practical water electrolyzers operate at a much higher voltage (1.8-2.0 V) relative to the theoretical water splitting voltage of 1.23 V, leading to a large overpotential.^[2] The use of efficient electrocatalysts in anodic oxygen evolution reaction (OER) and cathodic hydrogen evolution reaction (HER) can effectively decrease the overpotential and improve the sluggish kinetics of HER/OER and therefore enhance the energy efficiency of the process.^[3]

To date, the state-of-the-art electrocatalysts for HER are mostly Pt-based materials,^[4,5] whereas the oxides of precious metals such as Ru or Ir are used as electrocatalysts for OER.^[6] These precious metals, however, are scarce and expensive, limiting their widespread usage. Over the last several decades, it has become apparent that implementing large-scale water electrolysis will require the development of high-efficiency electrocatalysts, preferably composed of earth-abundant non-precious elements. Extensive research into designing such new electrocatalysts from earth-abundant elements has led to a class of catalyst compositions that exceed the present capabilities. Apart from enhanced performance, these novel compositions also broaden the knowledge and understanding of the factors that determine catalytic activity in order to customize catalyst surfaces atom by atom.^[7]

The electrocatalytic properties of any material are primarily influenced by its electronic structure, which depends on the central metal atom as well as the coordinating ligands. Hence, the main goal is to design catalysts through a proper understanding of structure-property correlation by varying the composition and physical structure of materials and understanding its effect on catalytic efficiency. Considerable attempts have been made to design efficient electrocatalysts for OER and HER comprising earth-abundant elements. Appreciable progress has been made over the past few years in designing highly active OER catalysts based on metal phosphate,^[8-10] oxides,^[11] chalcogenides,^[12-14] hydroxides,^[15] metal complexes.^[16,17] Some of these phosphates, chalcogenides, and some carbides have been used as HER catalysts.^[18-21] Among these transition metal chalcogenides, particularly metal sulfides, selenides, and tellurides, have made a significant impact as electrocatalysts in water oxidation due to their unprecedented

high catalytic activity,^[12,22–24] which is exemplified by their extremely low overpotential and high current density. One of the most commonly used commercial OER/HER electrocatalysts is porous Ni, due to its low cost, high robustness, and moderate catalytic activities. Also, it has been observed that in Ni-based chalcogenides, reducing anion electronegativity from O to Te (electronegativity order: $E = \text{Te} (2.1) < \text{Se} (2.55) < \text{S} (2.58) < \text{O} (3.44)$) lead to significant improvement in the intrinsic catalytic properties.^[12,24,25] This was primarily attributed to increased covalency in the Ni–chalcogen (Ni– E) bond with reduced anion electronegativity down the chalcogens group, i.e., covalency order Ni–O < Ni–S < Ni–Se < Ni–Te. Such an increase in covalency leads to the adjustment of the electronic band structure and better alignment of the valence and conduction band edges with the water oxidation/reduction level. Better band alignment enhances facile charge transfer at the electrolyte–electrocatalyst interface which subsequently minimizes the overpotential for water oxidation/reduction. A critical factor in catalyst design is the ability to understand and predict the catalytic activity through systematic variation of composition. The chalcogenide series presents an ideal opportunity to understand the effect of anion electronegativity and lattice covalency on the electrocatalytic properties through anion substitution. Mixed anionic systems will be especially interesting for understanding the subtle effect of tunable anion electronegativity. One of the probes for understanding the direct effect of anion electronegativity on the catalytic activity is the hydroxyl (-OH) adsorption energy on the catalyst site, which is considered as the primary surface activation step. Hence investigation of the -OH adsorption energy will be a key component for developing effective catalyst design principles. The mixed anionic chalcogenides offer a unique opportunity for investigating the subtle effects of changing electronegativity on the

-OH adsorption energy since these systems offer more systematic control of electronic band structure and electrochemical tunability.^[26,27] To the best of our knowledge, such mixed anionic chalcogenides have not been reported for electrocatalytic water-splitting reactions.

We report herein a novel nanocrystalline nickel (telluro)-selenide NiSeTe materials grown on Ni foam (NF) by one-pot *in-situ* hydrothermally method as an efficient water oxidation catalyst. We also illustrate the effect of adjusting the electronic structure of nickel-selenide (NiSe) by Te incorporation to form the mixed anionic coordination where both Se and Te are coordinated to the same catalytic (Ni) site. NiSeTe catalyst combines the characteristic favorable reaction kinetics and the synergistic effects between NiSe and nickel-telluride (NiTe) catalysts, as well as the stability of the nickel-supported structure. These mixed anionic compositions exhibit a significantly lower OER overpotential of 300 mV at 50 mAcm⁻² and a small Tafel slope (98 mVdec⁻¹). DFT calculations show favorable OH-adsorption energy as well as the charge transfer between the OH⁻ ion and the surface of NiSe, NiTe, and NiSeTe compositions during OER. The enhanced conductivity of NiSeTe can encourage fast electron transfer between the active NiSeTe composition while the nanostructured surface provides abundant surface area and active sites. This NiSeTe electrode based on non-precious Ni metal, exhibits superior catalytic performance and durability towards water oxidation in strongly alkaline media. This study is of a more fundamental nature exploring the effect of mixed anionic coordination on the electrochemical activity and comparing that with the mixture of binary phases. The results reveal that a subtle change in the nearest neighbor coordination to the catalytically active site leads to significant changes in the electrocatalytic activity. These

results unlock exciting new avenues to explore mixed-chalcogenide electrocatalysts for water splitting and to understand structure–property–activity relationships for advanced catalysts with industrial scalability.

2. EXPERIMENTAL PROCEDURE

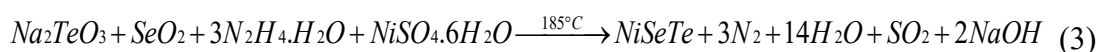
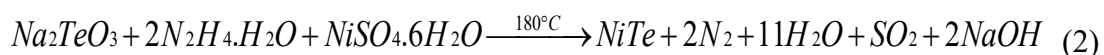
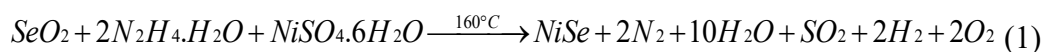
2.1. MATERIALS

NF was purchased from Shenzhen Green and Creative Environmental Science and Technology Co. Ltd., hydrazine hydrate ($\text{N}_2\text{H}_4\cdot\text{H}_2\text{O}$) was bought from (Fisher Scientific, Waltham, Massachusetts, USA), nickel sulfate hexahydrate ($\text{NiSO}_4\cdot 6\text{H}_2\text{O}$), Nafion (5 wt.%), sodium tellurite (Na_2TeO_3), and selenium (IV) oxide (SeO_2) were purchased from (Sigma–Aldrich Chemical Reagent Co., Ltd. St. Louis MO), sodium hydroxide (NaOH), hydrochloric acid (HCl) and isopropyl alcohol (iPrOH) were purchased from (Fisher Scientific Pittsburgh, USA). All the reagents were used as received. The deionized (D.I) water purified through a Millipore system was used in all experiments. NF pre-treatment: A piece of NF ($1 \times 2 \text{ cm}^2$) was washed with HCl, ethanol and D.I water several times to ensure the surface of the NF was well cleaned before use.

2.2. METHODS

The hydrothermal growth of the nickel chalcogenide series was performed at 160–185 °C. It was also observed that nickel telluride growth requires higher temperature for hydrothermal growth (185 °C) compared to the selenide (160 °C) to achieve a comparable catalyst loading. And since a surfactant-free approach is employed in this experiment, to control the size of nuclei, the nickel salt, and the reducing agent; hydrazine employed,

respectively causes nucleation and reduction to occur steadily. The NiSeTe, NiTe and NiSe nanosheets were grown hydrothermally *in-situ* on NF by reacting chalcogen precursors with nickel sulfate. The chalcogen precursors used were SeO₂ and Na₂TeO₃ which are highly reactive Se and Te sources respectively.^[13] NiSO₄.H₂O was dissolved and added as a secondary source of Ni to a sonicated solution of SeO₂ and Na₂TeO₃ in deionized water. Then, quantitative amount of N₂H₄.H₂O, which serves both as reducing agent as well as complexing agent,^[28] was gradually added into the solutions of SeO₂, Na₂TeO₃ and a mixture of SeO₂ and Na₂TeO₃ separately, to form a uniform and black, purple, and dark purple suspension respectively. Lastly, it was heated in the autoclave at 160 °C, 180 °C, 185 °C for 12 h, respectively, where the produced Se and Ni intermediate species from SeO₂, and NiSO₄.H₂O respectively, were reacted to form NiSe as shown in Equation (1). Similarly, Te species from Na₂TeO₃ and Ni species from NiSO₄.H₂O and NF, were reacted to form NiTe as represented in Equation (2), and lastly, Se species from SeO₂ together with Te species from Na₂TeO₃, combined with Ni species from NiSO₄.H₂O and NF, were reacted to form NiSeTe as represented in Equation (3). It is critical to state that in all cases, the NF serves both as a Ni source and a substrate.



2.2.1. Preparation of NiSeTe. In this composition NiSeTe is hydrothermally deposited on NF. NiSO₄.6H₂O (113.42 mg), was added into deionized water (5 mL) and mild stirring for a few minutes until the solution is clear, followed by the addition of SeO₂

(27.74 mg) and then Na_2TeO_3 (55.40 mg) under continuous stirring until the mixture is uniform. After which $\text{N}_2\text{H}_4\cdot\text{H}_2\text{O}$ (2 mL) was added dropwise and further stirred for 30 minutes. The mixture was then poured into 25 mL Teflon-lined stainless-steel autoclave containing a piece of pre-treated NF and heated at $180\text{ }^\circ\text{C}$ for 24 h in an electric oven. The autoclave was cooled naturally to ambient temperature, and the sample was collected and washed with water and isopropyl alcohol many times and then dried at $60\text{ }^\circ\text{C}$ for 8 h.

2.2.2. Preparation of NiTe. In this composition, NiTe is hydrothermally deposited on NF. $\text{NiSO}_4\cdot 6\text{H}_2\text{O}$ (56.71 mg), was added into deionized water (5 mL) and mild stirring for a few minutes until the solution is clear, followed by the addition of Na_2TeO_3 (55.40 mg), under continuous stirring until the mixture is uniform. After which $\text{N}_2\text{H}_4\cdot\text{H}_2\text{O}$ (1 mL) was added dropwise and further stirred for 30 minutes. The mixture was then poured into 25 mL Teflon-lined stainless-steel autoclave containing a piece of pre-treated NF and heated at $185\text{ }^\circ\text{C}$ for 12 h in an electric oven. The autoclave was cooled naturally to ambient temperature, and the sample was collected and washed with water and isopropyl alcohol many times and then dried at $60\text{ }^\circ\text{C}$ for 8 h.

2.2.3. Preparation of NiSe. In this composition, NiSe is hydrothermally deposited on NF. $\text{NiSO}_4\cdot 6\text{H}_2\text{O}$ (56.71 mg), was added into deionized water (5 mL) and mild stirring for a few minutes until the solution is clear, followed by the addition of SeO_2 (27.74 mg), under continuous stirring until the solution is clear. After which, $\text{N}_2\text{H}_4\cdot\text{H}_2\text{O}$ (1 mL) was added dropwise and further stirred for 30 minutes. The mixture was then poured into a 25 mL Teflon-lined stainless-steel autoclave containing a piece of pre-treated NF and heated at $160\text{ }^\circ\text{C}$ for 12 h in an electric oven. The autoclave was cooled naturally to ambient

temperature, and the sample was collected and washed with water and isopropyl alcohol many times and then dried at 60 °C for 8 h.

2.2.4. Preparation of NiSe@NiTe. In this composition, NiTe is hydrothermally deposited on NF, then followed by the hydrothermal deposition of NiSe on the top. Step 1: NiSO₄·6H₂O (56.71 mg), was added into deionized water (5 mL) and mild stirring for a few minutes until the solution is clear, followed by the addition of Na₂TeO₃ (55.40 mg), under continuous stirring until the mixture is uniform. After which, N₂H₄·H₂O (1 mL) was added dropwise and further stirred for 30 minutes. The mixture was then poured into a 25 mL Teflon-lined stainless-steel autoclave containing a piece of pre-treated NF and heated at 185 °C for 12 h in an electric oven. The autoclave was cooled naturally to ambient temperature, and the sample was collected and washed with water and isopropyl alcohol many times and then dried at 60 °C for 8 h. Step 2: NiSO₄·6H₂O (56.71 mg), was added into deionized water (5 mL) and gentle stirring for several minutes until the solution is clear, followed by the addition of SeO₂ (27.74 mg), under continuous stirring until the solution is clear. After which, N₂H₄·H₂O (1 mL) was added dropwise and further stirred for 30 minutes. The mixture was then poured into a 25 mL Teflon-lined stainless-steel autoclave containing NF/NiTe from step 1 and heated at 160 °C for 12 h in an electric oven. The autoclave was cooled naturally to ambient temperature, and the sample was collected and washed with water and isopropyl alcohol many times and then dried at 60 °C for 8 h.

2.2.5. Preparation of NiTe@NiSe. In this composition, NiSe is hydrothermally deposited on NF, then followed by the hydrothermal deposition of NiTe on the top Step 1: NiSO₄·6H₂O (56.71 mg), which was added into deionized water (5 mL) and mild stirring for a few minutes until the solution is clear, followed by the addition of SeO₂ (27.74 mg),

under continuous stirring until the solution is clear. After which, $\text{N}_2\text{H}_4\cdot\text{H}_2\text{O}$ (1 mL) was added dropwise and further stirred for 30 minutes. The mixture was then poured into a 25 mL Teflon-lined stainless-steel autoclave containing a piece of pre-treated NF and heated at $160\text{ }^\circ\text{C}$ for 12 h in an electric oven. The autoclave was cooled naturally to ambient temperature, and the sample was collected and washed with water and isopropyl alcohol many times and then dried at $60\text{ }^\circ\text{C}$ for 8 h. Step 2: $\text{NiSO}_4\cdot 6\text{H}_2\text{O}$ (56.71 mg), was added into deionized water (5 mL) and mild stirring for a few minutes until the solution is clear, followed by the addition of Na_2TeO_3 (55.40 mg), under continuous stirring until the mixture is uniform. After which, $\text{N}_2\text{H}_4\cdot\text{H}_2\text{O}$ (1 mL) was added dropwise and further stirred for 30 minutes. The mixture was then poured into a 25 mL Teflon-lined stainless-steel autoclave containing NF/NiSe from step 1 and heated at $185\text{ }^\circ\text{C}$ for 12 h in an electric oven. The autoclave was cooled naturally to ambient temperature, and the sample was collected and washed with water and isopropyl alcohol many times and then dried at $60\text{ }^\circ\text{C}$ for 8 h. The average crystallite sizes of NiSeTe phase particles were approximated from the Scherrer equation in Equation (4).

$$D = 0.9\lambda / \beta \cos \theta \quad (4)$$

where D is the average crystallite size, β is the full width at half maximum (FWHM), θ is the Bragg angle of the NiSeTe crystal with a peak at 2θ , and λ is the wavelength of X-rays (Cu $\text{K}\alpha_1$, $\lambda = 0.154056\text{ nm}$). The FWHM, values of the (011), (012), and (110) peaks at 31.50 , 43.41 , and 47.22 ° peaks for NiSeTe were found to be 0.1310 , 0.1319 , and 0.1287 respectively yielding crystallite sizes of 6.7 , 6.7 and 7.9 nm , and the computed average crystallite size was estimated to be 7.1 nm .

2.2.6. Electrode Preparation. The hydrothermally synthesized nickel chalcogenides are grown directly on nickel foam, and so, the resulting electrodes after drying at 60 °C for 8 h, do not need further processing before carrying out electrochemical and electrocatalytic studies, hence, were used as prepared for electrochemical measurements. The catalyst loading on each sample was calculated.

The mass of the pure phase catalyst on NF was calculated using Equation (5) and the mass of the layered phase catalyst on NF was calculated using Equation (6) as follows. The weight increment (x mg) of NF can be directly weighted after the growth of Ni chalcogenide.

$$x(\text{mg}) = (\text{Weight}_{\text{NF}} + \text{Weight}_{\text{catalyst}}) - \text{Weight}_{\text{pretreated NF}} \quad (5)$$

$$\text{NiSe} = 74.0 - 68.9 = 5.1 \text{ mg}$$

$$\text{NiTe} = 75.9 - 70.8 = 5.3 \text{ mg}$$

$$\text{NiSeTe} = 76.7 - 70.9 = 5.8 \text{ mg}$$

$$x(\text{mg}) = ((\text{Weight}_{\text{NF}} + \text{Weight}_{\text{1st deposition}}) + \text{Weight}_{\text{2nd deposition}}) - \text{Weight}_{\text{pretreated NF}} \quad (6)$$

$$\text{NiSe@NiTe} = 86.7 - 78.5 = 8.2$$

$$\text{NiTe@NiSe} = 87.1 - 79.4 = 7.7$$

where M is the molecular weight or atomic weight.

- a) NiSeTe electrode, the loading mass of NiSeTe is about 2.90 mgcm⁻².
- b) NiTe electrode, the loading mass of NiTe is about 2.65 mgcm⁻².
- c) NiSe electrode, the loading mass of NiSe is about 2.55 mgcm⁻².
- d) NiSe@NiTe electrode, the loading mass of NiTe is ~ mgcm⁻² and NiSe is ~4.10 mgcm⁻².

- e) NiTe@NiSe electrode, the loading mass of NiSe is $\sim \text{mgcm}^{-2}$ and NiTe is $\sim 3.85 \text{ mgcm}^{-2}$

2.2.7. Characterization Methods. The hydrothermally prepared nickel chalcogenide series directly grown on nickel foam were characterized through powder and thin film X-ray diffraction (XRD) using a Philips X-Pert X-ray diffractometer (PANalytical, Almelo, The Netherlands) with Cu $K\alpha$ (1.5418 Å) radiation. The morphology and chemistry of samples were analyzed with a scanning electron microscope (SEM) using a TESCAN-ASCAT system equipped with Bruker energy dispersive spectroscopy (EDX). For the cross-sectional area analysis, the samples were through their edge mounted in epoxy, and then ground using silicon carbide abrasive papers to 1200 grit and mechanically polished with 0.1 μm diamond under controlled low pressure to minimize the chances of the scale breaking. XPS measurements were performed using a KRATOS AXIS 165 X-ray photoelectron spectrometer (Kratos Analytical Limited, Manchester, United Kingdom) using a monochromatic Al X-ray source. The C 1s signal at 284.5 eV was used as a reference to correct all the XPS binding energies. All XPS spectra were collected from the pristine catalyst surface without sputtering. The Raman spectra of the catalyst were recorded with LabRam ARAMIS (HORIBA Jobin-Yvon Raman spectrometer equipped with a CCD detector) in the Raman shift range between 50 cm^{-1} to 1800 cm^{-1} , 1200 lines mm^{-1} grating, HeNe laser 632.8 nm excitation with a nominal output power of 100mW, 0.95 cm^{-1} /pixel spectral dispersion, 10% of laser power, 10x objective, 0.25 numerical aperture, 100 μm slit, 200 μm hole, 30 seconds exposure time, 10x accumulations for each sample acquisition. Electrochemical measurements were performed using a conventional three-electrode system connected to an IviumStat

potentiostat, with NF/Catalyst as the working electrode, while graphite rod and Ag/AgCl electrode were used as counter electrode and reference electrodes respectively, to measure the electrocatalytic performances. Linear sweep voltammetry (LSV), and cyclic voltammetry (CV) were carried out to study the OER catalytic performance and cycling stability. In addition, the catalyst durability was also examined by conducting a constant potential chronoamperometry test at 50 mAcm^{-2} current density for an extended period in N_2 -saturated 1.0 M KOH at room temperature.

All potentials measured were calibrated to RHE using the following Equation (7):

$$E_{(RHE)} = E_{(Ag / AgCl)} + 0.197 \text{ V} + 0.059 \times \text{pH} \quad (7)$$

All electrolytes were saturated by oxygen (for OER) bubbles before and during the experiments. It should be mentioned here that the KOH electrolyte used in this study was purified to get rid of the trace amount of Fe impurity following reported procedures.^[3] It has been reported previously that these trace Fe impurities in KOH can sometimes affect the observed OER electrocatalytic performance, especially in Ni-based systems.^[29]

IR-correction was done by correcting the Ohmic resistance according to Equation (8)

$$E = E_{(RHE)} - iR \quad (8)$$

Here, E is the iR-corrected potential, while $E_{(RHE)}$ is the measured potential vs RHE, i is the measured current, and R is the uncompensated resistance generated from EIS. The EIS analysis was conducted by collecting the AC impedance spectrum from 100 kHz to 0.1 Hz with a voltage perturbation of 10 mV versus open-circuit potential. The uncompensated resistance is found as the magnitude of the impedance where the phase angle is closest to zero in a Bode plot or equivalently as the real part of the impedance where the imaginary part of the impedance is zero in a Nyquist plot.^[30-32]

2.2.8. Chronoamperometry Stability Study. The steady-state performance and durability of the electrocatalysts in OER for long-term chronoamperometric stability for the nickel series catalysts carried out in the alkaline electrolyte of 1 M KOH solution at constantly applied potentials of 1.51, 1.52, and 1.58 V vs RHE for 12h, to reach a current density of around 50 mAcm⁻².

2.2.9. Tafel Slope. The Tafel slope, an important parameter to explain the electrokinetic activity of these thin film catalysts for OER and HER processes, was estimated from the Tafel plot. The Tafel equation is given as the dependence of overpotential η on the current density j as shown in Equation (9)

$$\eta = \alpha + (2.3RT/\alpha nF) \log j \quad (9)$$

where α is the transfer coefficient, n is the number of electrons involved in the reaction, and F is the Faraday constant. The Tafel slope is given by. The Tafel plots in this work were calculated from the reverse scan of CV collected at a scan rate of 2 mV s⁻¹ in a non-stirred N₂-saturated 1.0 M KOH solution.

2.2.10. Electrochemical Impedance Spectroscopy (EIS). The EIS experiments were performed within the 10⁵–10⁻² Hz frequency range, at an AC signal amplitude of 10 mV, to study the electrode kinetics and estimate the electrolyte resistance (R_1), and charge transfer resistance at the electrode (catalyst)-electrolyte interface (R_2). The Nyquist plots were collected in N₂-saturated 1.0 M KOH at an applied potential of 0.55 V vs. Ag|AgCl (KCl saturated). From the Nyquist plot, as fitted from the EIS equivalent circuit, electrolyte resistance (R_1), and charge-transfer resistance (R_2) were estimated.

2.2.11. Turnover Frequency (TOF). Turnover frequency (TOF) calculation of the catalysts The TOF value was calculated from Equation (10):

$$\text{TOF} = (jA) / (4mF) \quad (10)$$

where j is the current density in mA cm^{-2} at a given overpotential (e.g., $\eta = 0.36 \text{ V}$), A is the surface area of the electrode, F is the Faraday constant (a value of 96485 C mol^{-1}), and m is moles of catalyst on the electrode.^[33,34]

2.2.12. Mass Activity. Mass activity (A g^{-1}) is the current density per unit mass of the active catalyst at a given overpotential. It was calculated from the catalyst loading m and the measured current density j (mA cm^{-2}) for each sample,^[33,34] at $\eta = 0.36 \text{ V}$, calculated from Equation (11).

$$\text{Mass activity} = j / m \quad (11)$$

2.2.13. Density Functional Theory Calculations. To investigate the -OH adsorption energy, electronic, and charge transfer properties during the adsorption of the first hydroxyl group on the surface of nickel-selenide (Ni-Se), nickel-telluride (Ni-Te), and nickel-(telluro)-selenide (Ni-Se-Te) catalyst in OER, first principles Density Functional Theory (DFT) calculations are carried out using the Vienna ab initio simulation package (VASP).^[35,36] The ion-electron interaction is described using the projector augmented pseudopotential (PAW) method^[37,38] and the electron-electron interactions are treated using Perdew-Burke-Ernzerhof (PBE) exchange-correlation functional within the generalized gradient approximation (GGA).^[39] Since the Hubbard value (U_{eff}) incorporated GGA+U method has already proven its potential for accurately predicting the structural and electronic properties of materials in both bulk and slab forms, throughout the present calculations, we have used the same approach with U_{eff} values 5.9, 3.0 and 3.0 for Ni, Se and Te atoms, respectively.^[40-42] For the computations of both bulk and slab configurations, a 3×3 supercell of NiSe, NiTe, and NiSeTe is created. During the

calculation, the converged plane-wave energy cutoff was set to 500 eV followed by a Monkhorst-Pack^[43] k-point mesh scheme of $5 \times 5 \times 1$ for geometry optimization. However, a denser k-point mesh of $13 \times 13 \times 1$ is used for the electronic property calculations. During the entire calculation, we set the convergence limits of force tolerance and ground-state energy which are 10^{-3} eV/Å and 10^{-6} eV, respectively. A DFT-D3 approach^[44] was also considered to estimate the interaction between the Ni-series and the hydroxyl group. Sabatier plot was constructed using -OH adsorption energy to serve as a descriptor for observed catalytic activity, providing information about the catalytic efficiency (Tafel slopes and overpotential).^[3,45] During the calculation, the bottom lattice plane of the slab was fixed at the ground-state bulk distances, whereas atoms on the top lattice plane were set to be free to move and adsorb the hydroxyl group. After that, the OH⁻ ion was placed on top of the active Ni site of the relaxed free surface at 1.86 Å to calculate the adsorption energy. The adsorption energy of the first hydroxyl attachment was then calculated using Equation (12)

$$E_{ads} = E_{Ni-series+OH} - (E_{Ni-series} + E_{OH}) \quad (12)$$

where $E_{Ni-series+OH}$ is the total energy of the lowest energy configuration of NiSe, NiTe, and NiSeTe slab structures with the adsorbed OH⁻, $E_{Ni-series}$ is the total energy of the NiSe, NiTe, and NiSeTe structures without OH⁻, and is the lowest energy value of the free OH⁻ ion.

The isosurface charge density difference (CDD) is calculated using Equation (13) below:

$$\Delta\rho = \rho_{Ni-series+OH} - (\rho_{Ni-series} + \rho_{OH}) \quad (13)$$

where, and Field ρ^{OH} are the combined charge densities of Ni-series and OH⁻ ion, the charge density of the isolated NiSe, NiTe, and NiSeTe, and isolated OH⁻ ion, respectively.

3. RESULTS

Details of the hydrothermal synthesis along with a description of the layer-by-layer in situ deposition scheme are provided in the supporting information. The general synthesis and composition of each catalyst as grown on NF are schematically illustrated, as presented in Figure 1. Throughout this paper, NiSe@NiTe represents NiSe grown on top of NiTe which was first grown on NF substrate. And NiTe@NiSe describes NiTe grown on top of NiSe which was first grown on NF substrate. Both NiSe@NiTe and NiTe@NiSe represent a layer-by-layer morphology. The NiSeTe composition, on the other hand, represents the true mixed anionic phase of NiSeTe grown on an NF substrate. All the samples show a rough surface morphology relative to pure NF substrate indicating successful sample deposition on the NF substrate.

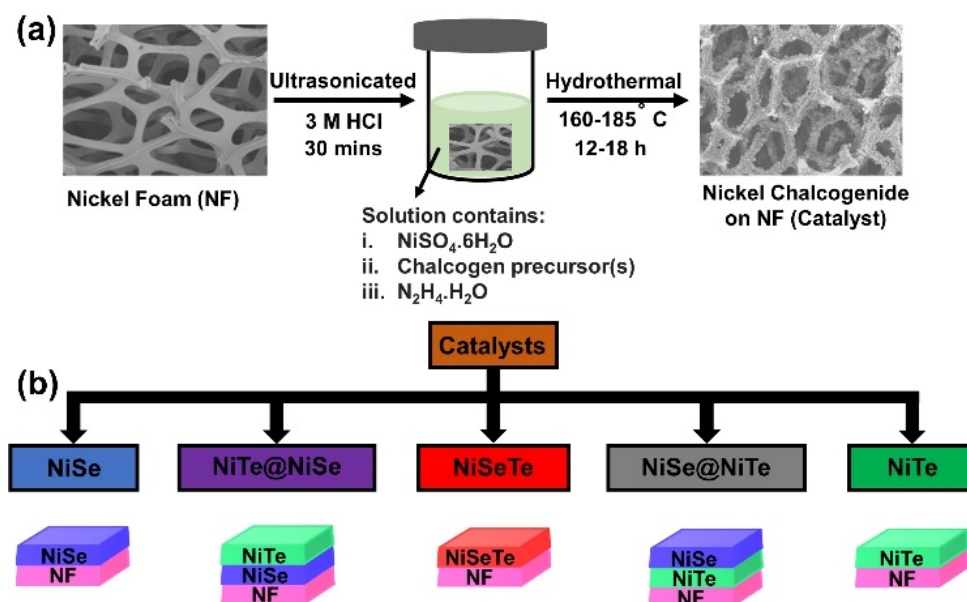


Figure 1. Schematic describing the (a) Preparation of nickel mixed anionic chalcogenide; (b) Composition of catalyst deposited on nickel Foam (NF).

Scanning electron microscopy (SEM) images (Figures 2a-f and S1) showed clear evidence of distinct phase growth of different morphologies as indicated by homogeneously covered densely packed nanostructured particles grown on NF. The morphologies exhibit some degree of surface roughness. NiTe and NiTe@NiSe show a clustered nanosheet-like structure, and NiSeTe, NiSe, and NiSe@NiTe exhibited homogeneous growth of vertically interconnected grains. The porous nature of NF-catalyst systems is believed to enhance accessibility to catalytic sites. Surface elemental compositions of NiSeTe, NiSe@NiTe, and NiTe@NiSe were estimated from EDS mapping analysis (Figure S2). It shows the average surface atomic ratio of Ni: Se (1:1) in NiSe@NiTe, suggesting NiSe dominated surface and NiTe bottom layer. Similarly, NiTe@NiSe showed the average surface atomic ratio of Ni: Te (1:1), implying the NiTe surface layer and NiSe bottom layer. NiSeTe revealed Se: Te (1:1) surface atomic ratio, confirming NiSeTe composition. The cross-sectional SEM analysis showed the different phases in the nickel chalcogenide composite samples (Figure 2g-i). NiSe@NiTe showed two phases supported by NF substrate: NiSe phase surface layer and NiTe phase bottom layer (Figure 2g). Similarly, NiTe@NiSe displayed two phases: NiTe phase surface layer and NiSe phase bottom layer, as shown by elemental mapping analysis in Figure 2i. This is consistent with the layer-by-layer hydrothermal growth hypothesis, suggesting that NiTe@NiSe and NiSe@NiTe each comprise two distinct layered phases rather than random phase distribution. Conversely, NiSeTe shows a single phase, corresponding to the NiSeTe phase. The cross-sectional SEM images were also used to estimate the thickness of the individual layers. NiSe@NiTe showed a composite layer thickness of 45 μm with the NiSe layer being approximately 20 μm thick atop a 25 μm NiTe layer. Similarly, the

NiTe@NiSe deposition showed a composite layer thickness of $\sim 124 \mu\text{m}$ with a $20 \mu\text{m}$ NiSe layer below an approximately $100 \mu\text{m}$ NiTe layer. The NiSeTe on the other hand, showed a deposition thickness of $134 \mu\text{m}$. These results are consistent with the cross-sectional EDX analysis data obtained for these samples (Figure S3-S5).

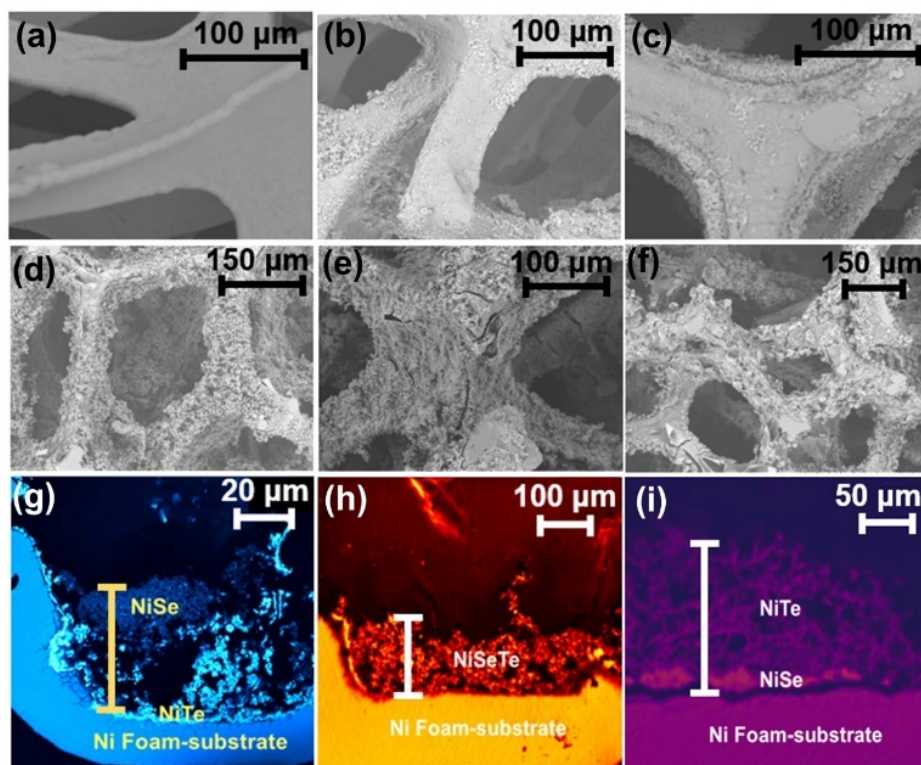


Figure 2. SEM images of nickel chalcogenide series and their deposition thickness. (a) Nickel foam (NF); (b) NiSeTe; (c) NiSe; (d) NiTe@NiSe; (e) NiSe@NiTe; (f) NiTe; cross-sectional SEM-EDX images of (g) NiSe@NiTe with a thickness of $45 \mu\text{m}$; (h) NiSeTe with a thickness of $135 \mu\text{m}$; (i) NiTe@NiSe with a thickness of $124 \mu\text{m}$.

The NiTe@NiSe and NiSe@NiTe composites both yielded NiSe and NiTe mixed phases, as observed in the powder X-ray diffraction (PXRD) patterns shown in Figure 3(a, b), rather than a new resultant phase. The NiTe@NiSe composite (Figure 3d) shows peaks at 124 and 143 cm^{-1} in Raman, corresponding to A_g and T_g modes in NiTe, indicating the

dominance of NiTe on the surface. Conversely, the NiSe@NiTe composite (Figure 3e) shows Raman peaks at 262, 226, 181, and 141 cm^{-1} corresponding to T_g , A_g , E_g , and T_g in NiSe, respectively,^[46,47] implying NiSe dominated the surface (see Figure S6). This is consistent with the layer-by-layer deposition growth order of the composites. Binary NiSe and NiTe, are used as a reference in this study, characterized as shown in (Figure S6). The XRD pattern for NiTe and NiSe were identical to the standard diffraction patterns (PDF # 01-075-0610), and (PDF # 01-089-2019), respectively. Their surface Raman spectra show peaks at 147, 225, and 265 cm^{-1} which corresponds to T_g , A_g , and T_g modes in NiSe (Figure S6), and peaks at 125 and 143 cm^{-1} presenting to A_g and T_g in NiTe (Figure S6), both of which were consistent with reported literature.^[47,48]

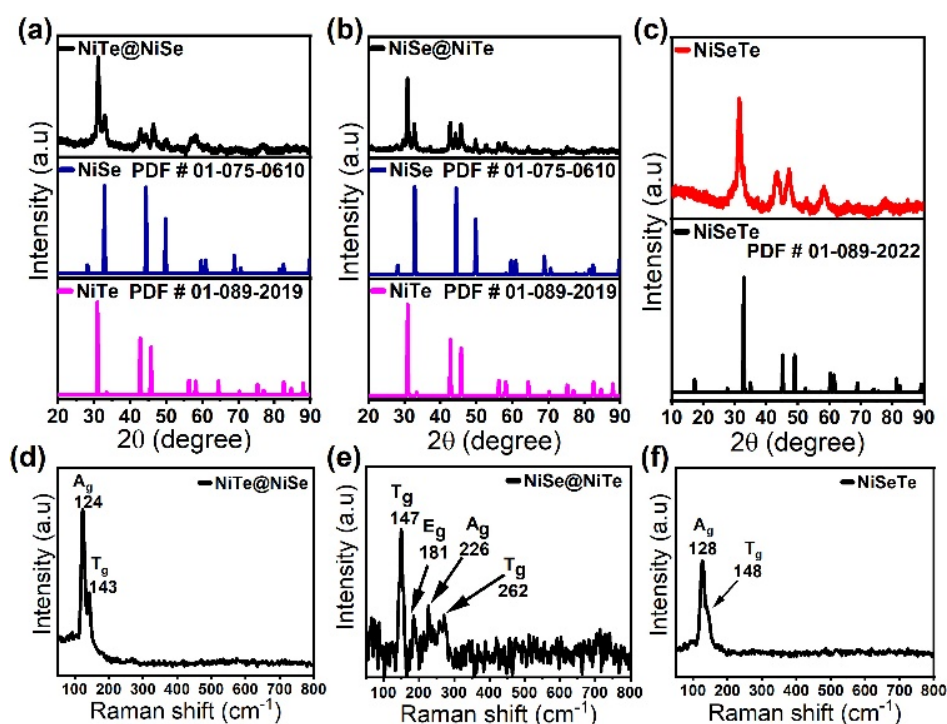


Figure 3. XRD spectra of (a) NiTe@NiSe; (b) NiSe@NiTe; (c) NiSeTe; Raman spectra of (d) NiTe@NiSe; (e) NiSe@NiTe (f) NiSeTe.

The crystal structure of NiSe (Figure S7) changes after hydrothermal tellurization into a single-phase trigonal NiSeTe nanocrystalline material as shown in the PXRD pattern in Figure 3c. NiSeTe occurs as a “*Kitkaite*” mineral and exhibits CdI₂-like trigonal crystal structure with $P\bar{3}m1$ space group of $\bar{3}m$ crystal class (Figure S7), similar to previous reports.^[49]

The PXRD peaks at 31.51, 43.41, 47.22, 49.95, and 59.5°, were indexed to (011), (012), (110), (111), and (201) planes of trigonal NiSeTe, respectively (Figure 3c), which is consistent with its standard diffraction pattern (PDF # 01-089-2022). Both Se and Te in NiSeTe have a site occupancy factors (SOF) of 0.5 for equivalent crystallographic positions, consequently, Ni(1)–Se(1)/Ni(1)–Te(1) bond lengths are all equivalent (2.499 Å). In this structure, the cations are no longer connected in the c direction and neighboring layers are held together by Van der Waals forces only. NiSeTe possesses metallic-like properties, hence, it has been reported to show weak and temperature-independent paramagnetism.^[49] The calculated unit cell parameters from the Rietveld refinements are $a = b = 3.716(5)$ Å and $c = 5.126(5)$ Å for trigonal NiSeTe. Furthermore, Raman at 128 and a shoulder at 148 cm⁻¹ correspond to A_g and T_g modes in NiSeTe (Figure 3f). This is consistent with averaging the Ni-Te and Ni-Se modes, as reported in similar composition types,^[47] supporting the coordination of both chalcogens (Se and Te) to the same metal atom (Ni) resulting in a true mixed anionic composition. The average crystallite size of NiSeTe was estimated to be 7.1 nm. This was calculated from the Scherrer equation (See Equation in S4) by fitting (011), (012) and (110) XRD reflection peak(s) using Lorentz function.^[50,51]

XPS spectra of the as-prepared NiSe@NiTe show Ni 2p at 873.7 and 855.8 eV assigned to the Ni²⁺ oxidation state in mostly the surface layer (NiSe) of the NiSe@NiTe, with satellite peaks at positions 880.28 and 861.6 eV corresponding to Ni 2p_{3/2} and Ni 2p_{1/2}, likely coming from NiSe and NiTe mixed phases. The higher binding energy of Ni 2p in NiSe@NiTe than that of NiTe indicates the strong synergetic interactions between the two layers; a similar observation has been reported previously.^[52] The Se 3d and Te 3d spectra are shown as insets of Figure S8. The Se 3d spectrum indicates three peaks after deconvolution at 58.6, 57.6, and 54.8 eV corresponding to SeO_x, Se 3d_{3/2}, and Se 3d_{5/2} respectively, indicating surface selenium oxidation. Interestingly, the inset showing Te 3d spectrum indicated very faint low-intensity peaks at 576.3 and 586.9 eV corresponding to Te 3d_{5/2} and Te 3d_{3/2} respectively. This indicates that the surface of NiSe@NiTe is mostly NiSe and has very little NiTe on it, which is consistent with layer-by-layer compositional growth. The binding energy of the Se 2p peak in NiSe@NiTe is lower than that of NiSe, suggesting extra charges in the Se, indicating electronic interactions. This phenomenon indicates that interfacial charge transfer may occur to Se from other atoms.^[52,53] The interfacial electronic interactions between NiTe and NiSe provide promising opportunities for modulating electrocatalytic properties. While the XPS spectra of NiTe@NiSe show Ni 2p at 873.7 and 855.8 eV assigned to the Ni²⁺ oxidation state of NiTe in NiTe@NiSe. The satellite peaks at positions 880.28 and 861.6 eV corresponding to Ni 2p_{3/2} and Ni 2p_{1/2}. The two insets correspond to Se 3d and Te 3d spectra, respectively (Figure S9). The Se 3d spectrum shows no Se 3d_{5/2} and Se 3d_{3/2} and or SeO_x peaks, indicating that the NiTe surface coverage is more effective than when NiSe is serving as the top surface layer. Again, this is consistent with layered growth. Further,

the inset showing Te 3d spectrum displays peaks at 576.3 and 586.9 eV assigned to Te $3d_{5/2}$ and Te $3d_{3/2}$, respectively, suggesting the surface is mainly NiTe (inset of Figure S9).

High-resolution XPS of NiSeTe shows Ni 2p peaks at 874.5 and 856.6 eV (Figure 4a) assigned to the Ni^{2+} oxidation state, while peaks at 880.6 and 862.4 eV are due to Ni $2p_{3/2}$ and Ni $2p_{1/2}$ satellite peaks. The peak at 853.1 eV representing Ni^0 corresponds to metallic Ni 2p arising from the NF substrate or from excess unreacted Ni^0 from reduced Ni^{2+} precursor. XPS spectra of Te and Se are shown in Figures 4b & c respectively. The Se 3d deconvoluted spectrum shows three peaks at 59.0, 57.4 eV, and 54.7 eV corresponding to SeO_x , Se $3d_{3/2}$, and Se $3d_{5/2}$ respectively. The binding energy of the Se 2p peak is slightly lower than that of NiSe, suggesting extra charges in the Se due to electronic interactions.

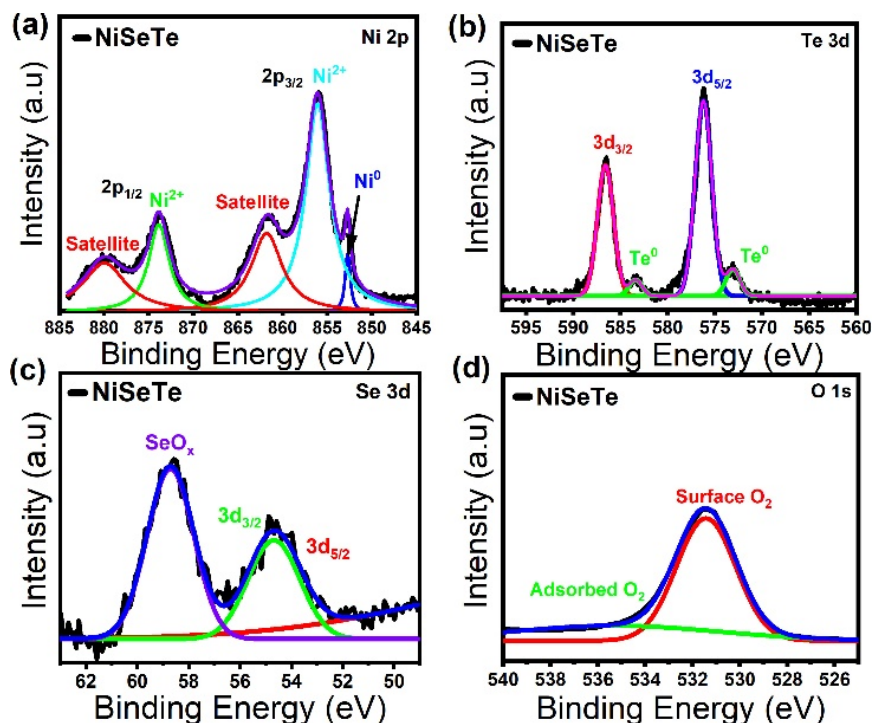


Figure 4. The high-resolution XPS spectra of NiSeTe. (a) Ni 2p peak; (b) Te 3d peak; (c) Se 3d peak; (d) surface O 1s peak.

This phenomenon indicates possible interfacial charge transfer from Te and Ni to Se.^[52,53] The oxidation states of Se were recognized as Se^{2-} and Se^{4+} , corresponding to NiTeSe and SeO_2 . SeO_2 could either be from mild surface oxidation of the Se in the system or from excess unreacted SeO_2 adsorbed on the surface. The C1s and O1s signals are largely due to the surface adsorption of atmospheric adventitious carbon and oxygen species. Furthermore, the Te 3d spectrum shown in (Figure 4b) indicated peaks at 576.4 and 586.9 eV which were ascribed to Te 3d_{5/2} and Te 3d_{3/2}, respectively. The Te spectrum also indicated the presence of metallic Te at 573.0 and 583.4 eV. This could be coming from surface-adsorbed traces of unreacted Te generated from the reduction of the TeO_2 precursor in the reaction mixture. This type of observation is well documented in the literature.^[20,24] The peak positions of the binding energies in the mixed anionic ternary NiSeTe phase are slightly shifted to more positive values relative NiSe phase due to differences in the coordination and difference in electronic structure which leads to subtle variation in electron density distribution, in agreement with previous reports.^[34,54,55] The binding energies for Ni 2p, Se 3d, and Te 3d in the XPS study of NiSe and NiTe (Figure S10) are also in agreement with the reported literature.^[14,52,56]

Nickel chalcogenides have shown superior electrochemical performance for OER, and overall water splitting.^[30,57] Both NiTe^[52] and NiSe^[56] grown on NF as nanoarray and nanowire film, respectively, have shown excellent OER and HER performance. In addition, a vertically grown catalyst on NF with a porous structure type is highly beneficial for OER, as it provides easier accessibility to active catalytic surface area for reactive substrates,^[42] which plays a vital role in electrolyte diffusion and gas discharge. In this work, OER electrocatalytic performance NiSe@NiTe and NiTe@NiSe catalysts were

compared to NiSeTe in O₂-saturated 1 M KOH measured under the same conditions, to elucidate the effect of mixed anionic coordination. The polarization curves from iR-corrected linear sweep voltammetry (LSV) scans (Figure 5a) indicate their OER performance, during which oxygen bubbles are observed from the electrode surface. The oxidation peaks around 1.37 V (vs RHE) correspond to the Ni²⁺ to Ni³⁺ redox couple, which shifts slightly on changing the anion composition.^[25] This observation was consistent with the shift noticed in the comparative cyclic voltammetry measurements conducted for these nickel series samples (Figure S11). In this series of compounds, NiTe exhibits the best activity toward OER, exhibiting an overpotential of 260 mV to achieve the current density of 50 mAcm⁻². The NiSe does not show any obvious anodic current until the potential reaches ≈1.53 V. In contrast, the NiSeTe-modified electrode displayed the onset of OER much earlier and achieved significantly higher catalytic current, thereby, demonstrating excellent activity with a low overpotential requirement of 300 mV to reach 50 mAcm⁻². The comparative efficiency towards OER for the nickel chalcogenides series is in the order NiTe > NiSeTe > NiSe, illustrating the critical effect of decreasing anion electronegativity around the catalytically active Ni center. As anion electronegativity decreases, covalency increases, thereby affecting the electronic structure and increasing the valence band edge comparable to the OER energy level.^[26] The OER performance of layer-by-layer binary phases, NiSe@NiTe, and NiTe@NiSe at 100 mAcm⁻², relative to the single-phase mixed anionic compositions is in the order NiTe > NiSe@NiTe > NiSeTe > NiTe@NiSe > NiSe (Table 1). Powder samples of NiTe, NiSeTe, and NiSe drop casted on carbon-cloth substrate exhibited identical electrocatalytic activity trends as those samples grown hydrothermally on NF (NiTe > NiSeTe > NiSe) (Figure 5b). This confirms the

inherent properties of these catalysts. However, a much higher current density is generated with a directly grown catalyst on a highly conducting substrate which is particularly beneficial in practical water electrolysis. Tafel plots shown in Figure 5c, reveal reaction kinetics in the electrocatalytic OER with a lower Tafel slope indicating faster kinetics. The Tafel slope showed an increase in the order NiTe (86 mVdec⁻¹) < NiSeTe (98 mVdec⁻¹) < NiSe@NiTe (112 mVdec⁻¹) < NiTe@NiSe (124 mVdec⁻¹) < NiSe (136 mVdec⁻¹), indicating that NiTe has the fastest OER kinetics, in agreement with the observation of electrocatalytic activity.

Table 1. Electrocatalytic parameter compared in nickel series catalytic systems.

Material	NiTe	NiSe	NiSeTe	NiTe @ NiSe	NiSe @ NiTe
Onset potential (V)	1.43	1.53	1.48	1.51	1.47
Overpotential @ 50 mA cm ⁻² (mV)	260	380	300	350	-
Overpotential @ 100 mA cm ⁻² (mV)	320	450	350	400	310
Ni ²⁺ →Ni ³⁺ oxidation peak potential (V)	1.36	1.32	1.34	1.33	1.42
Current density @ 300 mV (mA cm ⁻²)	70.09	19.46	56.64	36.04	97.39
Tafel slope (mV dec ⁻¹)	86	136	98	124	112
Mass activity (Ag ⁻¹)	138.1	33.7	90.3	29.2	57.1
TOF (s ⁻¹)	0.065	0.009	0.047	0.025	0.048

Conversely, the NiSe catalyst shows the highest Tafel slope value, corresponding to the slowest OER kinetics in the nickel chalcogenide series. Interestingly, NiSeTe exhibited a Tafel slope value, intermediate between the NiTe and NiSe. This suggests that changing the chalcogen anion from a more electronegative Se to a less electronegative Te facilitates the OER kinetics. Multistep chronoamperometry test on NiSeTe at different

applied potentials between 1.30 V to 1.65 V vs. RHE shows no obvious degradation of current density under any of the tested applied potentials (Figure 5d). This demonstrates the superior reliability of NiSeTe catalyst within a wide potential range, as well as its high mass transport, and mechanical robustness toward longevity in OER activity. The $\text{Ni}^{2+} \rightarrow \text{Ni}^{3+}$ pre-oxidation peak typically observed in OER of Ni-based systems provides an insight into the inherent property of the catalyst concerning its activation step.^[29,59]

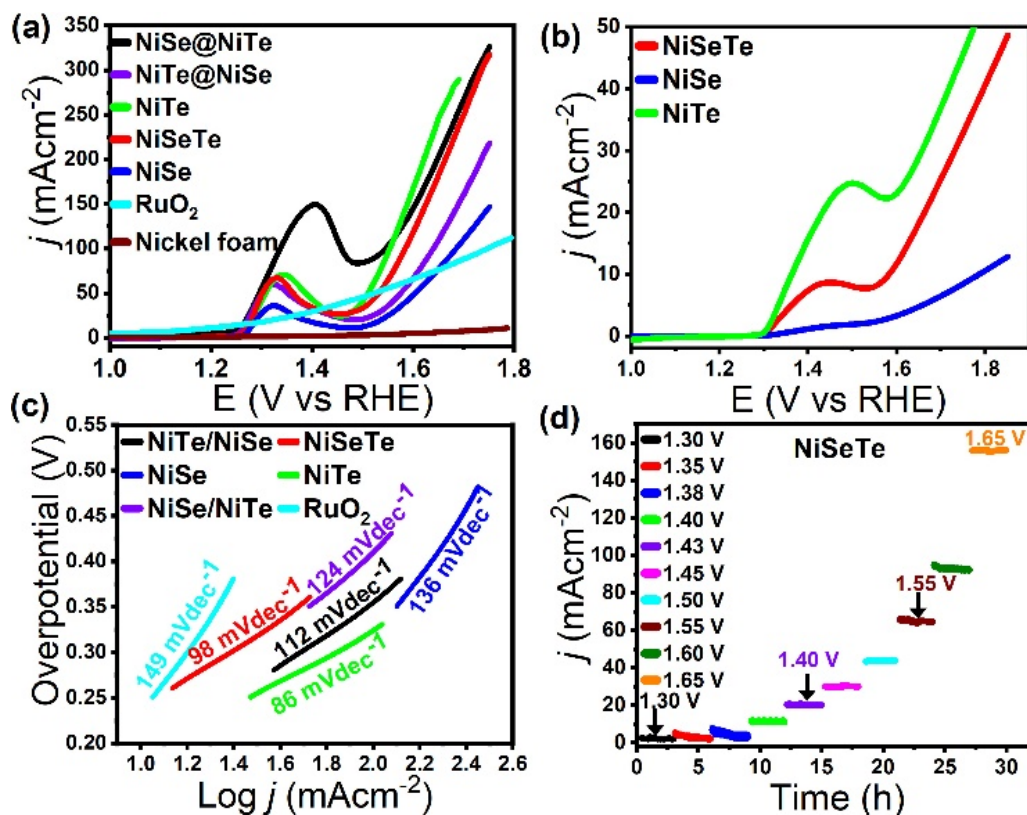


Figure 5. Electrocatalytic OER activity of nickel chalcogenide series. (a) LSV plots of catalysts on Nickel Foam; NiSe@NiTe (black), NiTe@NiSe (violet), NiSeTe (red), NiSe (blue), NiTe (green) RuO₂ (cyan), and nickel foam (brown); (b) LSV of catalysts on carbon cloth; NiSeTe (red), NiSe (blue), NiTe (green); (c) The Tafel slope obtained from LSV plots for different catalysts; (d) Multistep chronoamperometry study of the NiSeTe on NF electrode carried out at various constant applied potentials.

Additionally, the position of the $\text{Ni}^{2+}/\text{Ni}^{3+}$ oxidation peak is generally affected by the electronegativity of anion and coordination type around the Ni central atom.^[24] This effect is observed in the $\text{Ni}^{2+} \rightarrow \text{Ni}^{3+}$ oxidation peak potential (Table 1). It must be noted here that the effect of the thickness of grown catalyst layers was not moderated, although the sample loading was roughly comparable (Equations S5 and S6). For highly moderated samples, oxidation peak potential can be used to distinguish surface compositions. Since changes in anion composition and film thickness in catalysts could shift the Ni^{2+} oxidation peak position, one should be extremely quantitative when using this approach as a tool to appreciate the compositional evolution of active surfaces adequately.

The electrocatalytic performance towards OER can be substantially influenced by electronic structure, which is a direct consequence of the chemical composition as well as the crystal lattice structure of the electrocatalyst.^[7],37] Selenides have higher electronegativity and harder base characteristics, with a lesser degree of electron cloud delocalization, hence lower conductivity and charge mobility compared to telluride.^[20] Consequently, nickel selenides show lower electrocatalytic activity towards OER. However, changing covalency around the catalytically active Ni site leads to rearrangement of the electronic band structure, and movement of the valence and conduction band edges closer to the water oxidation-reduction level, consequently, reducing the overpotential requirement. It is therefore recommended that bond energies of intermediates and electronic structure (through chemical composition and crystal structure) should be tuned in catalysts to enhance OER performance.^[7,60] In NiSeTe crystal structure (trigonal), Ni atoms have unique coordination environments than those of NiSe and NiTe (hexagonal), thereby influencing its electrocatalytic activity towards OER.

To further appreciate the excellent OER performance of these nickel chalcogenide systems, the Tafel plot, mass activity, turnover frequency (TOF), and Electrochemical impedance spectroscopy (EIS) were computed as summarized in Figure 6. NiTe and NiSeTe catalysts exhibited the highest specific mass activities of 138.1 and 90.3 Ag^{-1} , respectively at 0.36 V overpotential (Figure 6b). TOF achieved for NiSeTe is 0.047 s^{-1} at the overpotential of 0.36 V, which was three folds ($3\times$) higher than NiSe. NiTe attained the highest TOF of 0.065 s^{-1} (Figure 6c). This demonstrates the higher intrinsic activity of NiSeTe and NiTe implying higher active sites and larger electrochemical surface area. The EIS analysis verified the fast OER kinetics of the catalysts. The charge-transfer resistance on NiSeTe at 1.55 V is 3.10 Ω , slightly smaller than that of NiSe@NiTe (3.55 Ω) and NiTe@NiSe (4.31 Ω) (Table S1), under similar conditions, implying faster electron transport in the NiSeTe. This is consistent with high activity kinetics observed in the nickel series. Overall, the charge transfer resistance follows the trend, NiTe (1.37 Ω) > NiSeTe (3.10 Ω) > NiSe@NiTe (3.55 Ω) > NiTe@NiSe (4.31 Ω) > NiSe (5.05 Ω), which corroborates well with the observed high catalytic efficiency.^[22] The electrolyte resistance of NiSeTe is 26.0 Ω , substantially, smaller than that of NiSe@NiTe (53.0 Ω), NiSe (42.32 Ω), NiTe (39.08 Ω), and NiTe@NiSe (37.99 Ω). The substrate-catalyst surface coverage resistance observed in some of the catalysts showed the least value in NiSeTe (29.00 Ω). The double layer capacitance on NiTe (350 μF), NiSe (43 μF), and NiTe@NiSe (279 μF) is smaller than that of NiSeTe (38.0 mF). The above observation implied that the diffusion effect on (NiTe, NiTe@NiSe, and NiSe) is more significant, as confirmed by their Warburg diffusion element contributions.^[61] Enhancement in electrocatalytic performance has been previously reported, ascribed to the synergistic effect of combining multi-component

compositions,^[62,63] and hetero-atomic doping, which could either be cationic, anionic, as well as interfacial engineering from the effects of ligands and electronic interactions around the different active centers.^[64] Incorporation of Te into NiSe results in electron density redistribution around the catalytically active Ni species in the resulting NiSeTe. This enables enhanced charge transport on surface structure and optimized bond strengths between the NiSeTe surface and intermediate adsorbates.^[22,65]

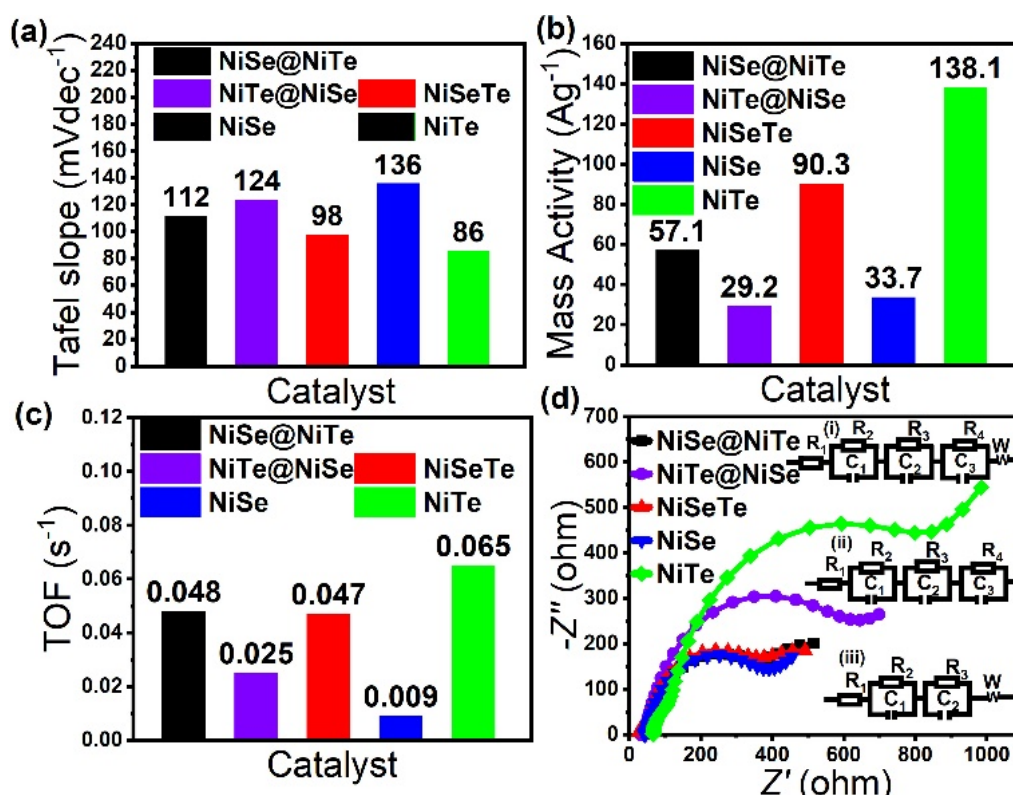


Figure 6. Electrocatalytic performance of NiSe@NiTe (black), NiTe@NiSe (violet), NiSeTe (red), NiSe (blue), and NiTe (green) catalysts. (a) Tafel slopes; (b) Mass activity at $\eta = 0.36$ V; (c) Turnover frequency (TOF) at $\eta = 0.36$ V; (d) Nyquist plots in the AC frequency range between 100 kHz and 0.1 Hz, at 1.55 V vs RHE. The inset shows the fitted equivalent circuit for (i) NiTe; (ii) NiSeTe and NiSe@NiTe; (iii) NiSe and NiTe@NiSe.

The long-term chronoamperometric stability of NiSeTe for 12h (Figure 7a) showed excellent catalytic stability with no significant degradation under uninterrupted OER conditions at constant 1.51 V. Furthermore, the LSV polarization curves of NiSeTe before and after the chronoamperometry study were almost identical as illustrated by inset in Figure 7a. This indicates the outstanding mass transfer property and mechanical robustness of the NiSeTe electrode. The chemical states and composition of the NiSeTe surface before and after stability showed that the catalyst is less susceptible to self-oxidation or corrosion, contrary to the belief that NiOOH formed on the catalyst surface during OER is the real active catalyst in nickel chalcogenide catalysts.^[56,66]

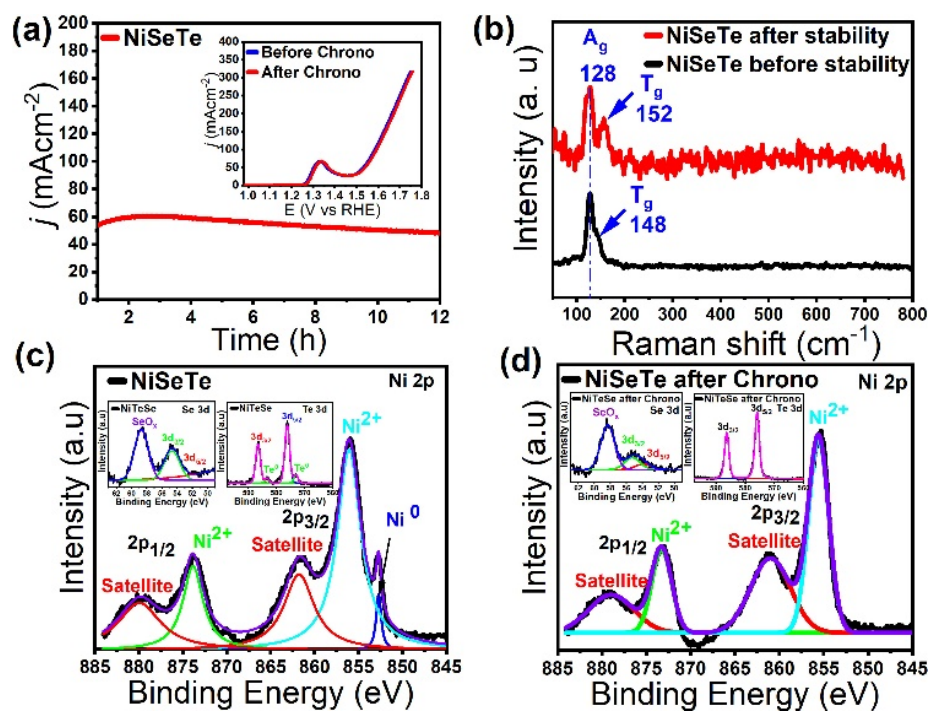


Figure 7. Chronopotentiometry curve of the NiSeTe recorded at 1.51 V for 12 h. The inset corresponds to the LSV of NiSeTe before and after chronoamperometry; (b) Raman spectrum of NiSeTe before and after stability (chronoamperometry). The high-resolution XPS spectra of (c) NiSeTe, Ni 2p; (d) NiSeTe after chronoamperometry, Ni 2p. The left side insets correspond to Se 3d peaks, while the left side insets correspond to Te 3d peaks.

Surface Raman spectral analysis reveals no formation of extra Ni-oxide phases on the surface as shown in Figure 7b. Also, there is no change in the relative intensity of the O1s peak in the XPS spectrum before and after stability, suggesting no surface oxide layer formation (Figure S12). Post-OER XPS analysis of NiSeTe indicates no increase in the intensity of the SeOx peak (inset Figure 7d), consistent with the Raman results. The metallic nickel peak at 853.1 eV (Figure 7c) and the tiny Te satellite peaks at 573.0 and 583.4 eV originating from precursor-based surface impurities were absent after activity (Figure 7d).

NiSeTe electrocatalysts indicated the least tendency towards oxidation compared to the other nickel chalcogenide catalysts, thereby preserving the structural coordination of NiSeTe in an alkaline medium. Similar observations have been made in NiSSe systems^[34] and nickel chalcogenide systems.^[25] Furthermore, the OER with NiSeTe may operate via a similar mechanism reported for other nickel chalcogenides, initiated by hydroxyl attachment on the catalytic site on the surface.^[22,34] This will form hydroxylated nickel mixed anionic (hydroxy)-telluro-selenide ($Ni(OH)SeTe$) as possible intermediate species.

The chronoamperometric study of NiSe@NiTe at a constant applied potential of 1.52 V for 12h, suggests that there is no degradation in the catalytic activity of NiSe@NiTe. The polarization curves compared before and after chronoamperometry (Figure S8), shows identical activity, suggesting excellent stability of the NiSe@NiTe composite under OER condition. The Raman spectra and XPS of NiSe@NiTe after chronoamperometry was analyzed. The Ni XPS spectrum after chronoamperometry study shows additional peaks after deconvolution, corresponding to Ni 2p_{3/2} and Ni 2p_{1/2} of Ni³⁺ at 857.9 and 875.5 eV respectively (Figure S8). This Ni oxidation is consistent with what was previously observed

for NF/NiSe catalysts,^[56] although it's very minimal in this composite catalyst, indicating that substrate and composition play a role in the oxidation process. Also, the peaks for Te at 576.3 and 586.9 eV corresponding to $3d_{5/2}$ and Te $3d_{3/2}$ become more visible indicating increased porosity of the surface NiSe layer. Similar observations were made in previous reports.^[58,67] While the XPS spectra of Se before and after chronoamperometry study looks very similar. The peak at around 58.9 eV for SeO_x increases slightly due to minimal oxidation on the surface of this catalyst (inset Figures S8 & S13). Overall, there is no indication of drastic change in the surface composition of the NiSe@NiTe catalyst.

A similar observation was made for NiTe@NiSe at a constant applied potential of 1.58 V over 12h. The polarization curve before and after chronoamperometry (Figure S13) shows no significant change in activity. Raman spectroscopy and XPS before and after stability shows that the identity of the catalyst was retained after chronoamperometry (Figures S9 & S14). The XPS spectrum after chronoamperometry studies shows no additional peaks after deconvolution, implying no nickel oxide formation. Again, this suggests that the composite setup minimizes nickel oxidation from the NF substrate. The peaks for Te at 576.3 and 586.9 eV corresponding to $3d_{5/2}$ and Te $3d_{3/2}$ remain at the same position after chronoamperometry, and no Se was detected before and after chronoamperometry, suggesting NiTe covers the bottom layer effectively. The excellent stability of NiTe@NiSe and NiSe@NiTe could be from the synergistic effect of the interaction of the two compositions in each composite. The chronoamperometry of NiSe shows high surface oxidation as indicated by the high relative intensity of SeO_x XPS peak after stability (Figure S15). The Raman shows a shift in E_g peak, which supports this claim.

While NiTe shows no significant changes in both Raman and XPS (Figures S15 & S16), indicating that NiTe is more stable than NiSe under the tested reaction conditions.

3.1. DENSITY FUNCTIONAL THEORY (DFT) STUDIES

OER in an alkaline medium is a complex multi-step process, initiated by a hydroxyl group (-OH^-) adsorption at the catalytic site which is considered the activation step.^[68] Besides, it is well understood that the kinetics of the OER is estimated by the rate-determining step. This happens either during (i) the first or second -OH attachment on the catalyst surface, or (ii) the release of O_2 . In both cases, the activation step is strongly influenced by the optimal surface coverage of the -OH^- on the catalytic surface which lowers OER onset potential.^[69] Understanding the catalyst activation step following -OH adsorption on the surface-active site is crucial in providing detailed insights into the catalytic activities. The -OH adsorption energy on the different catalyst surfaces as reported in this article was calculated through Density Functional Theory (DFT), details of which have been provided in the supplementary material.

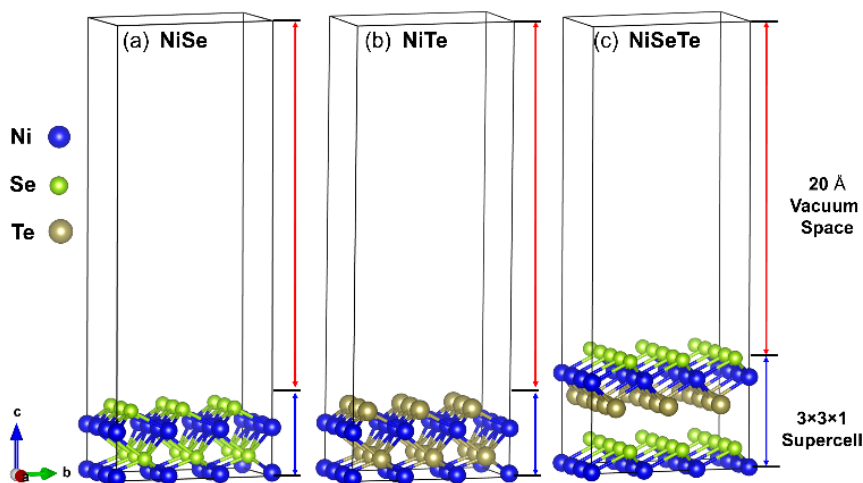


Figure 8. Slab models of (a) NiSe; (b) NiTe; and (c) NiSeTe supercells.

The crystal structures of NiSe, NiTe, and NiSeTe were constructed from reported crystallographic data. Atomic positions of bulk NiSe, NiTe, and NiSeTe were relaxed, and their optimized geometries were used to construct slab models of NiSe, NiTe, and NiSeTe configurations. During the calculations, a relatively large vacuum space of 20 Å was set in the direction perpendicular to the xy-plane of the slab model (Figure 8). This is to avoid interaction with the periodic images of the lower layer. NiSe belongs to the hexagonal crystal system with a space group of P6₃/mmc.^[70] Similarly, NiTe also belongs to the hexagonal crystal system (P6₃/mmc).^[71] On the contrary, NiSeTe crystallizes in a different structure, belonging to the trigonal crystal system.^[49] The crystal structures of bulk NiSe, NiTe, and NiSeTe are shown in Figure 9 (a-c). The DFT-optimized lattice constant and bond lengths of NiSe, NiTe, and NiSeTe bulk structures are provided in Table 2.

Table 2. DFT optimized lattice constant and bond lengths of bulk NiSe, NiTe, and NiSeTe structures.

Structure	Crystal System	Space Group	Lattice Constant (Å)	Bond Length (Å)				
				Ni-Se	Ni-Te	Se-Te (V)	Se-Se (V)	Te-Te (V)
NiSe	Hexagonal	P6 ₃ /mmc	3.659	2.476	-	-	3.337	
NiTe	Hexagonal	P6 ₃ /mmc	3.974	-	2.642	-	-	3.482
NiSeTe	Trigonal	P $\bar{3}$ m1	3.757	2.458	2.562	3.332	5.049	5.049

The (V) in bond length denotes the vertical distance between two adjacent atoms.

The active Ni site in each configuration was selected, and the system was relaxed to find the most stable binding location and corresponding energy. The -OH⁻ ion was placed

on the surface of the NiSe, NiTe, and NiSeTe slab structures in three different orientations: H-down, O-down, and OH-horizontal. Nine different DFT calculations were carried out to cover all possible configurations to compute the adsorption energy of -OH on the Ni-series surface. The H-down orientation gives the least favorable adsorption (Figure S17) because -OH adsorptions are expected to be directed towards the active Ni site through the more electronegative oxygen atom. Hence, the more probable -OH adsorption approaches are O-down and -OH-horizontal orientations, shown in Figure 9d-f. Previous studies reported that

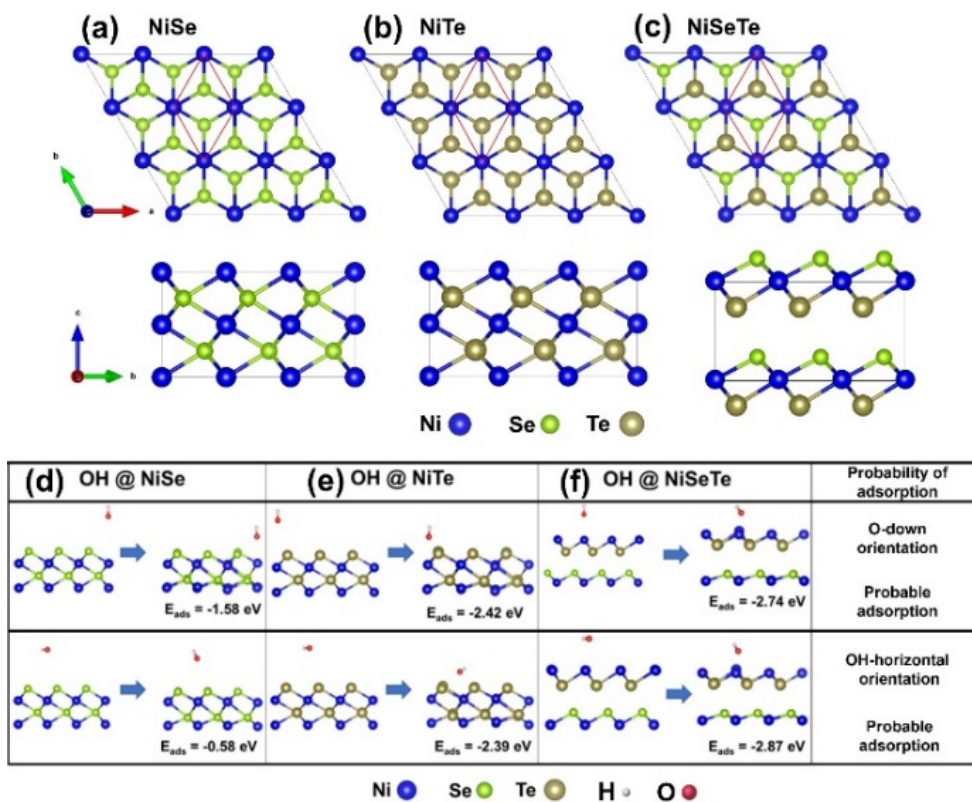


Figure 9. Crystal structures of $3 \times 3 \times 1$ supercells of bulk (a) hexagonal NiSe; (b) hexagonal NiTe; and (c) trigonal NiSeTe. In each configuration, Ni atoms are the active sites for OH adsorption, and the unit cell are marked as a red rhombus. Original and relaxed structures of (d) NiSe; (e) NiTe; and (f) NiSeTe, supercell slab models with an -OH ion adsorbed on the active Ni site.

stable -OH adsorptions (energetically favorable) are facilitated by decrease (more negative) in adsorption energy.^[65] A comparative analysis of the -OH adsorption energies on the different catalyst sites are shown in Figure 10a. The O-down orientation on NiTe and NiSeTe shows superior binding energy of -2.42 eV and -2.74 eV, respectively. Similarly, the -OH-horizontal orientation shows stable binding energy of -2.39 eV and -2.87 eV on NiTe and NiSeTe, respectively (Figure 10a). This shows that the more probable -OH adsorption orientations display consistent and favorable -OH adsorption energies.^[49]

However, NiSe showed wider adsorption energy difference with change in -OH orientation. This indicates that effects of anion electronegativity in the nearest neighbor coordination and molecular orientation could affect -OH adsorption energy of catalysts. The -OH adsorption energy analysis indicates that an energetically favorable -OH adsorption on the surface of Ni-site, may lead to optimal surface coverage and activation resulting in faster onset of OER catalytic activity. This is a critical pre-condition for superior OER performance. Hence, the average -OH adsorption energy for the more probable orientations (O-down and -OH-horizontal) was computed (Figure 10b), and it was observed that NiTe ($E_{\text{ave ads}}: -2.41$ eV) has higher adsorption energy than NiSeTe ($E_{\text{ave ads}}: -2.81$ eV). These results indicate that the adsorption of -OH on NiSeTe is more spontaneous and therefore energetically more favorable than that of NiTe and NiSe. This suggests that -OH adsorption is affected by changes in crystal structure, and anion composition. Conventionally, adsorptions with O-down in -OH orientation are employed for benchmark comparison since they are considered more likely. Under this orientation, NiSeTe shows very low adsorption energy, making it highly favorable (Figure 10c). This is consistent with the high activity of NiSeTe towards OER reaction. However, to adequately assess the

significance of the $\cdot\text{OH}$ adsorption on observed OER performance, we plotted OER overpotential as a function of $\cdot\text{OH}$ adsorption energy to create a volcano plot. This included few known catalysts (NiO , Ni_3Te_2 , Co_3O_4 , CoTe and CoTe_2),^[20] along with NiSe , NiTe and NiSeTe as shown in Figure 10d. It should be noted that the $\cdot\text{OH}$ adsorption energies for all these catalyst surfaces (NiO , Ni_3Te_2 , Co_3O_4 , CoTe , CoTe_2 , NiSe , NiTe and NiSeTe) were estimated following similar protocol and treated under similar conditions. It was

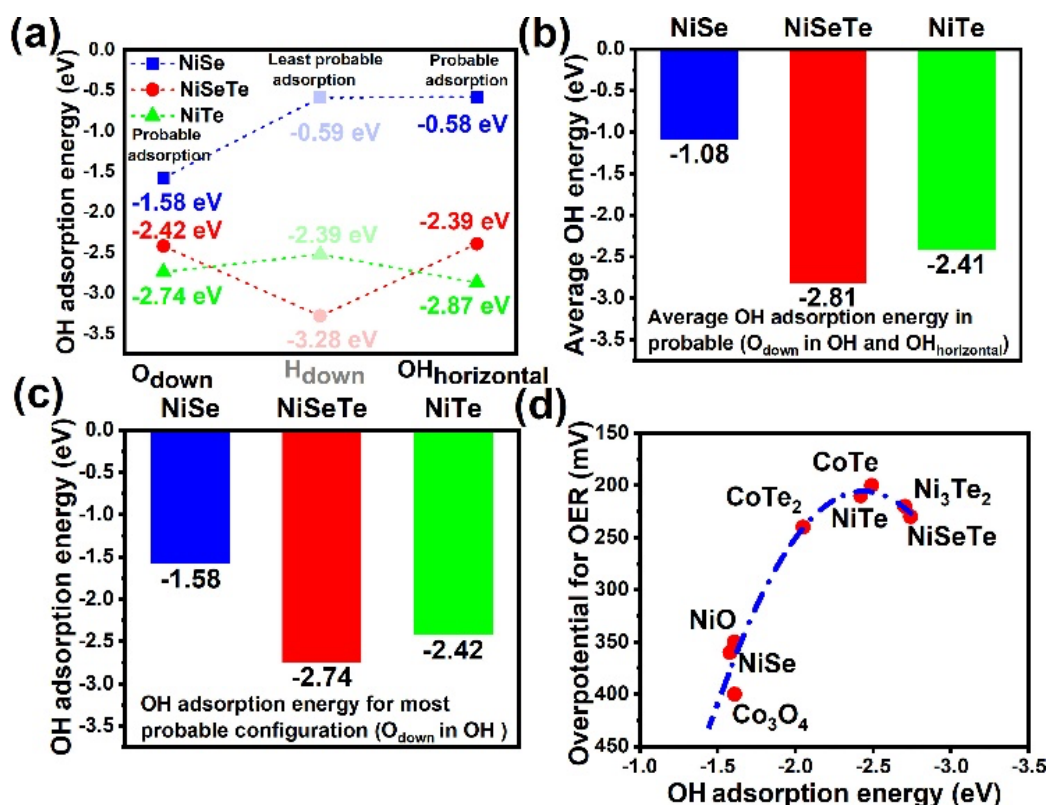


Figure 10. Adsorption energies of $\cdot\text{OH}$ and volcano plot of NiSe , NiTe and NiSeTe . (a) The adsorption energy of $\cdot\text{OH}$ at different orientations, when placed on top of the slab model of NiSe , NiTe and NiSeTe ; (b) Average adsorption energy of $\cdot\text{OH}$ for the most probable orientations when placed on top of the slab model of NiSe , NiTe and NiSeTe ; (c) Calculated adsorption energy of $\cdot\text{OH}$ -ions on NiSe , NiSeTe , and NiTe for O_{down} in $\cdot\text{OH}$; (most probable adsorption configuration). The more negative value indicates the lower adsorption energy; (d) Graph of overpotential as a function of $\cdot\text{OH}$ adsorption energy for various OER catalysts revealing a dependence, like the rising part of a volcano plot.

observed that as the -OH adsorption energy increases, the overpotential also decreases down to a minimum overpotential and then starts to increase. This resembles the rising part of a volcano or Sabatier plot,^[20,68,72,73] indicating that there is an optimum -OH adsorption energy for best OER activity, which is around (-2.5 eV) in this work. Such volcano plots can play a critical role in catalyst surface design by providing a simple descriptor for benchmarking catalyst efficiencies, which significantly simplifies catalytic surfaces comparison by reducing computational time.^[72,73] Furthermore, the adsorption distance of -OH from the surface of NiSe, NiTe and NiSeTe was estimated, and it was observed that they all possess stable adsorption distances, as shown in Table 3. The computed adsorption distance of -OH from the Ni site of NiSe, NiTe and NiSeTe are 2.789 Å, 3.931 Å and 1.821 Å, respectively. Bader charge analysis was performed to study the charge transfer between the -OH ion and Ni-series. The charge transfer is primarily ascribed to the difference in the electronegativity of the anions, which coupled with chemical bonding is theoretically associated with the adsorption energy.

Table 3. The bond length of -OH adsorbed NiSe, NiTe, and NiSeTe configurations as well as the shortest distance between -OH and the Ni-series.

System	Bond Length									Charge e	Style (Ni site)
	Ni-Ni	Ni-Se	Se-Se	Ni-Te	Te-Te	Se-O	Te-O	Ni-O	Ni-H		
NiSe+OH	3.496	2.385	3.608	-	-	2.702		2.789	-	-0.280	Acceptor
NiTe+OH	3.890	-	-	2.585	3.911	-	2.021	3.931	-	-0.233	Acceptor
NiSeTe+OH	3.752	2.272	3.774	2.431	3.743	-	-	1.821	2.398	-0.307	Acceptor

Computed Bader charge of -OH adsorbed Ni series is also provided. The OH molecule acts as a charge acceptor with considerable exchange of charges with the Ni-series and is reflected in the adsorption energy.

In general, strong adsorption energy denotes a strong chemical bond, whereas low adsorption energy indicates a weak chemical and/or van der Waal's bond.^[74] During the adsorption of -OH ion on the surface Ni-site along the series, the charge is transferred from the -OH ion to the surface and the computed charges are -0.280 e, -0.233 e, and -0.307 e for NiSe, NiTe, and NiSeTe, respectively. The charge density of isolated NiSe, NiTe, and NiSeTe structures and -OH ion is computed under the same adsorbed configuration. In Figure S17, we show the isosurface of the electronic CDD during the interaction of the -OH ion and the surface of the Ni series. The electron density accumulation and depletion can be correlated with the transfer of charges from the -OH ion to the surface.

The electronic properties of the slab models of the Ni-series and the computed band structure along with the high-symmetry points Γ -M-K- Γ -A-L-H-A are shown in Figure S18. We noticed that all the studied configurations show metallic characteristics, as there is no gap between the valence and conduction bands and a finite density of states is present at the Fermi level. To obtain a deeper understanding of the electronic properties of bulk NiSe, NiTe, and NiSeTe structures, we analyzed the total and projected density of states (TDOS and PDOS) which are shown in Figure S19 and Figure S20, respectively. The electronic property analysis revealed that the DOS at and around the Fermi level of all the studied configurations are dominated by the contribution of Ni atoms. The metallicity in NiSe, NiTe, and NiSeTe structures is mainly due to the partially occupied bands in the conduction band. The PDOS of NiSe, NiTe, and NiSeTe in Figure S20, shows valence band maximum (VBM) and conduction band minimum (CBM) mainly dominate from the d-orbital of Ni and p-orbital of Se/Te, respectively. In VBM, orbital mixing between Ni (dz^2), and Ni (d_{xz} , $d_x^2-d_y^2$) orbitals was observed in the range of 0 eV to -2.0 eV, while the

p_x orbital of the Se/Te atom was larger compared to d-orbital of Ni. Although the p-orbitals of Se/Te are dominant around the Fermi level, the metallicity in NiSe, NiTe, and NiSeTe is mainly due to the d-orbitals.

Furthermore, to understand the theoretical insights into the electronic properties of $\cdot\text{OH}$ adsorbed Ni-series, we analyzed the band structure, total, and projected DOS. We observed significant differences in the band structure of $\cdot\text{OH}$ adsorbed NiSe, NiTe, and NiSeTe structures compared to the bulk models. With the presence of $\cdot\text{OH}$ -ion, the conduction bands are shifted more towards the Fermi level, and an enhanced conductivity is observed. This increase in conductivity mainly arises from the shifting of valence bands up, as shown in Figure S21. The total DOS analysis reveals the metallic nature of $\cdot\text{OH}$ adsorbed Ni-series shown in Figure S22, which shows features similar to the slab structure of the Ni-series. The metallicity in the $\cdot\text{OH}$ adsorbed surfaces was observed to mainly come from the Ni atoms. Similarly, for $\cdot\text{OH}$ adsorbed NiSe and NiTe, the PDOS analysis reveals that the valence band maxima (VBM) and conduction band minima (CBM) mainly dominate from the d-orbital of Ni and p-orbital of Se/Te. In VBM, orbital mixing between Ni (dz^2), and Ni (d_{xz} , $d_x^2-d_y^2$) orbitals was observed in the range of 0 eV to -2.0 eV, significant contributions from the p_x and p_y orbitals of O atoms around the Fermi level were also observed for $\cdot\text{OH}$ -adsorbed NiSe. However, it is interesting to note that although the $\cdot\text{OH}$ adsorbed NiTe is showing metallicity at and around the Fermi level, the contributions from the O atoms in the $\cdot\text{OH}$ is insignificant compared to O atoms in the $\cdot\text{OH}$ of NiTe. Furthermore, the PDOS of $\cdot\text{OH}$ adsorbed NiSeTe was analyzed and the presence of density of states at and around the Fermi level was observed. This comes from the contribution of the d_{xz} , $d_x^2-d_y^2$, and dz^2 orbitals of Ni atoms, and p_x and p_z orbitals of Se and Te atoms, as

shown in Figure S23. while the p_x orbital of the Se/Te atom was larger than the d-orbital of Ni, as shown in Figure S24. Also, it was observed that the contribution from the p_z and p_y orbitals of O atoms in the OH-adsorbed NiSeTe is also significant and is essentially different from the OH-adsorbed NiSe and NiTe. Nonetheless, since the catalytic activity of the catalyst is strongly influenced by the electronic states, all the OH⁻ adsorbed Ni-series show superior electrical conductivity and are suitable for electrochemical water-splitting applications.

4. CONCLUSIONS

We presented *in-situ* hydrothermal growth of NiSeTe, NiSe, NiTe, (NiSe@NiTe), and (NiTe@NiSe) as efficient, high-performance, and durable OER electrocatalysts. The NiSe@NiTe and NiTe@NiSe were found to be phase-layered systems, each containing mixture NiSe and NiTe phases. Nickel (telluro)-selenide (NiSeTe) was found to be a single pure phase as indicated by XRD and EDX and allow excellent OER catalysis with ultralow overpotentials of 300 mV at 50 mAcm⁻², small Tafel slope of 98 mV/dec, high TOF (0.047 s⁻¹) and mass activity (90.3Ag⁻¹), superior to numerous non-precious OER catalysts in the literature. This highlights the effect of changing anion coordination geometry, crystal lattice structure, and electronic density around the metal center in OER performance. The stability and durability of the catalysts suggest that this facile fabrication approach minimizes catalyst surface oxidation. This can also be associated with the interfacial synergistic effect between NiSe and NiTe in the layered samples. This work unlocks exciting new avenues to explore transition-metal mixed anionic chalcogenides to

understand structure–property–performance relationships in catalysts and their electrochemical applications. DFT calculations of –OH adsorption energy, electronic, and charge transfer properties provide insights into the mechanism of improved OER catalytic activity in the NiSeTe.

SUPPLEMENTARY INFORMATION

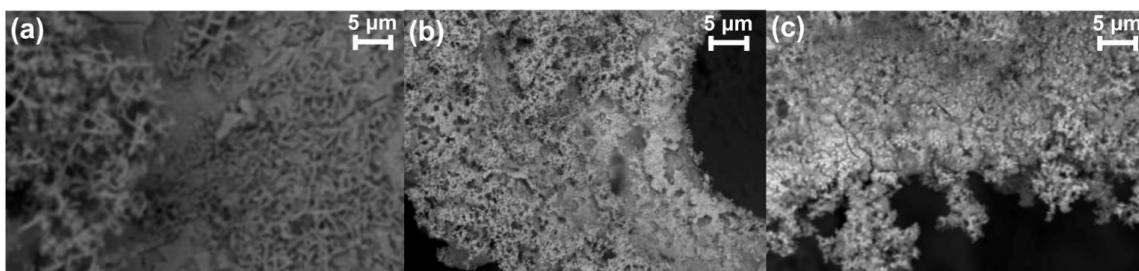


Figure S1. EDX SEM images of (a) NiSe@NiTe; (b) NiTe@NiSe; (c) NiSeTe.

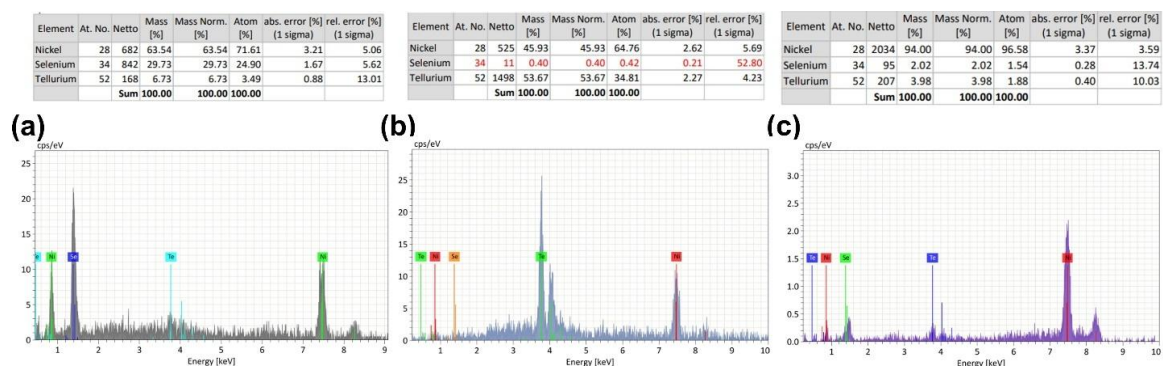


Figure S2. Surface EDX analysis of (a) NiSe@NiTe; (b) NiTe@NiSe; (c) NiSeTe.

The surface elemental ratio obtained for NiSe@NiTe showed a ratio of Ni:Se: Te (2:1:0.25), the average atomic ratio of 1:1, for the surface NiSe and masking most of the NiTe bottom layer, suggesting the NiSe layer is on the top (Figure S2). Similarly,

NiTe@NiSe showed a surface elemental ratio (2:1:0.01) for Ni:Se: Te, indicating that Ni: Te has an average atomic ratio of 1:1, suggesting NiTe composition is on the surface layer (Figure S2). Furthermore, the relative atomic percentage for NiSeTe showed an excess of Ni coming from the NF substrate while Se: Te came up as 1:1, suggesting the composition to be NiSeTe (Figure S2).

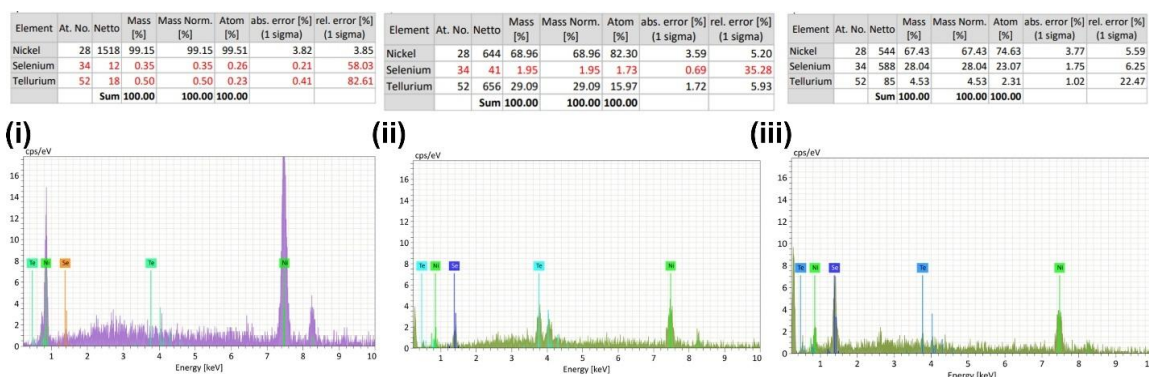


Figure S3. Cross-sectional EDX analysis of NiSe@NiTe; (i) phase 1 is the base layer, NF; (ii) phase 2 is the first deposition, NiTe. (iii) phase 3 is the second deposition, NiSe.

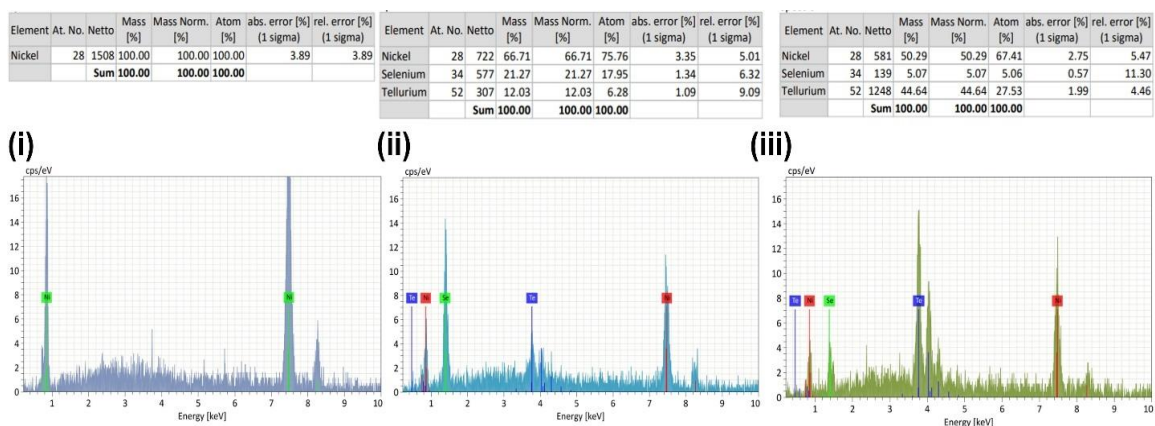


Figure S4. Cross-sectional EDX analysis of NiTe@NiSe; (i) phase 1 is the base layer, NF; (ii) phase 2 is the first deposition, NiSe. (iii) phase 3 is the second deposition, NiTe.

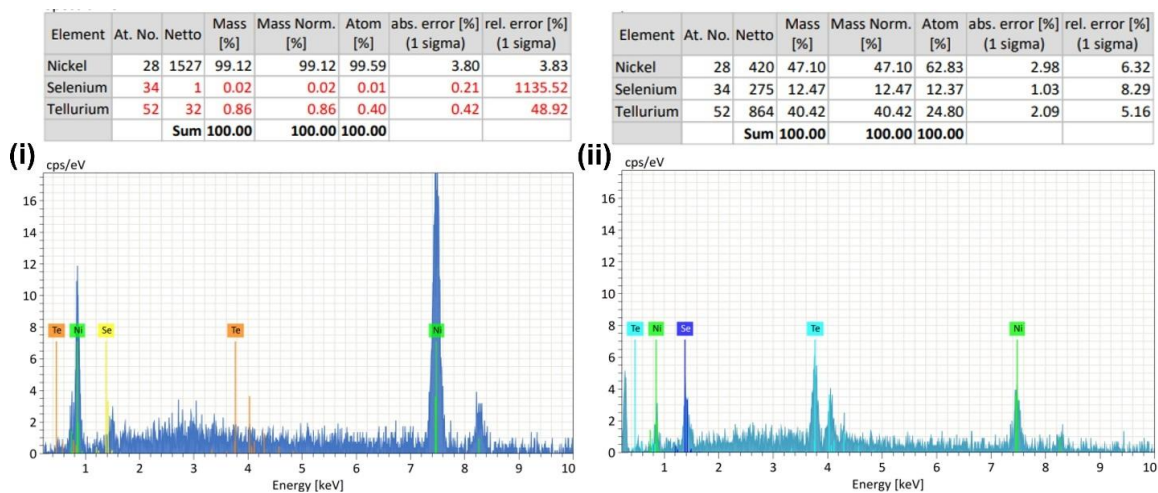


Figure S5. Cross-sectional EDX analysis of NiSeTe; (i) phase 1 is the base layer, NF; (ii) phase 2 is the first deposition, NiSeTe.

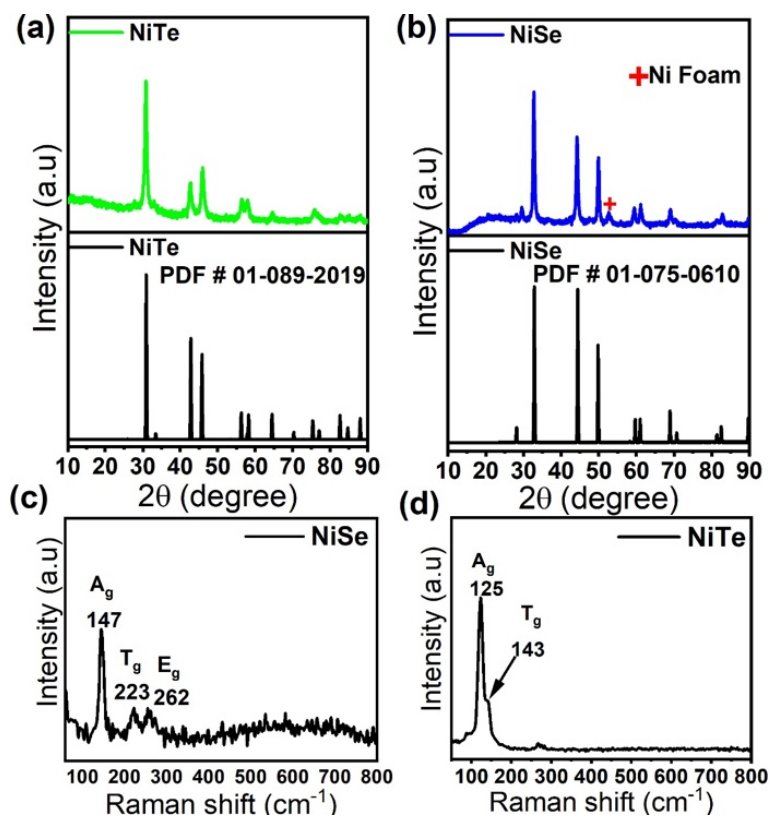


Figure S6. (a) XRD spectra of the NiTe; (b) XRD spectra of the NiSe; (c) Raman spectrum of NiSe; (d) Raman spectrum of NiTe.

NiSe occurs naturally as “*Sederholmite*” while NiTe occurs as “*Imgreite*” in nature. Their crystal lattice structures consist of Ni(1) in octahedral coordination with Se(1) and Te(1) atoms respectively, with the octahedra edge-shared and corner-shared resulting in a 3-D compact lattice. All Ni(1)–Se(1) bond lengths in NiSe were equivalent (2.498 Å), similar to equivalent Ni(1)–Te(1) bond lengths in NiTe (2.648 Å) (Figure S7), with calculated unit cell parameters from the Rietveld refinements of $a = b = 3.660(1)$ Å, $c = 5.330(1)$ for NiSe and $a = b = 3.956(1)$ Å, $c = 5.365(1)$ for NiTe. NiSe, NiTe, and NiSeTe respectively exhibit hexagonal $P6_3/m\bar{m}$ space group of $6/m\bar{m}m$ crystal class, hexagonal $P6_3/m\bar{m}c$ space group of $6/m\bar{m}m$ crystal class, and the CdI₂-like trigonal crystal structure with $P\bar{3}1m$ space group of $\bar{3}Pm$ crystal class (Figure S7).

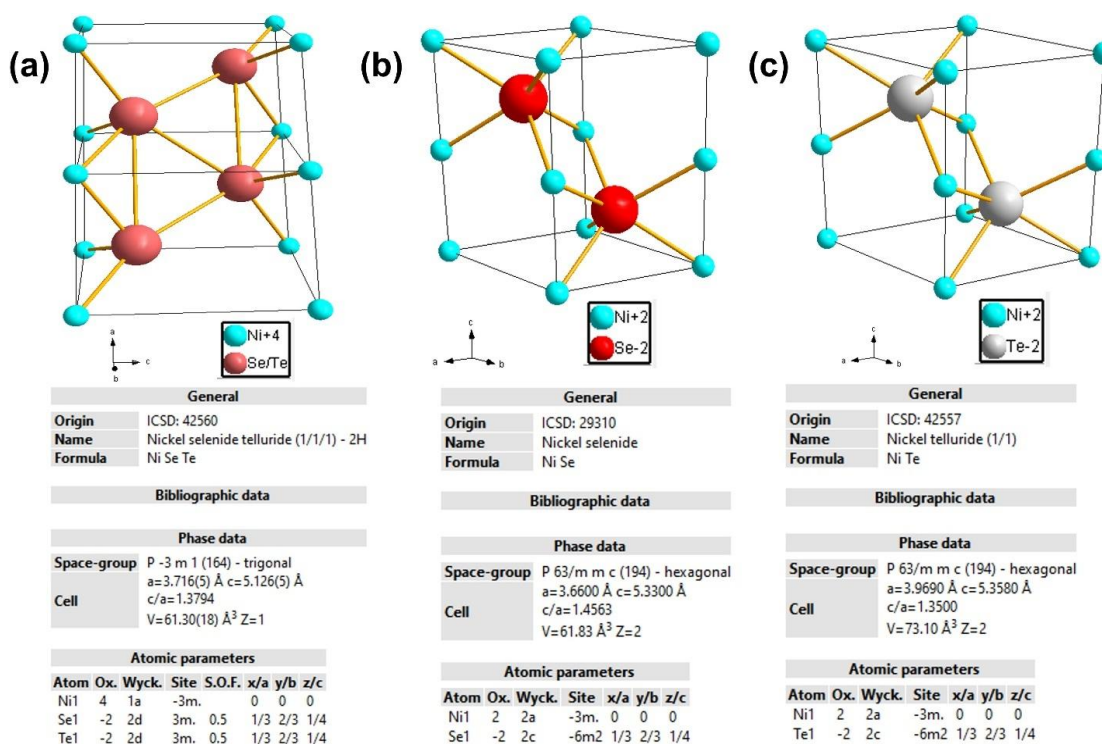


Figure S7. Crystal structure (a) NiSeTe; (b) NiSe; (c) NiTe.

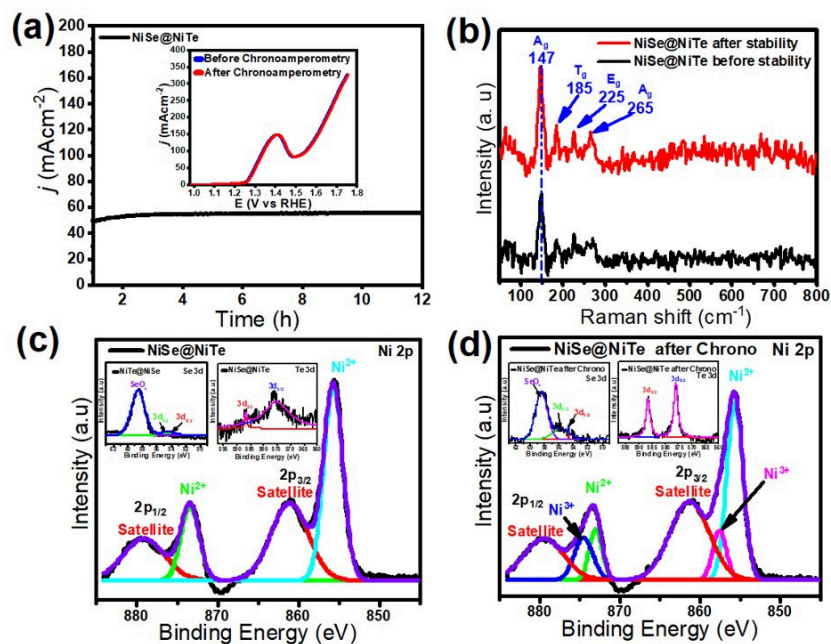


Figure S8. Characterization of NiSe@NiTe at (a) Chrono at 1.52 V for 12 h. LSVs as inset; (b) Raman). XPS spectra (c), Ni 2p; (d) after chronoamperometry, Ni 2p. The left side insets correspond to Se 3d peaks, while the right side insets correspond to Te 3d peaks.

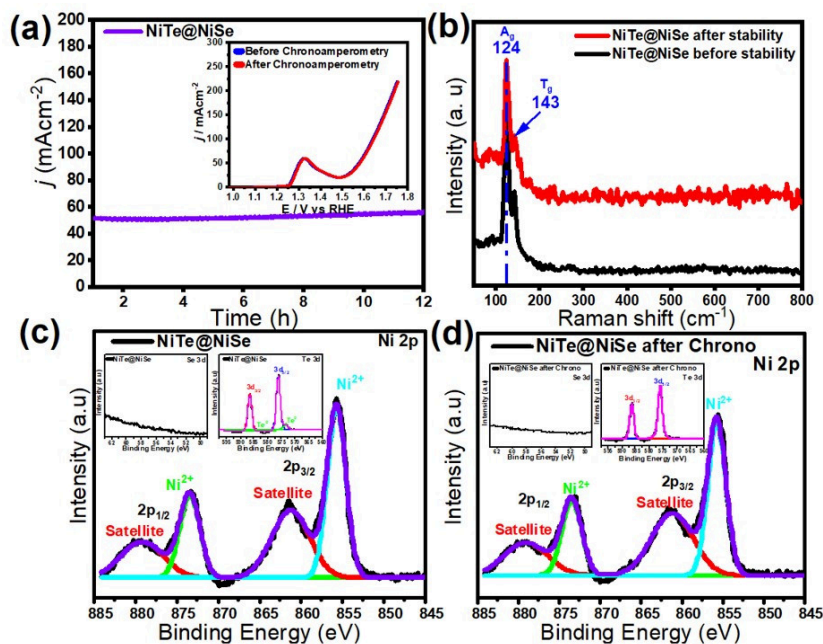


Figure S9. Characterization of NiTe@NiSe at (a) Chrono at 1.58 V for 12 h. LSVs as inset; (b) Raman). XPS spectra (c), Ni 2p; (d) after chronoamperometry, Ni 2p. The left side insets correspond to Se 3d peaks, while the right side insets correspond to Te 3d peaks.

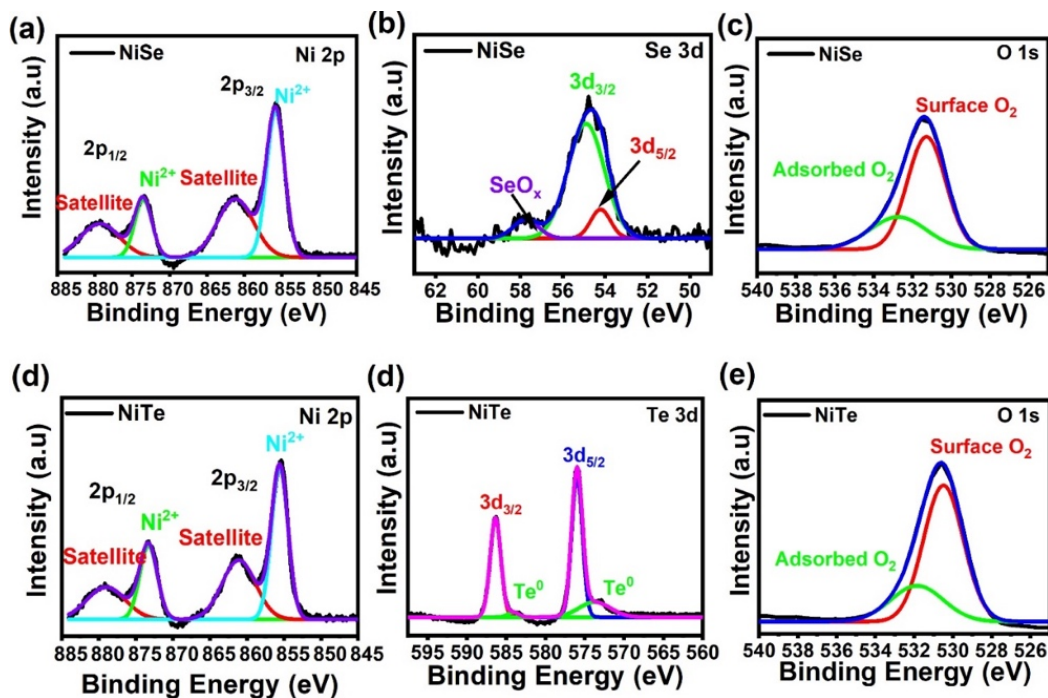


Figure S10. The high-resolution XPS spectra of NiSe (a) Ni 2p peak; (b) Te 3d peak; (c) Se 3d peak; (d) surface O 1s peak. NiTe (d) Ni 2p peak; (e) Te 3d peak; (f) surface O 1s peak.

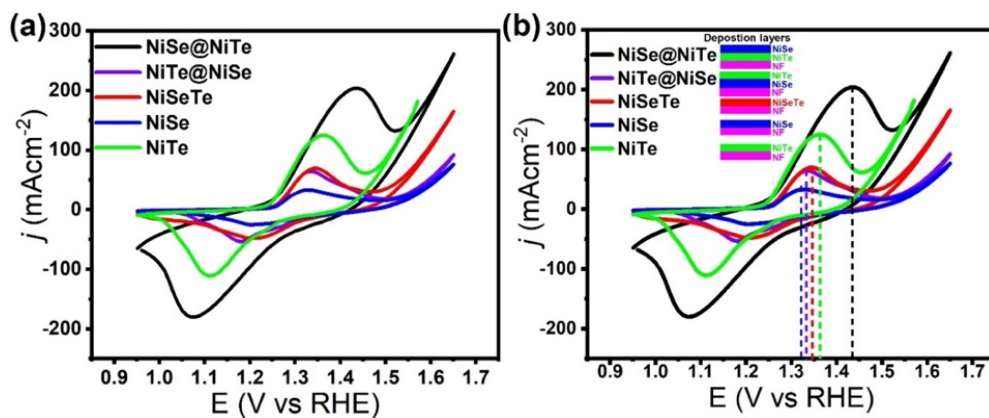


Figure S11. Comparison of (a) CVs measured for NiSe@NiTe (black), NiTe@NiSe (violet), NiSeTe (red), NiSe (blue) and NiTe (green) showing the Ni²⁺/Ni³⁺ oxidation peak; (b) Potential values of Ni²⁺ oxidation peaks in NiSe@NiTe (black), NiTe@NiSe (violet), NiSeTe (red), NiSe (blue) and NiTe (green). The inset indicates the deposition layer ordering in each sample.

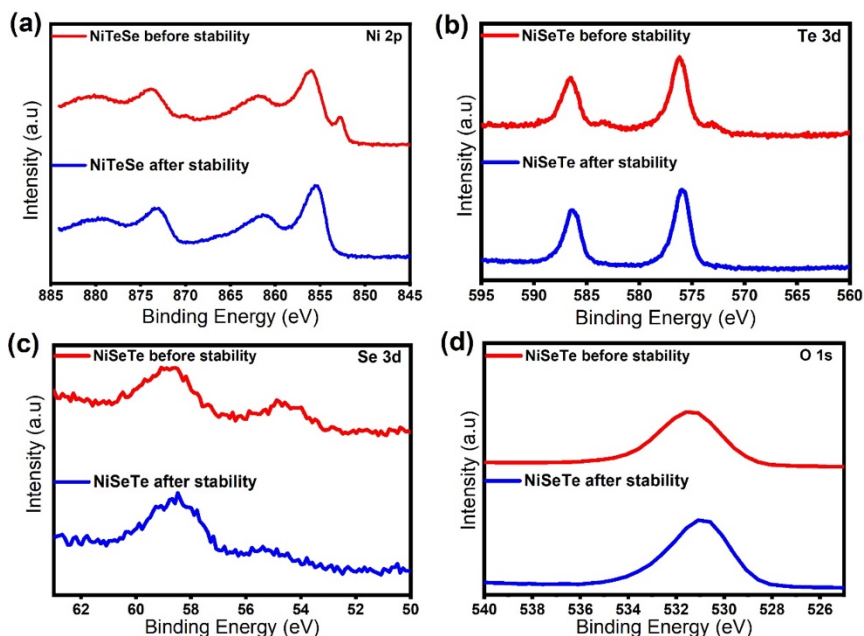


Figure S12. NiSeTe XPS compared before and after chronoamperometry for (a) Ni 2p peaks; (b) Te 3d peaks; (c) Se 3d peaks; (d) O 1s peaks.

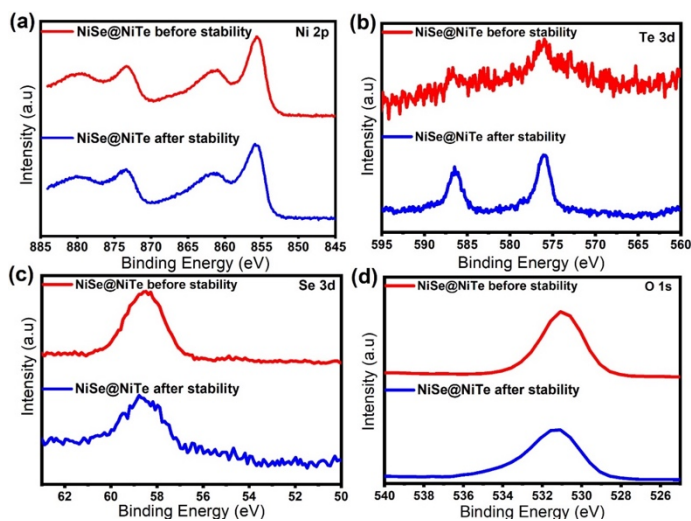


Figure S13. Comparison of NiSe@NiTe XPS before and after chronoamperometry for (a) Ni 2p peaks; (b) Te 3d peaks; (c) Se 3d peaks; (d) O 1s peaks.

O 1s spectra of NiSe@NiTe in Figure S13d revealed the presence of some amounts of surface-adsorbed oxygen at 531.2 eV before and after chronoamperometry

stability studies. There was no evidence of Ni-oxide formation on the surface or any other additional phases.

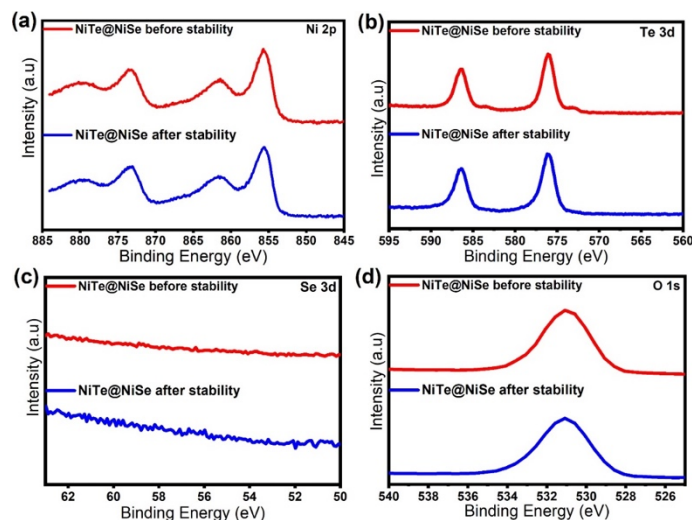


Figure S14. NiTe@NiSe XPS before and after chronoamperometry for (a) Ni 2p peaks; (b) Te 3d peaks; (c) Se 3d peaks; (d) O 1s peaks.

O 1s spectra of NiTe@NiSe in Figure S14d revealed the presence of some amounts of surface adsorbed oxygen at 531.2 eV before and after chronoamperometry stability studies, there was no evidence of surface Ni-oxide formation or any other additional phases. XPS studies of NiSe and NiTe control samples (Figure S15) were observed to have similar deconvoluted peaks corresponding to binding energies for Ni 2p, Se 3d, and Te 3d, to what was reported in the literature.^[14,52,56] NiSe shows surface selenium oxidation after chronoamperometry, while NiTe showed no significant change in the spectra before and after stability studies.

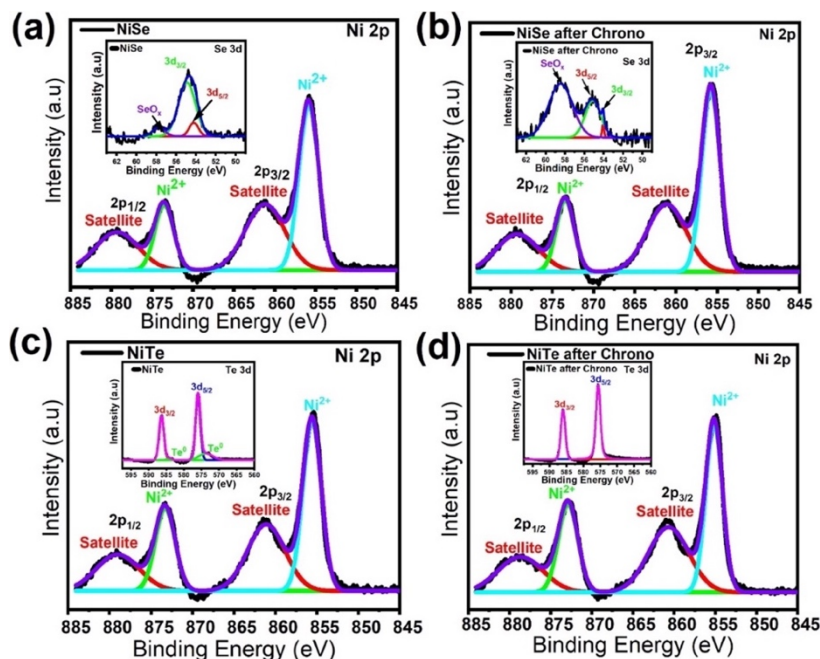


Figure S15. The high-resolution XPS spectra of (a) NiSe, Ni 2p; (b) NiSe after chrono, Ni 2p. The insets correspond to Se 3d peaks, peaks. (c) NiTe, Ni 2p; (d) NiTe after chrono, Ni 2p. The insets correspond to Te 3d peaks.

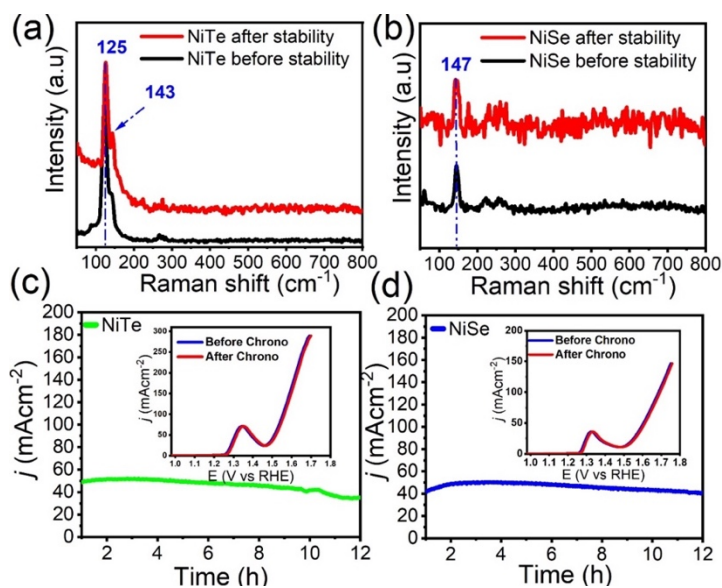


Figure S16. (a) Raman spectrum of NiTe before and after stability; (b) Raman spectrum of NiSe before and after stability; (c) Chrono of the NiTe for 12 h. LSV inset for NiTe before and after chrono; (d) Chrono curve of the NiSe for 12 h. LSV inset of NiSe before and after chrono.

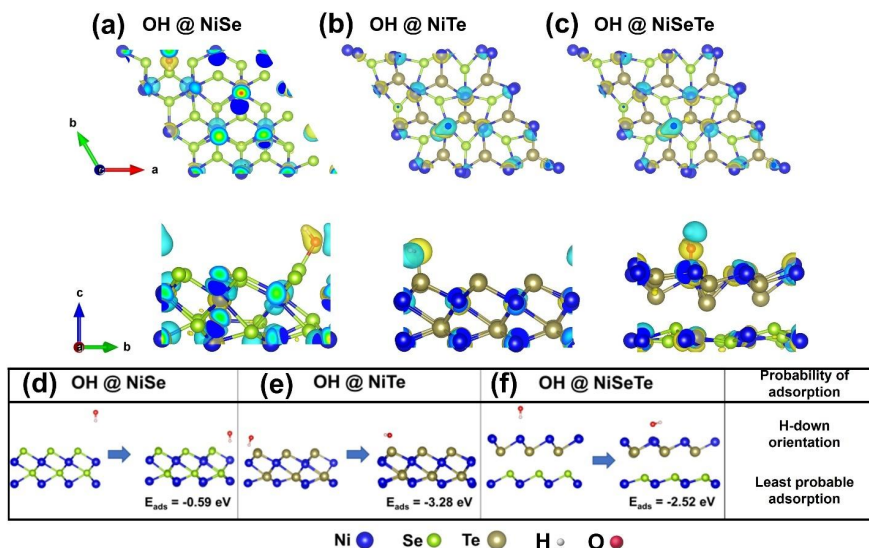


Figure S17. Side and top views of the charge density difference induced by the adsorption of OH on (a) NiSe (b) NiTe and (c) NiSeTe. The yellow and cyan colors represent charge accumulation and depletion, respectively (isosurface value: 1.06×10^{-1} electrons/ \AA^3). Original and relaxed structures of (d) NiSe; (e) NiTe; and (f) NiSeTe supercell slab models with an OH- ion adsorbed on the active Ni site.

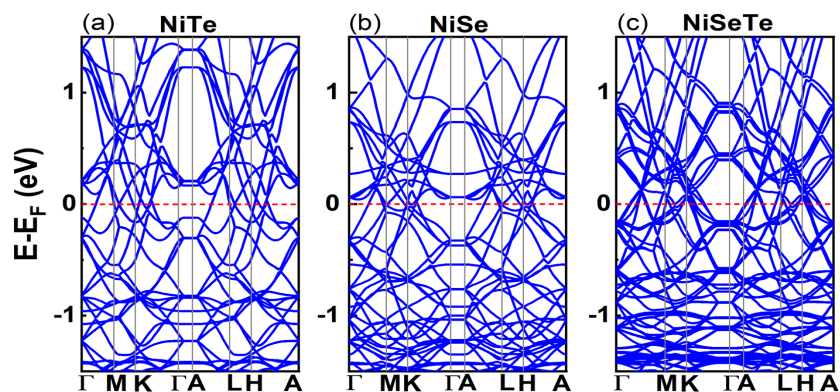


Figure S18. Calculated electronic band structure of the slab models of (a) NiSe; (b) NiTe (c) NiSeTe structures.

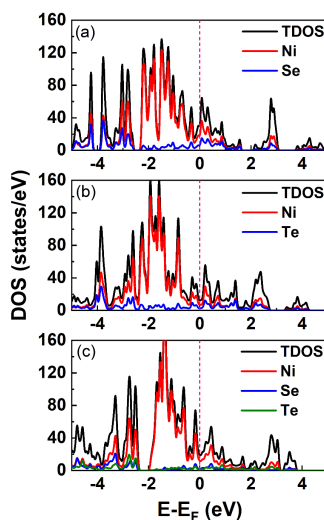


Figure S19. The total density of states in the slab models of (a) NiSe; (b) NiTe; (c) NiSeTe structures. The vertical pink dashed line represents the Fermi level, which is set to 0 eV.

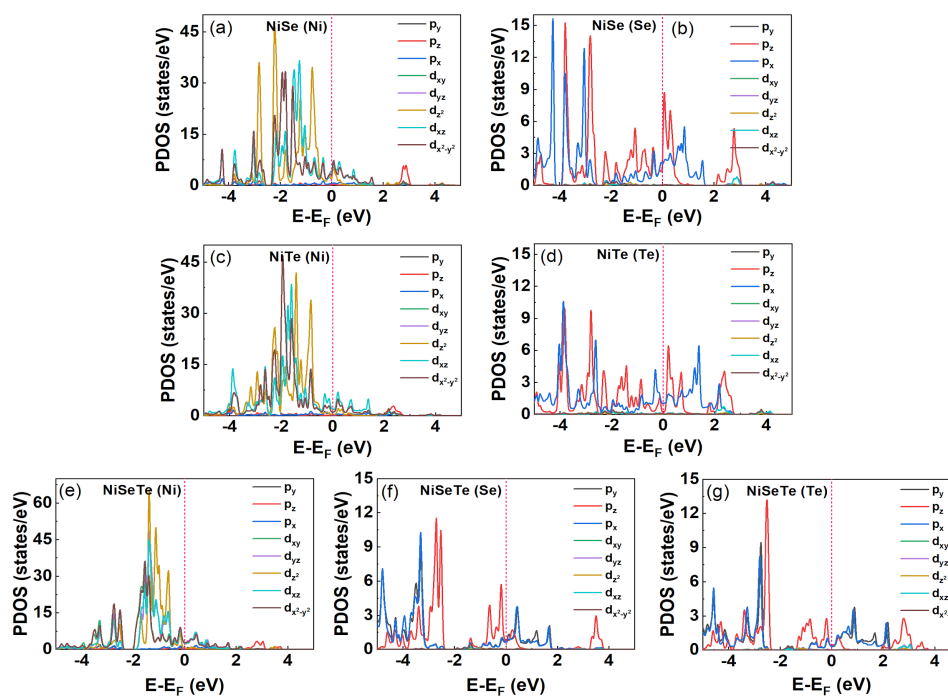


Figure S20. Projected density of states of NiSe, NiTe, and NiSeTe using the PBE+U approach in the adsorption energy.

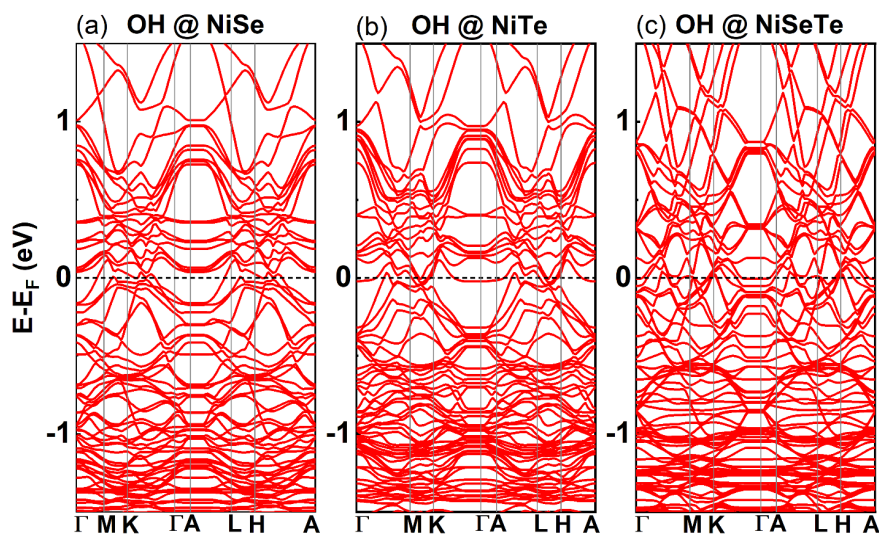


Figure S21. Calculated electronic band structure of OH adsorbed (d) NiSe; (e) NiTe; and (f) NiSeTe along the Γ -M-K- Γ -A-L-H-A path, using GGA+U functional showing the metallic characteristics. The horizontal red dashed line represents the Fermi level and is set to 0 eV.

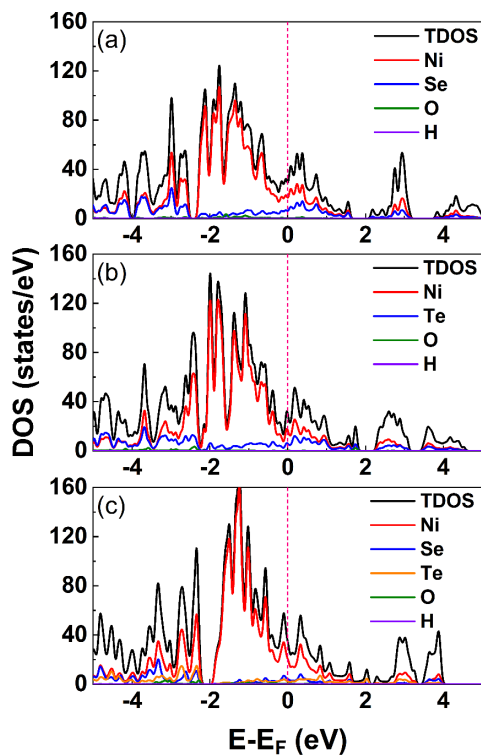


Figure S22. The total density of states of OH adsorbed on (a) NiSe; (b) NiTe; and (c) NiSeTe, using the PBE+U approach. The vertical pink dashed line represents the Fermi level, which is set to 0 eV.

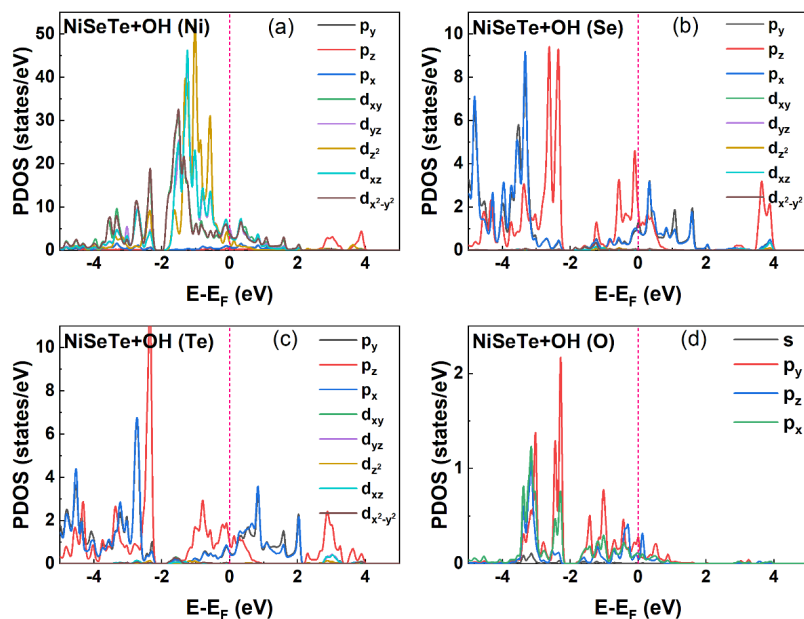


Figure S23. Projected density of states of OH⁻ adsorbed NiSeTe using the PBE+U approach.

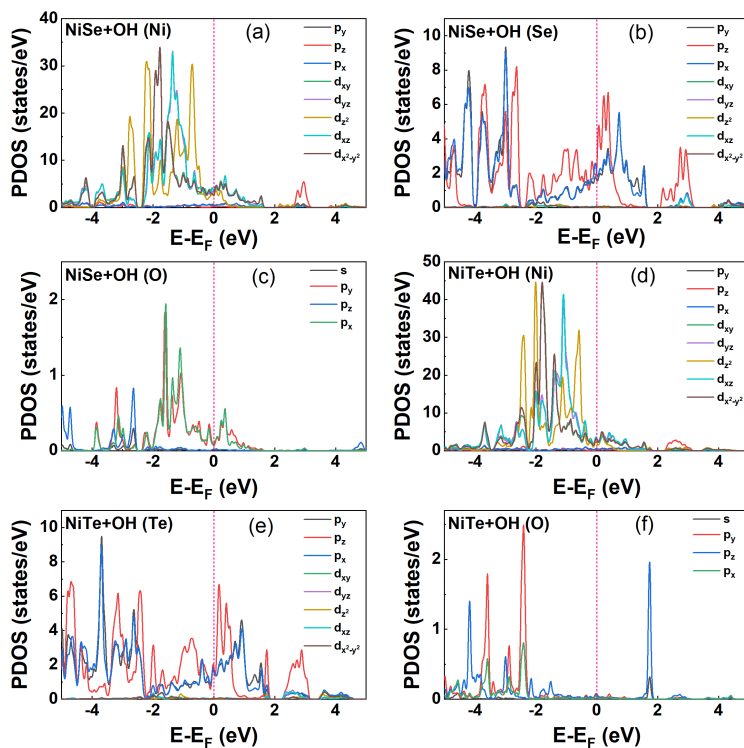


Figure S24. Projected density of states of OH adsorbed (a)-(c) NiSe and (d)-(f) NiTe using the PBE+U approach.

Table S1. Parameters of equivalent circuit obtained from fitting of EIS experimental data.

Catalyst	R_1/Ω	R_2/Ω	R_3/Ω	R_4/Ω	C_1/F	C_2/F	C_3/F	$W/s^{(1/2)}\Omega^{-1}$
NiSe@NiTe	53.0	3.55	27.15	47.05	4.25E ⁻⁰²	4.30E ⁻⁰³	7.70E ⁻⁰³	-
NiTe@NiSe	37.99	4.31	46.82	-	3.50E ⁻⁰⁴	4.10E ⁻⁰³	-	1.38E ⁻⁰²
NiSeTe	26.0	3.10	31.00	29.00	3.80E ⁻⁰²	3.40E ⁻⁰³	3.90E ⁻⁰⁷	-
NiSe	42.32	5.05	26.11	-	4.30E ⁻⁰⁵	4.80E ⁻⁰³	-	1.87E ⁻⁰²
NiTe	39.08	1.37	18.15	46.36	2.79E ⁻⁰⁴	5.58E ⁻⁰⁴	5.19 E ⁻⁰³	5.99E ⁻⁰³

R_1 is the resistance of the electrolyte, R_2 is the electron transfer resistance, C_1 is the constant phase element (CPE) of double layer nonideal capacitance, R_3 is the resistance of the catalyst layer, R_4 is the resistance due to a changing surface coverage of adsorbed species, C_2 is the capacitance, C_3 is the capacitance and W is the Warburg element.

REFERENCES

- (1) Turner, J. A. Sustainable Hydrogen Production. *Science (1979)* **2004**, 305 (August), 972–974. <https://doi.org/10.1016/b978-0-444-64203-5.00001-0>.
- (2) Zeng, K.; Zhang, D. Recent Progress in Alkaline Water Electrolysis for Hydrogen Production and Applications. *Prog Energy Combust Sci* **2010**, 36 (3), 307–326. <https://doi.org/10.1016/j.pecs.2009.11.002>.
- (3) Walter, M. G.; Warren, E. L.; McKone, J. R.; Boettcher, S. W.; Mi, Q.; Santori, E. A.; Lewis, N. S. Solar Water Splitting Cells. *Chem Rev* **2010**, 110 (11), 6446–6473. <https://doi.org/10.1021/cr1002326>.
- (4) Santos, D. M. F.; Sequeira, C. A. C.; Macciò, D.; Saccone, A.; Figueiredo, J. L. Platinum-Rare Earth Electrodes for Hydrogen Evolution in Alkaline Water Electrolysis. *Int J Hydrogen Energy* **2013**, 38 (8), 3137–3145. <https://doi.org/10.1016/j.ijhydene.2012.12.102>.
- (5) Wang, Z.; Yang, J.; Gan, J.; Chen, W.; Zhou, F.; Zhou, X.; Yu, Z.; Zhu, J.; Duan, X.; Wu, Y. Electrochemical Conversion of Bulk Platinum into Platinum Single-Atom Sites for the Hydrogen Evolution Reaction. *J Mater Chem A Mater* **2020**, 8 (21), 10755–10760. <https://doi.org/10.1039/d0ta02351e>.
- (6) Lee, Y.; Suntivich, J.; May, K. J.; Perry, E. E.; Shao-Horn, Y. Synthesis and Activities of Rutile IrO₂ and RuO₂ Nanoparticles for Oxygen Evolution in Acid and Alkaline Solutions. *Journal of Physical Chemistry Letters* **2012**, 3 (3), 399–404. <https://doi.org/10.1021/jz2016507>.

- (7) Nørskov, J. K.; Bligaard, T.; Rossmeisl, J.; Christensen, C. H. Towards the Computational Design of Solid Catalysts. *Nat Chem* **2009**, *1* (1), 37–46. <https://doi.org/10.1038/nchem.121>.
- (8) Meng, Y.; Wang, M.; Zhu, Z.; Jiang, T.; Liu, Z.; Chen, N.; Shen, C.; Peng, Q.; Chen, W. Multifunctional Nickel-Cobalt Phosphates for High-Performance Hydrogen Gas Batteries and Self-Powered Water Splitting. *ACS Appl Energy Mater* **2021**, *4* (11), 12927–12934. <https://doi.org/10.1021/acsaem.1c02582>.
- (9) Menezes, P. W.; Panda, C.; Loos, S.; Bunschei-Bruns, F.; Walter, C.; Schwarze, M.; Deng, X.; Dau, H.; Driess, M. A Structurally Versatile Nickel Phosphite Acting as a Robust Bifunctional Electrocatalyst for Overall Water Splitting. *Energy Environ Sci* **2018**, *11* (5), 1287–1298. <https://doi.org/10.1039/c7ee03619a>.
- (10) Wang, X.; Li, W.; Xiong, D.; Liu, L. Fast Fabrication of Self-Supported Porous Nickel Phosphide Foam for Efficient, Durable Oxygen Evolution and Overall Water Splitting. *J Mater Chem A Mater* **2016**, *4* (15), 5639–5646. <https://doi.org/10.1039/c5ta10317g>.
- (11) Wang, X. Y.; Han, X. P.; He, Y.; Hu, W. bin; Deng, Y. da. Hierarchical Porous NiS@NiO Nanoarrays in Situ Grown on Nickel Foam as Superior Electrocatalyst for Water Splitting. *Int J Electrochem Sci* **2020**, *15* (March), 3563–3577. <https://doi.org/10.20964/2020.04.19>.
- (12) Swesi, A. T.; Masud, J.; Nath, M. Nickel Selenide as a High-Efficiency Catalyst for Oxygen Evolution Reaction. *Energy Environ Sci* **2016**, *9* (5), 1771–1782. <https://doi.org/10.1039/c5ee02463c>.
- (13) Li, Y.; Zhao, C. Two-Dimensional NiTe Nanosheets Anchored on Three-Dimensional Nickel Foam as High-Performance Catalyst for Electrochemical Water Oxidation. *Adv Mater Lett* **2017**, *8* (9), 916–921. <https://doi.org/10.5185/amlett.2017.1669>.
- (14) Wang, Z.; Zhang, L. In Situ Growth of NiTe Nanosheet Film on Nickel Foam as Electrocatalyst for Oxygen Evolution Reaction. *Electrochem Commun* **2018**, *88* (December 2017), 29–33. <https://doi.org/10.1016/j.elecom.2018.01.014>.
- (15) Rao, Y.; Wang, Y.; Ning, H.; Li, P.; Wu, M. Hydrotalcite-like Ni(OH)₂ Nanosheets in Situ Grown on Nickel Foam for Overall Water Splitting. *ACS Appl Mater Interfaces* **2016**, *8* (49), 33601–33607. <https://doi.org/10.1021/acsaami.6b11023>.
- (16) Abdullahi, I. M.; Masud, J.; Ioannou Polydoros-Chrisovalantis; Ferentinos, E.; Kyritsis, P.; Nath, M. A Molecular Tetrahedral Cobalt–Seleno-Based Complex as an Efficient Electrocatalyst for Water Splitting. *Molecules* **2021**, *26* (4), 945. <https://doi.org/10.3390/molecules>.

- (17) Masud, J.; Ioannou, P. C.; Levesanos, N.; Kyritsis, P.; Nath, M. A Molecular Ni-Complex Containing Tetrahedral Nickel Selenide Core as Highly Efficient Electrocatalyst for Water Oxidation. *ChemSusChem* **2016**, *9* (22), 3128–3132. <https://doi.org/10.1002/cssc.201601054>.
- (18) Popczun, E. J.; McKone, J. R.; Read, C. G.; Biacchi, A. J.; Wiltrout, A. M.; Lewis, N. S.; Schaak, R. E. Nanostructured Nickel Phosphide as an Electrocatalyst for the Hydrogen Evolution Reaction. *J Am Chem Soc* **2013**, *135* (25), 9267–9270. <https://doi.org/10.1021/ja403440e>.
- (19) Tian, J.; Liu, Q.; Asiri, A. M.; Sun, X. Self-Supported Nanoporous Cobalt Phosphide Nanowire Arrays: An. *J. Am. Chem. Soc.* **2014**, *136* (50), 7587–7590.
- (20) Nath, M.; de Silva, U.; Singh, H.; Perkins, M.; Liyanage, W. P. R.; Umapathi, S.; Chakravarty, S.; Masud, J. Cobalt Telluride: A Highly Efficient Trifunctional Electrocatalyst for Water Splitting and Oxygen Reduction. *ACS Appl Energy Mater* **2021**, *4* (8), 8158–8174. <https://doi.org/10.1021/acsaem.1c01438>.
- (21) Liao, L.; Wang, S.; Xiao, J.; Bian, X.; Zhang, Y.; Scanlon, M. D.; Hu, X.; Tang, Y.; Liu, B.; Girault, H. H. A Nanoporous Molybdenum Carbide Nanowire as an Electrocatalyst for Hydrogen Evolution Reaction. *Energy Environ Sci* **2014**, *7* (1), 387–392. <https://doi.org/10.1039/c3ee42441c>.
- (22) Cao, X.; Medvedeva, J. E.; Nath, M. Copper Cobalt Selenide as a High-Efficiency Bifunctional Electrocatalyst for Overall Water Splitting: Combined Experimental and Theoretical Study. *ACS Appl Energy Mater* **2020**, *3* (3), 3092–3103. <https://doi.org/10.1021/acsaem.0c00262>.
- (23) Swesi, A. T.; Masud, J.; Liyanage, W. P. R.; Umapathi, S.; Bohannan, E.; Medvedeva, J.; Nath, M. Textured NiSe₂ Film: Bifunctional Electrocatalyst for Full Water Splitting at Remarkably Low Overpotential with High Energy Efficiency. *Sci Rep* **2017**, *7* (1). <https://doi.org/10.1038/s41598-017-02285-z>.
- (24) de Silva, U.; Masud, J.; Zhang, N.; Hong, Y.; Liyanage, W. P. R.; Asle Zaeem, M.; Nath, M. Nickel Telluride as a Bifunctional Electrocatalyst for Efficient Water Splitting in Alkaline Medium. *J Mater Chem A Mater* **2018**, *6* (17), 7608–7622. <https://doi.org/10.1039/c8ta01760c>.
- (25) De Silva, U.; See, J.; Liyanage, W. P. R.; Masud, J.; Wu, J.; Yang, W.; Chen, W. T.; Prendergast, D.; Nath, M. Understanding the Structural Evolution of a Nickel Chalcogenide Electrocatalyst Surface for Water Oxidation. *Energy and Fuels* **2021**, *35* (5), 4387–4403. <https://doi.org/10.1021/acs.energyfuels.0c04089>.

- (26) Rasmussen, F. A.; Thygesen, K. S. Computational 2D Materials Database: Electronic Structure of Transition-Metal Dichalcogenides and Oxides. *Journal of Physical Chemistry C* **2015**, *119* (23), 13169–13183. <https://doi.org/10.1021/acs.jpcc.5b02950>.
- (27) Liu, Y.; Vijayakumar, P.; Liu, Q.; Sakthivel, T.; Chen, F.; Dai, Z. *Shining Light on Anion-Mixed Nanocatalysts for Efficient Water Electrolysis: Fundamentals, Progress, and Perspectives*; Springer Singapore, 2022; Vol. 14. <https://doi.org/10.1007/s40820-021-00785-2>.
- (28) Peng, Q.; Dong, Y.; Li, Y. Synthesis of Uniform CoTe and NiTe Semiconductor Nanocluster Wires through a Novel Coreduction Method. *Inorg Chem* **2003**, *42* (7), 2174–2175. <https://doi.org/10.1021/ic0262031>.
- (29) Trotochaud, L.; Young, S. L.; Ranney, J. K.; Boettcher, S. W. Nickel-Iron Oxyhydroxide Oxygen-Evolution Electrocatalysts: The Role of Intentional and Incidental Iron Incorporation. *J Am Chem Soc* **2014**, *136* (18), 6744–6753. <https://doi.org/10.1021/ja502379c>.
- (30) Chen, S.; Mi, J. L.; Zhang, P.; Feng, Y. H.; Yong, Y. C.; Shi, W. D. Control Synthesis of Nickel Selenides and Their Multiwalled Carbon Nanotubes Composites as Electrocatalysts for Enhanced Water Oxidation. *Journal of Physical Chemistry C* **2018**, *122* (45), 26096–26104. <https://doi.org/10.1021/acs.jpcc.8b09259>.
- (31) Xing, Z.; Liu, Q.; Asiri, A. M.; Sun, X. Closely Interconnected Network of Molybdenum Phosphide Nanoparticles: A Highly Efficient Electrocatalyst for Generating Hydrogen from Water. *Advanced Materials* **2014**, *26* (32), 5702–5707. <https://doi.org/10.1002/adma.201401692>.
- (32) Xie, L.; Qu, F.; Liu, Z.; Ren, X.; Hao, S.; Ge, R.; Du, G.; Asiri, A. M.; Sun, X.; Chen, L. In Situ Formation of a 3D Core/Shell Structured Ni₃N@Ni-Bi Nanosheet Array: An Efficient Non-Noble-Metal Bifunctional Electrocatalyst toward Full Water Splitting under near-Neutral Conditions. *J Mater Chem A Mater* **2017**, *5* (17), 7806–7810. <https://doi.org/10.1039/c7ta02333b>.
- (33) Gao, M. R.; Cao, X.; Gao, Q.; Xu, Y. F.; Zheng, Y. R.; Jiang, J.; Yu, S. H. Nitrogen-Doped Graphene Supported CoSe₂ Nanobelt Composite Catalyst for Efficient Water Oxidation. *ACS Nano* **2014**, *8* (4), 3970–3978. <https://doi.org/10.1021/nn500880v>.
- (34) Wygant, B. R.; Poterek, A. H.; Burrow, J. N.; Mullins, C. B. Effect of Selenium Content on Nickel Sulfoselenide-Derived Nickel (Oxy)Hydroxide Electrocatalysts for Water Oxidation. *ACS Appl Mater Interfaces* **2020**, *12* (18), 20366–20375. <https://doi.org/10.1021/acsami.0c00425>.

- (35) Langmann, J.; Haas, C.; Wenger, E.; Schaniel, D.; Scherer, W.; Eickerling, G. Evidence for a Soft Phonon Mode Driven Peierls-Type Distortion in Sc₃CoC₄. *Phys Rev B* **2020**, *102* (9), 1–9. <https://doi.org/10.1103/PhysRevB.102.094109>.
- (36) Vargas-Hernández, R. A. Bayesian Optimization for Calibrating and Selecting Hybrid-Density Functional Models. *Journal of Physical Chemistry A* **2020**, *124* (20), 4053–4061. <https://doi.org/10.1021/acs.jpca.0c01375>.
- (37) Joubert, D. From Ultrasoft Pseudopotentials to the Projector Augmented-Wave Method. *Phys Rev B Condens Matter Mater Phys* **1999**, *59* (3), 1758–1775. <https://doi.org/10.1103/PhysRevB.59.1758>.
- (38) Blöchl, P. E. Projector Augmented-Wave Method. *Phys Rev B* **1994**, *50* (24), 17953–17979. <https://doi.org/10.1103/PhysRevB.50.17953>.
- (39) Perdew, J. P.; Burke, K.; Ernzerhof, M. Generalized Gradient Approximation Made Simple. *Phys Rev Lett* **1996**, *77* (18), 3865–3868. <https://doi.org/10.1103/PhysRevLett.77.3865>.
- (40) Tablero, C. Optical Properties of Sb(Se,Te)I and Photovoltaic Applications. *J Alloys Compd* **2016**, *678*, 18–22. <https://doi.org/10.1016/j.jallcom.2016.04.036>.
- (41) Pal, A.; Shirodkar, S. N.; Gohil, S.; Ghosh, S.; Waghmare, U. V.; Ayyub, P. Multiferroic Behavior in Elemental Selenium below 40 K: Effect of Electronic Topology. *Sci Rep* **2013**, *3*, 1–7. <https://doi.org/10.1038/srep02051>.
- (42) Yu, M.; Yang, S.; Wu, C.; Marom, N. Machine Learning the Hubbard U Parameter in DFT+U Using Bayesian Optimization. *NPJ Comput Mater* **2020**, *6* (1). <https://doi.org/10.1038/s41524-020-00446-9>.
- (43) Hu, K.; Wu, M.; Hinokuma, S.; Ohto, T.; Wakisaka, M.; Fujita, J. I.; Ito, Y. Boosting Electrochemical Water Splitting: Via Ternary NiMoCo Hybrid Nanowire Arrays. *J Mater Chem A Mater* **2019**, *7* (5), 2156–2164. <https://doi.org/10.1039/c8ta11250a>.
- (44) Allouche, A. Software News and Updates Gabedit — A Graphical User Interface for Computational Chemistry Softwares. *J Comput Chem* **2012**, *32*, 174–182. <https://doi.org/10.1002/jcc>.
- (45) Jiao, Y.; Zheng, Y.; Jaroniec, M.; Qiao, S. Z. Design of Electrocatalysts for Oxygen- and Hydrogen-Involving Energy Conversion Reactions. *Chem Soc Rev* **2015**, *44* (8), 2060–2086. <https://doi.org/10.1039/c4cs00470a>.

- (46) He, S.; Lin, H.; Sun, R.; Wang, Z. Growth of NiSe₂, NiTe₂ and Alloy NiSe₂-XTex Nanosheets with Tunable Shape Evolution and Chemical Composition. *2d Mater* **2020**, *7* (4), 0–6. <https://doi.org/10.1088/2053-1583/aba566>.
- (47) de las Heras, C.; Agullo-Rueda, F. Raman Spectroscopy of NiSe₂ and NiS_{2-x}Se_x (0 < X < 2) Thin Films. *J. Phys.: Condens. Matter* **2000**, *12* (1200), 5317–5324.
- (48) Zhou, H.; Wang, Y.; He, R.; Yu, F.; Sun, J.; Wang, F.; Lan, Y.; Ren, Z.; Chen, S. One-Step Synthesis of Self-Supported Porous NiSe₂/Ni Hybrid Foam: An Efficient 3D Electrode for Hydrogen Evolution Reaction. *Nano Energy* **2016**, *20*, 29–36. <https://doi.org/10.1016/j.nanoen.2015.12.008>.
- (49) Hulliger, F. Electrical Properties of Some Nickel-Group Chalcogenides. *Journal of Physics and Chemistry of Solids* **1965**, *26* (3), 639–645. [https://doi.org/10.1016/0022-3697\(65\)90140-X](https://doi.org/10.1016/0022-3697(65)90140-X).
- (50) Abdullahi, I. M.; Langenderfer, M.; Shenderova, O.; Nunn, N.; Torelli, M. D.; Johnson, C. E.; Mochalin, V. N. Explosive Fragmentation of Luminescent Diamond Particles. *Carbon N Y* **2020**, *164*, 442–450. <https://doi.org/10.1016/j.carbon.2020.03.057>.
- (51) Langford, J. I.; Wilson, J. C. Scherrer after Sixty Years: A Survey and Some New Results in the Determination of Crystallite Size. *J. Appl. Cryst.* **1978**, *11* (2), 102–113. <https://doi.org/10.1061/9780784479896.140>.
- (52) Xue, Z.; Li, X.; Liu, Q.; Cai, M.; Liu, K.; Liu, M.; Ke, Z.; Liu, X.; Li, G. Interfacial Electronic Structure Modulation of NiTe Nanoarrays with NiS Nanodots Facilitates Electrocatalytic Oxygen Evolution. *Advanced Materials* **2019**, *31* (21), 1–7. <https://doi.org/10.1002/adma.201900430>.
- (53) Peng, Q.; He, Q.; Hu, Y.; Isimjan, T. T.; Hou, R.; Yang, X. Interface Engineering of Porous Fe₂P-WO_{2.92} Catalyst with Oxygen Vacancies for Highly Active and Stable Large-Current Oxygen Evolution and Overall Water Splitting. *Journal of Energy Chemistry* **2022**, *65*, 574–582. <https://doi.org/10.1016/j.jechem.2021.06.037>.
- (54) Li, Y.; Chen, B.; Zhang, H.; Gao, J.; Sun, H.; Habibi-Yangjeh, A.; Wang, C. Synergistic Coupling of NiTe Nanoarrays with FeOOH Nanosheets for Highly Efficient Oxygen Evolution Reaction. *ChemElectroChem* **2021**, *8* (19), 3643–3650. <https://doi.org/10.1002/celec.202100703>.
- (55) Swesi, A. T.; Masud, J.; Nath, M. Nickel Selenide as a High-Efficiency Catalyst for Oxygen Evolution Reaction. *Energy Environ Sci* **2016**, *9* (5), 1771–1782. <https://doi.org/10.1039/c5ee02463c>.

- (56) Tang, C.; Cheng, N.; Pu, Z.; Xing, W.; Sun, X. NiSe Nanowire Film Supported on Nickel Foam: An Efficient and Stable 3D Bifunctional Electrode for Full Water Splitting. *Angewandte Chemie - International Edition* **2015**, *54* (32), 9351–9355. <https://doi.org/10.1002/anie.201503407>.
- (57) Liu, C.; Wang, K.; Zheng, X.; Liu, X.; Liang, Q.; Chen, Z. Rational Design of MoSe₂-NiSe@carbon Heteronanostructures for Efficient Electrocatalytic Hydrogen Evolution in Both Acidic and Alkaline Media. *Carbon N Y* **2018**, *139*, 1–9. <https://doi.org/10.1016/j.carbon.2018.06.034>.
- (58) Shit, S.; Chhetri, S.; Jang, W.; Murmu, N. C.; Koo, H.; Samanta, P.; Kuila, T. Cobalt Sulfide/Nickel Sulfide Heterostructure Directly Grown on Nickel Foam: An Efficient and Durable Electrocatalyst for Overall Water Splitting Application. *ACS Appl Mater Interfaces* **2018**, *10* (33), 27712–27722. <https://doi.org/10.1021/acsami.8b04223>.
- (59) Batchellor, A. S.; Boettcher, S. W. Pulse-Electrodeposited Ni-Fe (Oxy)Hydroxide Oxygen Evolution Electrocatalysts with High Geometric and Intrinsic Activities at Large Mass Loadings. *ACS Catal* **2015**, *5* (11), 6680–6689. <https://doi.org/10.1021/acscatal.5b01551>.
- (60) Chen, S.; Mi, J. L.; Zhang, P.; Feng, Y. H.; Yong, Y. C.; Shi, W. D. Control Synthesis of Nickel Selenides and Their Multiwalled Carbon Nanotubes Composites as Electrocatalysts for Enhanced Water Oxidation. *Journal of Physical Chemistry C* **2018**, *122* (45), 26096–26104. <https://doi.org/10.1021/acs.jpcc.8b09259>.
- (61) Freger, V. Diffusion Impedance and Equivalent Circuit of a Multilayer Film. *Electrochem commun* **2005**, *7* (9), 957–961. <https://doi.org/10.1016/j.elecom.2005.06.020>.
- (62) Zhang, X.; Ding, Y.; Wu, G.; Du, X. CoSe₂@NiSe₂ Nanoarray as Better and Efficient Electrocatalyst for Overall Water Splitting. *Int J Hydrogen Energy* **2020**, *45* (55), 30611–30621. <https://doi.org/10.1016/j.ijhydene.2020.08.096>.
- (63) Li, M.; Feng, L. NiSe₂-CoSe₂ with a Hybrid Nanorods and Nanoparticles Structure for Efficient Oxygen Evolution Reaction. *Jiegou Huaxue* **2022**, *41* (1), 2201019–2201024. <https://doi.org/10.14102/j.cnki.0254-5861.2021-0037>.
- (64) Gebreslase, G. A.; Martínez-Huerta, M. V.; Lázaro, M. J. Recent Progress on Bimetallic NiCo and CoFe Based Electrocatalysts for Alkaline Oxygen Evolution Reaction: A Review. *Journal of Energy Chemistry* **2022**, *67*, 101–137. <https://doi.org/10.1016/j.jechem.2021.10.009>.

- (65) Cao, X.; Hong, Y.; Zhang, N.; Chen, Q.; Masud, J.; Zaeem, M. A.; Nath, M. Phase Exploration and Identification of Multinary Transition-Metal Selenides as High-Efficiency Oxygen Evolution Electrocatalysts through Combinatorial Electrodeposition. *ACS Catal* **2018**, *8* (9), 8273–8289. <https://doi.org/10.1021/acscatal.8b01977>.
- (66) Louie, M. W.; Bell, A. T. An Investigation of Thin-Film Ni-Fe Oxide Catalysts for the Electrochemical Evolution of Oxygen. *J Am Chem Soc* **2013**, *135* (33), 12329–12337. <https://doi.org/10.1021/ja405351s>.
- (67) Ma, X.; Yang, J.; Xu, X.; Yang, H.; Peng, C. NiSe/Ni₃Se₂ on Nickel Foam as an Ultra-High-Rate HER Electrocatalyst: Common Anion Heterostructure with Built-in Electric Field and Efficient Interfacial Charge Transfer. *RSC Adv* **2021**, *11* (55), 34432–34439. <https://doi.org/10.1039/d1ra06183f>.
- (68) Suen, N. T.; Hung, S. F.; Quan, Q.; Zhang, N.; Xu, Y. J.; Chen, H. M. Electrocatalysis for the Oxygen Evolution Reaction: Recent Development and Future Perspectives. *Chem Soc Rev* **2017**, *46* (2), 337–365. <https://doi.org/10.1039/c6cs00328a>.
- (69) Shinagawa, T.; Garcia-Esparza, A. T.; Takanabe, K. Insight on Tafel Slopes from a Microkinetic Analysis of Aqueous Electrocatalysis for Energy Conversion. *Sci Rep* **2015**, *5* (August), 1–21. <https://doi.org/10.1038/srep13801>.
- (70) X-Ray and Magnetic Study of Nickel Selenides in the Range NiSe and NiSe₂. *Acta Chem Scand* **1956**, *10*, 1440–1454.
- (71) Norén, L.; Ting, V.; Withers, R. L.; van Tendeloo, G. An Electron and X-Ray Diffraction Investigation of Ni_{1+x}Te₂ and Ni_{1+x}Se₂ CdI₂/NiAs Type Solid Solution Phases. *J Solid State Chem* **2001**, *161* (2), 266–273. <https://doi.org/10.1006/jssc.2001.9309>.
- (72) Hong, W. T.; Risch, M.; Stoerzinger, K. A.; Grimaud, A.; Suntivich, J.; Shao-Horn, Y. Toward the Rational Design of Non-Precious Transition Metal Oxides for Oxygen Electrocatalysis. *Energy Environ Sci* **2015**, *8* (5), 1404–1427. <https://doi.org/10.1039/c4ee03869j>.
- (73) Craig, M. J.; Coulter, G.; Dolan, E.; Soriano-López, J.; Mates-Torres, E.; Schmitt, W.; García-Melchor, M. Universal Scaling Relations for the Rational Design of Molecular Water Oxidation Catalysts with Near-Zero Overpotential. *Nat Commun* **2019**, *10* (1), 1–9. <https://doi.org/10.1038/s41467-019-12994-w>.

- (74) Thomas, S.; Asle Zaeem, M. Superior Sensing Performance of Two-Dimensional Ruthenium Carbide (2D-RuC) in Detection of NO, NO₂ and NH₃ Gas Molecules. *Appl Surf Sci* **2021**, *563* (March), 150232. <https://doi.org/10.1016/j.apsusc.2021.150232>.

IV. CHROMIUM CARBONYL SELENIDE MOLECULAR CLUSTERS COMPLEX AS EFFICIENT ELECTROCATALYTIC CO₂ REDUCTION INTO C₂₊ PRODUCT(S)

Ibrahim Munkaila Abdullahi, and Mansahi Nath

Department of Chemistry, Missouri University of Science and Technology, Rolla, MO
65409

ABSTRACT

Electrochemical CO₂ reduction into multi-carbon products attracts considerable attention due to its ability to employ renewable electricity to generate value-added fuels and feedstocks. However, the CO₂ conversion efficiency to C₂₊ products still needs improvement, and better catalysts have still been explored. Developing simple, affordable, environmentally friendly catalysts with high selectivity and relatively low potential is highly desirable. We report a highly selective electrocatalytic reduction of carbon dioxide to ethanol on selenium-capped tri-chromium carbonyl cluster [Se₂Cr₃(CO)₁₀](Et₄N)₂ as a catalyst with a unique bonding structure in 0.3 M KHCO₃ at constant CO₂ purging rate of 20 standard cubic centimeters per minute (sccm) for 2hr. A highly selective C₂ (ethanol) was produced as the primary product, showing a 98 % liquid product yield and Faradaic efficiency (FE_{EtOH}) of 74.2% and a partial current density (j_{EtOH}) of 35.28 mA cm⁻² in an H-cell reactor, on the molecular chromium carbonyl clusters and further showed high durability for ~24 hours of the electrochemical CO₂RR. The work exemplifies the potential of using carbonyl clusters to optimize the available reaction intermediate binding sites for highly selective and efficient electrocatalytic CO₂ conversion into C₂₊ products.

Keywords: Molecular carbonyl clusters, C₂₊ products, Chromium selenide, electrocatalytic CO₂ conversion.

1. INTRODUCTION

The growing global consumption of fossil fuels has expedited the dwindling of these limited natural resources and increased greenhouse gas carbon dioxide (CO₂).¹ To sustainably meet the current energy demands, the high accumulation of CO₂ generated must be converted into value-added chemicals such as CO, formic acid (HCOOH), alcohols (ROH), etc.² Electrochemical CO₂ reduction is considered among many other methods, one of the most promising and potentially environmentally friendly methods since the supply of sustainable electric energy drives the process.³ However, an efficient catalyst is required to accelerate the reaction rate and increase the selectivity of this electrochemical conversion by mediating multi-step electron and proton transfers and energy pathways to CO₂ at low overpotential. Despite the steadily expanding number of investigations necessitating remarkable progress, present catalysts operate at high overpotentials to attain reasonable reaction rates.^{4,5} Various carbon-containing products can be produced during the electrochemical CO₂ reduction reaction (CO₂RR), which form at comparable reduction potentials and compete with H₂ production. The selectivity toward the desired products could be higher.

Chromium is an early high-valance transition metal with high reactivity relative to late-transition metals and can exhibit different structures and orthogonal reactivity.⁶ Chromium being slightly oxophilic, tends to adsorb CO₂ on the surface. This can be

valuable in catalyst design and identifying other electrocatalysts. Despite the unique properties of chromium favoring catalytic properties, very limited literature on Cr-based coordination complexes is available for CO₂ electrocatalytic reduction,^{6,7} There is a very limited number of reports that use chromium molecular complexes, or clusters that are electrochemically or electrocatalytically active for CO₂ conversion, most of which produces CO.⁸ Molecular clusters are a relatively unexplored class of materials in electrocatalytic CO₂ conversion. They consist of tens of atoms and have been regarded as a link that interconnects molecular and solid-state chemistry.⁹ Metal chalcogenide carbonyls^{10,11} clusters are an excellent example of compounds with metal-metal bonds ring stabilized by groups such as arenes¹², phosphines^{13,14} or bridged chalcogen (such as μ_3 -S,^{11,15} μ_3 -Se,¹⁶ and μ_3 -Te,¹³), forming an extended metal cluster.⁹ Most studies on these clusters are focused on structural determinations to probe their structural bonding integrity. Few studies have shown them to exhibit unique magnetic and low energy gap properties.¹⁷ Chromium carbonyl clusters have recently been reported to be active for oxygen evolution reaction (OER)¹⁸, but they have not been explored for CO₂ electrochemical CO₂ reduction. The structural features of these clusters, the effect of the core of the Cr-Se bond, and the presence of Cr-Cr bonds could play a role in the CO₂ reduction application.

Herein, we report a chromium selenium-capped carbonyl cluster electrocatalyst with quantitative current efficiencies for reducing CO₂ to ethanol and acetic acid. Even at low catalytic overpotentials, CO and H₂ gaseous products are generated. Here, turnover is defined as the passing of charge corresponding to two electron equivalents per catalyst molecule in solution. This excellent activity and selectivity are attributed to the unique properties of the molecular clusters, which contain coordinated carbonyls and two bridging

selenium atoms, enhancing the optimal binding strength provided by Cr active sites favorable for adsorbing CO₂ enough to initiate the formation of intermediates leading to C₂₊ products.

2. EXPERIMENTAL PROCEDURE

2.1. MATERIALS

Conductive carbon paper (CCP) suitable for battery, fuel cell, and supercapacitor research purchased from MSE supplies, Tucson, AZ 85711 USA. While chromium hexacarbonyl, Nafion (5 wt.%), and selenium (IV) oxide (SeO₂), isopropanol (iPr-OH), cyclohexane (C₆H₁₂) were purchased from Sigma–Aldrich Chemical Reagent Co., Ltd. St. Louis MO, sodium hydroxide (NaOH), methanol (MeOH), dichloromethane (CH₂Cl₂) and tetraethyl bromide [Et₄N]Br were purchased from Fisher Scientific Pittsburgh, USA. All the reagents were used as received. The deionized (D.I.) water purified through a Millipore system was used in all experiments. The CCP was washed with iPr-OH and D.I water several times to ensure the surface was cleaned before use.

2.2. METHODS

2.2.1. Preparation of Cr-Se Clusters (decacarbonyltrichromium diselenide ditetraethylamine). The synthesis of this compound has been reported in a previous report.¹⁹ All reactions were carried out under the N₂ atmosphere. A mixed solution of MeOH (30 mL) and cyclohexane (7.5 mL) was added to a mixture containing [Cr(CO)₆] (0.8 g, 3.64 mmol), SeO₂ (0.21 g, 1.89 mmol) and NaOH (3.0 g, 82.5 mmol) taken in 100 mL three neck round flask. This mixture was heated to reflux at 70 °C for 12 h yielding a

filtered dark-red solution, and the filtrate was concentrated. A MeOH solution of [Et₄N]Br (3.0 g, 14.3 mmol) was added to the concentrated filtrate dropwise, whereby the red Cr₃Se₂(CO)₁₀[(Et₄N)₂] was precipitated as a solid product in a metathesis reaction. The solid product was washed several times with MeOH and CH₂Cl₂ and dried as Cr-Se red complex. Elemental Analysis found the following composition for Cr-Se red: C, 36.20; H, 5.61; N, 3.28%. Calculated: C, 36.55; H, 4.72; N, 3.28%. Compound Cr-Se red is soluble in acetonitrile and acetone but insoluble in other organic solvents.

2.2.2. Characterization Methods. Using a monochromatic Al X-ray source, XPS measurements were performed using a KRATOS AXIS 165 X-ray photoelectron spectrometer (Kratos Analytical Limited, Manchester, United Kingdom). The C 1s signal at 284.5 eV was used as a reference to correct all the XPS binding energies.²⁰ All XPS spectra were collected from the pristine catalyst surface without sputtering. The Raman spectra of the catalyst were recorded with LabRam ARAMIS (HORIBA Jobin-Yvon Raman spectrometer equipped with a CCD detector) in the Raman shift range between 50 cm⁻¹ to 1800 cm⁻¹, 1200 lines mm⁻¹ grating, HeNe laser 632.8 nm excitation with a nominal output power of 100mW, 0.95 cm⁻¹/pixel spectral dispersion, 10% of laser power, 10x objective, 0.25 numerical aperture, 100 μm slit, 200 μm hole, 30 seconds exposure time, 10x accumulations for each sample acquisition.²¹ Fourier Transform Infrared (FTIR) spectra were recorded using a Thermo Nicolet NEXUS 470 FT -IR Spectrometer between 400 -4000 cm⁻¹ with 1 cm⁻¹ resolution. Pellets were prepared by pressing a mixture of 2 mg catalyst and 200 mg KBr under a 10 -15 tons load.^{22,23} Thermal gravimetric analysis (TGA) was performed with a heating rate of 10 °C min⁻¹ on a Netzsch STA 449C instrument.²⁴

2.2.3. Electrocatalytic Studies. Linear sweep voltammetry (LSV) was performed in an N₂-saturated and CO₂-saturated 0.3 M NaHCO₃ electrolyte with a scan rate of 10 mV⁻¹. An electrochemical H-cell was used in this study consisting of separate cathode and anode compartments with a volume of 30 mL each, separated by an anion exchange Nafion (115) membrane. This study used a carbon rod, Cr-Se clusters, and Ag/AgCl/KCl(sat.) as a counter, working, and reference electrodes, respectively. The Ag/AgCl reference electrode was calibrated using open circuit potential (OCP, -0.198 V) measured with a Pt wire in an H₂-saturated H₂SO₄ solution. The potential measured in Ag/AgCl was converted to the reversible hydrogen electrode (RHE) using equation (1):

$$E_{(\text{RHE})} = E_{(\text{Ag}/\text{AgCl})} + E^0_{(\text{Ag}/\text{AgCl})} + 0.059 \cdot \text{pH} \quad (1)$$

where $E_{(\text{RHE})}$ is the converted potential vs. RHE, $E_{(\text{Ag}/\text{AgCl})}$ is the experimentally obtained potential, $E^0_{(\text{Ag}/\text{AgCl})}$ is the standard potential of Ag/AgCl (0.198 V), and the pH of CO₂ saturated 0.3 M NaHCO₃ was measured to be 6.8. 0.3 M NaHCO₃ in the cathode compartment was saturated with CO₂ through continuous flow at a controlled rate of 10 sccm using a mass flow controller during the experiments.

2.2.4. Tafel Plots. The Tafel slope parameter obtained from the Tafel equation is employed in explaining the kinetics of the electrocatalytic reaction and activity; the equation is expressed as follows:

$$\eta = \alpha + (2.3RT/\alpha nF) * \log(j) \quad (2)$$

where η is the overpotential, α is the transfer coefficient, n is the number of electrons involved in the reaction, F is the Faraday constant, j is the current density, and $2.3RT/nF$ gives the slope. The Tafel equation is acquired from the kinetically controlled region of the CO₂RR and correlates current density j with the overpotential η , where $2.3RT/nF$ gives the

Tafel slope. The Tafel slopes were calculated using LSV plots from a slow scan speed (10 mVs^{-1}) in a non-stirred solution.

2.2.5. NMR Analysis. Liquid products formed during CO_2 electrochemical reduction were analyzed with $^1\text{H-NMR}$. Aliquots were collected at regular intervals, and 2 μL DMSO (internal standard) and 200 μL D_2O solvent were added to 0.5 ml electrolyte. The NMR experiments were performed on a Bruker 400 MHz spectrometer, using a pre-saturation sequence to suppress the water signal. NMR spectra of the reaction mixture were measured before starting any electrochemical reaction to ensure no impurity in the solution, which could lead to false results.

3. RESULTS

The chromium selenide carbonyl ($[\text{Se}_2\text{Cr}_3(\text{CO})_{10}](\text{Et}_4\text{N})_2$) cluster was prepared under basic conditions in methanol. The counter ion was introduced by cation metathesis with $[\text{Et}_4\text{N}]\text{Br}$ to produce the Cr-Se cluster, as shown in Figure 1a. This molecular chromium cluster complex is structurally attractive; it exhibits trigonal bipyramidal coordination with bridging μ_3 -Se atoms capped above and below Cr_3 -ring bonded. In this bonding situation, the Se atom donates four electrons to the Cr_3 ring, making it a $48e^-$ species, supporting the three-chromium having three Cr–Cr bonds. The Cr-Se cluster was soluble in acetonitrile and acetone but insoluble in other organic solvents. The detailed X-Ray single crystal structure analysis of the Cr-Se cluster has been reported in a previous report.¹⁹ Raman and FTIR analysis was used to further characterize the samples by revealing the vibrational modes in the clusters. The Raman spectra show the presence of a

Raman peak at 117 cm^{-1} corresponding to Cr_3 , while peaks around 250 and 342 cm^{-1} attributed to E_{1g} and A_{1g} of both clusters. The 847 cm^{-1} corresponds to Cr-C in Cr-Se red cluster Figure 1b. The FTIR spectra (Figure 1c) show broad peaks around 3461 cm^{-1} indicating the presence of moisture H_2O molecules, assigned to the stretching vibration of O-H groups present in both Cr-Se red.

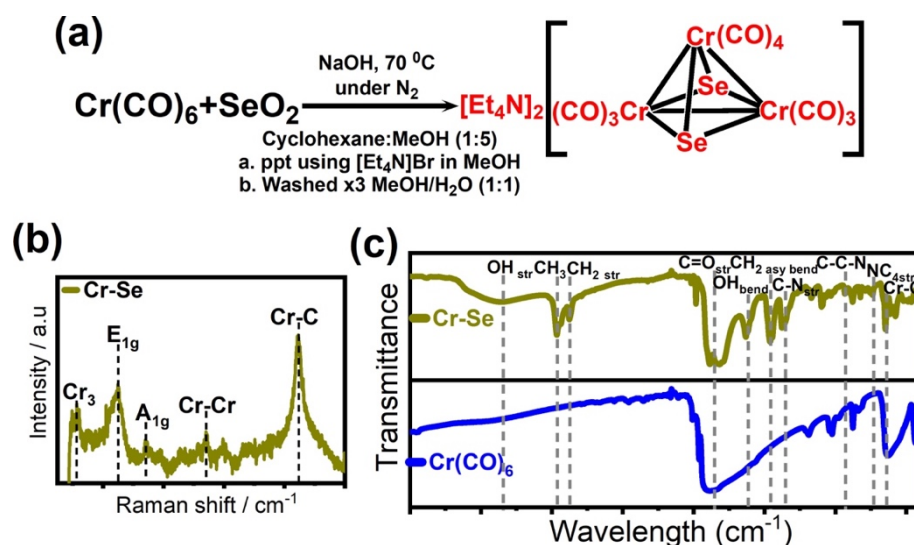


Figure 1. Synthesis and spectroscopic characterizations of Cr-Se electrocatalyst. (a) reaction scheme describing synthesis; (b) Raman spectra, excited with 632.8 nm HeNe laser radiation; (c) FTIR spectra.

The peak at 1623 cm^{-1} can be attributed to the O-H bending of moisture H_2O molecules. It also shows a doublet peak at around 1800 cm^{-1} , indicating the presence of the CO group.²⁵ Furthermore, the stretching and bending vibrational absorption peaks that appeared at 1461 cm^{-1} were assigned to CH_3 while 2963 cm^{-1} , and 2877 cm^{-1} , corresponding to CH_3 and CH_2 modes, respectively, confirming the presence of Et_4N counter ions in the clusters. The rest of the absorption peaks under 800 cm^{-1} are responsible for the bending and stretching vibration modes, including Cr-Se at 668 cm^{-1} ; other less

prominent peaks most likely correspond to O–M–O and M–O–O–H. The CHN elemental analysis of the Cr-Se cluster reveals the total atomic percentage of C, H, and N in the samples as C, 36.20; H, 5.61; N, 3.28%. Calculated: C, 36.55; H, 4.72; N, 3.28%.

The morphology of the Cr-Se cluster was studied by SEM, which suggests needle-like clustered particles (Figure 2a) intertwined and intercalated together, with sizes in the range of 100 nm by 1 μm and displaying considerable surface roughness. The chemical compositions of these molecular clusters are examined by energy-dispersive X-ray spectroscopy (EDS) in (Figure 2b), the EDS mapping analysis indicating a uniform distribution of Cr, Se, C, O, and N. The N is mainly coming from the counter $[\text{Et}_3\text{N}]_4^+$. The thermogravimetric analysis (TGA) of the Cr-Se clusters describes the stepwise decomposition of each sample (Figure 2c). The TGA carried out under argon gas showed

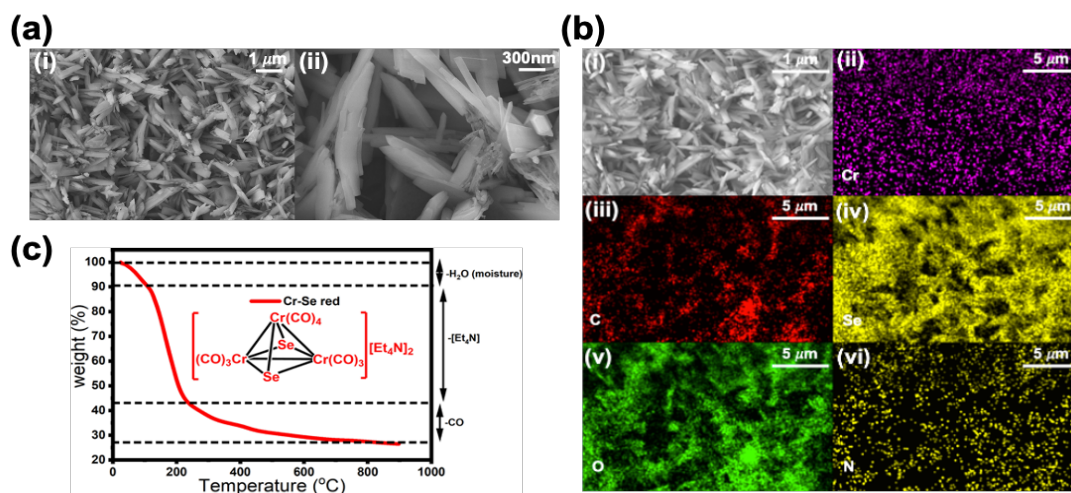


Figure 2. Characterizations of Cr-Se electrocatalyst. (a) SEM images: (i) Low resolution; (ii) High resolution; (b) EDX: (i) SEM map; and EDS mapping profiles of (ii) Cr; (iii) C; (iv) Se; (v) O; (vi) N; (c) TGA.

a gradual decrease in weight in three steps; at the first step between 0 $^{\circ}\text{C}$ and 180 $^{\circ}\text{C}$, 13.3 % weight loss was observed, due to the loss of lattice water.²⁶ The second weight loss from

180–240 °C corresponds to 38.7% (calcd. 30.5%), which can be attributed to the decomposition of tetraethyl amine.²⁷

Finally, in the range of 240–900 °C, a weight loss of 21.52% (calcd. 22.9%) is attributable to the loss of seven coordinated CO molecules. The percentage weight loss in the complexes agrees with the calculated values. X-ray photoelectron spectroscopy (XPS) was carried out to characterize the chemical states, composition, and local coordination of the cluster surface (Figure 3).

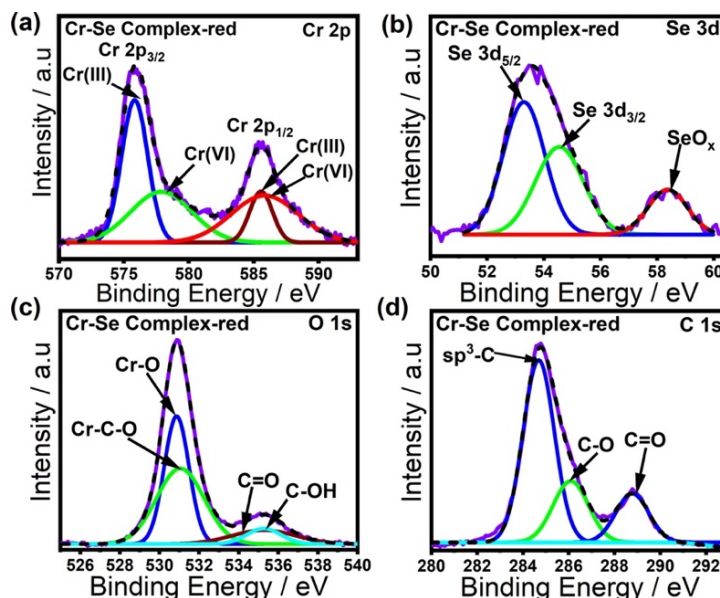


Figure 3. The high-resolution XPS spectra of the Cr-Se red complex showing its elemental states. (a) Cr 2p peak; (b) Se 3d peak; (c) C 1s peak; (d) surface O 1s peak.

High-resolution XPS spectra for the Cr-Se cluster were measured to determine the valence states of the Cr species, by the deconvolution of the Cr 2p spectrum. The peaks at 576.0 eV and 585.9 eV were assigned to Cr(III) $2p_{3/2}$ and $2p_{1/2}$, respectively, whereas the other two peaks at 578.4 eV and 586.7 eV were attributed to Cr(VI) $2p_{3/2}$ and $2p_{1/2}$, respectively.²⁸ This indicates Cr(III) and Cr(VI) states co-exist in the cluster, with Cr(III)

as the main species. The Se 3d spectrum shows peaks at 53.3 and 54.6 eV corresponding to Se 3d_{5/2} and Se 3d_{3/2}, respectively, which confirm the presence of Se²⁻. The peak at ~58.6 eV indicates the existence of partial SeO_x species, which could be from selenide surface oxidation.^{20,29,30} However, no metal oxides were detected on the catalyst surface from XPS analysis. The C 1s spectra were deconvoluted into three symmetric Lorentzian-Gaussian peaks, corresponding to the Sp³-C bond at 284.8 eV, the C-O bond of hydroxyl, carboxyl, or carbonyl functional groups at 286.1 eV, and the C=O bond of carbonyl groups at 288.8 eV. The electrochemical CO₂RR measurements, product detection, and quantification were carried out following the standard protocol described in previous reports^{31,32}. At the same time, the electrochemical performance set-up was calibrated and verified by measuring the CO₂RR activity of the standard polycrystalline Ag electrode³³. Entirely different CO₂ reduction products were identified with our Cr-Se cluster electrode under conditions of 0.3 M NaHCO₃ at room RT, showing the novelty of the Cr-Se cluster catalyst. Linear scan voltammetry (LSV) was carried out in CO₂ or N₂-saturated 0.3 M NaHCO₃ at a 10 mVs⁻¹ scan rate. Hydrogen evolution reaction (HER) is observed following applying a negative potential in an N₂-saturated electrolyte. The catalyst attained a reduction current density of 108 mA cm⁻² at - 1.0 V vs. RHE during CO₂RR, which is higher than the current density exhibited by most other molecular-based catalysts^{34,35}. But, in CO₂-saturated electrolytes, both CO₂RR and HER co-occur. The LSV of the Cr-Se cluster collected shows slightly increased current density in CO₂-saturated electrolytes relative to N₂-saturated electrolytes at the same potentials (Figure 4a), indicating the activity of the Cr-Se cluster electrode toward CO₂RR. The CO₂RR products were identified at the applied potentials - 0.3, - 0.6, - 0.9, - 1.2 V vs. RHE from the chronoamperometric study under steady CO₂ flow at 20

sccm in 0.3 M NaHCO₃ to study the effect of applied potential on product composition and selectivity. The products were collected from the cathodic chamber after 2 h. ¹H NMR identified and quantified liquid products, while gaseous products were detected and quantified using GC-TCD. The products were observed to vary in composition depending

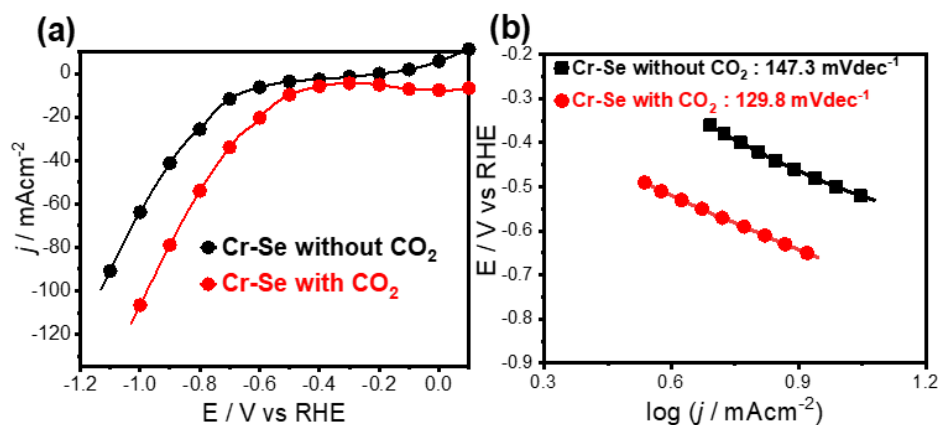


Figure 4. Electrocatalytic performance of Cr-Se in the presence and absence of CO₂. (a) LSVs recorded in 0.3 M NaHCO₃ at a scan rate of 10 mV s⁻¹; (b) Tafel plots recorded in 0.3 M NaHCO₃.

on the applied potential and showed selectivity towards specific products to a particular potential. The Faradaic efficiency for the formation of each product was estimated from absolute product quantity obtained through NMR (Figure 5a) and GC-TCD measurements and by employing the standard reported procedures.^{31,36} Interestingly, the products generated at all applied potentials (-0.3 to -1.2 V vs. RHE) were selectively C₂ compounds, mainly ethanol and acetic acid. At -0.3 V vs. RHE, ethanol yield (up to 88 % relative liquid product) was very high at appreciable current density. However, minimal acetone (12 %) was detected as a C₃ product (Figure 5b). The Cr-Se cluster showed high faradaic efficiency for forming acetic acid at a potential of -1.2 V vs. RHE with a 91 % relative liquid product. Such high selectivity towards forming acetic acid with moderate

energy expense is unusual in CO₂RR for Cr-based catalysts. To our knowledge, this was the best selectivity towards acetic acid for any Cr-based catalyst. This observation suggests that the Cr-Se catalyst, which requires a moderate potential for CO₂RR and exhibits a higher FE for high-value products such as acetic acid than any other Cr-based catalyst at a similar applied potential. Previous reports have shown that productivity is enhanced by increased selectivity for C₂₊ products, including EtOH, and the surface area using nanoparticle structures or rough surfaces.^{32,37} Cr-Se has an attractive, intertwined needle-like morphology with a high surface area. The production of C₁ and C₃ chemicals, including CO and HCOOH, (CH₃)₂CO was significantly suppressed in all the potential windows, while C₁ chemicals were the major products of CO₂RR at less negative applied potentials. Also, the HER decreased to an FE of < 14%, leading to a more selective CO₂RR at a more negative potential higher than -0.9 V vs. RHE. At a potential of -0.9 V vs. RHE, Cr-Se clusters gave the best selectivity towards ethanol, with a 98 % relative liquid product. This high ethanol productivity and selectivity at -0.3 and -0.9 V vs. RHE could be attributed to the effect of the inherent properties of the efficient Cr-Se cluster catalysts with sites that can efficiently adsorb CO and CO₂ long enough for the reaction to be initiated towards a C₂ product(s) pathway and the systematic advantage of flow-cell reactors. It must be noted here that the product composition at -0.6 V vs. RHE was a mixture of acetic acid and ethanol. Also, Ethanol and acetic acid are industrially valuable chemicals and the selectivity towards their generation at lower and moderate applied potential highlights the novelty of this catalyst. Specifically, this catalyst, just by changing potential, can bring about, with high selectivity, the direct synthesis of ethanol and acetic acid from CO₂, replacing the conventional multi-step industrial process, which typically begins with the

synthesis of syngas and ends with the generation of methanol followed by its carbonylation,³⁸ or from the fermentation of carbohydrates followed by fractional distillation.^{39,40} Furthermore, only two gaseous products (H_2 and CO) were detected at all

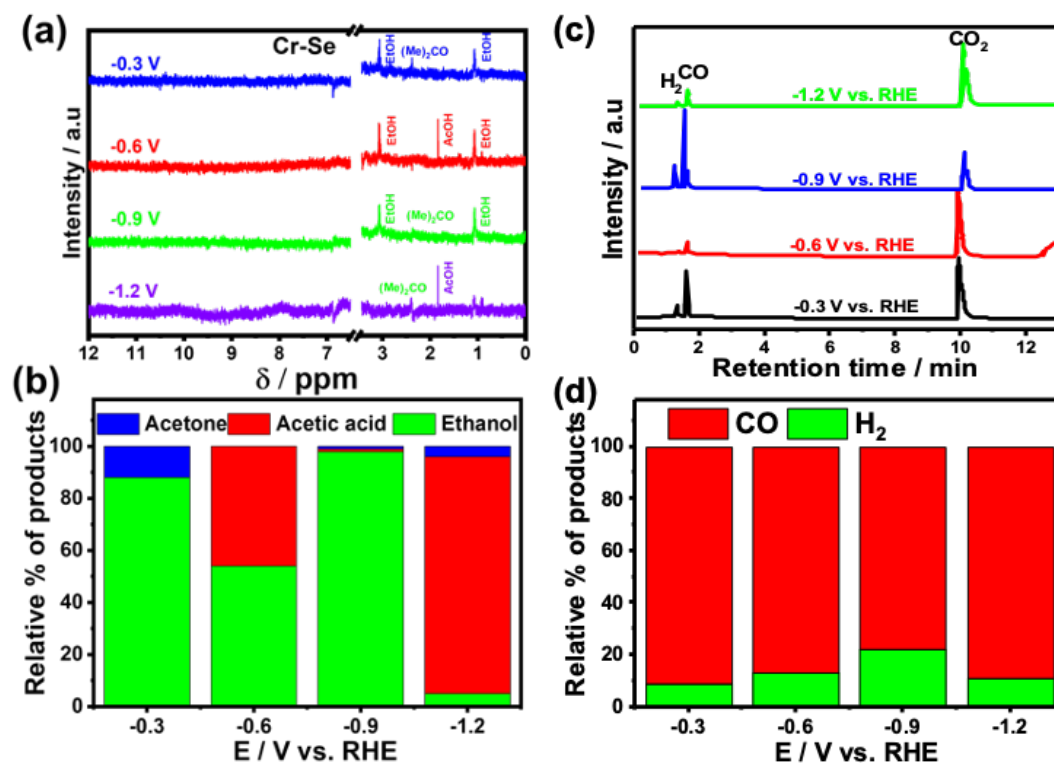


Figure 5. CO_2 Reduction products distribution. (a) NMR spectra identifying reduction products in reaction aliquots collected at different potentials; (b) GC-TCD spectra identifying reduction products in reaction gaseous phase collected at different potentials (c) Bar chart showing the relative % concentrations of liquid products quantified from NMR at various applied potentials. (d) Bar chart showing the relative % concentrations of gaseous products quantified from GC-TCD at various applied potentials.

potentials. Furthermore, only two gaseous products (H_2 and CO) were detected at all potentials. CO was selectively dominant at all potentials for the gaseous products detected, with a percentage product ratio of 78-91 %, summarized in Table 1. Reports have shown that most chromium-based catalysts employed for electrochemical CO_2RR predominantly

yield CO products.^{8,41,42} The functional stability of the Cr-Se cluster in CO₂RR for long-term hydrocarbon generation is essential in evaluating the catalyst's performance and practicability. The stability of Cr-Se clusters during the CO₂RR electrochemical reaction was investigated using a chronoamperometry study at various applied potentials for 24 h period (as shown in Figure 6). There was no significant degradation in current density. Faradaic Efficiency was observed at all the potentials (-0.3 , -0.6 , -0.9 , and -1.2 V vs. RHE), indicating the high functional stability of the catalyst for CO₂RR.

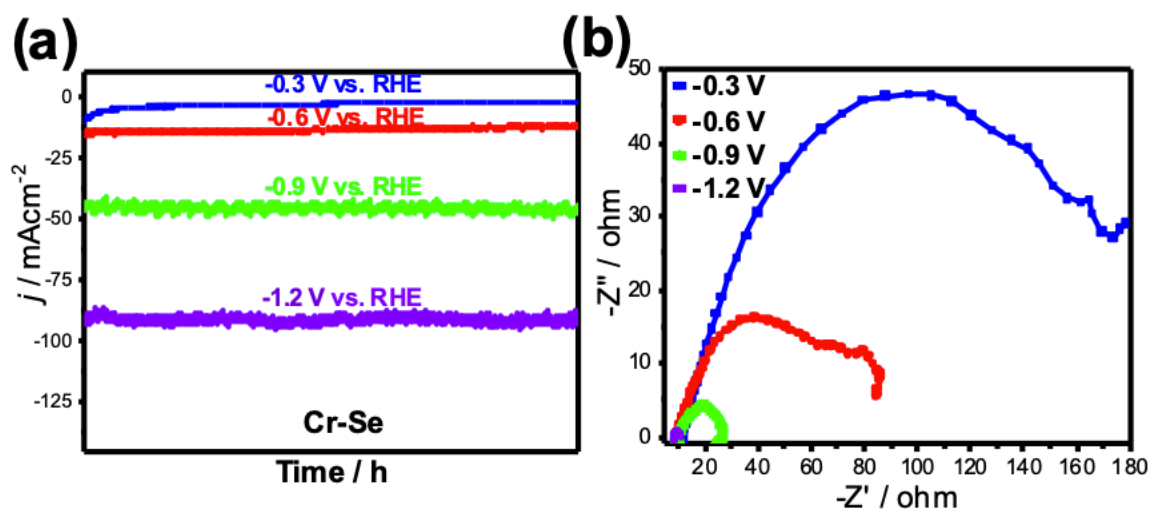


Figure 6. (a) Current density plot for 12 h of chronoamperometry; (b) EIS of Cr-Se electrocatalyst study at the different applied potentials.

Moreover, there is no change in product composition after long chronoamperometry, as revealed by NMR analysis of the aliquots collected at 3 h intervals, confirming a high degree of operational stability and minimal poisoning of the catalyst surface, which is common in noble metal-based electrocatalysts in CO₂RR. Factors such as catalysis agglomeration⁴³ active-phase composition transformation,^{44,45} and elemental dissolution^{46,47} considerably decrease CO₂RR activity during high-rate reactions. Very few

studies have shown that the catalyst is stable at commercially relevant current densities. To our knowledge, such extended functional stability for molecular chromium-based complexes in CO₂RR with continuous product formation for 24 h is yet to be reported.

Table 1. Liquid and gaseous product ratios in electrocatalytic CO₂RR.

E(V) vs. RHE	EtOH (%)	AcOH (%)	Acetone (%)	H₂ (%)	CO (%)
-0.3	88	0	12	9	91
-0.6	54	46	0	13	87
-0.9	98	1	1	22	78
-1.2	5	91	4	11	89

Hence, Cr-Se clusters have displayed excellent activity and stability relative to many CO₂RR catalysts. To produce ethanol and acetic acid products in a practical yield, highly active and stable during operation. The integrity of the catalyst during CO₂RR at different potentials to understand the possible adsorbed intermediate and to confirm structural integrity was studied using operando-XPS spectra (Figure 7). The operando-XPS spectra of O 1s and C 1s at various potentials (-0.3 V to -1.2 V vs. RHE) were used to observe any shift or evolution of XPS bands. The O 1s spectra at ~ 530.2 eV correspond to Cr-O, which is more prominent in Cr-Se before the reaction. Cr-C-O was assigned to the peak at 532.0 eV, in Cr-Se @ -1.2 V vs. RHE, but appears as shoulder in all other samples, indicating more CO adsorption on the catalyst surface for samples with applied potentials. Furthermore, the shoulder at 532.1 and 534.1 eV is assigned to C=O and C-O, respectively.

While the C-OH peak at 535.7 eV was present in all samples after CO₂RR but absent before the reaction, indicating the formation of organic products and intermediates. This could be

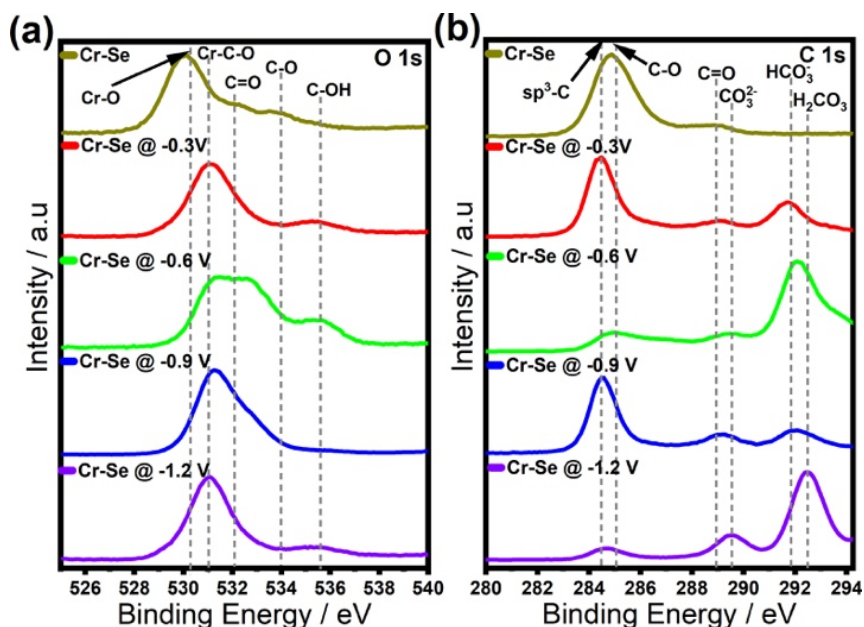


Figure 7. Operando XPS spectra of Cr-Se complex red after CO₂RR at different potentials from -0.3 to -1.2 V vs. RHE. (a) surface O 1s peak; (b) C 1s peak.

attributed to different CO adsorption configurations, including bridge-bonded and top-bonded CO or CO adsorbed on the surface and defect sites. The C 1s spectra band at 284.8 eV to assigned to the Sp³-C bond, while the C-O bond of hydroxyl, carboxyl, or carbonyl functional groups came up as a shoulder at 285.2 eV, and the peak at 288.9 eV was assigned to the C=O bond of carbonyl groups. The spectra in Cr-Se @ -0.6 V vs. RHE and Cr-Se @ -1.2 V vs. RHE show intense peaks at 291.9 and 292.6 eV corresponding to the adsorbed intermediate bicarbonate, and carbonic acid, indicating the possible pathway for the formation of acetic acid. A small amount of CO₃²⁻ was detected in all samples after the reaction, suggesting that they are essential as possible intermediate at all potentials while

maintaining the C=O peak at around 288.9 eV. The High-resolution XPS spectra for the Cr-Se cluster after CO₂RR was carried out at -0.9 V vs. RHE (Figure 8) shows the Cr 2p spectrum with peaks at 576.0 eV and 585.9 eV corresponding to Cr(III) 2p_{3/2} and 2p_{1/2}, respectively, similar to the peaks before reaction, indicating no significant changes around the chromium site of the catalyst after the reaction. Whereas the other two peaks at 578.4 eV and 586.7 eV were attributed to Cr(VI) 2p_{3/2} and 2p_{1/2}, indicating the presence of higher oxidation states of chromium,²⁸ while still co-existing as Cr(III) and Cr(VI) the cluster.

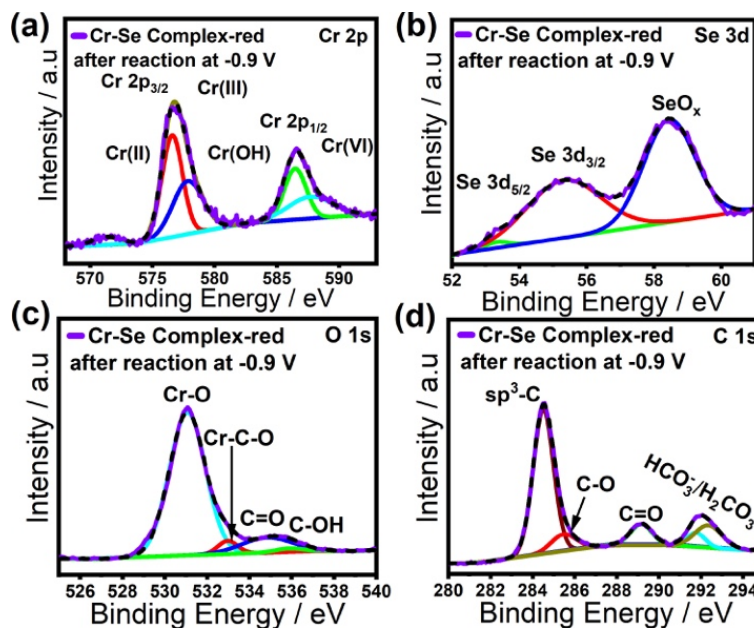


Figure 8. The high-resolution XPS spectra of Cr-Se complex red after CO₂RR at -0.9 V vs. RHE. (a) Cr 2p peak; (b) Se 3d peak; (c) C 1s peak; (d) surface O 1s peak.

The Se 3d spectrum shows peaks at 53.3 and 54.6 eV corresponding to Se 3d_{5/2} and Se 3d_{3/2}, respectively, which confirm the presence of Se²⁻. The peak at ~58.6 eV indicates a more pronounced 1 SeO_x species after the reaction due to selenide surface oxidation.^{20,29,30} The C 1s spectra at 284.8 eV correspond to the Sp³-C bond, while the C-

O bond of hydroxyl, carboxyl, or carbonyl functional groups was assigned to the peak at 286.1 eV, and the C=O bond of carbonyl groups at 288.8 eV. New peaks at around 289.9 and 293 eV correspond to the adsorbed HCO_3^- and H_2CO_3 on the catalyst surface, suggesting a pathway that goes through HCO_3^- species. The SEM image at -0.9 V vs. RHE was used for unlocking any changes in morphology after prolonged activity, and the SEM images of the Cr-Se clusters we compared before and after activity (Figure 9). It was observed that the needle-like structure was retained even after prolonged activity on the catalyst surface, and the intertwining of the needle-like structure became more deagglomerated and more diminutive, most likely due to applied potential. Also, some spheric particles were observed after CO_2RR at -0.9 V vs. RHE; this could be the bicarbonate detected in the XPS analysis. This indicates that although the size of the Cr-Se cluster decreased, the integrity of the catalyst is retained, as characterized by XPS. The

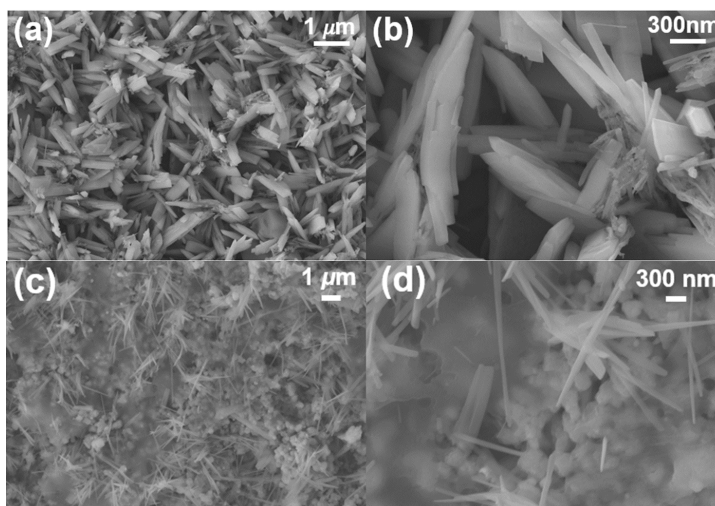


Figure 9. SEM images of Cr-Se cluster before CO_2RR . (a) Low resolution; (b) High resolution; SEM images of Cr-Se cluster after CO_2RR at -0.9 V vs. RHE: (c) Low resolution; (d) High resolution.

catalyst surface integrity after CO₂RR activity @ -0.9 V vs. RHE was further analyzed using SEM-EDS for elemental composition, as observed in Figure 10, uniform distribution of the Cr, Cr, C, O, and N was observed throughout the sample surface area, indicating that the catalyst integrity has not been affected. No significant leaching is taking place during the CO₂RR process. This signifies a potentially highly active and durable catalyst for electrochemical CO₂RR.

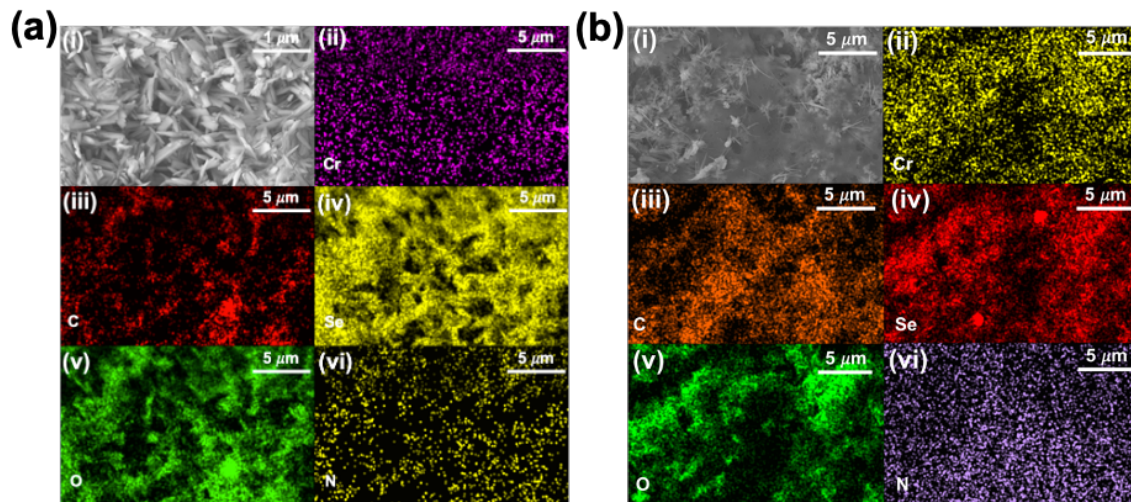


Figure 10. SEM-EDS of Cr-Se cluster. (a) Before CO₂RR; (b) After CO₂RR at -0.9 V vs. RHE.

4. CONCLUSIONS

In conclusion, we have successfully demonstrated the use of molecular chromium selenide carbonyl [Se₂Cr₃(CO)₁₀](Et₄N)₂ cluster as a highly efficient CO₂RR catalyst with high selectivity towards ethanol and acetic acid at very low and moderate potentials,

respectively. A high yield of 98 % ethanol was produced selectively as a liquid product at a low potential of -0.9 V vs. RHE, as a 91 % acetic acid at -1.2 V vs. RHE, indicating the high potential of this catalyst in C₂ products production. Furthermore, CO and H₂ are produced as two main gaseous products, with CO predominantly dominant yielding 79-91% relative gaseous ratio to H₂. This Cr-Se cluster consists of a catalytically active Se-Cr-Se coordinated sphere with an increased tendency to adsorb CO₂ on its surface. It also showed high durability over 24 h of CO₂RR with no degradation in current. This indicates the vast potential of high-valence chromium carbonyl clusters as highly active electrocatalysts towards CO₂RR. This observed activity could be attributed to the inherent surface sites on the Cr-Se cluster to adsorb CO₂ moderately to bring about valuable product formation. Also, the covalency of the multiple Cr-Se bonds and the enhanced conductivity of Cr-Cr bonds could be contributing factors too. Also, any loss in terminal CO under applied potential opens another site to facilitate the adsorption of more CO₂ on the Cr atoms, thereby boosting the electrocatalytic activity. This could open a new direction to explore the electrocatalytic CO₂RR of the carbonyl cluster of high-valence metal, whose electronic structure is perturbed by other surrounding ligands.

REFERENCES

1. A. Goepfert, M. Czaun, R. B. May, G. K. S. Prakash, G. A. Olah and S. R. Narayanan, *J Am Chem Soc*, 2011, **133**, 20164–20167.
2. C. Graves, S. D. Ebbesen, M. Mogensen and K. S. Lackner, *Renewable and Sustainable Energy Reviews*, 2011, **15**, 1–23.
3. D. T. Whipple and P. J. A. Kenis, *Journal of Physical Chemistry Letters*, 2010, **1**, 3451–3458.

4. C. Costentin, M. Robert and J. M. Savéant, *Chem Soc Rev*, 2013, **42**, 2423–2436.
5. M. Gattrell, N. Gupta and A. Co, *Journal of Electroanalytical Chemistry*, 2006, **594**, 1–19.
6. S. Kong, M. Lu, S. Yan and Z. Zou, *Dalton Transactions*, 2022, **51**, 16890-16897
7. D. Jin, J. Kang, S. Prabhakaran, Y. Lee, M. H. Kim, D. H. Kim and C. Lee, *J Mater Chem A Mater*, 2022, **10**, 13803–13813.
8. A. G. Reid, S. L. Hooe, J. J. Moreno, D. A. Dickie and C. W. Machan, *Inorg Chem*, 2022, **61**, 16963–16970.
9. G. Schmid, *Clusters and Colloids. From Theory to Applications*, VCH Verlagsgesellschaft Weinheim, 1994.
10. D. J. Darensbourg, D. J. Zalewski, K. M. Sanchez and T. Delord, *Inorg Chem*, 1988, **27**, 821–829.
11. M. Hoefler, K.-F. Tebbe, H. Veit and N. E. Weiler, *J. Am. Chem. Soc.*, 1983, **3**, 6338–6339.
12. W. Wang, X. Wang, Z. Zhang, N. Yuan and X. Wang, *Chemical Communications*, 2015, **51**, 8410–8413.
13. B. Hessen, / T Siegrist, T. Palstra, S. M. Tanzler and M. L. Steigerwald, *Inorg. Chem*, 1993, **32**, 5165.
14. K. Tsuge, H. Imoto and T. Saito, *Bull Chem Soc Jpn*, 1996, **69**, 627–636.
15. D. J. Darensbourg and D. J. Zalewskl, *Organometallics*, 1984, **3**, 1598–1600.
16. M. H. Hsu, C. Y. Miu, Y. C. Lin and M. Shieh, *J Organomet Chem*, 2006, **691**, 966–974.
17. H. H. Yeh, M. C. Hsu, Y. H. Li, Y. N. Hsu, F. Y. Shr and M. Shieh, *J Organomet Chem*, 2021, **937**, 121717.
18. I. M. Abdullahi and M. Nath, *Catalysts*, 2023, **13**, 721.
19. M. Shieh, L. F. Ho, L. F. Jang, C. H. Ueng, S. M. Peng and Y. H. Liu, *Chemical Communications*, 2001, **3**, 1014–1015.

20. I. M. Abdullahi, J. Masud, Ioannou Polydoros-Chrisovalantis, E. Ferentinos, P. Kyritsis and M. Nath, *Molecules*, 2021, **26**, 945.
21. I. M. Abdullahi, M. Langenderfer, O. Shenderova, N. Nunn, M. D. Torelli, C. E. Johnson and V. N. Mochalin, *Carbon N Y*, 2020, **164**, 442–450.
22. T. A. Saleh, S. A. Al-Hammadi, I. M. Abdullahi and M. Mustaqeem, *J Mol Liq*, 2018, **272**, 715–721.
23. J. Beltz, A. Pfaff, I. M. Abdullahi, A. Cristea, V. N. Mochalin and N. Ercal, *Diam Relat Mater*, , DOI:10.1016/j.diamond.2019.107590.
24. B. Liu, W. Han, X. Li, L. Li, H. Tang, C. Lu, Y. Li and X. Li, *Appl Catal B*, , DOI:10.1016/j.apcatb.2019.117939.
25. L. Shufler, H. W. Sternberg and R. A. Friedel, *J. Am. Chem. Soc.*, 1956, **78**, 2687–2688.
26. P. Bügel, I. Krummenacher, F. Weigend and A. Eichhöfer, *Dalton Transactions*, 2022, **51**, 14568–14580.
27. H. Gao, J. Li and K. Lian, *RSC Adv*, 2014, **4**, 21332–21339.
28. S. Khatun and P. Roy, *Chemical Communications*, 2022, **58**, 1104–1107.
29. A. T. Swesi, J. Masud and M. Nath, *Energy Environ Sci*, 2016, **9**, 1771–1782.
30. J. Masud, P. C. Ioannou, N. Levesanos, P. Kyritsis and M. Nath, *ChemSusChem*, 2016, **9**, 3128–3132.
31. E. L. Clark, J. Resasco, A. Landers, J. Lin, L. T. Chung, A. Walton, C. Hahn, T. F. Jaramillo and A. T. Bell, *ACS Catal*, 2018, **8**, 6560–6570.
32. Y. Zhou, F. Che, M. Liu, C. Zou, Z. Liang, P. De Luna, H. Yuan, J. Li, Z. Wang, H. Xie, H. Li, P. Chen, E. Bladt, R. Quintero-Bermudez, T. K. Sham, S. Bals, J. Hofkens, D. Sinton, G. Chen and E. H. Sargent, *Nat Chem*, 2018, **10**, 974–980.
33. T. Kottakkat, K. Klingan, S. Jiang, Z. P. Jovanov, V. H. Davies, G. A. M. El-Nagar, H. Dau and C. Roth, *ACS Appl Mater Interfaces*, 2019, **11**, 14734–14744.
34. N. Elgrishi, M. B. Chambers, X. Wang and M. Fontecave, *Chem Soc Rev*, 2017, **46**, 761–796.
35. S. Zhang, Q. Fan, R. Xia and T. J. Meyer, *Acc Chem Res*, 2020, **53**, 255–264.

36. K. P. Kuhl, E. R. Cave, D. N. Abram and T. F. Jaramillo, *Energy Environ Sci*, 2012, **5**, 7050–7059.
37. F. S. Roberts, K. P. Kuhl and A. Nilsson, *Angewandte Chemie - International Edition*, 2015, **54**, 5179–5182.
38. J. H. Jones, *Platin Met Rev*, 2000, **44**, 94–105.
39. A. S. Mathew, J. Wang, J. Luo and S. T. Yau, *Sci Rep*, 2015, **5**, 1–6.
40. M. V. Semkiv, K. V. Dmytruk, C. A. Abbas and A. A. Sibirny, *BMC Biotechnol*, 2014, **14**, 1–9.
41. S. L. Hooe, J. M. Dressel, D. A. Dickie and C. W. Machan, *ACS Catal*, 2020, **10**, 1146–1151.
42. J. J. Moreno, S. L. Hooe, and C. W. Machan, *Inorg Chem*, 2021, **60**, 3635–3650.
43. J. Wu, S. G. Sun and X. D. Zhou, *Nano Energy*, 2016, **27**, 225–229.
44. K. Ye, Z. Zhou, J. Shao, L. Lin, D. Gao, N. Ta, R. Si, G. Wang and X. Bao, *Angewandte Chemie - International Edition*, 2020, **59**, 4814–4821.
45. Y. Shi, Y. Ji, J. Long, Y. Liang, Y. Liu, Y. Yu, J. Xiao and B. Zhang, *Nat Commun*, 2020, **11**, 3415
46. J. H. Zhou, K. Yuan, L. Zhou, Y. Guo, M. Y. Luo, X. Y. Guo, Q. Y. Meng and Y. W. Zhang, *Angewandte Chemie - International Edition*, 2019, **58**, 14197–14201.
47. H. Cheng, S. Liu, J. Zhang, T. Zhou, N. Zhang, X. S. Zheng, W. Chu, Z. Hu, C. Wu and Y. Xie, *Nano Lett*, 2020, **20**, 6097–6103.

SECTION

3. CONCLUSIONS AND RECOMMENDATIONS

3.1. CONCLUSIONS

The metal, ligand (anion), particle size, morphology, and bonding coordination that change the electron density distribution in materials are some of the key properties that are critical for most water oxidation and CO₂ reduction reactions. A fundamental study was developed to allow for catalytic activity prediction in catalyst series for both water oxidation and CO₂ reduction reactions. Metal complexes serving as an isolated core of the active metal center were created with a structural motif of similar bonding coordination as the metal–chalcogenide bulk solid materials were synthesized to understand the effect of anion coordination on the catalytic stability performance and to accurately identify the active surface composition of these transition metal chalcogenide-based electrocatalysts in water oxidation reaction. While molecular clusters, with are more extended structures than molecular complexes but less than bulk solids, were also tested for water oxidation. These are exciting materials because they have multimetallic coordination, forming catalytically active nanostructures. They are considered a link between molecular and solid-state chemistry. Furthermore, tuning the electronic structure of nickel-chalcogenide using mixed anionic chalcogenide (with Se and Te bonded to the same Ni atom) and the effect of changing crystal-type coordination were screened to understand its impact on the activity of changing chalcogen anion and coordination environment in water oxidation reaction. On the other hand, the effect of chalcogen anion (Se) and carbon monoxide as ligands in

CO₂ conversion using chromium chalcogenide clusters containing Cr–Cr bonds stabilized by CO and μ_3 -Se atoms in the form of Cr-Se bonds was evaluated, and C₂ value-added products were favorably generated, with very high selectivity for ethanol and acetic acid at -0.9 and -1.2 V vs. RHE respectively.

3.2. RECOMMENDATIONS

In-depth density functional theory (DFT) calculations on the mechanistic study of molecular carbonyl cluster in CO₂RR. Our findings have shown that C₂ products can be produced from selenium-based chromium carbonyl clusters, contrary to most chromium complexes with organic ligands that produce CO as the main product. DFT will supplement our experimental results. Other transition metal molecular carbonyl clusters will be interesting to study.

Our findings have shown that molecular complexes based on bis(diselenodiisopropylimidophosphinanto) and decacarbonyltrichromium diselenide ditetraethylamine) molecular cluster with more extended structures has the potential to be used in identifying the next start-of-the-art OER catalyst. More systems need to be systematically studied. The synthesis of complexes from multi-metal, mixed chalcogen chelating ligands can be explored in more nanostructured bulk solids systems to construct a more complete volcano plot for catalytic performance prediction.

BIBLIOGRAPHY

1. S.H. et. al. N. Abram, J.-P. Gattuso, A. Prakash, L. Cheng, M.P. Chidichimo, S. Crate, H. Enomoto, M. Garschagen, N. Gruber, Framing and Context of the Report: Special Report on the Ocean and Cryosphere in a Changing Climate, in: IPCC, 2022: pp. 73–130. <https://doi.org/10.1017/9781009157964.003>.
2. M. Jouny, W. Luc, F. Jiao, General Techno-Economic Analysis of CO₂ Electrolysis Systems, *Industrial and Engineering Chemistry Research*. 57 (2018) 2165–2177. <https://doi.org/10.1021/acs.iecr.7b03514>.
3. P. Guionneau, M. Marchivie, G. Bravic, J.F. Létard, D. Chasseau, Co(II) molecular complexes as a reference for the spin crossover in Fe(II) analogues, *J Mater Chem*. 12 (2002) 2546–2551. <https://doi.org/10.1039/b202610d>.
4. G. Cepriá, J.R. Castillo, Electrocatalytic behaviour of several cobalt complexes: Determination of hydrazine at neutral pH, *J Appl Electrochem*. 28 (1998) 65–70. <https://doi.org/10.1023/A:1003249802216>.
5. R.N. Bose, B. Fonkeng, G. Barr-David, R.P. Farrell, R.J. Judd, P.A. Lay, D.F. Sangster, Redox Potentials of Chromium(V)/(IV),-(V)/(III), and -(IV)/(III) Complexes with 2-Ethyl-2-hydroxybutanoato(2-/1-) Ligands, *J Am Chem Soc*. 118 (1996) 7139–7144.
6. A. Panneerselvam, C.Q. Nguyen, J. Waters, M.A. Malik, P. O'Brien, J. Raftery, M. Helliwell, Ligand influence on the formation of P/Se semiconductor materials from metal-organic complexes, *Journal of the Chemical Society. Dalton Transactions*. (2008) 4499–4506. <https://doi.org/10.1039/B802012D>.
7. S. Mehrabani, R. Bikas, Z. Zand, Y. Mousazade, S.I. Allakhverdiev, M.M. Najafpour, Water splitting by a pentanuclear iron complex, *Int J Hydrogen Energy*. 45 (2020) 17434–17443. <https://doi.org/10.1016/j.ijhydene.2020.04.249>.
8. M.M. Najafpour, S.I. Allakhverdiev, Manganese compounds as water oxidizing catalysts for hydrogen production via water splitting: From manganese complexes to nano-sized manganese oxides, *Int J Hydrogen Energy*. 37 (2012) 8753–8764. <https://doi.org/10.1016/j.ijhydene.2012.02.075>.
9. A.M. Geer, C. Musgrave, C. Webber, R.J. Nielsen, B.A. McKeown, C. Liu, P.P.M. Schleker, P. Jakes, X. Jia, D.A. Dickie, J. Granwehr, S. Zhang, C.W. Machan, W.A. Goddard, T.B. Gunnoe, Electrocatalytic Water Oxidation by a Trinuclear Copper(II) Complex, *ACS Catal*. 11 (2021) 7223–7240. <https://doi.org/10.1021/acscatal.1c01395>.

10. M. Bera, K. Keshari, A. Bhardwaj, G. Gupta, B. Mondal, S. Paria, Electrocatalytic Water Oxidation Activity of Molecular Copper Complexes: Effect of Redox-Active Ligands, *Inorg Chem.* 61 (2022) 3152–3165. <https://doi.org/10.1021/acs.inorgchem.1c03537>.
11. M. Zhang, M.T. Zhang, C. Hou, Z.F. Ke, T.B. Lu, Homogeneous electrocatalytic water oxidation at neutral pH by a robust macrocyclic nickel(II) complex, *Angewandte Chemie - International Edition.* 53 (2014) 13042–13048. <https://doi.org/10.1002/anie.201406983>.
12. A.G. Reid, S.L. Hooe, J.J. Moreno, D.A. Dickie, C.W. Machan, Homogeneous Electrocatalytic Reduction of CO₂ by a CrN₃O Complex: Electronic Coupling with a Redox-Active Terpyridine Fragment Favors Selectivity for CO, *Inorg Chem.* 61 (2022) 16963–16970. <https://doi.org/10.1021/acs.inorgchem.2c02013>.
13. M. Loipersberger, M. Loipersberger, D.Z. Zee, D.Z. Zee, J.A. Panetier, J.A. Panetier, C.J. Chang, C.J. Chang, C.J. Chang, J.R. Long, J.R. Long, J.R. Long, M. Head-Gordon, M. Head-Gordon, Computational Study of an Iron(II) Polypyridine Electrocatalyst for CO₂ Reduction: Key Roles for Intramolecular Interactions in CO₂ Binding and Proton Transfer, *Inorg Chem.* 59 (2020) 8146–8160. <https://doi.org/10.1021/acs.inorgchem.0c00454>.
14. I. Azcarate, C. Costentin, M. Robert, J.M. Savéant, Through-Space Charge Interaction Substituent Effects in Molecular Catalysis Leading to the Design of the Most Efficient Catalyst of CO₂-to-CO Electrochemical Conversion, *J Am Chem Soc.* 138 (2016) 16639–16644. <https://doi.org/10.1021/jacs.6b07014>.
15. N.W. Kinzel, C. Werlé, W. Leitner, Transition Metal Complexes as Catalysts for the Electroconversion of CO₂: An Organometallic Perspective, *Angewandte Chemie - International Edition.* 60 (2021) 11628–11686. <https://doi.org/10.1002/anie.202006988>.
16. T. Liu, Q. Liu, A.M. Asiri, Y. Luo, X. Sun, An amorphous CoSe film behaves as an active and stable full water-splitting electrocatalyst under strongly alkaline conditions, *Chemical Communications.* 51 (2015) 16683–16686. <https://doi.org/10.1039/c5cc06892d>.
17. L. Nisar, M. Sadaqat, A. Hassan, N.U.A. Babar, A. Shah, M. Najam-Ul-Haq, M.N. Ashiq, M.F. Ehsan, K.S. Joya, Ultrathin CoTe nanoflakes electrode demonstrating low overpotential for overall water splitting, *Fuel.* 280 (2020) 118666. <https://doi.org/10.1016/j.fuel.2020.118666>.

18. C. Yang, Y. Lu, W. Duan, Z. Kong, Z. Huang, T. Yang, Y. Zou, R. Chen, S. Wang, Recent Progress and Prospective of Nickel Selenide-Based Electrocatalysts for Water Splitting, *Energy and Fuels*. 35 (2021) 14283–14303. <https://doi.org/10.1021/acs.energyfuels.1c01854>.
19. U. De Silva, J. Masud, N. Zhang, Y. Hong, W.P.R. Liyanage, M. Asle Zaeem, M. Nath, Nickel telluride as a bifunctional electrocatalyst for efficient water splitting in alkaline medium, *J Mater Chem A Mater*. 6 (2018) 7608–7622. <https://doi.org/10.1039/c8ta01760c>.
20. J. Wang, W. Cui, Q. Liu, Z. Xing, A.M. Asiri, X. Sun, Recent Progress in Cobalt-Based Heterogeneous Catalysts for Electrochemical Water Splitting, *Advanced Materials*. 28 (2016) 215–230. <https://doi.org/10.1002/adma.201502696>.
21. T. Fang, L.Z. Fu, L.L. Zhou, S.Z. Zhan, S. Chen, Electrochemical-driven water reduction catalyzed by a water soluble cobalt(III) complex with Schiff base ligand, *Electrochim Acta*. 178 (2015) 368–373. <https://doi.org/10.1016/j.electacta.2015.07.180>.
22. H.T. Shi, X.X. Li, F.H. Wu, W. Bin Yu, Electrocatalytic oxygen evolution with a cobalt complex, *Dalton Transactions*. 46 (2017) 16321–16326. <https://doi.org/10.1039/c7dt03653a>.
23. A.Y. Konokhova, M.Y. Afonin, T.S. Sukhikh, S.N. Konchenko, New Chalcogenide Cobalt Complexes with Diimine Ligands: Synthesis and Crystal Structure, *Journal of Structural Chemistry*. 60 (2019) 1463–1467. <https://doi.org/10.1134/S0022476619090105>.
24. L.M. Gilby, B. Piggott, The synthesis and X-ray structure of cobalt(II) complexes of iminobis(phosphinechalcogenides), $[Co\{N(XPR_2)_2-X,X'\}_2](X=S \text{ or } Se; R=Ph \text{ or } iPr)$, *Polyhedron*. 18 (1999) 1077–1082.
25. A. Schmidpeter, R. Bohm, H. Groeger, Imidodiphosphinatometal Chelates, Neutral Complexes with carbon-Free Chelate Rings, *Angewandte Chemie International Edition*. 3 (1964) 1964.
26. P. Ph, P.N.P.S. Ph, S.N. Sepph, H. Se, L.E.I. Leicestershire, Preparation and Characterisation of $[Pt\{N(SePPh)_2-Se,Se'\}_2(PR)_2]Cl$ (R = alkyl or aryl); Crystal Structure of $0.3CH_2Cl_2$, *Journal*. (1995) 2489–2495.
27. D. Cupertino, D.J. Birdsall, A.M.Z. Slawin, J. Derek Woollins b, The preparation and coordination chemistry of $iPr_2P(E)NHP(E')iPr_2$ (E, E'=Se; E=Se, E'=S; E=S, E'=O; E,E'=O), *Inorganica Chim Acta*. 290 (1999) 1–7.

28. T. Chivers, D.J. Eisler, J.S. Ritch, Synthesis and structures of $M[N(\text{TePPri}_2)_2\text{-Te}_n\text{Te}']_n$ ($n = 2, M = \text{Zn, Cd, Hg}$; $n = 3, M = \text{Sb, Bi}$): the first ditelluroimidodiphosphinato p- and d-block metal complexes, *Dalton Transactions*. (2005) 2675–2677.
29. A.J. Gaunt, B.L. Scott, M.P. Neu, A molecular actinide-tellurium bond and comparison of bonding in $[M \text{ III}\{N(\text{TePiPr}_2)_2\}_3]$ ($M = \text{U, La}$), *Angewandte Chemie - International Edition*. 45 (2006) 1638–1641. <https://doi.org/10.1002/anie.200503372>.
30. J. Masud, P.C. Ioannou, N. Levesanos, P. Kyritsis, M. Nath, A Molecular Ni-complex Containing Tetrahedral Nickel Selenide Core as Highly Efficient Electrocatalyst for Water Oxidation, *ChemSusChem*. 9 (2016) 3128–3132. <https://doi.org/10.1002/cssc.201601054>.
31. S. Sottini, G. Poneti, S. Ciattini, N. Levesanos, E. Ferentinos, J. Krzystek, L. Sorace, P. Kyritsis, Magnetic Anisotropy of Tetrahedral CoII Single-Ion Magnets: Solid-State Effects, *Inorg Chem*. 55 (2016) 9537–9548. <https://doi.org/10.1021/acs.inorgchem.6b00508>.
32. N. Levesanos, W.P.R. Liyanage, E. Ferentinos, G. Raptopoulos, P. Paraskevopoulou, Y. Sanakis, A. Choudhury, P. Stavropoulos, M. Nath, P. Kyritsis, Investigating the Structural, Spectroscopic, and Electrochemical Properties of $[\text{Fe}\{(\text{EPiPr}_2)_2\text{N}\}_2]$ ($E = \text{S, Se}$) and the Formation of Iron Selenides by Chemical Vapor Deposition, *Eur J Inorg Chem*. 2016 (2016) 5332–5339. <https://doi.org/10.1002/ejic.201600833>.
33. E. Ferentinos, C.P. Raptopoulou, V. Psycharis, A. Terzis, J. Krzystek, P. Kyritsis, Magnetostructural correlations in $S = 1$ trans- $[\text{Ni}\{(\text{OPPh}_2)(\text{EPh}_2)\text{N}\}_2(\text{dmsO})_2]$, $E = \text{S, Se}$, and related complexes, *Polyhedron*. 151 (2018) 177–184. <https://doi.org/10.1016/j.poly.2018.05.032>.
34. M. Afzaal, D.J. Crouch, P. O'Brien, J. Raftery, P.J. Skabara, A.J.P. White, D.J. Williams, The synthesis, X-ray structures and CVD studies of some group 11 complexes of iminobis(diisopropylphosphine selenides) and their use in the deposition of I/III/VI photovoltaic materials, *J Mater Chem*. 14 (2004) 233–237. <https://doi.org/10.1039/b311743j>.
35. S.S. Garje, D.J. Eisler, J.S. Ritch, M. Afzaal, P. O'Brien, T. Chivers, A new route to antimony telluride nanoplates from a single-source precursor, *J Am Chem Soc*. 128 (2006) 3120–3121. <https://doi.org/10.1021/ja0582408>.

36. S.S. Garje, M.C. Copsey, M. Afzaal, P. O'Brien, T. Chivers, Aerosol-assisted chemical vapour deposition of indium telluride thin films from $(\text{In}(\mu\text{-Te})[\text{N}(\text{iPr}2\text{PTe})2])_3$, *J Mater Chem.* 3 (2006) 4542–4547. <https://doi.org/10.1039/b608700k>.
37. S.S. Garje, J.S. Ritch, D.J. Eisler, M. Afzaal, P. O'Brien, T. Chivers, Chemical vapour deposition of II-VI semiconductor thin films using $\text{M}[(\text{TePiPr}2)\text{N}]_2$ ($\text{M} = \text{Cd}, \text{Hg}$) as single-source precursors, *J Mater Chem.* 16 (2006) 966–969. <https://doi.org/10.1039/b515362j>.
38. G. Schmid, *Clusters and Colloids. From Theory to Applications*, VCH Verlagsgesellschaft Weinheim, 1994.
39. F. Cecconi, C.A. Ghilardi, S. Midollini, A. Orlandini, One electron reduction of a cobalt-sulfur cluster. Synthesis and molecular structure of $[\text{Co}_6(\mu_3\text{-S})_8(\text{PET}_3)_6] \cdot \text{nthf}$, *Inorganica Chim Acta.* 76 (1983) 183–184. [https://doi.org/10.1016/S0020-1693\(00\)81499-1](https://doi.org/10.1016/S0020-1693(00)81499-1).
40. M. Bacci, A “Quasi-atomic” picture of the electronic structure of metal clusters, *Physics Letters.* 99A (1983) 230–232. [https://doi.org/10.1016/0375-9601\(83\)90913-1](https://doi.org/10.1016/0375-9601(83)90913-1).
41. J.F. Corrigan, S. Balter, D. Fenske, Synthesis and structural characterisation of new copper-tellurium clusters: $\text{TeBun}(\text{SiMe}_3)$ as a source of RTe^- - and Te_2^- - ligands, *Journal of the Chemical Society - Dalton Transactions.* (1996) 729–738. <https://doi.org/10.1039/DT9960000729>.
42. K. Tsuge, H. Imoto, T. Saito, Syntheses, Structures, and Molecular-Orbital Calculations of Chromium Chevrel-Type Cluster Complexes $[\text{Cr}_6\text{E}_8(\text{PR}_3)_6]$ ($\text{E} = \text{S}, \text{PR}_3 = \text{PEt}_3, \text{PMe}_3$; $\text{E} = \text{Se}, \text{PR}_3 = \text{PEt}_3, \text{PMe}_3, \text{PMe}_2\text{Ph}$), *Bull Chem Soc Jpn.* 69 (1996) 627–636. <https://doi.org/10.1246/bcsj.69.627>.
43. B. Hessen, T. Siegrist, T. Palstra, S.M. Tanzler, M.L. Steigerwald, $\text{Cr}_6\text{Te}_8(\text{PET}_3)_6$ and a Molecule-Based Synthesis of Cr_3Te_4 , *Inorg Chem.* 32 (1993) 5165–5169. <https://doi.org/10.1021/ic00075a037>.
44. S. Kamiguchi, T. Saito, W. Mori, Magnetic properties of the octahedral chromium chalcogenide cluster complexes $[\text{Cr}_6\text{Se}_8(\text{PET}_3)_6]$, $[\text{Cr}_6\text{Se}_8(\text{H})(\text{PET}_3)_6]$, and $[\text{Cr}_6\text{S}_8(\text{H})(\text{PET}_3)_6]$, *Bull Chem Soc Jpn.* 73 (2000) 2487–2491. <https://doi.org/10.1246/bcsj.73.2487>.
45. M. Shieh, C.H. Ho, W.S. Sheu, H.W. Chen, Selective insertion of oxygen and selenium into an electron-precise paramagnetic selenium-manganese carbonyl cluster $[\text{Se}_6\text{Mn}_6(\text{CO})_{18}]^{4-}$, *J Am Chem Soc.* 132 (2010) 4032–4033. <https://doi.org/10.1021/ja9091566>.

46. C. Schenk, A. Schnepf, $\{\text{Ge}_9\text{R}_3\text{Cr}(\text{CO})_5\}$ - and $\{\text{Ge}_9\text{R}_3\text{Cr}(\text{CO})_3\}$ -: A metalloid cluster (Ge_9R_3 -) as a flexible ligand in coordination chemistry [R = Si(SiMe₃)₃], *Chemical Communications*. 09 (2009) 3208–3210. <https://doi.org/10.1039/b901870k>.
47. D.J. Darensbourg, D.J. Zaleski, K.M. Sanchez, T. Delord, Cluster Synthesis via Aggregation: Synthesis and Solution and Solid-State Characterization of Sulfur-Capped Group 6 Metal Carbonyl Clusters, *Inorg Chem.* 27 (1988) 821–829. <https://doi.org/10.1021/ic00278a016>.
48. W. Wang, X. Wang, Z. Zhang, N. Yuan, X. Wang, The long-sought seventeen-electron radical $[(\text{C}_6\text{Me}_6)\text{Cr}(\text{CO})_3]^+$: Isolation, crystal structure and substitution reaction, *Chemical Communications*. 51 (2015) 8410–8413. <https://doi.org/10.1039/c5cc01941a>.
49. M. Shieh, L.F. Ho, L.F. Jang, C.H. Ueng, S.M. Peng, Y.H. Liu, First selenium-capped carbonyltrichromium complex $[\text{Se}_2\text{Cr}_3(\text{CO})_{10}]_2^-$: A novel Cr₃ ring cluster, *Chemical Communications*. 3 (2001) 1014–1015. <https://doi.org/10.1039/b101283p>.
50. M. Shieh, R.L. Chung, C.H. Yu, M.H. Hsu, C.H. Ho, S.M. Peng, Y.H. Liu, The unusual paramagnetic mixed-metal carbonyl chalcogenide clusters: $[\text{E}_2\text{Cr}_2\text{Fe}(\text{CO})_{10}]_2^-$ (E = Te, Se), *Inorg Chem.* 42 (2003) 5477–5479. <https://doi.org/10.1021/ic034081m>.
51. M. Shieh, C.N. Lin, C.Y. Miu, M.H. Hsu, Y.W. Pan, L.F. Ho, Chromium-manganese selenide carbonyl complexes: Paramagnetic clusters and relevance to C = O activation of acetone, *Inorg Chem.* 49 (2010) 8056–8066. <https://doi.org/10.1021/ic101118y>.
52. P. Bügel, I. Krummenacher, F. Weigend, A. Eichhöfer, Experimental and theoretical evidence for low-lying excited states in $[\text{Cr}_6\text{E}_8(\text{PEt}_3)_6]$ (E = S, Se, Te) cluster molecules, *Dalton Transactions*. 51 (2022) 14568–14580. <https://doi.org/10.1039/d2dt01690g>.
53. J.E. McGrady, Periodic trends in metal–metal bonding in cubane clusters, $(\text{C}_5\text{H}_5)_4\text{M}_4\text{E}_4$ [M=Cr,Mo, E=O,S], *Dalton Transactions*. (1999) 1393–1399.
54. H.H. Yeh, M.C. Hsu, Y.H. Li, Y.N. Hsu, F.Y. Shr, M. Shieh, Ternary antimony–chalcogen iron carbonyl complexes and their derivatives: Syntheses, structures, reactivities, and low-energy-gap characteristics, *J Organomet Chem.* 937 (2021) 121717. <https://doi.org/10.1016/j.jorganchem.2021.121717>.

55. T. Saito, N. Yamamoto, T. Nagase, T. Tsuboi, K. Kobayashi, T. Yamagata, H. Imoto, K. Unoura, Molecular Models of the Superconducting Chevrel Phases: Syntheses and Structures of $[\text{Mo}_6\text{X}_8(\text{PEt}_3)_6]$ and $[\text{PPN}][\text{Mo}_6\text{X}_8(\text{PEt}_3)_6]$ ($\text{X} = \text{S}, \text{Se}$; $\text{PPN} = (\text{Ph}_3\text{P})_2\text{N}$), *Inorg Chem.* 29 (1990) 764–770. <https://doi.org/10.1021/ic00329a039>.
56. S.J. Hilsenbeck, V.G. Young, R.E. McCarley, Synthesis, Structure, and Characterization of N-Ligated $\text{Mo}_6\text{S}_8\text{L}_6$ Cluster Complexes. Molecular Precursors to Chevrel Phases, *Inorg Chem.* 33 (1994) 1822–1832. <https://doi.org/10.1021/ic00087a017>.
57. T. Saito, N. Yamamoto, T. Yamagata, H. Imoto, Synthesis of $[\text{Mo}_6\text{S}_8(\text{PEt}_3)_6]$ by Reductive Dimerization of a Trinuclear Molybdenum Chloro Sulfido Cluster Complex Coordinated with Triethylphosphine and Methanol: A Molecular Model for Superconducting Chevrel Phases, *Journal of American Chemical Society.* 110 (1988) 1646–1647.
58. R.E. Bachman, K.H. Whitmire, The Synthesis and Characterization of a Series of Iron Carbonyl Clusters Containing Selenium and Tellurium, *Inorg Chem.* 33 (1994) 2527–2533. <https://doi.org/10.1021/ic00090a010>.
59. M. Pradeep, S. Ajeet, Recent approach to incorporate tellurium in metal carbonyl cluster utilizing extrusion reaction, *Annals of Advances in Chemistry.* 3 (2019) 014–016. <https://doi.org/10.29328/journal.aac.1001020>.
60. J. Dijkstra, C.F. Van Bruggen, C. Haas, R.A. De Groot, Electronic band-structure calculations of some magnetic chromium compounds, *Journal of Physics: Condensed Matter.* 1 (1989) 9163–9174. <https://doi.org/10.1088/0953-8984/1/46/009>.
61. J. Dijkstra, C.F. Van Bruggen, C. Haas, R.A. De Groot, Electronic band-structure calculations of some magnetic chromium compounds, *Journal of Physics: Condensed Matter.* 1 (1989) 9163–9174. <https://doi.org/10.1088/0953-8984/1/46/009>.
62. J. Warczewski, J. Krok-Kowalski, Magnetic, electrical and structural properties of some ternary and quaternary spinels with chromium, *Journal of Physics and Chemistry of Solids.* 64 (2003) 1609–1614. [https://doi.org/10.1016/S0022-3697\(03\)00066-0](https://doi.org/10.1016/S0022-3697(03)00066-0).
63. X. Song, T. Yang, H. Du, W. Dong, Z. Liang, New binary Mn and Cr mixed oxide electrocatalysts for the oxygen evolution reaction, *Journal of Electroanalytical Chemistry.* 760 (2016) 59–63. <https://doi.org/10.1016/j.jelechem.2015.11.044>.

64. D. Jin, J. Kang, S. Prabhakaran, Y. Lee, M.H. Kim, D.H. Kim, C. Lee, Chromium-rich $\text{Cr}_x\text{Ir}_{1-x}\text{O}_2$ wire-in-tube alloys for boosted water oxidation with long standing electrocatalytic activity, *J Mater Chem A Mater.* 10 (2022) 13803–13813. <https://doi.org/10.1039/d2ta02984g>.
65. S. Kong, M. Lu, S. Yan, Z. Zou, High-valence chromium accelerated interface electron transfer for water oxidation, *Dalton Transactions.* (2022) 16890–16897. <https://doi.org/10.1039/d2dt02908a>.
66. U.N. Kumar, A. Malek, G.R. Rao, T. Thomas, Chromium Oxynitride (CrON) Nanoparticles: an Unexplored Electrocatalyst for Oxygen Evolution Reaction, *Electrocatalysis.* 13 (2022) 62–71. <https://doi.org/10.1007/s12678-021-00693-4>.
67. [69] C.C. Lin, C.C.L. McCrory, Effect of Chromium Doping on Electrochemical Water Oxidation Activity by $\text{Co}_3\text{-xCr}_x\text{O}_4$ Spinel Catalysts, *ACS Catal.* 7 (2017) 443–451. <https://doi.org/10.1021/acscatal.6b02170>.
68. C.T.K. Thaminimulla, T. Takata, M. Hara, J.N. Kondo, K. Domen, Effect of chromium addition for photocatalytic overall water splitting on $\text{Ni-K}_2\text{La}_2\text{Ti}_3\text{O}_{10}$, *J Catal.* 196 (2000) 362–365. <https://doi.org/10.1006/jcat.2000.3049>.
69. P. Ramakrishnan, K.B. Lee, J.I. Sohn, Ternary metal-based inverse spinel oxide NiCrFeO_4 nanoparticles as a highly efficient oxygen evolution catalyst, *Appl Surf Sci.* 566 (2021) 150653. <https://doi.org/10.1016/j.apsusc.2021.150653>.
70. X. Liu, J. Wu, Coupling interface constructions of $\text{NiO-Cr}_2\text{O}_3$ heterostructures for efficient electrocatalytic oxygen evolution, *Electrochim Acta.* 320 (2019) 134577. <https://doi.org/10.1016/j.electacta.2019.134577>.
71. C. Zhou, T. Gao, J. Tan, Z. Luo, L. Mutallip, D. Xiao, Synthesis of flower-like nickel-iron-chromium nanostructure compound deposited stainless steel foil as an efficient binder-free electrocatalyst for water splitting, *Sustain Energy Fuels.* 5 (2021) 2649–2659. <https://doi.org/10.1039/d1se00002k>.
72. T.A. Shifa, R. Mazzaro, V. Morandi, A. Vomiero, Controllable Synthesis of 2D Nonlayered Cr_2S_3 Nanosheets and Their Electrocatalytic Activity Toward Oxygen Evolution Reaction, *Frontiers in Chemical Engineering.* 3 (2021) 1–7. <https://doi.org/10.3389/fceng.2021.703812>.
73. L. Shufler, H.W. Sternberg, R.A. Friedel, Infrared Spectrum and Structure of Chromium Hexacarbonyl, $\text{Cr}(\text{CO})_6$, *J. Am. Chem. Soc.* 78 (1956) 2687–2688.
74. D.J. Darensbourg, D.J. Zalewski, Synthesis and Characterization of Sulfur-Capped Trlnuclear Group 6B Metal Clusters, *Organometallics.* 3 (1984) 1598–1600.

75. C.H. Ho, Y.Y. Chu, C.N. Lin, H.W. Chen, C.Y. Huang, M. Shieh, Selenium-manganese carbonyl clusters: Synthesis, reversible transformation, electrochemical properties, and theoretical calculations, *Organometallics*. 29 (2010) 4396–4405. <https://doi.org/10.1021/om1006819>.
76. M.H. Hsu, C.Y. Miu, Y.C. Lin, M. Shieh, Selenium-capped trimolybdenum and tungsten carbonyl clusters $[\text{Se}_2\text{M}_3(\text{CO})_{10}]_2^-$ (M = Mo, W), *J Organomet Chem*. 691 (2006) 966–974. <https://doi.org/10.1016/j.jorganchem.2005.10.039>.
77. M. Hoefler, K.-F. Tebbe, H. Veit, N.E. Weiler, Synthesis and Structure of $[\text{PPN}]_2[\text{m}^2\text{-CO}]_3(\text{CO})_9\text{Cr}_3(\text{m}^4\text{-S})\text{Cr}(\text{CO})_5$: A Chromium Cluster, *J. Am. Chem. Soc.* 3 (1983) 6338–6339.
78. E.P. Beaumier, A.J. Pearce, X.Y. See, I.A. Tonks, Modern applications of low-valent early transition metals in synthesis and catalysis, *Nat Rev Chem*. 3 (2019) 15–34. <https://doi.org/10.1038/s41570-018-0059-x>.
79. S. Kong, M. Lu, S. Yan, Z. Zou, High-valence chromium accelerated interface electron transfer for water oxidation, *Dalton Transactions*. (2022). <https://doi.org/10.1039/d2dt02908a>.
80. M. Shamsipur, A. (Arman) Taherpour, H. Sharghi, V. Lippolis, A. Pashabadi, A low-overpotential nature-inspired molecular chromium water oxidation catalyst, *Electrochim Acta*. 265 (2018) 316–325. <https://doi.org/10.1016/j.electacta.2018.01.202>.
81. S.L. Hooe, J.M. Dressel, D.A. Dickie, C.W. Machan, Highly Efficient Electrocatalytic Reduction of CO_2 to CO by a Molecular Chromium Complex, *ACS Catal*. 10 (2020) 1146–1151. <https://doi.org/10.1021/acscatal.9b04687>.
82. J.J. Moreno, S.L. Hooe, C.W. Machan, DFT Study on the Electrocatalytic Reduction of CO_2 to CO by a Molecular Chromium Complex, *Inorg Chem*. 60 (2021) 3635–3650. <https://doi.org/10.1021/acs.inorgchem.0c03136>.
83. J.A. Wilson, A.D. Yoffe, The transition metal dichalcogenides discussion and interpretation of the observed optical, electrical and structural properties, *Advances in Physics*. 18 (1969) 193–335. <https://doi.org/10.1080/00018736900101307>.
84. M.A. Lukowski, A.S. Daniel, F. Meng, A. Forticaux, L. Li, S. Jin, Enhanced hydrogen evolution catalysis from chemically exfoliated metallic MoS_2 nanosheets, *J Am Chem Soc*. 135 (2013) 10274–10277. <https://doi.org/10.1021/ja404523s>.

85. Q. Yun, Q. Lu, X. Zhang, C. Tan, H. Zhang, Three-Dimensional Architectures Constructed from Transition-Metal Dichalcogenide Nanomaterials for Electrochemical Energy Storage and Conversion, *Angewandte Chemie - International Edition*. 57 (2018) 626–646. <https://doi.org/10.1002/anie.201706426>.
86. M.S. Faber, S. Jin, Earth-abundant inorganic electrocatalysts and their nanostructures for energy conversion applications, *Energy and Environmental Science*. 7 (2014) 3519–3542. <https://doi.org/10.1039/c4ee01760a>.
87. V. Nicolosi, M. Chhowalla, M.G. Kanatzidis, M.S. Strano, J.N. Coleman, Liquid exfoliation of layered materials, *Science* (1979). 340 (2013) 72–75. <https://doi.org/10.1126/science.1226419>.
88. M.R. Gao, M.K.Y. Chan, Y. Sun, Edge-terminated molybdenum disulfide with a 9.4-Å interlayer spacing for electrochemical hydrogen production, *Nature Communications*. 6 (2015). <https://doi.org/10.1038/ncomms8493>.
89. X. Huang, Z. Zeng, H. Zhang, Metal dichalcogenide nanosheets: Preparation, properties and applications, *Chemical Society Reviews*. 42 (2013) 1934–1946. <https://doi.org/10.1039/c2cs35387c>.
90. Q.H. Wang, K. Kalantar-Zadeh, A. Kis, J.N. Coleman, M.S. Strano, Electronics and optoelectronics of two-dimensional transition metal dichalcogenides, *Nature Nanotechnology*. 7 (2012) 699–712. <https://doi.org/10.1038/nnano.2012.193>.
91. R. Kappera, D. Voiry, S.E. Yalcin, B. Branch, G. Gupta, A.D. Mohite, M. Chhowalla, Phase-engineered low-resistance contacts for ultrathin MoS₂ transistors, *Nature Materials*. 13 (2014) 1128–1134. <https://doi.org/10.1038/nmat4080>.
92. K. Xu, Z. Wang, X. Du, M. Safdar, C. Jiang, J. He, Atomic-layer triangular WSe₂ sheets: Synthesis and layer-dependent photoluminescence property, *Nanotechnology*. 24 (2013). <https://doi.org/10.1088/0957-4484/24/46/465705>.
93. Rothschild, A.; Sloan, J.; Tenne, R. Growth of WS₂ Nanotubes Phases. *J. Am. Chem. Soc.* **2000**, *122*, 5169–5179. <https://doi.org/10.1021/ja994118v>
94. Brorson, M.; Hansen, T.W.; Jacobsen, C.J.H. Rhenium (IV) Sulfide Nanotubes. *J. Am. Chem. Soc.* **2002**, *124*, 11582–11583. <https://doi.org/10.1021/ja027084r>
95. M. Nath, C.N.R. Rao, New metal disulfide nanotubes [3], *J Am Chem Soc.* 123 (2001) 4841–4842. <https://doi.org/10.1021/ja010388d>.

96. K.S. Coleman, J. Sloan, N.A. Hanson, G. Brown, G.P. Clancy, M. Terrones, H. Terrones, M.L.H. Green, The formation of ReS₂ inorganic fullerene-like structures containing Re₄ parallelogram units and metal-metal bonds, *J Am Chem Soc.* 124 (2002) 11580–11581. <https://doi.org/10.1021/ja0261630>.
97. T.F. Jaramillo, K.P. Jørgensen, J. Bonde, J.H. Nielsen, S. Horch, I. Chorkendorff, Identification of active edge sites for electrochemical H₂ evolution from MoS₂ nanocatalysts, *Science* (1979). 317 (2007) 100–102. <https://doi.org/10.1126/science.1141483>.
98. B. Hinnemann, P.G. Moses, J. Bonde, K.P. Jørgensen, J.H. Nielsen, S. Horch, I. Chorkendorff, J.K. Nørskov, Biomimetic hydrogen evolution: MoS₂ nanoparticles as catalyst for hydrogen evolution, *J Am Chem Soc.* 127 (2005) 5308–5309. <https://doi.org/10.1021/ja0504690>.
99. Y.R. Zheng, M.R. Gao, Q. Gao, H.H. Li, J. Xu, Z.Y. Wu, S.H. Yu, An efficient CeO₂/CoSe₂ nanobelt composite for electrochemical water oxidation, *Small.* 11 (2015) 182–188. <https://doi.org/10.1002/smll.201401423>.
100. Y. Liu, H. Cheng, M. Lyu, S. Fan, Q. Liu, W. Zhang, Y. Zhi, C. Wang, C. Xiao, S. Wei, B. Ye, Y. Xie, Low overpotential in vacancy-rich ultrathin CoSe₂ nanosheets for water oxidation, *J Am Chem Soc.* 136 (2014) 15670–15675. <https://doi.org/10.1021/ja5085157>.
101. M.R. Gao, X. Cao, Q. Gao, Y.F. Xu, Y.R. Zheng, J. Jiang, S.H. Yu, Nitrogen-doped graphene supported CoSe₂ nanobelt composite catalyst for efficient water oxidation, *ACS Nano.* 8 (2014) 3970–3978. <https://doi.org/10.1021/nn500880v>.
102. S. Mao, Z. Wen, S. Ci, X. Guo, K. Ostrikov, J. Chen, Perpendicularly oriented MoSe₂/graphene nanosheets as advanced electrocatalysts for hydrogen evolution, *Small.* 11 (2015) 414–419. <https://doi.org/10.1002/smll.201401598>.
103. L. Zhang, T. Wang, L. Sun, Y. Sun, T. Hu, K. Xu, F. Ma, Hydrothermal synthesis of 3D hierarchical MoSe₂/NiSe₂ composite nanowires on carbon fiber paper and their enhanced electrocatalytic activity for the hydrogen evolution reaction, *Journal of Materials Chemistry A.* 5 (2017) 19752–19759. <https://doi.org/10.1039/c7ta05352e>.
104. B. Qu, C. Li, C. Zhu, S. Wang, X. Zhang, Y. Chen, Growth of MoSe₂ nanosheets with small size and expanded spaces of (002) plane on the surfaces of porous N-doped carbon nanotubes for hydrogen production, *Nanoscale.* 8 (2016) 16886–16893. <https://doi.org/10.1039/c6nr04619c>.

105. J.D. Benck, T.R. Hellstern, J. Kibsgaard, P. Chakthranont, T.F. Jaramillo, Catalyzing the hydrogen evolution reaction (HER) with molybdenum sulfide nanomaterials, *ACS Catalysis*. 4 (2014) 3957–3971. <https://doi.org/10.1021/cs500923c>.
106. C.Z. Guo, W.L. Liao, L.T. Sun, C.G. Chen, Synthesis of non-noble nitrogen-containing catalysts for cathodic oxygen reduction reaction: A critical review, *International Journal of Electrochemical Science*. 10 (2015) 2467–2477.
107. Z.W. She, J. Kibsgaard, C.F. Dickens, I. Chorkendorff, J.K. Nørskov, T.F. Jaramillo, Combining theory and experiment in electrocatalysis: Insights into materials design, *Science* (1979). 355 (2017). <https://doi.org/10.1126/science.aad4998>.
108. O. Mabayoje, A. Shoola, B.R. Wygant, C.B. Mullins, The Role of Anions in Metal Chalcogenide Oxygen Evolution Catalysis: Electrodeposited Thin Films of Nickel Sulfide as “pre-catalysts,” *ACS Energy Letters*. 1 (2016) 195–201. <https://doi.org/10.1021/acsenergylett.6b00084>.
109. M. Liao, G. Zeng, T. Luo, Z. Jin, Y. Wang, X. Kou, D. Xiao, Three-dimensional coral-like cobalt selenide as an advanced electrocatalyst for highly efficient oxygen evolution reaction, *Electrochimica Acta*, 194 (2016) 59–66. <https://doi.org/10.1016/j.electacta.2016.02.046>.
110. A.T. Swesi, J. Masud, M. Nath, Nickel selenide as a high-efficiency catalyst for oxygen evolution reaction, *Energy and Environmental Science*. 9 (2016) 1771–1782. <https://doi.org/10.1039/c5ee02463c>.
111. J. Masud, A.T. Swesi, W.P.R. Liyanage, M. Nath, Cobalt Selenide Nanostructures: An Efficient Bifunctional Catalyst with High Current Density at Low Coverage, *ACS Applied Materials and Interfaces*. 8 (2016) 17292–17302. <https://doi.org/10.1021/acsami.6b04862>.
112. M. Nath, U. de Silva, H. Singh, M. Perkins, W.P.R. Liyanage, S. Umapathi, S. Chakravarty, J. Masud, Cobalt Telluride: A Highly Efficient Trifunctional Electrocatalyst for Water Splitting and Oxygen Reduction, *ACS Applied Energy Materials*. 4 (2021) 8158–8174. <https://doi.org/10.1021/acsaem.1c01438>.
113. Q. Gao, C.Q. Huang, Y.M. Ju, M.R. Gao, J.W. Liu, D. An, C.H. Cui, Y.R. Zheng, W.X. Li, S.H. Yu, Phase-Selective Syntheses of Cobalt Telluride Nanofleeces for Efficient Oxygen Evolution Catalysts, *Angewandte Chemie - International Edition*. 56 (2017) 7769–7773. <https://doi.org/10.1002/anie.201701998>.

114. S. Shit, S. Chhetri, W. Jang, N.C. Murmu, H. Koo, P. Samanta, T. Kuila, Cobalt Sulfide/Nickel Sulfide Heterostructure Directly Grown on Nickel Foam: An Efficient and Durable Electrocatalyst for Overall Water Splitting Application, *ACS Applied Materials and Interfaces*. 10 (2018) 27712–27722. <https://doi.org/10.1021/acsami.8b04223>.
115. R. Akram, M.D. Khan, C. Zequine, C. Zhao, R.K. Gupta, M. Akhtar, J. Akhtar, M.A. Malik, N. Revaprasadu, M.H. Bhatti, Cobalt sulfide nanoparticles: Synthesis, water splitting and supercapacitance studies, *Materials Science in Semiconductor Processing*. 109 (2020) 104925. <https://doi.org/10.1016/j.mssp.2020.104925>.
116. B. Yan, D. Krishnamurthy, C.H. Hendon, S. Deshpande, Y. Surendranath, V. Viswanathan, Surface Restructuring of Nickel Sulfide Generates Optimally Coordinated Active Sites for Oxygen Reduction Catalysis, *Joule*. 1 (2017) 600–612. <https://doi.org/10.1016/j.joule.2017.08.020>.
117. C. Zhang, S. Bhoyate, P.K. Kahol, K. Siam, T.P. Poudel, S.R. Mishra, F. Perez, A. Gupta, G. Gupta, R.K. Gupta, Highly Efficient and Durable Electrocatalyst Based on Nanowires of Cobalt Sulfide for Overall Water Splitting, *ChemNanoMat*. 4 (2018) 1240–1246. <https://doi.org/10.1002/cnma.201800301>.
118. H. Singh, M. Marley-Hines, S. Chakravarty, M. Nath, Multi-walled carbon nanotube supported manganese selenide as a highly active bifunctional OER and ORR electrocatalyst, *Journal of Materials Chemistry A*. 10 (2022) 6772–6784. <https://doi.org/10.1039/d1ta09864k>.
119. I.H. Kwak, H.S. Im, D.M. Jang, Y.W. Kim, K. Park, Y.R. Lim, E.H. Cha, J. Park, CoSe₂ and NiSe₂ Nanocrystals as Superior Bifunctional Catalysts for Electrochemical and Photoelectrochemical Water Splitting, *ACS Applied Materials, and Interfaces*. 8 (2016) 5327–5334. <https://doi.org/10.1021/acsami.5b12093>.
120. A.T. Swesi, J. Masud, W.P.R. Liyanage, S. Umaphathi, E. Bohannan, J. Medvedeva, M. Nath, Textured NiSe₂ Film: Bifunctional Electrocatalyst for Full Water Splitting at Remarkably Low Overpotential with High Energy Efficiency, *Scientific Reports*. 7 (2017). <https://doi.org/10.1038/s41598-017-02285-z>.
121. Feng, Z.; Shi, T.; Liu, W.; Zhang, W.; Zhang, H. Highly Active Bifunctional Electrocatalyst: Nanoporous (Ni,Co)_{0.85}Se Anchored on RGO for Water and Hydrazine Oxidation. *Int J Energy Res* **2022**, *46*, 15938–15947, doi:10.1002/er.8292.

122. Xiao, K.; Zhou, L.; Shao, M.; Wei, M. Fabrication of (Ni,Co)_{0.85}Se Nanosheet Arrays Derived from Layered Double Hydroxides toward Largely Enhanced Overall Water Splitting. *J Mater Chem A Mater* **2018**, *6*, 7585–7591, doi:10.1039/c8ta01067f.
123. C. Xia, Q. Jiang, C. Zhao, M.N. Hedhili, H.N. Alshareef, Selenide-Based Electrocatalysts and Scaffolds for Water Oxidation Applications, *Advanced Materials*. *28* (2016) 77–85. <https://doi.org/10.1002/adma.201503906>.
124. L.L. Feng, G. Yu, Y. Wu, G.D. Li, H. Li, Y. Sun, T. Asefa, W. Chen, X. Zou, High-Index Faceted Ni₃S₂ Nanosheet Arrays as Highly Active and Ultrastable Electrocatalysts for Water Splitting, *J Am Chem Soc.* *137* (2015) 14023–14026. <https://doi.org/10.1021/jacs.5b08186>.
125. U. de Silva, J. See, W.P.R. Liyanage, J. Masud, J. Wu, W. Yang, W.T. Chen, D. Prendergast, M. Nath, Understanding the Structural Evolution of a Nickel Chalcogenide Electrocatalyst Surface for Water Oxidation, *Energy and Fuels*. *35* (2021) 4387–4403. <https://doi.org/10.1021/acs.energyfuels.0c04089>.
126. X. Cao, J.E. Medvedeva, M. Nath, Copper Cobalt Selenide as a High-Efficiency Bifunctional Electrocatalyst for Overall Water Splitting: Combined Experimental and Theoretical Study, *ACS Applied Energy Materials*. *3* (2020) 3092–3103. <https://doi.org/10.1021/acsaem.0c00262>.
127. A.K. Gautam, M. Faraz, N. Khare, Enhanced thermoelectric properties of MoS₂ with the incorporation of reduced graphene oxide (RGO), *Journal of Alloys and Compounds*. *838* (2020) 155673. <https://doi.org/10.1016/j.jallcom.2020.155673>.
128. X. Cao, Y. Hong, N. Zhang, Q. Chen, J. Masud, M.A. Zaem, M. Nath, Phase Exploration, and Identification of Multinary Transition-Metal Selenides as High-Efficiency Oxygen Evolution Electrocatalysts through Combinatorial Electrodeposition, *ACS Catalysis*. *8* (2018) 8273–8289. <https://doi.org/10.1021/acscatal.8b01977>.
129. Chuprakov, I.S.; Dahmen, K.H. CVD of Metal Chalcogenide Films. *Journal De Physique. IV : JP* **1999**, *9*, 313–319, doi:10.1051/jp4:1999838.
130. Tang, L.; Li, T.; Luo, Y.; Feng, S.; Cai, Z.; Zhang, H.; Liu, B.; Cheng, H.M. Vertical Chemical Vapor Deposition Growth of Highly Uniform 2D Transition Metal Dichalcogenides. *ACS Nano* **2020**, doi:10.1021/acsnano.0c00296.
131. Xie, C.; Yang, P.; Huan, Y.; Cui, F.; Zhang, Y. Roles of Salts in the Chemical Vapor Deposition Synthesis of Two-Dimensional Transition Metal Chalcogenides. *Dalton Transactions* **2020**, *49*, 10319–10327, doi:10.1039/d0dt01561j.

132. He, S.; Lin, H.; Sun, R.; Wang, Z. Growth of NiSe₂, NiTe₂ and Alloy NiSe₂-XTeX nanosheets with Tunable Shape Evolution and Chemical Composition. *2d Mater* **2020**, *7*, 0–6, doi:10.1088/2053-1583/aba566.
133. S. Anantharaj, J. Kennedy, S. Kundu, Microwave-Initiated Facile Formation of Ni₃Se₄ Nanoassemblies for Enhanced and Stable Water Splitting in Neutral and Alkaline Media, *ACS Applied Materials and Interfaces*. *9* (2017) 8714–8728. <https://doi.org/10.1021/acsami.6b15980>.
134. K. Ding, H. Lu, Y. Zhang, M.L. Snedaker, D. Liu, J.A. Maciá-Agulló, G.D. Stucky, Microwave synthesis of microstructured and nanostructured metal chalcogenides from elemental precursors in phosphonium ionic liquids, *J Am Chem Soc*. *136* (2014) 15465–15468. <https://doi.org/10.1021/ja508628q>.
135. S. Sarwar, Z. Liu, J. Li, Y. Wang, R. Wang, X. Zhang, High-performance hybrid-capacitor based on MoTe₂/graphene through ultra-fast, facile microwave-initiated synthesis, *Journal of Alloys and Compounds*. *846* (2020) 155886. <https://doi.org/10.1016/j.jallcom.2020.155886>.
136. X. Zheng, X. Han, H. Liu, J. Chen, D. Fu, J. Wang, C. Zhong, Y. Deng, W. Hu, Controllable Synthesis of Ni_xSe (0.5 ≤ x ≤ 1) Nanocrystals for Efficient Rechargeable Zinc-Air Batteries and Water Splitting, *ACS Applied Materials and Interfaces*. *10* (2018) 13675–13684. <https://doi.org/10.1021/acsami.8b01651>.
137. Vamvasakis, I.; Subrahmanyam, K.S.; Kanatzidis, M.G.; Armatas, G.S. Template-Directed Assembly of Metal-Chalcogenide Nanocrystals into Ordered Mesoporous Networks. *ACS Nano* **2015**, *9*, 4419–4426, doi:10.1021/acsnano.5b01014.
138. Ondry, J.C.; Robbenolt, S.; Kang, H.; Yan, Y.; Tolbert, S.H. A Room-Temperature, Solution Phase Method for the Synthesis of Mesoporous Metal Chalcogenide Nanocrystal-Based Thin Films with Precisely Controlled Grain Sizes. *Chemistry of Materials* **2016**, *28*, 6105–6117, doi:10.1021/acs.chemmater.6b01681.
139. Chen, H.; Cao, C.; Ge, B.; Li, Y.; Han, J.; Chen, Z. Wafer-Scale Metal Chalcogenide Thin Films: Via an Ion Exchange Approach. *J Mater Chem C Mater* **2020**, *8*, 14393–14401, doi:10.1039/d0tc03540h.
140. Shaw, G.A.; Morrison, D.E.; Parkin, I.P. Solid State Synthesis of Binary Metal Chalcogenides. *Journal of the Chemical Society, Dalton Transactions* **2001**, 1872–1875, doi:10.1039/b101645h.

141. Zhao, W.; Zhang, C.; Geng, F.; Zhuo, S.; Zhang, B. Nanoporous Hollow Transition Metal Chalcogenide Nanosheets Synthesized via the Anion-Exchange Reaction of Metal Hydroxides with Chalcogenide Ions. *ACS Nano* **2014**, *8*, 10909–10919, doi:10.1021/nm504755x.
142. Yang, C.; Zhang, J.; Gao, G.; Liu, D.; Liu, R.; Fan, R.; Gan, S.; Wang, Y.; Wang, Y. 3D Metallic Ti@Ni_{0.85}Se with Triple Hierarchy as High-Efficiency Electrocatalyst for Overall Water Splitting. *ChemSusChem* **2019**, *12*, 2271–2277, doi:10.1002/cssc.201900181.
143. Ghosh, D.; Manikanta Kumar, M.; Raj, C.R.; Pradhan, D. Bifunctional Catalytic Activity of Solvothermally Synthesized CeO₂Nanosphere/NiO Nanoflake Nanocomposites. *ACS Appl Energy Mater* **2022**, *5*, 5666–5679, doi:10.1021/acsaem.1c04036.
144. Yang, Q.; Chen, X.; Zhan, H.; Wu, S.; Hu, Q.; Zhou, R.; Xue, Y. Mixing Solvothermal Synthesis of Surfactant Free Nanoflower-Sphere-like Nickel Selenide for Supercapacitor Application. *Synth Met* **2019**, *257*, 116167, doi:10.1016/j.synthmet.2019.116167.
145. Li, X.; Yan, K.L.; Rao, Y.; Dong, B.; Shang, X.; Han, G.Q.; Chi, J.Q.; Hu, W.H.; Liu, Y.R.; Chai, Y.M.; et al. Electrochemically Activated NiSe-NixSy Hybrid Nanorods as Efficient Electrocatalysts for Oxygen Evolution Reaction. *Electrochim Acta* **2016**, *220*, 536–544, doi:10.1016/j.electacta.2016.10.138.
146. Dong, L.; Chu, Y.; Sun, W. Controllable Synthesis of Nickel Hydroxide and Porous Nickel Oxide Nanostructures with Different Morphologies. *Chemistry - A European Journal* **2008**, *14*, 5064–5072, doi:10.1002/chem.200701627.
147. X. Cao, E. Johnson, M. Nath, Expanding Multinary Selenide Based High-Efficiency Oxygen Evolution Electrocatalysts through Combinatorial Electrodeposition: Case Study with Fe-Cu-Co Selenides, *ACS Sustainable Chemistry, and Engineering*. **7** (2019) 9588–9600. <https://doi.org/10.1021/acssuschemeng.9b01095>.
148. Van Der Stam, W.; Gantapara, A.P.; Akkerman, Q.A.; Soligno, G.; Meeldijk, J.D.; Van Roij, R.; Dijkstra, M.; De Mello Donega, C. Self-Assembly of Colloidal Hexagonal Bipyramid- and Bifrustum-Shaped ZnS Nanocrystals into Two-Dimensional Superstructures. *Nano Lett* **2014**, *14*, 1032–1037, doi:10.1021/nl4046069.
149. Hu, C.; Lin, K.; Wang, X.; Liu, S.; Yi, J.; Tian, Y.; Wu, B.; Chen, G.; Yang, H.; Dai, Y.; et al. Electrostatic Self-Assembling Formation of Pd Superlattice Nanowires from Surfactant-Free Ultrathin Pd Nanosheets. *J Am Chem Soc* **2014**, *136*, 12856–12859, doi:10.1021/ja507409p.

150. Zhuang, Z.; Peng, Q.; Zhang, B.; Li, Y. Controllable Synthesis of Cu₂S Nanocrystals and Their Assembly into a Superlattice. *J Am Chem Soc* 2008, 130, 10482–10483, doi:10.1021/ja803644g.
151. Dong, L.; Chu, Y.; Sun, W. Controllable Synthesis of Nickel Hydroxide and Porous Nickel Oxide Nanostructures with Different Morphologies. *Chemistry - A European Journal* 2008, 14, 5064–5072, doi:10.1002/chem.200701627.
152. Zhao, B.; Liu, J.W.; Yin, Y.R.; Wu, D.; Luo, J.L.; Fu, X.Z. Carbon Nanofibers@NiSe Core/Sheath Nanostructures as Efficient Electrocatalysts for Integrating Highly Selective Methanol Conversion and Less-Energy Intensive Hydrogen Production. *J Mater Chem A Mater* 2019, 7, 25878–25886, doi:10.1039/c9ta09782a.
153. Taheri, P.; Wang, J.; Xing, H.; Destino, J.F.; Arik, M.M.; Zhao, C.; Kang, K.; Blizzard, B.; Zhang, L.; Zhao, P.; et al. Growth Mechanism of Largescale MoS₂ Monolayer by Sulfurization of MoO₃ Film. *Mater Res Express* 2016, 3, 1–10, doi:10.1088/2053-1591/3/7/075009.
154. S. Choi, J.H. Drese, C.W. Jones, Adsorbent materials for carbon dioxide capture from large anthropogenic point sources, *ChemSusChem*. 2 (2009) 796–854. <https://doi.org/10.1002/cssc.200900036>.
155. A. Somoza-Tornos, O.J. Guerra, A.M. Crow, W.A. Smith, B.M. Hodge, Process modeling, techno-economic assessment, and life cycle assessment of the electrochemical reduction of CO₂: a review, *IScience*. 24 (2021) 102813. <https://doi.org/10.1016/j.isci.2021.102813>.
156. Zhu, W.; Michalsky, R.; Metin, Ö.; Lv, H.; Guo, S.; Wright, C.J.; Sun, X.; Peterson, A.A.; Sun, S. Monodisperse Au Nanoparticles for Selective Electrocatalytic Reduction of CO₂ to CO. *J Am Chem Soc* 2013, 135, 16833–16836, doi:10.1021/ja409445p.
157. Yang, H.P.; Qin, S.; Wang, H.; Lu, J.X. Organically Doped Palladium: A Highly Efficient Catalyst for Electroreduction of CO₂ to Methanol. *Green Chemistry* 2015, 17, 5144–5148, doi:10.1039/c5gc01504a.
158. Chen, Y.; Li, C.W.; Kanan, M.W. Aqueous CO₂ Reduction at Very Low Overpotential on Oxide-Derived Au Nanoparticles. *J Am Chem Soc* 2012, 134, 19969–19972, doi:10.1021/ja309317u.
159. Lim, R.J.; Xie, M.; Sk, M.A.; Lee, J.M.; Fisher, A.; Wang, X.; Lim, K.H. A Review on the Electrochemical Reduction of CO₂ in Fuel Cells, Metal Electrodes and Molecular Catalysts. *Catal Today* 2014, 233, 169–180, doi:10.1016/j.cattod.2013.11.037.

160. J.Y. Kim, C.H. Ryu, J.H. Lee, A.U. Pawar, W.D. Jang, Y.S. Kang, H.S. Ahn, Electrodeposited CuAgHg Multimetallic Thin Films for Improved CO₂ Conversion: The Dramatic Impact of Hg Incorporation on Product Selectivity, *ACS Applied Energy Materials*. 3 (2020) 6670–6677. <https://doi.org/10.1021/acsaem.0c00784>.
161. J.T. Feaster, C. Shi, E.R. Cave, T. Hatsukade, D.N. Abram, K.P. Kuhl, C. Hahn, J.K. Nørskov, T.F. Jaramillo, Understanding Selectivity for the Electrochemical Reduction of Carbon Dioxide to Formic Acid and Carbon Monoxide on Metal Electrodes, *ACS Catalysis*. 7 (2017) 4822–4827. <https://doi.org/10.1021/acscatal.7b00687>.
162. J. Wang, H. Yang, Q. Liu, Q. Liu, X. Li, X. Lv, T. Cheng, H. bin Wu, Fastening Br-Ions at Copper-Molecule Interface Enables Highly Efficient Electroreduction of CO₂ to Ethanol, *ACS Energy Letters*. 6 (2021) 437–444. <https://doi.org/10.1021/acsenenergylett.0c02364>.
163. C. Kim, K.M. Cho, K. Park, J.Y. Kim, G.T. Yun, F.M. Toma, I. Gereige, H.T. Jung, Cu/Cu₂O Interconnected Porous Aerogel Catalyst for Highly Productive Electrosynthesis of Ethanol from CO₂, *Advanced Functional Materials*. 31 (2021) 1–9. <https://doi.org/10.1002/adfm.202102142>.
164. Saxena, A.; Liyanage, W.P.R.; Kapila, S.; Nath, M. Nickel Selenide as an Efficient Electrocatalyst for Selective Reduction of Carbon Dioxide to Carbon-Rich Products. *Catal Sci Technol* 2022, 12, 4727–4739, doi:10.1039/d2cy00583b.
165. T. Cheng, H. Xiao, W.A. Goddard, Reaction Mechanisms for the Electrochemical Reduction of CO₂ to CO and Formate on the Cu(100) Surface at 298 K from Quantum Mechanics Free Energy Calculations with Explicit Water, *J Am Chem Soc*. 138 (2016) 13802–13805. <https://doi.org/10.1021/jacs.6b08534>.
166. J. Santatiwongchai, K. Faungnawakij, P. Hirunsit, Comprehensive Mechanism of CO₂ Electroreduction toward Ethylene and Ethanol: The Solvent Effect from Explicit Water-Cu(100) Interface Models, *ACS Catalysis*. 11 (2021) 9688–9701. <https://doi.org/10.1021/acscatal.1c01486>.
167. Z. Gu, H. Shen, Z. Chen, Y. Yang, C. Yang, Y. Ji, Y. Wang, C. Zhu, J. Liu, J. Li, T.K. Sham, X. Xu, G. Zheng, Efficient Electrocatalytic CO₂ Reduction to C₂+ Alcohols at Defect-Site-Rich Cu Surface, *Joule*. 5 (2021) 429–440. <https://doi.org/10.1016/j.joule.2020.12.011>.
168. E. Bertheussen, T. v. Hogg, Y. Abghoui, A.K. Engstfeld, I. Chorkendorff, I.E.L. Stephens, Electroreduction of CO on Polycrystalline Copper at Low Overpotentials, *ACS Energy Letters*. 3 (2018) 634–640. <https://doi.org/10.1021/acsenenergylett.8b00092>.

169. S. Hanselman, M.T.M. Koper, F. Calle-Vallejo, Computational Comparison of Late Transition Metal (100) Surfaces for the Electrocatalytic Reduction of CO to C₂ Species, *ACS Energy Letters*. 3 (2018) 1062–1067. <https://doi.org/10.1021/acsenergylett.8b00326>.
170. T.K. Todorova, M.W. Schreiber, M. Fontecave, Mechanistic Understanding of CO₂ Reduction Reaction (CO₂RR) Toward Multicarbon Products by Heterogeneous Copper-Based Catalysts, *ACS Catalysis*. 10 (2020) 1754–1768. <https://doi.org/10.1021/acscatal.9b04746>.
171. X. Chang, A. Malkani, X. Yang, B. Xu, Mechanistic Insights into Electroreductive C-C Coupling between CO and Acetaldehyde into Multicarbon Products, *J Am Chem Soc*. 142 (2020) 2975–2983. <https://doi.org/10.1021/jacs.9b11817>.
172. A.J. Garza, A.T. Bell, M. Head-Gordon, Mechanism of CO₂ Reduction at Copper Surfaces: Pathways to C₂ Products, *ACS Catalysis*. 8 (2018) 1490–1499. <https://doi.org/10.1021/acscatal.7b03477>.
173. C.M. Gunathunge, X. Li, J. Li, R.P. Hicks, V.J. Ovalle, M.M. Waegele, Spectroscopic Observation of Reversible Surface Reconstruction of Copper Electrodes under CO₂ Reduction, *Journal of Physical Chemistry C*. 121 (2017) 12337–12344. <https://doi.org/10.1021/acs.jpcc.7b03910>.
174. Kas, R.; Kortlever, R.; Milbrat, A.; Koper, M.T.M.; Mul, G.; Baltrusaitis, J. Electrochemical CO₂ Reduction on Cu₂O-Derived Copper Nanoparticles: Controlling the Catalytic Selectivity of Hydrocarbons. *Physical Chemistry Chemical Physics* 2014, 16, 12194–12201, doi:10.1039/c4cp01520g.
175. I. v. Chernyshova, P. Somasundaran, S. Ponnurangam, On the origin of the elusive first intermediate of CO₂ electroreduction, *Proc Natl Acad Sci U S A*. 115 (2018) E9261–E9270. <https://doi.org/10.1073/pnas.1802256115>.
176. Saxena, A.; Liyanage, W.; Masud, J.; Kapila, S.; Nath, M. Selective Electroreduction of CO₂ to Carbon-Rich Products with a Simple Binary Copper Selenide Electrocatalyst. *J Mater Chem A Mater* 2021, 9, 7150–7161, doi:10.1039/d0ta11518e.
177. Rahaman, M.; Dutta, A.; Zanetti, A.; Broekmann, P. Electrochemical Reduction of CO₂ into Multicarbon Alcohols on Activated Cu Mesh Catalysts: An Identical Location (IL) Study. *ACS Catal* 2017, 7, 7946–7956, doi:10.1021/acscatal.7b02234.

178. Albo, J.; Sáez, A.; Solla-Gullón, J.; Montiel, V.; Irabien, A. Production of Methanol from CO₂ Electroreduction at Cu₂O and Cu₂O/ZnO-Based Electrodes in Aqueous Solution. *Appl Catal B* 2015, 176–177, 709–717, doi:10.1016/j.apcatb.2015.04.055.
179. Yanga, H.; Liub, H.; Liub, X.; Zhaob, Z.; Luo, J. Electroreduction of Carbon Dioxide to Formate over a Thin-Layered Tin Diselenide Electrode. *Catal Sci Technol* 2018, 8, 5428–5433, doi:10.1039/C8CY01240G.
180. Gao, F.Y.; Wu, Z.Z.; Gao, M.R. Electrochemical CO₂ Reduction on Transition-Metal Chalcogenide Catalysts: Recent Advances and Future Perspectives. *Energy and Fuels* 2021, 35, 12869–12883, doi:10.1021/acs.energyfuels.1c01650.
181. Asadi, M.; Kim, K.; Liu, C.; Addepalli, A.V.; Abbasi, P.; Yasaei, P.; Phillips, P.; Behranginia, A.; Cerrato, J.M.; Haasch, R.; et al. Nanostructured Transition Metal Dichalcogenide Electrocatalysts for CO₂ Reduction in Ionic Liquid. *Science (1979)* 2016, 353, 467–470, doi:10.1126/science.aaf4767.
182. García-Muelas, R.; Dattila, F.; Shinagawa, T.; Martín, A.J.; Pérez-Ramírez, J.; López, N. Origin of the Selective Electroreduction of Carbon Dioxide to Formate by Chalcogen Modified Copper. *Journal of Physical Chemistry Letters* 2018, 9, 7153–7159, doi:10.1021/acs.jpcclett.8b03212.
183. Zhang, X.; Guo, S.X.; Gandionco, K.A.; Bond, A.M.; Zhang, J. Electrocatalytic Carbon Dioxide Reduction: From Fundamental Principles to Catalyst Design. *Mater Today Adv* 2020, 7, doi:10.1016/j.mtadv.2020.100074.
184. Y. Hori, A. Murata, T. Tsukamoto, H. Wakebe, O. Koga, H. Yamazaki, Adsorption of carbon monoxide at a copper electrode accompanied by electron transfer observed by voltammetry and IR spectroscopy, *Electrochimica Acta*. 39 (1994) 2495–2500. [https://doi.org/10.1016/0013-4686\(94\)00259-2](https://doi.org/10.1016/0013-4686(94)00259-2).
185. T. Jaster, A. Gawel, D. Siegmund, J. Holzmann, H. Lohmann, E. Klemm, U.-P. Apfel, Electrochemical CO₂ reduction toward multicarbon alcohols - The microscopic world of catalysts & process conditions, *IScience*. 25 (2022) 104010. <https://doi.org/10.1016/j.isci.2022.104010>.
186. D. Cheng, Z.J. Zhao, G. Zhang, P. Yang, L. Li, H. Gao, S. Liu, X. Chang, S. Chen, T. Wang, G.A. Ozin, Z. Liu, J. Gong, The nature of active sites for carbon dioxide electroreduction over oxide-derived copper catalysts, *Nature Communications*. 12 (2021) 1–8. <https://doi.org/10.1038/s41467-020-20615-0>.

187. R. Kortlever, J. Shen, K.J.P. Schouten, F. Calle-Vallejo, M.T.M. Koper, Catalysts and Reaction Pathways for the Electrochemical Reduction of Carbon Dioxide, *Journal of Physical Chemistry Letters*. 6 (2015) 4073–4082. <https://doi.org/10.1021/acs.jpcclett.5b01559>.
188. J.H. Montoya, C. Shi, K. Chan, J.K. Nørskov, Theoretical insights into a CO dimerization mechanism in CO₂ electroreduction, *Journal of Physical Chemistry Letters*. 6 (2015) 2032–2037. <https://doi.org/10.1021/acs.jpcclett.5b00722>.
189. E. Pérez-Gallent, M.C. Figueiredo, F. Calle-Vallejo, M.T.M. Koper, Spectroscopic Observation of a Hydrogenated CO Dimer Intermediate During CO Reduction on Cu(100) Electrodes, *Angewandte Chemie*. 129 (2017) 3675–3678. <https://doi.org/10.1002/ange.201700580>.
190. J.D. Goodpaster, A.T. Bell, M. Head-Gordon, Identification of Possible Pathways for C-C Bond Formation during Electrochemical Reduction of CO₂: New Theoretical Insights from an Improved Electrochemical Model, *Journal of Physical Chemistry Letters*. 7 (2016) 1471–1477. <https://doi.org/10.1021/acs.jpcclett.6b00358>.
191. K. Jiang, R.B. Sandberg, A.J. Akey, X. Liu, D.C. Bell, J.K. Nørskov, K. Chan, H. Wang, Metal ion cycling of Cu foil for selective C-C coupling in electrochemical CO₂ reduction, *Nature Catalysis*. 1 (2018) 111–119. <https://doi.org/10.1038/s41929-017-0009-x>.
192. Jin, L.; Seifitokaldani, A. In Situ Spectroscopic Methods for Electrocatalytic CO₂ Reduction. *Catalysts* 2020, 10, 481–588, doi:10.3390/catal10050481.
193. Zhan, C.; Dattila, F.; Rettenmaier, C.; Bergmann, A.; Kühn, S.; García-Muelas, R.; López, N.; Roldan Cuenya, B. Revealing the CO Coverage-Driven C-C Coupling Mechanism for Electrochemical CO₂ Reduction on Cu₂O Nanocubes via Operando Raman Spectroscopy. *ACS Catal* 2021, 11, 7694–7701, doi:10.1021/acscatal.1c01478.
194. Jiang, S.; Klingan, K.; Pasquini, C.; Dau, H. New Aspects of Operando Raman Spectroscopy Applied to Electrochemical CO₂ Reduction on Cu Foams. *Journal of Chemical Physics* 2019, 150, doi:10.1063/1.5054109.
195. da Silva, A.H.M.; Lenne, Q.; Vos, R.E.; Koper, M.T.M. Competition of CO and Acetaldehyde Adsorption and Reduction on Copper Electrodes and Its Impact on n-Propanol Formation. *ACS Catal* 2023, 13, 4339–4347, doi:10.1021/acscatal.3c00190.

196. Nitopi, S.; Bertheussen, E.; Scott, S.B.; Liu, X.; Engstfeld, A.K.; Horch, S.; Seger, B.; Stephens, I.E.L.; Chan, K.; Hahn, C.; et al. Progress and Perspectives of Electrochemical CO₂ Reduction on Copper in Aqueous Electrolyte. *Chem Rev* 2019, 119, 7610–7672, doi:10.1021/acs.chemrev.8b00705.
197. Rutkowska, I.A.; Chmielnicka, A.; Krzywiecki, M.; Kulesza, P.J. Toward Effective CO₂ Reduction in an Acid Medium: Electrocatalysis at Cu₂O-Derived Polycrystalline Cu Sites Immobilized within the Network of WO₃ Nanowires. *ACS Measurement Science Au* 2022, 2, 553–567, doi:10.1021/acsmesuresciau.2c0001
198. J.A. Turner, Sustainable Hydrogen Production, *Science*. 305 (2004) 972–974. <https://doi.org/10.1016/b978-0-444-64203-5.00001-0>.
199. K. Zeng, D. Zhang, Recent progress in alkaline water electrolysis for hydrogen production and applications, *Progress in Energy and Combustion Science*. 36 (2010) 307–326. <https://doi.org/10.1016/j.pecs.2009.11.002>.
200. D.M.F. Santos, C.A.C. Sequeira, D. Macciò, A. Saccone, J.L. Figueiredo, Platinum-rare earth electrodes for hydrogen evolution in alkaline water electrolysis, *International Journal of Hydrogen Energy*. 38 (2013) 3137–3145. <https://doi.org/10.1016/j.ijhydene.2012.12.102>.
201. Z. Wang, J. Yang, J. Gan, W. Chen, F. Zhou, X. Zhou, Z. Yu, J. Zhu, X. Duan, Y. Wu, Electrochemical conversion of bulk platinum into platinum single-atom sites for the hydrogen evolution reaction, *Journal of Materials Chemistry A*. 8 (2020) 10755–10760. <https://doi.org/10.1039/d0ta02351e>.
202. Y. Lee, J. Suntivich, K.J. May, E.E. Perry, Y. Shao-Horn, Synthesis and activities of rutile IrO₂ and RuO₂ nanoparticles for oxygen evolution in acid and alkaline solutions, *Journal of Physical Chemistry Letters*. 3 (2012) 399–404. <https://doi.org/10.1021/jz2016507>.
203. J.K. Nørskov, T. Bligaard, J. Rossmeisl, C.H. Christensen, Towards the computational design of solid catalysts, *Nature Chemistry*. 1 (2009) 37–46. <https://doi.org/10.1038/nchem.121>.
204. Y. Meng, M. Wang, Z. Zhu, T. Jiang, Z. Liu, N. Chen, C. Shen, Q. Peng, W. Chen, Multifunctional Nickel-Cobalt Phosphates for High-Performance Hydrogen Gas Batteries and Self-Powered Water Splitting, *ACS Applied Energy Materials*. 4 (2021) 12927–12934. <https://doi.org/10.1021/acsaem.1c02582>.
205. P.W. Menezes, C. Panda, S. Loos, F. Bunschei-Bruns, C. Walter, M. Schwarze, X. Deng, H. Dau, M. Driess, A structurally versatile nickel phosphite acting as a robust bifunctional electrocatalyst for overall water splitting, *Energy and Environmental Science*. 11 (2018) 1287–1298. <https://doi.org/10.1039/c7ee03619a>.

206. M.G. Walter, E.L. Warren, J.R. McKone, S.W. Boettcher, Q. Mi, E.A. Santori, N.S. Lewis, Solar water splitting cells, *Chemical Reviews*. 110 (2010) 6446–6473. <https://doi.org/10.1021/cr1002326>.
207. S.K. Han, C. Gu, S. Zhao, S. Xu, M. Gong, Z. Li, S.H. Yu, Precursor Triggering Synthesis of Self-Coupled Sulfide Polymorphs with Enhanced Photoelectrochemical Properties, *J Am Chem Soc*. 138 (2016) 12913–12919. <https://doi.org/10.1021/jacs.6b06609>.
208. X. Wang, W. Li, D. Xiong, L. Liu, Fast fabrication of self-supported porous nickel phosphide foam for efficient, durable oxygen evolution and overall water splitting, *Journal of Materials Chemistry A*. 4 (2016) 5639–5646. <https://doi.org/10.1039/c5ta10317g>.
209. X.Y. Wang, X.P. Han, Y. He, W. bin Hu, Y. da Deng, Hierarchical porous NiS@NiO nanoarrays in situ grown on nickel foam as superior electrocatalyst for water splitting, *International Journal of Electrochemical Science*. 15 (2020) 3563–3577. <https://doi.org/10.20964/2020.04.19>.
210. Y. Li, C. Zhao, Two-dimensional NiTe nanosheets anchored on three-dimensional nickel foam as high-performance catalyst for electrochemical water oxidation, *Advanced Materials Letters*. 8 (2017) 916–921. <https://doi.org/10.5185/amlett.2017.1669>.
211. Z. Wang, L. Zhang, In situ growth of NiTe nanosheet film on nickel foam as electrocatalyst for oxygen evolution reaction, *Electrochemistry Communications*. 88 (2018) 29–33. <https://doi.org/10.1016/j.elecom.2018.01.014>.
212. Y. Rao, Y. Wang, H. Ning, P. Li, M. Wu, Hydrotalcite-like Ni(OH)₂ Nanosheets in Situ Grown on Nickel Foam for Overall Water Splitting, *ACS Applied Materials and Interfaces*. 8 (2016) 33601–33607. <https://doi.org/10.1021/acsami.6b11023>.
213. F.A. Rasmussen, K.S. Thygesen, Computational 2D Materials Database: Electronic Structure of Transition-Metal Dichalcogenides and Oxides, *Journal of Physical Chemistry C*. 119 (2015) 13169–13183. <https://doi.org/10.1021/acs.jpcc.5b02950>.
214. E.J. Popczun, J.R. McKone, C.G. Read, A.J. Biacchi, A.M. Wiltrout, N.S. Lewis, R.E. Schaak, Nanostructured nickel phosphide as an electrocatalyst for the hydrogen evolution reaction, *J Am Chem Soc*. 135 (2013) 9267–9270. <https://doi.org/10.1021/ja403440e>.
215. J. Tian, Q. Liu, A.M. Asiri, X. Sun, Self-Supported Nanoporous Cobalt Phosphide Nanowire Arrays : An, *J. Am. Chem. Soc*. 136 (2014) 7587–7590.

216. L. Liao, S. Wang, J. Xiao, X. Bian, Y. Zhang, M.D. Scanlon, X. Hu, Y. Tang, B. Liu, H.H. Girault, A nanoporous molybdenum carbide nanowire as an electrocatalyst for hydrogen evolution reaction, *Energy and Environmental Science*. 7 (2014) 387–392. <https://doi.org/10.1039/c3ee42441c>.
217. L. Trotochaud, S.L. Young, J.K. Ranney, S.W. Boettcher, Nickel-Iron oxyhydroxide oxygen-evolution electrocatalysts: The role of intentional and incidental iron incorporation, *J Am Chem Soc*. 136 (2014) 6744–6753. <https://doi.org/10.1021/ja502379c>.
218. J. Yin, J. Jin, H. Lin, Z. Yin, J. Li, M. Lu, L. Guo, P. Xi, Y. Tang, C.H. Yan, Optimized Metal Chalcogenides for Boosting Water Splitting, *Advanced Science*. 7 (2020). <https://doi.org/10.1002/advs.201903070>.
219. N.T. Suen, S.F. Hung, Q. Quan, N. Zhang, Y.J. Xu, H.M. Chen, Electrocatalysis for the oxygen evolution reaction: Recent development and future perspectives, *Chemical Society Reviews*. 46 (2017) 337–365. <https://doi.org/10.1039/c6cs00328a>.
220. B.M. Pires, P.L. dos Santos, V. Katic, S. Strohauer, R. Landers, A.L.B. Formiga, J.A. Bonacin, Electrochemical water oxidation by cobalt-Prussian blue coordination polymer and theoretical studies of the electronic structure of the active species, *Dalton Transactions*. 48 (2019) 4811–4822. <https://doi.org/10.1039/c8dt04660c>.
221. M.J. Craig, G. Coulter, E. Dolan, J. Soriano-López, E. Mates-Torres, W. Schmitt, M. García-Melchor, Universal scaling relations for the rational design of molecular water oxidation catalysts with near-zero overpotential, *Nature Communications*. 10 (2019) 1–9. <https://doi.org/10.1038/s41467-019-12994-w>.
222. I. Roger, M.A. Shipman, M.D. Symes, Earth-abundant catalysts for electrochemical and photoelectrochemical water splitting, *Nature Reviews Chemistry*. 1 (2017). <https://doi.org/10.1038/s41570-016-0003>.
223. M. Wilken, I. Siewert, Electrocatalytic Hydrogen Production with a Molecular Cobalt Complex in Aqueous Solution *ChemElectroChem* 2020, 7, 217–221. <https://doi.org/10.1002/celec.201901913>

VITA

Ibrahim Munkaila Abdullahi obtained a Bachelor of Science degree in Chemistry (Honors) from Ahmadu Bello University, Zaria, Nigeria, in 2011, then attended King Fahd University of Petroleum and Minerals, Dhahran, Saudi Arabia, and graduated with a Master of Science degree in Chemistry (Organic Catalysis) in 2016. In Spring of 2017, he joined Dr. Vadym Mochalin's group at Missouri University of Science and Technology. He worked on fabricating luminescence nanodiamonds from high-pressure, high-temperature microcrystalline diamond and carbon nano-onions/silica glass composites for mechanical, electrical, and optical properties. He received a Master of Science in Chemistry (Nanomaterials) from Missouri University of Science and Technology in December 2020. And continued research in the nanomaterials field with Dr. Manshi Nath, where he focused on understanding catalysts design based on transition metal chalcogenides for electrochemical carbon dioxide reduction and water oxidation reactions. He received a Doctor of Philosophy in Chemistry from Missouri University of Science and Technology in July 2023.